Structural dynamics analysis in the presence of unmeasured excitations

Author:
Moore, Stephen

Publication Date:
2007

DOI:
https://doi.org/10.26190/unsworks/18059

School of Aerospace, Civil, and Mechanical Engineering
The University of New South Wales
Australian Defence Force Academy

Structural Dynamics Analysis in the Presence of Unmeasured Excitations

Stephen Moore

A thesis submitted for the Degree of Doctor of Philosophy

August 2006

Statement of Originality

I hereby declare that this submission is my own work and to the best of my knowledge it contains no materials previously published or written by another person, or substantial proportions of material which have been accepted for the award of any other degree or diploma at UNSW or any other educational institution, except where due acknowledgement is made in the thesis. Any contribution made to the research by others, with whom I have worked at UNSW or elsewhere, is explicitly acknowledged in the thesis. I also declare that the intellectual content of this thesis is the product of my own work, except to the extent that assistance from others in the project's design and conception or in style, presentation and linguistic expression is acknowledged.

Stephen Moore

August 2006

Copyright Statement

Authenticity Statement

'I certify that the Library deposit digital copy is a direct equivalent of the final officially approved version of my thesis. No emendation of content has occurred and if there are any minor variations in formatting, they are the result of the conversion to digital format.'

Signed ……………………………………………………..........................

Date ……………………………………………………..........................

Abstract

Methods for comprehensive structural dynamic analysis generally employ input-output modal analysis with a mathematical model of structural vibration using excitation and response data. Recently operational modal analysis methods using only vibration response data have been developed. In this thesis, both input-output and operational modal analysis, in the presence of significant unmeasured excitations, is considered. This situation arises when a test structure cannot be effectively isolated from ambient excitations or where the operating environment imposes dynamically-important boundary conditions.

The limitations of existing deterministic frequency-domain methods are assessed. A novel time-domain estimation algorithm, based on the estimation of a discrete-time autoregressive moving average with exogenous excitation (ARMAX) model, is proposed. It includes a stochastic component to explicitly account for unmeasured excitations and measurement noise. A criterion, based on the sign of modal damping, is incorporated to distinguish vibration modes from spurious modes due to unmeasured excitations and measurement noise, and to identify the most complete set of modal parameters from a group of estimated models.

Numerical tests demonstrate that the proposed algorithm effectively identifies vibration modes even with significant unmeasured random and periodic excitations. Random noise is superimposed on response measurements in all tests. Simulated systems with low modal damping, closely spaced modes and high modal damping are considered independently. The accuracy of estimated modal parameters is good except for degrees-of-freedom with a low response level but this could be overcome by appropriate placement of excitation and response measurement points.

These observations are reflected in experimental tests that include unmeasured periodic excitations over 200% the level of measured excitations, unmeasured random excitations at 90% the level of measured excitations, and the superposition of periodic and random unmeasured excitations. Results indicate advantages of the proposed algorithm over a deterministic frequency domain algorithm. Piezoceramic plates are used for structural excitation in one experimental case and the limitations of distributed

excitation for broadband analysis are observed and characterised in terms of actuator geometry and modal deformation.

The ARMAX algorithm is extended for use with response measurements exclusively. Numerical and experimental tests demonstrate its performance using time series data and correlation functions calculated from response measurements.

Acknowledgments

Acknowledgment and thanks are due to people who provided advice, support, and encouragement, as well as those that I have collaborated with during my time as a research student.

In particular, Professor Joseph Lai has patiently supervised my studies and I acknowledge his considerable efforts in facilitating this research project. My co-supervisors, Dr Frank Polanco and Dr Krishnakumar Shankar have both taken the time to offer advice and guidance on different aspects of my work, and I appreciate their interest in this work. Thanks to Professor Bob Randall, another of my co-supervisors, for his advice and for initially encouraging me to consider post-graduate study.

This research project was conducted as a task funded under the Australian Defence Science and Technology Organisation (DSTO) Centre of Expertise in Helicopter Structures and Diagnostics. I gratefully acknowledge research grants from DSTO as well as a University College Postgraduate Research Scholarship, which have supported my research.

I would like to thank a number of staff at the School of Aerospace, Civil, and Mechanical Engineering. Mrs Marion Burgess, Dr Andrew Dombek, Mr Andrew Roberts, and Dr Zhang Biaobiao have provided advice and technical expertise, and helped with experimentation during my studies.

Acknowledgment is due to Jon Couldrick, Orio Kieboom, Jeff McGuire, Antti Papinniemi, Chris Hang, and David Hanson; fellow students, who have provided support, friendship and much stimulating conversation over the years.

I am grateful for the support of my family; Christine, Peter, Tony & Sarah. Their understanding and encouragement, particularly during busy times, has been significant, and critical in enabling me to complete this project.

I have dedicated this thesis to my parents, Robert and Christine, in recognition of their many sacrifices made in support of my education.

Contents

List of Figures

List of Tables

Nomenclature

Acronyms and Abbreviations

AR	Autoregressive
ARMA	Autoregressive moving average
ARMAX	Autoregressive moving average with exogenous excitation
ARX	Autoregressive with exogenous excitation
BIC	Bayesian Information Criterion
CMIF	Complex modal indicator function
CVA	Canonical variate analysis
DFT	Discrete Fourier transform
DOF	Degree of freedom
EFDD	Enhanced frequency domain decomposition
EMA	Experimental modal analysis
ERA	Eigensystem realisation algorithm
FDD	Frequency domain decomposition
FEM	Finite element model
FFT	Fast Fourier transform
FIR	Finite impulse response
FPE	Final prediction error
FRF	Frequency response function
IIR	Infinite impulse response
I/O	Input-output
IRF	Impulse response function
ITD	Ibrahim time domain
IV	Instrumental variable
LS	Least squares
LSCE	Least squares complex exponential
MA	Moving average
MAC	Modal assurance criterion
MDOF	Multiple degree of freedom
MIMO	Multiple input multiple output
MISO	Multiple input single output

NExT	Natural excitation technique
NPDP	Number of positively damped poles
PC	Principal components
RFLS	Rational fraction least squares
SDOF	Single degree of freedom
SIMO	Single input multiple output
s/n	Signal-to-noise ratio
SISO	Single input single output
SSI	Stochastic subspace identification
SVD	Singular value decomposition
TF	Transfer function
UPC	Unweighted principal components

General Conventions

Scalar variables are italicised lower case; e.g. s

Vectors are lower case bold; e.g. $\mathbf{f}$

Matrices are upper case bold; e.g. $\mathbf{A}$

Symbols and Operators

$\mathbf{A}$	Autoregressive matrix
A	Cross-sectional area
$\mathbf{B}$	Exogenous matrix
$\mathbf{C}$	Moving average matrix
$\mathbf{D}$	Equivalent viscous damping
$\boldsymbol{D}$	Vector of electric flux density (C/m^2)
$\boldsymbol{E}$	Applied electric field vector (V/m)
E, E_x	Young's modulus; Young's modulus, x direction
$E(\cdot)$	Expectation
G_{xy}	Shear modulus, x-y plane.
$\mathbf{H}$	Transfer function matrix
$H(x-a)$	Heaviside step function

$\mathbf{I}, \mathbf{I}_s$	Identity matrix, $s \times s$ identity matrix
I	Moment of inertia
$\mathbf{K}$	Stiffness matrix
$\mathbf{L}_r$	Modal participation matrix for rth mode
$\mathbf{M}$	Mass matrix
M	Number of averages
N	Number of samples
$R_{ij}^{(r)}$	Residue for rth mode of the ijth transfer function or frequency response function
$\boldsymbol{S}^E$	Matrix of compliance coefficients (m^2/N)
T_s	Sampling period, seconds
V	Voltage (volts)

Φ_r	Mode shape matrix for rth mode
Ψ_r	Normal mode shape vector for rth mode
Ω	Rotor speed (rad/s)

b	Number of rotor blades
d_{mi}	Piezoelectric strain constant relating direction m and direction i
$\mathbf{f}(t)$	Continuous-time force vector
$\mathbf{f}[t]$	Discrete-time force vector
f	Frequency (Hz)
Δf	Frequency line spacing or resolution (Hz)
f_s	Sampling frequency (Hz)
i,j,k	Index, integer
j	$\sqrt{-1}$
m	Number of excitation channels; Index
n	Index
na	Order (degree) of autoregressive matrix polynomial
nb	Order of exogenous matrix polynomial

nc	Order of moving average matrix polynomial
p	Order of high order AR or ARX model;
	Index
q	Backshift operator: $\mathbf{x}[t].q^j = \mathbf{x}[t\text{-}j]$;
	Index
s	Laplace transform variable;
	Number of response channels
t	Time index
$\mathbf{w}[t]$	Discrete-time innovations sequence;
	Unmeasured disturbance or model error
$\mathbf{x}(t)$	Continuous-time displacement vector (displacement, velocity, or acceleration)
$\mathbf{y}[t]$	Discrete-time response vector
z	z transform variable

δ_{ij}	Kronecker delta function
$\delta(x\text{-}a)$	Dirac delta function
ε_i	Strain in direction i
ζ_r	Damping ratio of rth mode
λ, λ^*	Conjugate poles of a continuous-time transfer function
μ, μ^*	Conjugate poles of a discrete-time transfer function
ν, ν_{xy}	Poisson's ratio; Poisson's ratio, x-y plane
ξ^{σ}	Permittivity under constant stress conditions (F/m)
ρ	Material density (kg/m^3)
σ_i	Stress in direction i
ϕ	Modal constant
ω	Circular frequency (rad/s)
$\omega_{n\,r}$	Natural circular frequency of rth mode (rad/s)
$\omega_{d\,r}$	Damped natural circular frequency of rth mode (rad/s)

$\{\cdot\cdot\}$	Vector or series

$[\cdots]$	Matrix
$[\cdot]^H$	Complex conjugate (Hermitian) transpose
$[\cdot]^T$	Transpose
$[\cdot]^{-1}$	Matrix inverse
$(\cdot)^*$	Conjugate
$\dot{v}, \ddot{v}$	Time derivatives: $\frac{dv}{dt}, \frac{d^2v}{dt^2}$
$*$	Convolution operator
$\otimes$	Kronecker product
$col(\cdot)$	Column vector formed by stacking matrix columns under each other, starting with the left-hand column at the top
$\det(\cdot)$	Matrix determinant
$eig[\cdot]$	Eigenvalues of matrix
$\hat{\mathbf{A}}$	Estimate of **A**
$\Im$	Fourier transform
$\Im^{-1}$	Inverse Fourier transform

Chapter 1 Introduction

1.1 Introduction

The work described in this thesis is motivated by the longer term goal of being able to predict the effects of structural modification on helicopter structures. In order to achieve this goal, it is essential to develop methodologies that could be used to establish a good dynamics model of a helicopter structure. The dynamic behaviour or vibration response of a helicopter fuselage is also a critical consideration in the design, operation, and ongoing maintenance of the helicopter. The general aim, therefore, is to develop experimental and analytical tools for more accurate and comprehensive analysis of helicopter structural dynamics, particularly during flight. This would ultimately allow a wider range of predictive work to be carried out with analytical or numerical models given that these models could initially be validated and updated using good quality experimental data. The work in this thesis is largely concerned with experimental methods that yield accurate structural dynamic properties and have the potential to be used for grounded helicopters or for helicopters in flight.

A variety of experimental, analytical and numerical methods are currently used to study the dynamic behaviour of helicopter fuselage structures. Historically, the most basic requirement of structural dynamics analysis was to identify structural resonances and ensure they were not close to the frequency or harmonics of main-rotor excitation forces [1]. The main-rotor loads are periodic and occur at the rotor angular frequency (Ω) and its harmonics, as well as integer multiples of the blade pass frequency, denoted $k{\cdot}b{\cdot}\Omega$, where $k = 1, 2, 3, \ldots$, and b is the number of rotor blades. In addition to these loads, other sources of vibration are summarised by Bielawa [2]: excitation by pressure pulses from main-rotor blade downwash and trailing vortices, which also occur at frequencies of $k{\cdot}b{\cdot}\Omega$; excitation due to other rotating components, for example, engines, gearboxes and tail-rotor drive shafts; and excitation by aerodynamic sources like buffeting from turbulent flow. The effect of these loads on the helicopter fuselage and the coupled dynamic behaviour of the rotor and fuselage are extremely complex phenomena and have attracted a range of experimental and numerical analysis methods [1, 2].

Design and modification of helicopter fuselages usually relies on finite-element models (FEMs) for detailed static and dynamic analysis [3-7]. FEMs are necessarily simplified models and in many cases do not include accurate parameter specifications for joints and other secondary structural elements, for example engines and drive train components, main and tail rotors. Model updating can be employed to improve the accuracy of FEMs and is obviously dependent on the accuracy of experimental data and the capacity of the FEM to account for boundary conditions and uncertainties in structural configurations. Several model updating methods have been developed over the last few years, ranging from manual modification of FEM parameters to more sophisticated techniques based on intelligent algorithms [8-14]. An issue with updating helicopter FEMs is obtaining experimental data that accurately represents the dynamic behaviour of helicopters, as this is dependent on the configuration and state (flying, grounded etc.) of the helicopter. A number of experimental techniques based on modal analysis can be used to obtain data for a grounded helicopter [5, 7, 15-18]; however, these techniques cannot be readily applied to a helicopter in flight. An alternative approach, termed response-only or operational modal analysis, only requires response measurements to estimate the dynamic behaviour of structures. To date, these methods have been applied successfully to civil structures, for example bridges and towers [19, 20], as well as aircraft [20-24], including helicopters [25, 26]. Results from these response-only methods can be used in addition to input-output modal analysis results for updating of FEMs, or direct updating of modal parameters [27, 28].

An area that has not been widely considered is the application of modal analysis methods to cases where significant unmeasured excitations are present in addition to measured excitations applied to the structure under test. Such a technique could be applied in the analysis of structures in their operational environment, given that a wide range of ambient (unmeasured) excitation types could be accounted for. This would be useful for the study of helicopter structural dynamics as it would allow modal analysis to be carried out in a wide range of operating conditions: while the helicopter is grounded and possibly stripped down or when the helicopter is in flight. A subsequent issue that arises is the application of a measurable excitation force. Existing methods include electrodynamic or hydraulic actuators, although the use of piezoceramic actuators could be advantageous because of their relatively small size.

Therefore, in this thesis, the problem of structural dynamics analysis in the presence of unmeasured excitations using experimental modal analysis is considered. Preliminary investigations of existing experimental and numerical methods are carried out before in-depth analysis of a modal analysis algorithm for use with excitation and response data obtained in the presence of significant unmeasured excitations. Piezoceramic actuators are considered as an alternative method for structural excitation in experimental modal analysis; the unique characteristics of piezoceramic actuators could allow distributed excitation of a large structure in operational conditions.

1.2 Thesis Outline

In Chapters 2 and 3, existing experimental and numerical analysis methods are reviewed. Input-output modal parameter estimation algorithms, as well as signal processing methods used to enhance signal-to-noise ratio (s/n) of measured data, are discussed in Chapter 3. Two experimental case studies are considered: modal testing of an aluminium beam and modal testing of a helicopter-like structure. The experimental case studies demonstrate the use of an existing frequency-domain modal analysis technique used in conjunction with periodic excitation and synchronous averaging. The effect of unmeasured excitations on estimated results is investigated and the structural excitation of the aluminium beam using piezoceramic actuators is demonstrated as an alternative to typical excitation methods.

In Chapter 3, FEM updating methods are reviewed and experimental results from the helicopter-like structure are used to gain insight into a number of common issues in FEM updating: correlation of experimental and FEM dynamic behaviour; FEM updating in the presence of non-linear behaviour and poor measurements; and the use of updated FEMs to predict the effects of structural modifications.

A more formal analysis of piezoceramic plates for structural excitation in experimental modal analysis is presented in Chapter 4. An approximate analytical model is derived for pairs of actuators applied to an aluminium beam. The effectiveness of pairs of actuators in exciting vibration modes is assessed in order to gain insight into experimental results discussed in Chapter 2. In addition, the extraction of mode shapes from measured or estimated transfer functions is discussed. The approximate analytical model is verified by FEM results and experimental measurements on a free-free aluminium beam. The approximate analytical model is then used to predict the effectiveness of actuator pairs in exciting modes of a cantilever aluminium beam used for experiments discussed in Chapter 6.

In Chapter 5, the use of system identification techniques for modal parameter estimation is investigated. A novel algorithm is derived based on the estimation of an autoregressive moving average with exogenous excitation (ARMAX) model. This new algorithm explicitly models unmeasured excitations and is therefore appropriate for situations where the structure under test cannot be effectively isolated from other sources of excitation, or where the boundary conditions present during operation impose important dynamic constraints on the structure under test. As noted above, these situations are encountered in the study of helicopter structural dynamics. The algorithm includes tools to distinguish vibration modes from spurious modes, which arise in cases with significant measurement noise and also when unmeasured excitations include periodic components. In addition, a novel model selection criterion is incorporated into the algorithm.

Numerical tests on a simple lumped mass system are discussed in Chapter 6 to demonstrate the performance of the ARMAX algorithm in identifying modal parameters in the presence of measurement noise and significant unmeasured periodic and random excitations. Further tests demonstrate the algorithm's effectiveness for systems with high damping and also for cases with closely spaced modes where the frequency of an unmeasured periodic excitation is close to a modal natural frequency. A method to incorporate the frequencies of unmeasured periodic excitations into the estimation algorithm is also introduced and tested using simulated systems. Experimental testing of the algorithm is conducted using data obtained from a cantilever aluminium beam. Cases including unmeasured periodic and random excitation are considered and piezoceramic actuators are used for structural excitation in these cases.

Further testing of the ARMAX algorithm is reported in Chapter 7. A helicopter-like structure is used as a representative case and the effect of unmeasured random and periodic excitations is again considered. Closely spaced modes, local modes, and unmeasured periodic excitations at frequencies close to vibration modes are characteristics of this experimental case. Periodic measured excitation allows synchronous averaging of measured data and the effect of this method in improving the accuracy of estimated modal parameters is assessed. Results from an existing frequency domain modal analysis method are used to compare with results from the ARMAX algorithm.

A preliminary investigation into the adaptation of the ARMAX estimation algorithm for use with response measurements in the absence of any measured excitation is reported in Chapter 8. Two adapted algorithms are proposed and tested with simulated and also experimental data.

Concluding remarks, a summary of major work, and recommendations for future work are included in Chapter 9.

Chapter 2 Modal Analysis Techniques

2.1 Introduction

The introduction in Chapter 1 suggested that modal analysis is a principal experimental technique used for analysis of helicopter structural dynamics. In the following section, the theoretical concepts of modal analysis and some of the common algorithms for modal parameter estimation are reviewed. Time-domain or synchronous averaging is a method for improving signal-to-noise ratio (s/n) of measured data and the theory of time-domain averaging is reviewed in section 2.3. Two experimental case studies are discussed in sections 2.4 and 2.5. These studies investigate the use of periodic impulse excitation and synchronous averaging as a means of improving signal-to-noise ratio of measurements where a component of the excitation is not explicitly measured. The use of piezoceramic actuators for structural excitation in modal analysis is demonstrated in the first experimental case study.

2.2 Review of Modal Parameter Estimation Techniques

Experimental modal analysis is a method for comprehensive analysis of a structure's dynamic behaviour. It involves measuring vibration response due to a known excitation force and processing these data to estimate a set of modal parameters (the modal model), namely natural frequencies, damping, and mode shapes, which summarise the structural dynamics in a given frequency range.

The elastic dynamic behaviour of a structure is assumed to be governed by an *n* degree-of-freedom (DOF) linear differential equation [29]:

$$\mathbf{M} \cdot \ddot{\mathbf{x}}(t) + \mathbf{D} \cdot \dot{\mathbf{x}}(t) + \mathbf{K} \cdot \mathbf{x}(t) = \mathbf{f}(t), \tag{2.1}$$

which is also known as the physical or spatial model. $\mathbf{f}(t)$ is a vector of forces acting at each DOF and $\mathbf{x}(t)$ and its time derivatives correspond to the displacement, velocity, and acceleration at each DOF. $\mathbf{M}$ and $\mathbf{K}$ are the real, symmetric mass and stiffness matrices and $\mathbf{D}$ is the real, symmetric damping matrix that describes the equivalent viscous damping of the system. A transfer function relating the excitation and response vectors is established by taking the Laplace transform of equation (2.1), assuming zero initial conditions:

$$\left[\mathbf{M}s^2 + \mathbf{C}s + \mathbf{K}\right]\{X(s)\} = \{F(s)\}, \tag{2.2}$$

and rearranging;

$$\{X(s)\} = \mathbf{H}(s)\{F(s)\} = \left[\mathbf{M}s^2 + \mathbf{C}s + \mathbf{K}\right]^{-1}\{F(s)\}, \tag{2.3}$$

where $\mathbf{H}(s)$ is the transfer function matrix. The transfer function matrix can be factorised into [29]

$$\mathbf{H}(s) = \sum_{r=1}^{n} \frac{[R_r]}{s-\lambda_r} + \frac{[R_r^*]}{s-\lambda_r^*}; \tag{2.4}$$

λ_r is a transfer function pole, $[R_r]$ is the residue matrix, and $(\cdot)^*$ denotes the complex conjugate. Frequency and damping information is extracted from the transfer function poles using the relation $\lambda_r, \lambda_r^* = -\varsigma_r \omega_{n\,r} \pm j\omega_{n\,r}\sqrt{1-\varsigma^2}$; $\omega_{n\,r}$ and ς_r are the undamped natural frequency and the damping ratio of the *r*th mode, respectively.

The frequency response function (FRF) matrix is obtained by substituting $s = j\omega$ into equation (2.4)

$$\mathbf{H}(j\omega) = \sum_{r=1}^{n} \mathbf{\Phi}_r \left[\frac{1}{j\omega - \lambda_r}\right] \mathbf{L}_r \, . \tag{2.5}$$

The modal residue matrix is factorised into modal participation factors and mode shape vectors: $[R_r] = \mathbf{L}_r \mathbf{\Phi}_r^T$; or $R_{pq}^{(r)} = L_{pq}^{(r)} \Phi_{pq}^{(r)}$ for the participation factor and modal coefficient between points *p* and *q* for mode *r*. Mode shapes are defined as

$$\Phi_{p\,r} = \begin{Bmatrix} \phi_{p1} \\ \phi_{p2} \\ \vdots \\ \phi_{pn} \end{Bmatrix}, \tag{2.6}$$

where $\Phi_{p\,r}$ is the pth column of $\mathbf{\Phi}_r$, but can also be defined in terms of the modal residues

$$\Phi_{p\,r} = \begin{Bmatrix} R_{p1} \\ R_{p2} \\ \vdots \\ R_{pn} \end{Bmatrix}. \tag{2.7}$$

Equation (2.7) implies that the modal participation factor for that reference point (excitation or response) is normalised to unity.

A range of methods to identify modal parameters from measured data have been developed, and these can be broadly grouped by the type of the mathematical model, equivalent to equations (2.1) - (2.5), that is used as a basis for modal parameter estimation.

The simplest and perhaps most intuitively attractive method is the peak picking method [30, 31]. For a lightly damped structure with well-spaced modes, the resonant peaks will be easily identifiable in the FRF. An estimate of damping can be obtained by a number methods, for example, measuring half-power (3dB) bandwidth [30, 31], or by transforming a band-limited (about the resonant peak) FRF into the time domain and using logarithmic decrement relationships. For the case of light damping, equation (2.5) is approximated by

$$\mathbf{H}(j\omega_r) \approx \sum_{r=1}^{n} \frac{R_{pq\,r}}{\varsigma_r \omega_r}, \tag{2.8}$$

which is solved for the modal residue $R_{pq\,r}$ using the estimated natural frequency and damping.

This method is also categorised as a single degree-of-freedom (SDOF) method, which follows from the fact that it uses a SDOF model as a basis for identifying modal parameters. While this method is quick to implement with spectrum analysers, the accuracy of results suffers due to limited resolution of the FRF, the presence of closely spaced or coupled modes, and high modal damping.

The complex modal indicator function (CMIF) [32, 33] is a modal parameter estimation method based on the singular value decomposition of the FRF matrix. The SVD of the FRF matrix is defined as [32]

$$\mathbf{H}(j\omega) = \mathbf{U}(j\omega)\mathbf{\Sigma}(j\omega)\mathbf{V}^{H}(j\omega), \tag{2.9}$$

where $\mathbf{U}(j\omega)$ and $\mathbf{V}(j\omega)$ are the left and right singular vector matrices, $\mathbf{\Sigma}(j\omega)$ is a diagonal matrix of singular values, and $(\cdot)^{H}$ is the complex conjugate transpose. Evaluating equation (2.9) at a natural frequency and comparing with equation (2.5) shows that the left singular vectors correspond to the mode shapes and the right singular vectors correspond to the modal participation factors. Plotting the singular values as a function of frequency reveals that local maxima correspond to natural frequencies. The CMIF also reveals the presence of repeated modes for the cases where the number of reference channels (columns of the LHS equation 2.9) is greater or equal to the degree of multiplicity of the repeated modes [32, 33]. Shih et al [32] demonstrated this technique in an experimental study of a circular plate. The multiple repeated roots were clearly shown by the CMIF, and estimated modal parameters compared well with results obtained from a polyreference time domain algorithm. The authors noted that initial pole estimates were limited by the resolution of the FRF and a second stage was required to obtain more accurate frequency and damping estimates, as well as properly scaled mode shapes. The SVD in the CMIF method rejects the effects of measurement noise and pre-processing of measured data, for example using spectral averaging, can enhance the accuracy of the CMIF when used with noisy measurements.

Other approaches to modal parameter estimation have been inspired by system identification theory. These have been developed independently and are based on both frequency domain and time domain techniques. It has since been shown that these methods can be derived from a general matrix polynomial model of a dynamic system [33, 34], and a summary of this approach is taken from Allemang and Brown [33].

Consider a rational polynomial description of a FRF between points p and q on a structure:

$$H_{pq}(j\omega)=\frac{X_p(j\omega)}{F_q(j\omega)}=\frac{\beta_n(j\omega)^n+\beta_{n-1}(j\omega)^{n-1}+\cdots+\beta_1(j\omega)^1+\beta_0(j\omega)^0}{\alpha_m(j\omega)^m+\alpha_{m-1}(j\omega)^{m-1}+\cdots+\alpha_1(j\omega)^1+\alpha_0(j\omega)^0}\,. \tag{2.10}$$

Equation (2.10) is rewritten as a linear combination of the excitation and response,

$$\sum_{k=0}^{m}\alpha_k(j\omega)^k X_p(j\omega)=\sum_{k=0}^{n}\beta_k(j\omega)^k F_q(j\omega), \tag{2.11}$$

and further rearranged to yield an expression in terms of unknown coefficients and a FRF (which can easily be measured):

$$\sum_{k=0}^{m}\alpha_k(j\omega)^k H_{pq}(j\omega)=\sum_{k=0}^{n}\beta_k(j\omega)^k\,. \tag{2.12}$$

The single-input single-output (SISO) model in equation (2.12) can be generalised to the multiple-input multiple-output (MIMO) case

$$\sum_{k=0}^{m}\left[[\boldsymbol{\alpha}_k](j\omega)^k\right][\mathbf{H}(j\omega)]=\sum_{k=0}^{n}\left[[\boldsymbol{\beta}_k](j\omega)^k\right]. \tag{2.13}$$

Equation (2.12) and (2.13) are the basis for a number of frequency domain estimation algorithms, for example rational fraction polynomial (RFP) [35] and orthogonal polynomial [36, 37]. It should be noted that frequency domain models like equation (2.13) can model the effects of out-of-band modes by increasing the order of the RHS polynomial, which effectively includes ‘residual’ terms in equation (2.10). It is well known [31] that this has a significant effect on the accuracy of estimated modal parameters within the analysis frequency band.

An analogous development can be carried out in the time domain. A rational polynomial representation of the discrete-time transfer function is [30]

$$H_{pq}(z) = \frac{X_p(z)}{F_q(z)} = \frac{b_n(z)^n + b_{n-1}(z)^{n-1} + \cdots + b_1(z)^1 + b_0(z)^0}{a_m(z)^m + a_{m-1}(z)^{m-1} + \cdots + a_1(z)^1 + 1} \tag{2.14}$$

or

$$\left(a_m(z)^m + a_{m-1}(z)^{m-1} + \cdots + a_1(z)^1 + 1\right)X_p(z) = \left(b_n(z)^n + b_{n-1}(z)^{n-1} + \cdots + b_1(z)^1 + b_0(z)^0\right)F_q(z) \tag{2.15}$$

Applying the inverse *z*-transform to equation (2.15) yields the time-domain expression

$$\begin{aligned} x[t] + a_1 x[t-1] + \ldots + a_{m-1}x[t-m+1] + a_m x[t-m] \\ = b_0 f[t] + b_1 f[t-1] + \cdots + b_{n-1} f[t-n+1] + b_n f[t-n], \end{aligned} \tag{2.16}$$

which can be generalised to the MIMO case

$$\sum_{k=0}^{m} \mathbf{A}_k \cdot \mathbf{x}[t-k] = \sum_{k=0}^{n} \mathbf{B}_k \cdot \mathbf{f}[t-k]. \tag{2.17}$$

Equation (2.16) and its vector equivalent are referred to as autoregressive with exogenous excitation (ARX) models.

Impulse response or free decay measurements are modelled by equation (2.16) after setting the RHS to zero. This is the starting point for the polyreference method, least squares complex exponential methods (LSCE), and Ibrahim Time Domain (ITD) method [34].

The polyreference method solves the coefficients of the system [34]

$$\mathbf{h}(k)+\mathbf{A}_{p-1}\mathbf{h}(k-1)+\cdots+\mathbf{A}_0\mathbf{h}(k-p)=\mathbf{e}(k), \tag{2.18}$$

where $\mathbf{h}(k)$ is the kth sample of an impulse response function (IRF). The modal parameters are obtained from the eigenvalue decomposition of the companion matrix, which is formed from the estimated coefficients:

$$\mathbf{A}_c=\begin{bmatrix} \mathbf{0} & \mathbf{I} & \mathbf{0} & \cdots & \mathbf{0} \\ \mathbf{0} & \mathbf{0} & \mathbf{I} & \cdots & \mathbf{0} \\ \vdots & \vdots & \vdots & \vdots & \vdots \\ \mathbf{0} & \mathbf{0} & \mathbf{0} & \cdots & \mathbf{I} \\ -\mathbf{A}_0 & -\mathbf{A}_1 & -\mathbf{A}_2 & \cdots & -\mathbf{A}_{p-1} \end{bmatrix} \tag{2.19}$$

$$\mathbf{A}_c=\mathbf{\Pi}\begin{bmatrix} \boldsymbol{\mu} & \mathbf{0} \\ \mathbf{0} & \boldsymbol{\mu}' \end{bmatrix}\mathbf{\Pi}^{-1} \tag{2.20}$$

where $\boldsymbol{\mu}$ is a diagonal matrix of discrete-time eigenvalues corresponding to vibration modes, and $\mu_r=e^{\lambda_r T_s}$ is a diagonal element. $\boldsymbol{\mu}'$ corresponds to noise eigenvalues, which result from setting the order of equation (2.18) higher than the number of modes represented in measured data. Mode shapes are obtained from

$$\Pi_r=\begin{Bmatrix} \Phi_r \\ \lambda_r\Phi_r \\ \vdots \\ \lambda_r^{p-1}\Phi_r \end{Bmatrix}, \tag{2.21}$$

where Π_i is the ith column of $\mathbf{\Pi}$.

The LSCE method is the same as the polyreference method, but can be derived from the fact that IRFs are sums of complex exponential functions [30]. The ITD method involves setting up a system of equations from impulse response data [30]

$$x_i(t+\tau)=\sum_{r=1}^{2N}\phi_{i\,r}e^{\lambda_r(t+\tau)} \tag{2.22}$$

for a number of response measurement points, *i*, time instants *t*, and delays, τ, such that

$$\begin{bmatrix} x_1(t_1+\tau) & \dots & x_1(t_{2N}+\tau) \\ \dots & \dots & \dots \\ x_N(t_1+\tau) & \dots & x_N(t_{2N}+\tau) \end{bmatrix} = \begin{bmatrix} \{\phi\}_1 & \dots & \{\phi\}_{2N} \end{bmatrix} \begin{bmatrix} e^{\lambda_1\tau} & & \mathbf{0} \\ & \ddots & \\ \mathbf{0} & & e^{\lambda_{2N}\tau} \end{bmatrix} \begin{bmatrix} e^{\lambda_1 t_1} & \dots & e^{\lambda_1 t_{2N}} \\ \dots & \dots & \dots \\ e^{\lambda_{2N} t_1} & \dots & e^{\lambda_{2N} t_{2N}} \end{bmatrix} \tag{2.23}$$

or

$$\mathbf{X}_\tau = \mathbf{\Psi}\,\mathbf{\Delta}\,\mathbf{\Lambda} \tag{2.24}$$

The following system of equations is set up using IRF data at different time delays, $\tau = 0,1,2$

$$\mathbf{V}_1 = \begin{bmatrix} \mathbf{X}_0 \\ \mathbf{X}_1 \end{bmatrix},\ \mathbf{V}_2 = \begin{bmatrix} \mathbf{X}_1 \\ \mathbf{X}_2 \end{bmatrix},\ \boldsymbol{\upsilon} = \begin{bmatrix} \mathbf{\Psi} \\ \mathbf{\Psi\Delta} \end{bmatrix}, \tag{2.25}$$

and it can be shown [30] that the following eigenvalue problem exists if $\mathbf{V_1}$ is non-singular and there are no repeated eigenvalues.

$$\mathbf{V}_2\,\mathbf{V}_1^{-1}\,\boldsymbol{\upsilon} = \boldsymbol{\upsilon}\,\mathbf{\Delta} \tag{2.26}$$

Mode shape information is obtained from the upper half of υ, and global properties are extracted from the eigenvalues.

The eigensystem realisation algorithm (ERA) is another time-domain modal parameter estimation algorithm, which has been shown to be a special case of state-space based modal parameter estimation [38]. The ERA algorithm is summarised from Petsounis and Fassois [39].

A general state-space representation of a dynamic system relating excitation and response data is

$$\mathbf{x}[t+1] = \mathbf{A}(\boldsymbol{\theta})\mathbf{x}[t] + \mathbf{B}(\boldsymbol{\theta})\mathbf{f}[t],$$

$$\mathbf{y}[t] = \mathbf{C}(\boldsymbol{\theta})\mathbf{x}[t] + \mathbf{D}(\boldsymbol{\theta})\mathbf{x}[t], \tag{2.27}$$

where $\mathbf{x}[t]$ is the state vector, **A**, **B**, **C**, **D**, are the state, input, output and direct transmission matrices, respectively, whose unknown elements are summarised by $\boldsymbol{\theta}$**,** the parameter vector. $\mathbf{f}[t]$ is the m-dimensional excitation vector and $\mathbf{y}[t]$ is the s-dimensional response vector. The ERA estimates modal parameters by relating the system matrices to a SVD of a Hankel matrix formed from impulse response data;

$$\mathbf{H}[t-1] = \begin{bmatrix} \mathbf{Y}[t] & \mathbf{Y}[t+1] & \dots & \mathbf{Y}[t+\beta-1] \\ \mathbf{Y}[t+1] & \mathbf{Y}[t+2] & \dots & \mathbf{Y}[t+\beta] \\ \vdots & \vdots & & \vdots \\ \mathbf{Y}[t+\alpha-1] & \mathbf{Y}[t+\alpha] & \dots & \mathbf{Y}[t+\alpha+\beta-2] \end{bmatrix}, \tag{2.28}$$

where $\mathbf{Y}[t] = [\ \mathbf{y}^1[t] \quad \mathbf{y}^2[t] \quad \dots \quad \mathbf{y}^m[t]\ ]$ is a vector containing impulse response data, $\mathbf{y}^i[t]$, at time t due to an input at point i. α, β are chosen depending on the number of vibration modes and the expected level of noise present in the measured data.

The SVD of the Hankel matrix is

$$\mathbf{H}[0] = \mathbf{R}\boldsymbol{\Sigma}\mathbf{S}^T; \tag{2.29}$$

R and **S** are the matrices of left and right singular vectors, respectively, and Σ is a diagonal matrix of singular values. These matrices can be partitioned according to the magnitude of singular values; for ideal data, there will be n non-zero singular values corresponding to the n vibration modes. Matrices formed from the non-zero singular values and the corresponding left and right singular vectors are used in subsequent operations.

The state-space system matrices are related to the SVD by the following equations

$$
\begin{aligned}
&\mathbf{A} = \boldsymbol{\Sigma}^{-1/2} \cdot \mathbf{R}^T \cdot \mathbf{H}[1] \cdot \mathbf{S} \cdot \boldsymbol{\Sigma}^{-1/2} \\
&\mathbf{B} = \boldsymbol{\Sigma}^{-1/2} \cdot \mathbf{S}^T \cdot \mathbf{E}_m \\
&\mathbf{C} = \mathbf{E}_s \cdot \mathbf{R}^T \cdot \boldsymbol{\Sigma}^{1/2} .
\end{aligned}
\tag{2.30}
$$

$\mathbf{E}_m$ and $\mathbf{E}_s$ are matrices containing zeros except for the top element, which contain identity matrices of dimension $m \times m$ and $s \times s$, respectively. Modal parameters are obtained from the eigenvalue decomposition of a companion matrix formed from the state-matrices, similar to equations (2.19) – (2.21). The resulting eigenvector matrix is transformed to mode shape data at measurement points by pre-multiplication by the output matrix, **C**, and modal participation factors are obtained via the expression $\mathbf{L} = \boldsymbol{\Psi}^{-1}\mathbf{B}$.

Studies have shown the effectiveness of the ERA method for cases where the signal-to-noise ratio (s/n) is favourable [39] and averaging of FRFs can be used to improve the s/n of data before transformation to IRFs. Modifications to the ERA method, for example the ERA/DC method introduced by Lew et al [40], attempt to address this problem by replacing the Hankel matrix by a new matrix with correlation function elements. This is similar to response-only methods based on state-space models (with the ERA as a special case), and will be discussed in Chapter 8. More recently, a range of subspace estimation algorithms have been compared by Abdelghani et al [41] using data simulating the dynamic behaviour of a mast structure. These algorithms are more robust than the ERA algorithm for non-white noise excitation sequences, and also perform more effectively in the presence of measurement noise. More information on state-space estimation algorithms can be found in Van Overschee and De Moor [42].

Recall the ARX model in equation (2.17). It can be extended to include a stochastic component, $\mathbf{w}[t]$, which is white noise and can be considered as the model error or an unmeasured disturbance, as indicated in equation (2.31).

$$
\sum_{k=0}^{m} \mathbf{A}_k \cdot \mathbf{x}[t-k] = \sum_{k=0}^{n} \mathbf{B}_k \cdot \mathbf{f}[t-k] + \mathbf{w}[t]
\tag{2.31}
$$

An extension of the ARX model involves applying a moving average to $\mathbf{w}[t]$ to more effectively model non-white noise disturbances, resulting in an autoregressive moving average with exogenous excitation (ARMAX) model [43], which is described by equation (2.32).

$$\sum_{k=0}^{m} \mathbf{A}_k \cdot \mathbf{x}[t-k] = \sum_{k=0}^{n} \mathbf{B}_k \cdot \mathbf{f}[t-k] + \sum_{k=0}^{p} \mathbf{C}_k \cdot \mathbf{w}[t-k] \tag{2.32}$$

A large body of work has been carried out in the area of system identification techniques applied to time-series models. In particular, the estimation of deterministic ARMA or ARX models, as well as ARMAX models, using a wide range of techniques for example least-squares, maximum likelihood, and instrumental variable estimation [43, 44]. Studies that apply these techniques to structural dynamics are considered here.

Batill and Hollkamp [45] introduced a two stage algorithm for estimation of ARMA (ARX) models. The first stage estimated a higher-order backwards AR model from free decay (impulse) responses. The backwards AR model was estimated from reversed time-series data; i.e. decaying responses became responses with increasing amplitude. The backwards models are distinguished from standard or forwards AR (or ARX) models, which are estimated from non-reversed time-series data. The backwards AR model enabled vibration poles to be distinguished from spurious numerical poles and the vibration poles were used to form a reduced AR model. The MA (or X) matrix of the model was estimated using excitation and response data from a second test and the reduced AR model. This algorithm was adapted by Hollkamp and Batill [46] into a single-stage algorithm estimating a backwards ARMA (ARX) model. The effectiveness of the method was demonstrated using experimental data from a composite sailplane.

Cooper [47] also studied the use of backwards models for estimation of modal parameters. A number of least-squares estimation schemes were applied to forwards and backwards autoregressive models and tested using simulated and experimental impulse response data. The experimental results showed that the use of backwards models produced accurate estimates of modal parameters with the additional benefit that vibration modes could be easily distinguished from numerical modes for models with over-specified model orders.

Yang et al [34] represented a multiple DOF vibrating system by a discrete-time state-space model and derived an equivalent ARX model. It was shown that ARMAX-based and polyreference algorithms followed from the basic MIMO ARX representation by adopting a particular noise model and excitation. The relationships between the MIMO ARX representation and the ITD, and ERA were also established.

Yun et al [48] discussed a sequential prediction error method for estimating ARMAX models. This is an iterative technique based on minimising the prediction error of the model and required initial guesses for unknown model parameters. A number of different data-weighting methods were considered, as well as a square-root method for estimating the gain matrix. The authors concluded that these methods improve the convergence properties of the algorithm in conditions where initial parameter guesses were poor and where significant noise was present in measured excitation and response signals. A further conclusion was that the technique was appropriate for structures with many DOFs, when only a few measurements were taken; however, only a 2 DOF simulated system and an experimental study of a model 3-story building (considering 3 modes) were discussed.

Hu et al [49] derived the relationship between a physical model of a dynamic system and a discrete-time state-space representation. They applied an estimation algorithm using a matrix of covariance functions similar to the Modified Yule-Walker equations [43, 44]. One disadvantage of these types of algorithms is that the calculation of covariance matrices can decrease the conditioning of the linear system of equations due to the squaring of the data. These problems and alternative estimation schemes are well-known, see for example Golub and Van Loan[50], and Ljung [43]. Hu et al [49] tested their algorithm with a 3-DOF system using measured excitation and response data and also for the case where excitation data were not explicitly measured but are assumed to be white noise. Accurate modal parameters were obtained for the I/O case and it was found the algorithm could identify modal parameters for the response-only case, but results were less accurate than the I/O analysis. A method to quantify the contribution of vibration modes to the vibration response, using 'dispersion coefficients', was discussed and it was noted that modes with a poor response were affected by measurement noise to a greater extent than modes with good vibration response.

Park and Kim [51] introduced two parameterisations of an ARMAX model structure for modal parameter estimation. One parameterisation followed from the fact that the AR matrix models the global modal parameters (frequency and damping) and therefore a scalar AR polynomial was used to describe global modal parameters for every measurement point. The second parameterisation estimated a different AR polynomial for each response measurement point, i.e. the MIMO problem was separated into a series of MISO problems. Parameters of the ARMAX model were estimated by an approximate maximum likelihood algorithm and this method required initial values for the model parameters, which were obtained by a least-squares method. The Akaike Information Criterion (AIC) was employed for model order selection. The performance of the algorithm using the two model structures was assessed with data simulating the behaviour of a 3-DOF structure. Results were found to be of good accuracy with approximately 5% random measurement noise added to the response measurements. It was found that separating the MIMO model into MISO models lead to a slight decrease in the accuracy of the estimated modal parameters.

The development and study of a linear multistage (LMS) estimation algorithm for MIMO ARMAX model structures was reported by Fassois and colleagues [52-56]. The algorithm was based around least-squares estimation and a series of linear operations, which addressed the computational complexity of some maximum likelihood methods and included guaranteed stability of the estimated model. A feature of this method was the use of dispersion analysis [55, 57] to identify the contribution of an estimated mode to the vibration response, and this could be used as an aid for model order selection and for distinguishing between vibration and spurious numerical modes. This algorithm is discussed in more detail in Chapter 5. Variations of the algorithm applied to ARMA (ARX) [58] models; using correlation functions [59, 60], and a recursive least-squares variation [61, 62] have also been reported. These studies show the benefit of including a moving average (MA) description of the model noise, and the most recent work by Florakis et al [56] is one of the few studies to demonstrate the feasibility of ARX or ARMAX modelling of more complex structures that include difficult characteristics like closely spaced modes and local modes, which have poor responses at a number of measurement points. The performance of this method was further assessed by Petsounis and Fassois [39] using data simulating the behaviour of a train car and compared favourably with other stochastic methods, namely the prediction error method and instrumental variable methods, and also deterministic methods, for example, the ERA. The effects of coloured measurement noise were also assessed and the LMS algorithm produced acceptable results.

The modal analysis algorithms discussed above assume that the measured excitation is the only excitation of the system, and that the s/n of measured signals is favourable. Most studies have investigated the effects of added measurement noise and strategies to improve the signal-to-noise ratio are well known. Spectral averaging improves s/n for FRF-based modal analysis and similar improvements occur in correlation functions calculated with spectra. Model order over-specification accompanied by SVD or QR-based LS estimation is used to account for noisy measurements used with time-domain algorithms. As noted above, ARMAX and state-space model structures are more robust to measurement noise because these models explicitly model the noise components. Maximum likelihood estimation has also been shown to perform well with noisy FRFs [63, 64].

More recently, operational modal analysis methods have been developed for cases where measurement of excitation forces is not possible. This is discussed in detail in Chapter 8. A situation that has not been widely considered is when modal analysis with measured excitations is carried out in the presence of unmeasured excitations. While operation modal analysis methods have been shown to be quite successful [65] they do not directly yield scaled mode shapes and make assumptions about the nature of the excitation sources [38]. In-flight testing of a fixed-wing aircraft was discussed by Mevel et al [24] and this is a situation where significant ambient (and unmeasurable) excitations were applied to a structure. This study concluded that if it was possible to apply a measurable excitation, then I/O modal analysis yielded more accurate modal parameters than operational modal analysis methods, but the difference in accuracy became less significant for longer data records. Stochastic subspace (state-space based estimation) and a frequency domain method were used for modal parameter estimation. A frequency domain method that explicitly modelled the effects of unmeasured excitation was developed by Cauberghe et al [66] and included terms to model transient effects in signals, which mitigated the effect of leakage in frequency-domain representation of non-periodic signals. Another frequency domain method was outlined by Vanlanduit et al [67]. This method used periodic measured excitation signals and separated the response due to these signals from the response due to unmeasured excitation in the frequency domain. The periodic responses were represented on particular frequency lines, while the unmeasured excitations, assumed to be reasonably flat and correlated in the frequency domain (e.g. an impulse) produced responses that were represented at all frequency lines. This study used the estimated FRF matrix in an inverse problem to identify the unmeasured impulse excitation, assuming it was applied at a measurement point.

2.3 Time-Domain Averaging

This section introduces the concept of time-domain (synchronous) averaging and discusses its effectiveness in attenuating wide- and narrow-band random noise and also periodic components of a signal.

It is well known that time-domain averaging is effective in improving the signal-to-noise ratio of periodic signals. Ernst [68] carried out a theoretical analysis of time-domain averaging using statistical methods applied to time-domain signals. For additive white noise, the signal-to-noise ratio was shown to improve by a factor of $1/\sqrt{M}$, where M is the number of averages. Analysis investigating the attenuation of non-white noise showed that the $1/\sqrt{M}$ rule was "qualitatively" correct given that the noise exhibited a reasonably smooth power spectrum.

Braun [69] analysed time-domain averaging using the concept of filtering in the frequency domain. A more intuitive model of time-domain averaging was introduced and results describing the attenuation of broad- and narrow-band random noise, and also periodic components, were derived. The effects of triggering error and jitter, which can arise in the extraction of periodic components of signals generated by rotating machinery including gear trains [70], were also discussed. In many cases the measured signal has to be re-sampled, which often requires interpolation between the original samples, or alternatively, the sampling of the original signal is governed by a trigger synchronised to a particular rotating element. Liu et al [71] investigated the effects of period cutting error in cyclic-averaging (where no time elapses between averaged sections) and proposed a strategy to reduce the effects of period cutting error.

Triggering error, jitter, and period cutting error in general result in the attenuation of the periodic components of interest. For the case of modal analysis, these effects can be minimised by accurate triggering of the data acquisition system by the periodic excitation signal.

McFadden [72] proposed an alternative frequency domain model for time-domain averaging for application in the frequency domain. This alternative model included the effects of a finite time series by applying a rectangular window and guaranteed a periodic averaged waveform by sampling in the frequency domain.

The following discussion of the properties of synchronous averaging is based on that by Braun [69, 70].

Time-domain averaging of a discrete time signal $x[t]$, $t = 0, \ldots, N\text{-}1$, with sampling period T_s is described by

$$y[t] = \frac{1}{M}\sum_{r=0}^{M-1} x[t - r \cdot p \cdot T_s], \tag{2.33}$$

where $y[t]$ is the averaged signal, M the number of averages, and $T_p = p{\cdot}T_s$ is the period of the signal component to be extracted. Note that no time elapses between the sections of record to be averaged, as shown in figure 2.1.

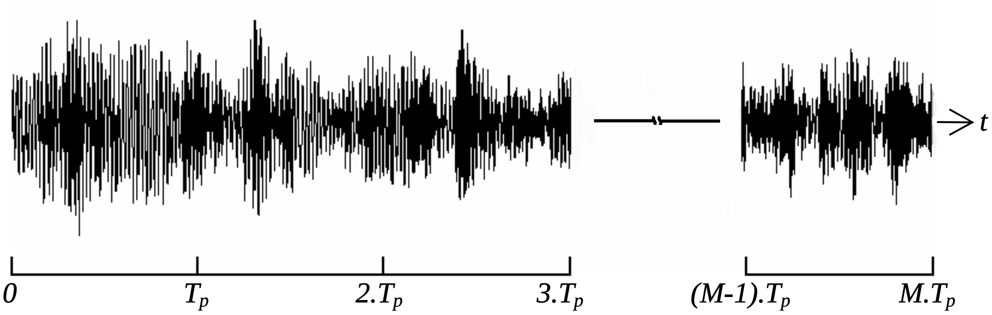

Figure 2.1 Cyclic time-domain averaging. T_p is the period of the averaged record.

The z-transform is used to derive the transfer function

$$H(z)=\frac{Y(z)}{X(z)}=\frac{1}{M}\cdot\frac{1-z^{-pM}}{1-z^{-p}}, \tag{2.34}$$

which is evaluated along the unit circle, $z=e^{j\omega T_s}$, to obtain the frequency and phase response in terms of frequency $f = \omega/(2\pi)$ Hz:

$$H(f/f_p)=\frac{1}{M}\cdot\frac{\sin(\pi\cdot M\cdot f/f_p)}{\sin(\pi\cdot f/f_p)}; \tag{2.35}$$

$$\phi(f/f_p)=-\pi\cdot(M-1)\cdot\frac{f}{f_p}. \tag{2.36}$$

$f_p = 1/(p\cdot T_s)$ is the frequency of the signal component to be extracted. A plot of the frequency response (equation (2.35)) is shown in figure 2.2 for $M = 4$ and $M = 10$. The frequency response is a comb filter with peaks of the main lobes located at integer multiples of f_p Hz (up to the Nyquist frequency), which have unity gain and zero phase shift. Increasing M reduces the bandwidth of the main lobes, increases the number of side lobes, and also increases the attenuation of frequency components away from the side lobes.

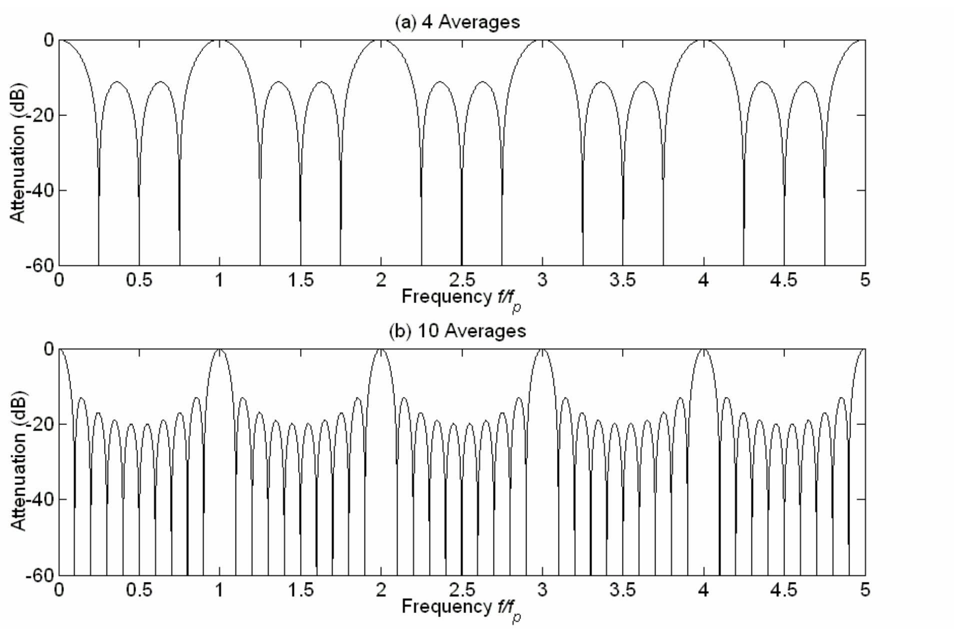

Figure 2.2 Frequency response of time-domain averaging: (a) 4 averages (top figure); (b) 10 averages.

Braun [69] calculated the equivalent noise bandwidth for the comb filter to be *1/M* and it follows that the RMS level of broad-band noise is reduced by a factor of $\sqrt{M}$. Therefore, for a desired reduction in noise, α, the number of averages is set to [70]

$$M > \frac{1}{\alpha^2}. \tag{2.37}$$

The rejection of narrow-band noise and periodic signals is easily determined from equation (2.35). For a periodic noise at a single frequency, the number of averages can be set so that a zero of the comb filter occurs at the frequency of noise. For more complex signals, *M* can be chosen such that the attenuation of the noise components is set to a desirable level. The peaks of the side lobes are scaled by $1/\left(M \cdot \sin\left(\pi \cdot f / f_p\right)\right)$ and the number of averages required for a desired noise reduction is therefore [70]

$$M > 1/\left(\alpha \cdot \sin\left(\pi \cdot f / f_p\right)\right). \tag{2.38}$$

It should be noted that equation (2.38) applies to *cyclic* averaging; i.e. where no time elapses between consecutive time records. The attenuation of random components by time domain averaging does not change for the case where an arbitrary time period separates averaged record sections; however, the attenuation of periodic components is only approximated by equations (2.35) and (2.36), depending on the distribution of time separating sections of time record to be averaged.

2.4 Experimental Case Study I

The aim of this study was to investigate the feasibility of using measured periodic excitation and synchronous averaging for the purpose of modal analysis of a simple structure in the presence of unmeasured excitations. A further aim was to investigate the use of piezoceramic actuators for structural excitation.

An aluminium beam of dimensions $1.050 \times 0.05 \times 0.003$m was suspended with string to approximate free-free conditions in the transverse direction. Figure 2.3 shows the suspended beam and a schematic of the apparatus is shown in figure 2.4.

Figure 2.3 Aluminium beam suspended to approximate free-free conditions in the transverse direction in the horizontal plane. Piezoceramic actuators are located on the left-hand side and are covered by tape.

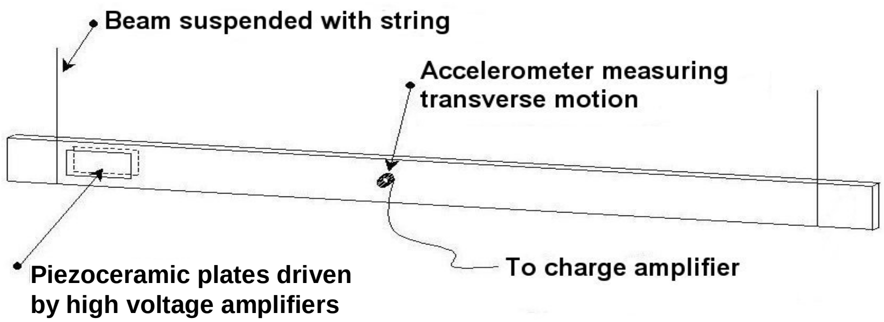

Figure 2.4 Schematic of experimental apparatus.

The two 70×25×1mm piezoceramic plates were bonded to each major surface of the beam; 60mm from one end, and centred in the lateral direction, as shown in figure 2.4. The surface of the beam was coated with etch primer and the plates were bonded with a thin layer of epoxy. For each experiment, response measurements were made at thirty equally spaced points along the length of the beam using a Brüel&Kjær (B&K) 4374 accelerometer. B&K 2032 FFT analysers were used to calculate FRFs and also to generate the excitation signals for each experiment: either random noise or impulse signals. These signals were used as a measure of the excitation force for experiments using piezoceramic actuators for measured excitation. One of the aims of this set of experiments was to investigate whether this assumption allowed estimation of accurate modal parameters. A constant-gain high voltage amplifier was used to drive the piezoceramic actuators. Modal parameters were estimated using a global RFLS method, implemented in the Spectral Dynamics STAR Modal v. 5.23 software. This involved identifying resonant peaks from the averaged imaginary part of measured FRFs and selecting bands around these peaks for curve fitting. Estimates of global properties were obtained first, and the averaged estimates were used in a second stage that yielded transfer function residues.

An impact hammer test was carried out to establish a baseline set of results that could be compared with modal parameters estimated using piezoceramic actuators for excitation. B&K 2635 charge amplifiers were used to condition (2 Hz high-pass filter, 3 kHz low-pass filter) accelerometer and impact hammer signals. FRFs were calculated with a frequency range of 400 Hz and a resolution of 0.5 Hz. Up to twenty spectral averages were taken for each measurement point; a transient window was applied to the excitation signal, and an exponential window with time constant 0.5 seconds was applied to the response measurements. Equation (2.39) was used to correct estimated damping values for the additional damping imposed by the exponential window [73].

$$1/\varsigma_{corrected} = 1/\varsigma_{measured} - 1/\varsigma_{window} \tag{2.39}$$

Table 2.1 lists estimated modal frequencies from the impact hammer test.

Mode	1	2	3	4	5	6	7
Frequency (Hz)	12.81	36.04	71.78	119.74	180.25	253.64	339.69

Table 2.1 Modal frequencies estimated from impact hammer test.

Further experiments were carried out using the piezoceramic plates for excitation and a summary of all experiments and noise conditions is included in table 2.2. The listed noise level is the RMS of the noise signal divided by the amplitude of the impulse excitation signal. As impulse excitation was used for the measured excitation, an exponential window (time constant 0.5 seconds) was applied to the response measurements and the estimated damping was corrected as for the impact hammer test.

A finite element model (FEM) of the beam was developed in ANSYS to predict the undamped natural frequencies and normal mode shapes of the beam. The aluminium beam and piezoceramic actuators were modelled with 840 and 56 brick elements (solid95), respectively, and ideal bonding between the actuators and the beam was assumed. Material properties for the aluminium beam were density: 2650 kg/m^3; Young's modulus: 62 GPa; and Poisson's ratio: 0.33. The piezoceramic actuators were approximated as orthotropic materials with Young's modulus: E_x = E_y = 99 *GPa*; E_z = 118 *GPa*; Poisson's ratio: $\nu_{xy} = \nu_{yz} = \nu_{xz} = 0.31$; shear modulus: G_{xy} = 37.8 *GPa*; G_{yz} = G_{xz} = 4.5 *GPa*; and density: 7600 kg/m^3.

Experiment	Description
Hammer	Impact hammer test, up to 20 averages
Piezo (random)	Random noise excitation using one piezoceramic actuator, 15 averages.
Piezo (impulse)	Impulse excitation using one piezoceramic actuator, 40 averages
0.125/20	Measured impulse excitation by one piezoceramic actuator; unmeasured random excitation by second piezoceramic actuator; 20 averages; unmeasured excitation level 0.125.
0.125/40	Measured impulse excitation by one piezoceramic actuator; unmeasured random excitation by second piezoceramic actuator; 40 averages; unmeasured excitation level 0.125.
0.125/80	Measured impulse excitation by one piezoceramic actuator; unmeasured random excitation by second piezoceramic actuator; 80 averages; unmeasured excitation level 0.125.
0. 25/80	Measured impulse excitation by one piezoceramic actuator; unmeasured random excitation by second piezoceramic actuator; 80 averages; unmeasured excitation level 0.25.
Per/40	Measured impulse excitation by one piezoceramic actuator; unmeasured periodic excitation (95Hz) by second piezoceramic actuator; 40 averages; unmeasured excitation level 0.354.
Per/80	Measured impulse excitation by one piezoceramic actuator; unmeasured periodic excitation (95Hz) by second piezoceramic actuator; 80 averages; unmeasured excitation level 0.354.

Table 2.2 Summary of free-free aluminium beam experiments

2.4.1 Impact Hammer and Piezoceramic Actuator Experiments

Results from tests applying measured impulse and random excitation using one piezoceramic actuator were compared with impact hammer results in order to assess the effectiveness of using piezoceramic actuators for structural excitation. Differences in modal frequencies, compared to the hammer test, are plotted in figure 2.5. There is a small bias present between the FEM and experimental results and this was due to reference values of Young's modulus being used in the FEM. Results from the experiments show very good agreement except for the first mode and this trend is reflected in the damping estimates, shown in figure 2.6. Damping results from the impulse excitation and hammer experiments were corrected to account for the exponential window. Differences can be seen when compared to random noise excitation for modes 1- 4 and the Hanning window used for the random excitation may have resulted in higher damping being estimated.

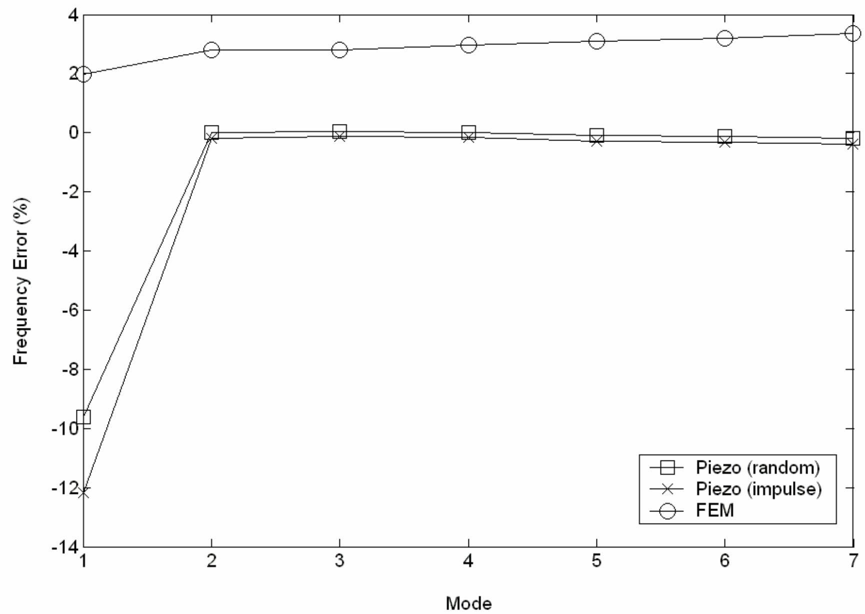

Figure 2.5 Error in modal frequencies for random and impulse excitation (piezoceramic actuator), and FEM results compared to impact hammer results.

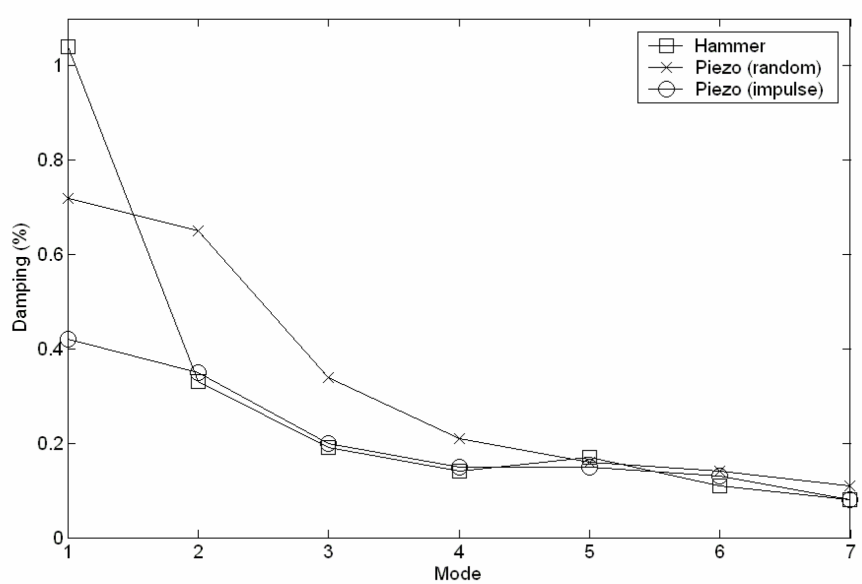

Figure 2.6 Modal damping estimates for random and impulse excitation (piezoceramic actuator), and impact hammer experiments.

The modal assurance criterion is a measure of correlation between two mode shapes, and is defined in equation (2.40) for normal modes [74].

$$MAC(\psi_1, \psi_2) = \frac{\left|\left(\{\psi_1\}^t\{\psi_2\}\right)\right|^2}{\left(\{\psi_1\}^t\{\psi_1\}\right)\left(\{\psi_2\}^t\{\psi_2\}\right)} \tag{2.40}$$

Figure 2.7 shows MAC values comparing mode shape estimated from the piezo (random), piezo (impulse), and impact tests with FEM mode shapes.

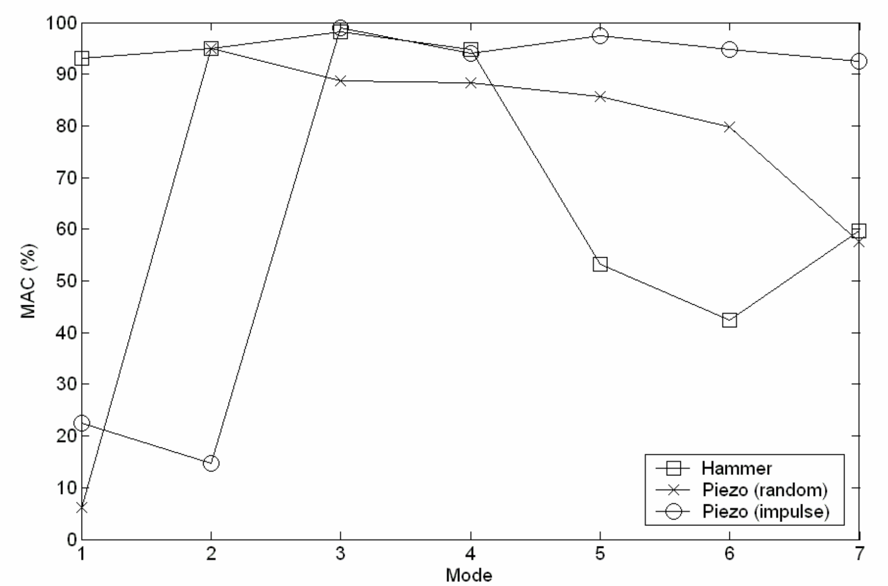

Figure 2.7 MAC comparing mode shapes from impact hammer, piezo (random), and piezo (impulse) experiments with FEM results.

A disadvantage of the MAC value is that large differences in modal amplitude at a small number of measurement points can significantly lower the MAC, and this is the case for modes 5, 6, and 7 in the hammer test. MAC values for the first four modes show good agreement with FEM results. The modes 3 – 7 estimated in the piezo (random) experiments included errors at a small number of measurement points; however, this was not the case for mode 1 results obtained from piezo (random) and piezo (impulse) excitation. The poor mode shape estimates, combined with the relatively poor frequency and damping results suggested that the piezoceramic actuators did not effectively excite the beam for the first mode, and to a lesser extent the second mode. This was expected because the piezoceramic actuators apply distributed moments to the beam over the contact area of the actuators. The contact area is small relative to the deflection of the first two transverse bending modes and the moment applied by the actuators will not effectively excite the first two modes. However, the results of these experiments suggested that the piezoceramic actuators could be used in further experiments investigating the effects of unmeasured excitations. The use of piezoceramic actuators in experimental modal analysis will be discussed in detail in Chapter 4.

2.4.2 Unmeasured Random Excitation

Figures 2.8 – 2.10 show modal parameters estimated for experiments involving unmeasured random excitation and different numbers of averages. Frequency and damping results agree reasonably well with impact hammer values, except for the first mode, and suggest that the RFLS modal parameter estimation algorithm is effective in estimating frequency and damping results for moderate levels of unmeasured random excitation.

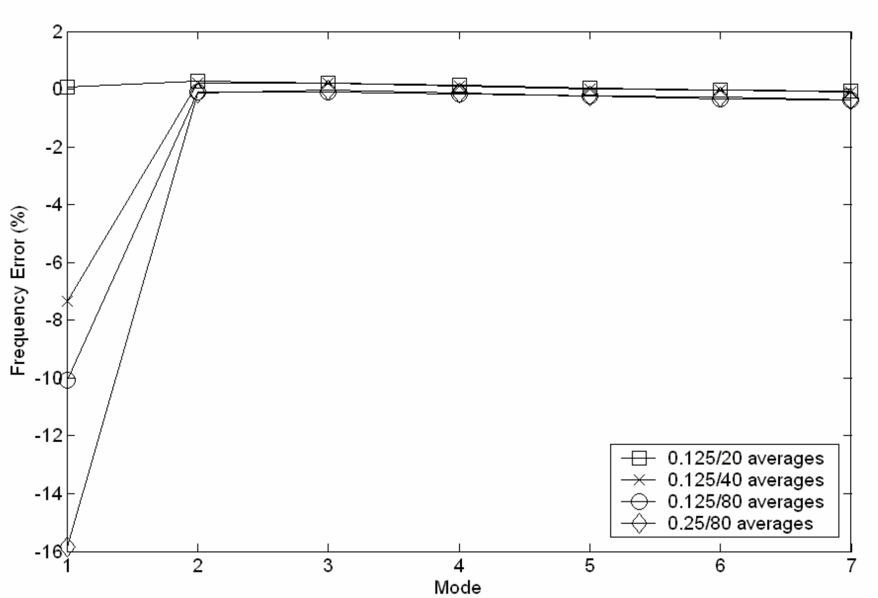

Figure 2.8 Modal frequency results from experiments with unmeasured random excitation compared with impact hammer results.

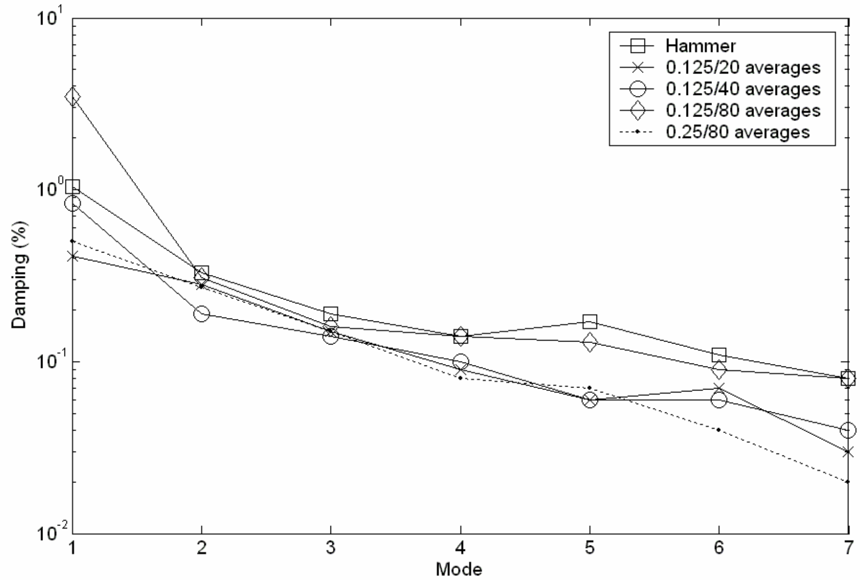

Figure 2.9 Modal damping results from impact hammer test and experiments with unmeasured random excitation.

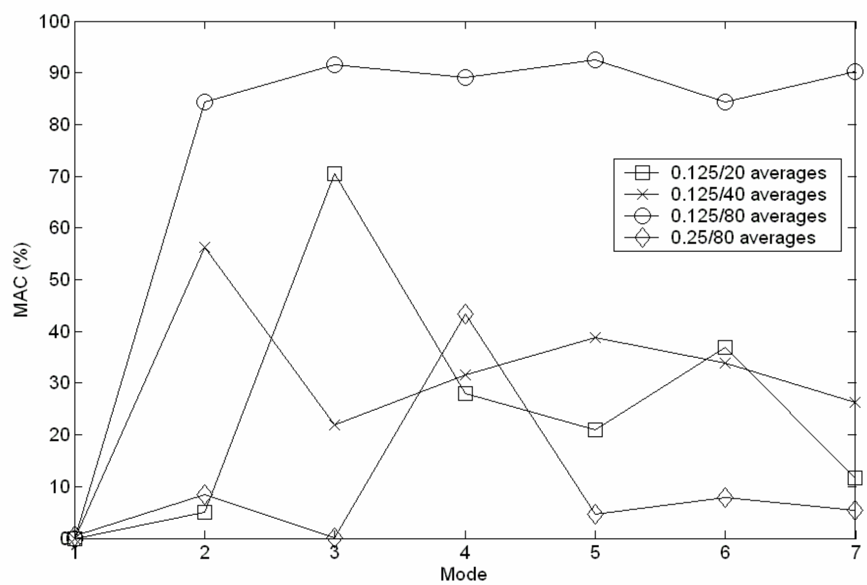

Figure 2.10 MAC comparing mode shapes from experiments with unmeasured random excitation with FEM results.

The MAC values shown in figure 2.10 more clearly show the effect of increasing numbers of averages. Mode shapes are estimated poorly for the 0.125/20 and 0.125/40 experiments, but increasing the number of averages to eighty leads to acceptable accuracy of mode shapes for modes 2 - 7, as shown by the 0.125/80 results. Doubling the level of noise while maintaining the number of averages leads to poorly estimated mode shapes. The attenuation of broad-band noise by synchronous averaging, discussed in section 2.3, suggests that the noise present in the 0.250/80 experiments is approximately equal in level to that of the 0.125/20 experiments, and mode shape estimates obtained from each experiment are similarly poor. The RFLS technique, like other modal parameter estimation algorithms discussed in section 2.2, does not explicitly model the effects of measurement noise or unmeasured excitations and therefore any amount of noise can be expected to bias results.

2.4.3 Unmeasured Periodic Excitation

Further tests were carried out using impulse excitation and synchronous averaging in the presence of unmeasured periodic excitation under the conditions described in table 2.2 for Per/40 and Per/80 experiments. The estimated modal parameters are plotted in figures 2.11 – 2.13. Frequency and damping results reflect conclusions drawn in previous experiments and MAC values show accurate mode shapes were estimated for modes 3 – 7.

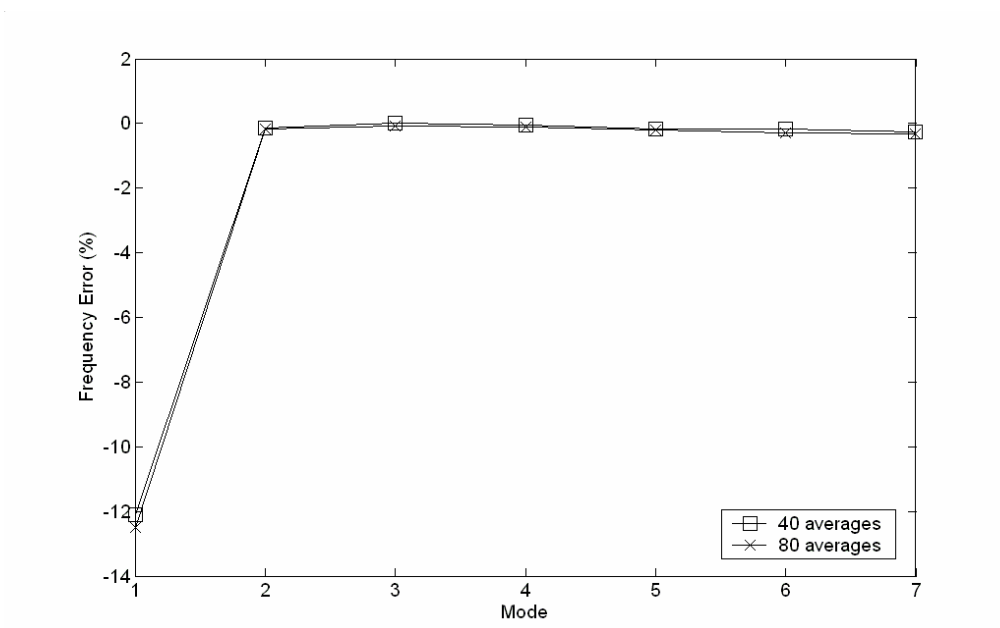

Figure 2.11 Modal frequency results from experiments with unmeasured periodic excitation (40 and 80 averages) compared with impact hammer results.

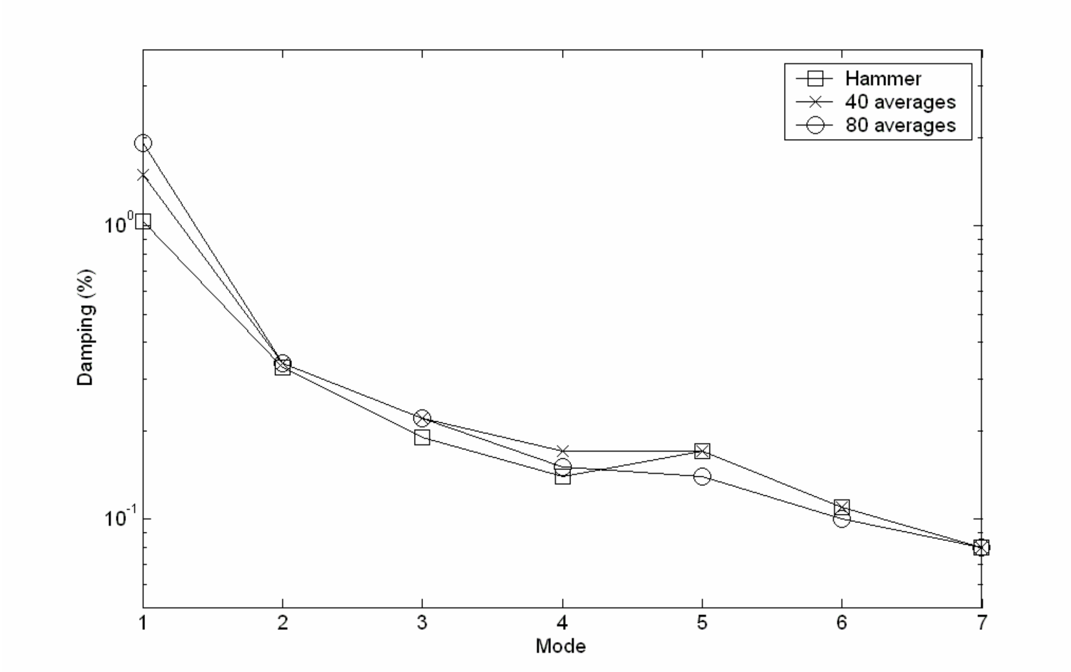

Figure 2.12 Modal damping results from impact hammer test and experiments with unmeasured periodic excitation (40 and 80 averages).

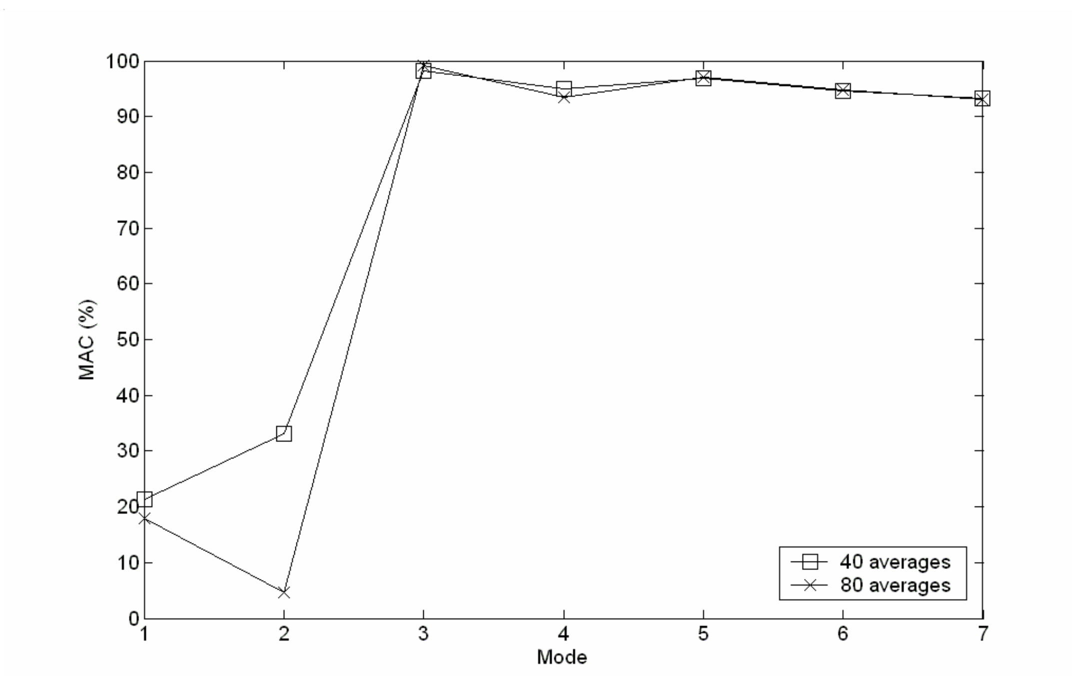

Figure 2.13 MAC comparing mode shapes from experiments with unmeasured periodic excitation (40 and 80 averages) with FEM results.

Good accuracy was expected for per/40 and per/80 tests due to the high number of averages and because the unmeasured periodic excitation occurred midway between modes three and four, and could be excluded from curve-fitting bands. The most significant difficulty in dealing with unmeasured periodic excitations is distinguishing the responses from responses due to vibration modes. In the absence of a priori knowledge of excitation frequencies, the RFLS provides no systematic means of identifying the effects of unmeasured periodic excitation.

2.5 Experimental Case Study II

The second experimental study involved modal testing of a 'helicopter-like' structure, which was suspended from elastic cord to approximate free-free conditions. The suspended structure is shown in figure 2.14 and two B&K 4809 shakers can be seen, which were used for applying measured impulse excitation and unmeasured random excitations.

Figure 2.14 Suspended helicopter-like structure used for the second experimental case study. Two shakers can be seen: (1) measured impulse excitation; (2) unmeasured random excitation.

The helicopter-like structure had approximate total dimensions of $986 \times 366 \times 223$ mm; a mass of 11.53 kg; and was constructed of steel beams welded together.

Three experiments were conducted using impulse excitation with different levels of unmeasured excitation and are summarised in table 2.3. The listed unmeasured excitation level is the RMS of the unmeasured excitation divided by the amplitude of the measured impulse excitation.

Experiment	Description
Impulse	Measured impulse excitation (shaker 1); 20 averages.
0.125/20	Measured impulse excitation (shaker 1); unmeasured random excitation (shaker 2); 20 averages; unmeasured excitation level 0.125.
0.625/30	Measured impulse excitation (shaker 1); unmeasured random excitation (shaker 2); 30 averages; unmeasured excitation level 0.625.

Table 2.3 Summary of experiments on helicopter-like structure.

The two shakers were each driven by a B&K 2706 power amplifier and a single B&K 4374 accelerometer was used for taking acceleration response measurements at 179 points on the structure. A B&K 2635 charge amplifier applied high and low pass filtering; 3db cut-offs 2Hz, and 1kHz, respectively. FRFs were calculated by a HP3566A FFT analyser and global RFLS modal parameter estimation of modal parameters was carried out using the STAR Modal v5.23 software.

Table 2.4 lists the estimated modal frequencies from the impulse experiment, and figure 2.15 shows the natural frequency error for the 0.125/20 and 0.625/30 experiments compared to the impulse experiment. Very little difference is observed in estimated frequencies between the experiments. Similarly, damping results from each experiment, plotted in figure 2.16, show good agreement.

Mode	1	2	3	4	5	6	7	8
Frequency (Hz)	74.360	76.886	85.147	143.14	159.71	185.76	199.28	238.31
Mode	9	10	11	12	13	14	15	16
Frequency (Hz)	244.14	262.47	276.03	277.80	281.88	297.49	313.93	317.84
Mode	17	18	19	20	21	22		
Frequency (Hz)	322.26	341.73	356.81	363.73	367.26	380.35		

Table 2.4 Estimated natural frequencies from Impulse experiment.

Mode shapes from 0.125/20 and 0.625/30 experiments are compared with results from the Impulse experiment in figure 2.17. Better estimates are typically obtained from the 0.125/20 experiment than for 0.625/30 experiment, which is expected given the relative levels of unmeasured excitation and the numbers of averages used in each test.

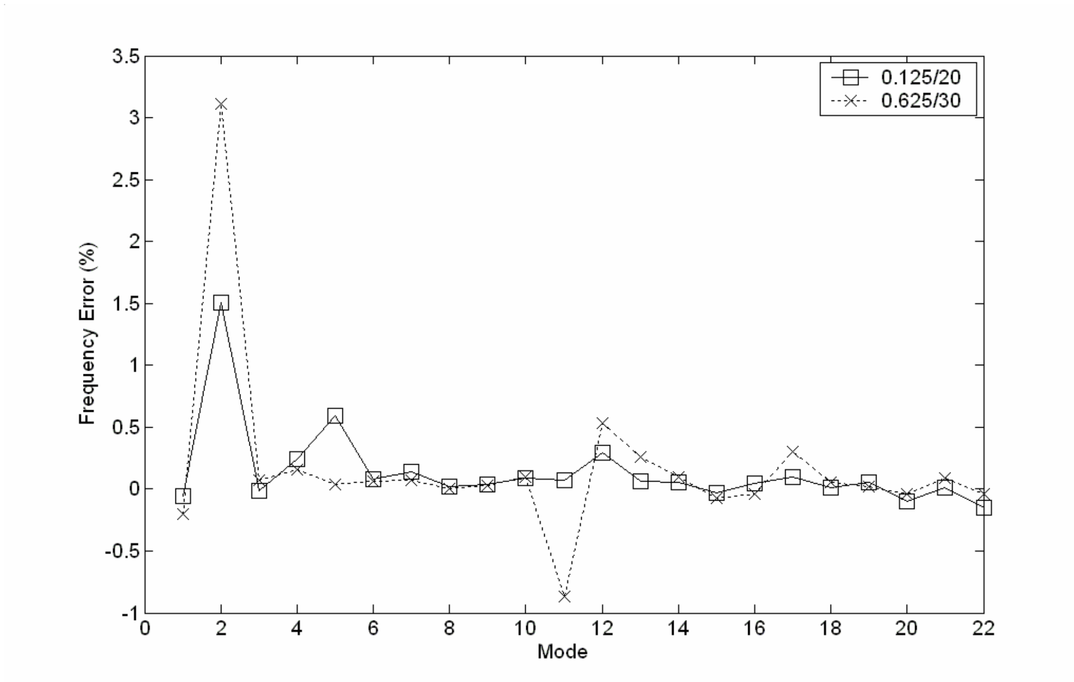

Figure 2.15 Frequency error for 0.125/20 and 0.625/30 experiments compared with Impulse experiment.

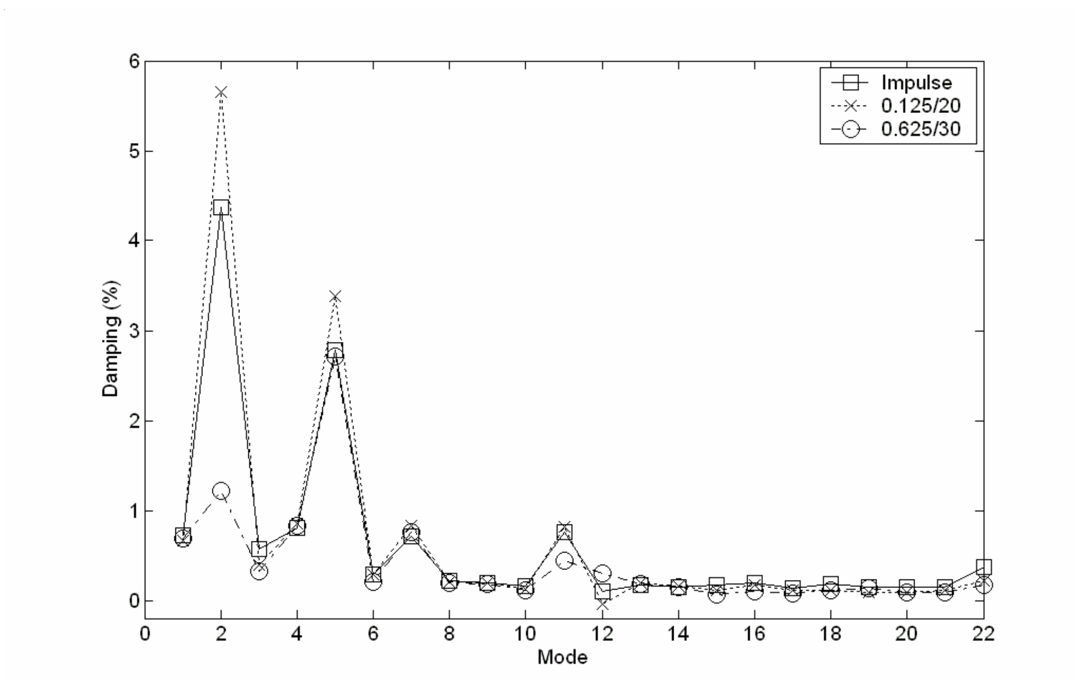

Figure 2.16 Modal damping estimated from Impulse, 0.125/20, and 0.625/30 experiments.

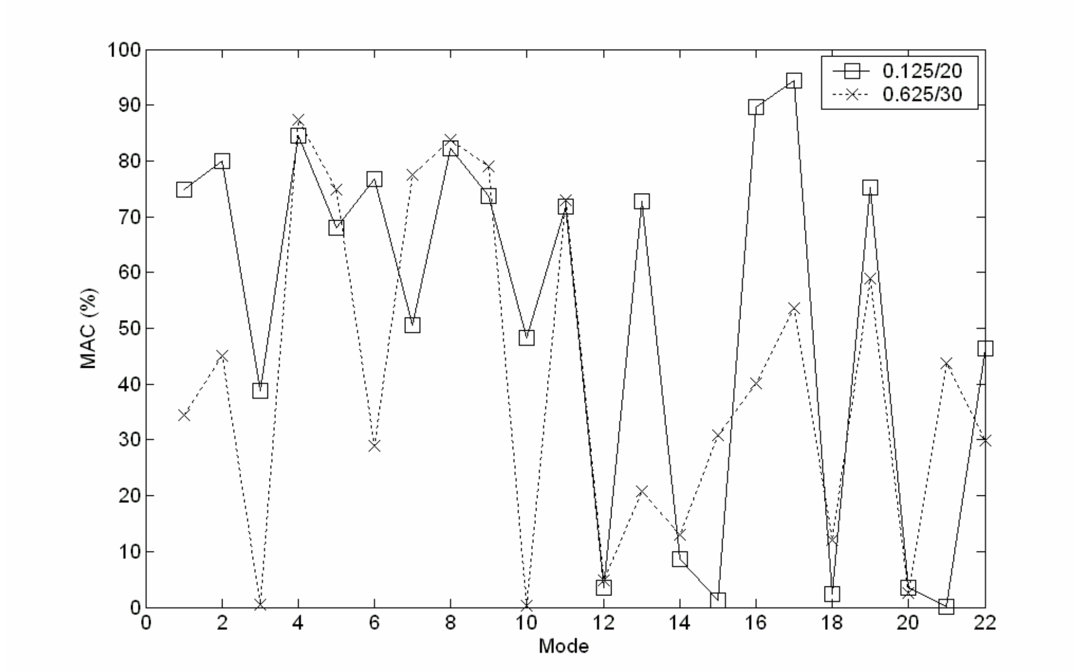

Figure 2.17 MAC comparing mode shapes from 0.125/20, and 0.625/30 experiments with results from Impulse experiment.

The addition of the second shaker may have constrained the helicopter-like structure in the horizontal plane, due to the shaker's mass and rigid coupling. Both shakers were suspended using elastic cord to minimise this effect. The good agreement between frequency and damping results suggests that the addition of the second shaker did not significantly affect estimated dynamic properties. In order to further investigate this, modal parameters were calculated using measurements in the vertical direction only; i.e. in the direction of the excitations. Coupling between modal displacements in the three principal directions was expected, but discounting DOFs in the horizontal plane was an attempt to minimise the effect of any constrained motions in that plane and also to eliminate a number of measurement points that were observed to have poor responses. MAC values comparing modal displacements in the vertical (z) direction from experiments 0.125/20 and 0.625/30 experiments with those from the Impulse experiments are shown in figure 2.18. A pattern of results similar to that shown in figure 2.17 (results for all measurement points) is apparent, although the well-correlated modes have marginally higher MAC values. This is most likely due to the omission of measurement points with poor responses, hence relatively inaccurate mode shape estimates.

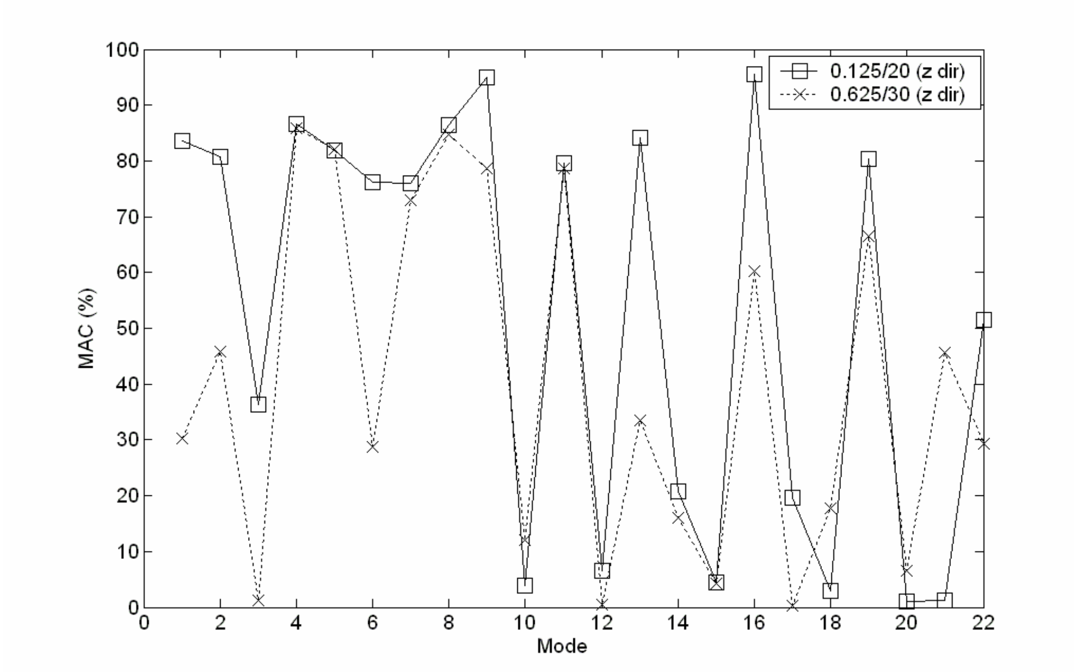

Figure 2.18 MAC comparing z-direction modal displacements from 0.125/20, and 0.625/30 experiments with results from Impulse experiment.

Periodic impulsive excitation has been used in conjunction with synchronous averaging; however, any other periodic excitation could be used, for example a pseudo-random sequence, burst random, or a low crest-factor sum of sinusoids. An advantage of such signals over impulse signals is the distribution of power of over a wide frequency band accompanied by a relatively low crest factor (although it could be argued random signals may include outliers contributing to high crest-factor). In addition, measurement noise and unmeasured excitations will reduce the s/n uniformly across the time record compared to impulse response records, which obviously decay with time. The use of periodic excitation signals is an advantage with frequency domain methods as it reduces bias errors (leakage) in discrete Fourier transforms (DFT), given that an integer number of periods of the excitation signal (hence response signal) occur within the time record.

2.6 Conclusions

The theoretical concepts of modal parameter estimation have been summarised in a review of common techniques. A variety of mathematical models are used in the algorithms, and while a significant amount of literature discusses the application of techniques for cases where excitation and response measurements are corrupted with measurement noise, only a few studies investigate techniques for dealing with cases where significant unmeasured excitation is present in addition to measured excitations. Time-domain averaging is a signal processing method commonly used for improving the signal-to-noise ratio in modal analysis and a frequency domain model of time-domain averaging has been reviewed.

Two experimental case studies applied periodic impulsive excitation and synchronous averaging in modal testing where unmeasured excitation is present. The first case considered a free-free aluminium beam excited with piezoceramic actuators. It was shown that piezoceramic actuators effectively excited higher order modes but did not excite the first mode well because of the limited deflection of the low-order modes in the contact area of the piezoceramic actuators. Approximating the excitation force by the applied voltage was found to yield accurate FRFs, hence estimated modal parameters. The use of piezoceramic actuators for structural excitation in modal analysis will be discussed in detail in Chapter 4.

Global RFLS modal parameter estimation was found to yield reasonably accurate modal parameters for low levels of unmeasured random excitation, while averaging time records synchronised with the excitation signal improved the accuracy of the modal parameter estimates. Unmeasured periodic excitation at frequencies away from modal frequencies did not affect modal parameter estimates as long as the periodic response was not mistaken for a modal frequency.

A second experimental case further demonstrated the use of periodic impulsive excitation and synchronous averaging for a more complex structure: a helicopter-like structure. Modal frequency and damping information could be accurately estimated for moderate levels of noise (0.625); though estimated mode shapes were typically poor. The coupling between the electrodynamic shakers and the structure was shown to only have a marginal influence on the estimated mode shapes.

The experimental case studies in this chapter have shown that periodic impulsive excitation (or more generally, periodic excitation) is effective in improving the signal-to-noise ratio, hence the estimated modal parameters. The RFLS modal parameter estimation algorithm assumes that all sources of structural excitation are measured and noise present in excitation and response measurements is minimal. An alternative modal parameter estimation algorithm, which explicitly models the effect of unmeasured excitations, as well as measurement noise, will be introduced in Chapter 5. In the following chapter, the use of experimentally determined modal parameters for validation and updating of finite element models is investigated.

Chapter 3 Finite Element Model Updating of a Helicopter-Like Structure

3.1 Introduction

Finite element models (FEMs) are typically used in the design process of helicopter structures and the introduction in Chapter 1 suggested that the correlation between an initial FEM and experimental data is often poor. This can arise due to inaccurate experimental data or an inadequate FEM. Some limitations of existing modal analysis methods were highlighted in Chapter 2. Factors that contribute to poor accuracy of FEMs include poor modelling of the physical components, for example omitting difficult-to-model components like structural joints. Changes in the values of physical parameters and material properties can alter FEM predictions significantly and are also a potential source of error. Nevertheless, FEMs present several advantages over experimental procedures and approximate analytical models. Experimentation is usually case specific and therefore multiple experiments are required to obtain results that fully describe the behaviour in a number of configurations or after structural modification. Furthermore, experiments are often expensive, time consuming and in some cases not practical due to safety issues or operational reasons. The flexibility of FEMs allows complex structures to be considered more efficiently than analytical models, and analytical models are typically limited to representative cases with relatively simple solutions.

A necessary step to improve the accuracy of FEMs is the use of experimental results to validate or update the FEM. The most basic approach is the use of engineering judgement to modify modal parameters, based on the correlation of one or two properties, for example the natural frequencies of dominant modes. More systematic approaches to model updating have been proposed and these can be automated and implemented in software. In this chapter, three case studies using experimental modal parameters to update FEMs are discussed.

Mottershead and Friswell [75] produced a comprehensive review of model updating theory outlining some of the difficult issues encountered: incompleteness of experimental data; i.e. due to a finite frequency range, or poorly excited modes; limited numbers of experimental measurement points compared to numerical model DOFs; and numerical issues arising from the highly undetermined nature of the model-updating problem. Model updating methods were categorised as representation model techniques or penalty techniques. Representation model techniques modify the FEM such that it exactly models measured (therefore incomplete) modal data and penalty techniques maximise the correlation between experimental and FEM data by adjusting FEM parameters according to a penalty function.

A series of studies have investigated the penalty technique applied to a simple structure [76]. The effect of different response parameters in the penalty (objective) function were reported: minimisation of natural frequency errors [77], natural frequency and mode shape errors [12], natural frequency and anti-resonance errors [8], mode shape, natural frequency and FRF data errors [9]. These methods effectively updated a FEM resulting in better correlation with experimental data. This was the first goal, and further assessment of the methods discussed in these studies involved predicting the effect of structural modification using the updated model. Improved correlation between experimental modal parameters from a modified structure and those from a similarly modified updated FEM was observed. This was compared with the correlation achieved by non-updated modified FEMs. Similar results were reported by Bohle and Fritzen [78], who used minimisation of natural frequency and mode shape errors for model updating. Identification of modelling errors in the FEM using error localisation techniques was also discussed in this study.

Model updating based on genetic algorithms has been considered by Levin and Lievin [79], and Dunn [10], and Lu and Tu [80] introduced a neural network approach. These methods are an alternative way to deal with the complex relationship between FEM parameters and measured response data. Penalty methods, discussed above, typically linearise the sensitivity functions, which relate a change in a set of FEM parameters to a change in the measured response.

Göge [11] reported on model updating of a civil aircraft structure using the classical sensitivity approach, which minimised modal frequency and mode shape errors. Joints were identified as sources of error in the FEM due to the difficulty of modelling welded, riveted, and bolted joints, in such a large structure. The updating procedure was judged to be successful as good correlation between experimental and FEM modal parameters was achieved in the active frequency range as well as for modal parameters outside the active frequency range. The active frequency range included modes used in the updating process. The updated FEM also predicted driving point FRFs that showed good correlation with measured data.

In this chapter, the use of experimental data to update a FEM of a helicopter-like structure is discussed. The experimental apparatus, instrumentation, the range of experiments, and curve fitting of experimental data are described in section 3.2. Formulation of the FEM and the updating procedure is described in sections 3.3 and 3.4, respectively. Results are discussed in section 3.5 and concluding remarks are made in section 3.6.

3.2 Experimental Modal Analysis of a Helicopter-Like Structure

The helicopter-like structure used for these experiments, shown in figure 3.1(a), consisted of a primary structure made up of bar and tube sections and a secondary structure consisting of steel sheet spot welded to the primary structure. Elastic cords were used to suspend the helicopter-like structure, as shown in figure 3.1(a), and preliminary testing indicated that the natural frequencies of the rigid-body vibration modes were less than 20% of the natural frequency of the first elastic vibrational mode. The structure was excited at 134 points using a B&K 8202 impact hammer and fixed response measurements in the direction of the three principal axes were taken using three B&K 4374 mono-axial accelerometers with preliminary signal conditioning applied using B&K 2635 charge amplifiers (high-pass filter cut-off 2Hz, low-pass filter cut-off 3kHz). A plastic tip was used on the impact hammer to provide a spectral input of up to approximately 2kHz [81]. The excitation points and position of the accelerometers are shown in figure 3.1(b).

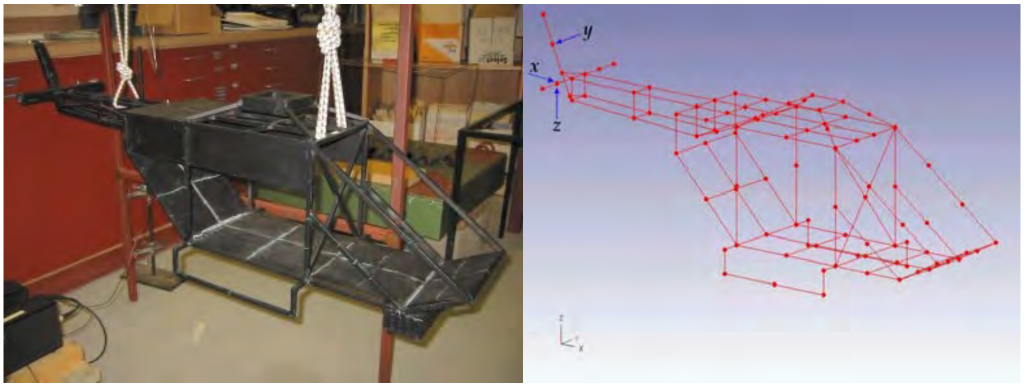

(a) *(b)*

Figure 3.1 (a) Helicopter-like structure used for case 1 (EMA1) experiments. (b) Wire-frame model of helicopter-like structure showing excitation points (dots) and response measurement points (arrows).

Data acquisition and signal processing was carried out using a Hewlett-Packard HP 3566A FFT analyser. Measurement parameters for the test were: analysis bandwidth 400Hz; frequency resolution 0.5Hz; transient and exponential weighting (time constant 0.5 seconds) on excitation and response signals respectively, with 5 averages per measurement. The software package STAR Modal v. 5.23 was used to curve fit the FRF data and extract the modal parameters using a global RFLS algorithm.

Three experiments were conducted with the helicopter-like structure in a different configuration for each experiment.

3.2.1 Case 1: Helicopter-like structure with panels (EMA1)

The first configuration was the helicopter-like structure with panels, shown in figure 3.1(a). Modal frequency results are listed in table 3.1 for the first 19 modes.

3.2.2 Case 2: Helicopter-like structure with panels removed (EMA2)

Results for the first experiments were believed to be inaccurate due to the non-linear behaviour of the joints between the secondary structure panels and the primary structure. The panels were spot welded at points along the edges and the remaining parts of the panel in contact with the primary structure rattled against the primary structure. This interfered with the assumption that the dynamic behaviour of the structure was linear, and therefore limited the accuracy of the experimental data. In order to rectify this situation the panels were removed, as shown in figure 3.2. Modal frequencies for this configuration are listed in table 3.1.

Figure 3.2 Helicopter-like structure with panels removed used for case 2 (EMA2) experiments.

3.2.3 Case 3: Helicopter-like structure with additional mass, panels removed (EMA2_m)

This configuration of the helicopter-like structure is shown in figure 3.3. A steel beam of mass 2.09kg, was bonded to the central longitudinal floor member using epoxy. Modal frequency results are shown in table 3.1. The steel beam resulted in significant changes to the dynamic properties of the structure and this is illustrated by comparing FRFs measured at the same point in EMA2 and EMA2_m experiments, which are plotted in figure 3.4.

Figure 3.3 Helicopter-like structure with panels removed, used for case 3 (EMA2_m) experiments. Additional mass (thick steel beam) can be seen bonded to the central-longitudinal floor member.

	Modal Frequencies (Hz)		
Mode	Case 1 (EMA1)	Case 2 (EMA2)	Case 3 (EMA2_m)
1	100.1	73.92	68.04
2	171.6	77.24	73.1
3	195.3	85.1	80.75
4	197.3	143.4	148.09
5	222.6	164.87	152.48
6	237.3	185.53	154.05
7	247	201.14	188.99
8	267.5	238.5	191.55
9	273.4	244.3	220.44
10	290.1	262.62	235.74
11	303.6	280.38	247.48
12	326.5	282.28	266.28
13	328.5	297.58	274.96
14	347.8	313.9	289.05
15	352.9	317.14	292.47
16	358.8	322.08	317.44
17	371.4	341.22	339.98
18	378.3	356.62	353.41
19	387.5	363.6	356.84

Table 3.1 Modal frequency results from experimental modal analysis, cases 1 – 3.

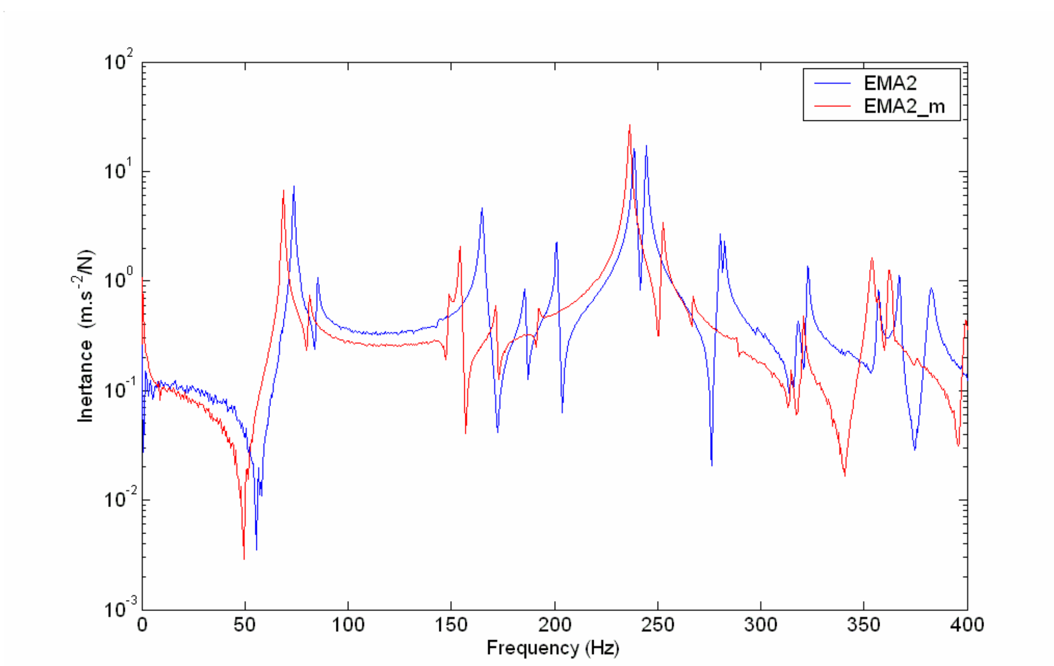

Figure 3.4 FRFs for the same measurement points obtained in EMA2 and EMA2_m experiments.

3.3 FEM of Helicopter-Like Structure

A preliminary FEM, denoted FEM0, was developed in ANSYS based on the work described by Endo and Randall [82]. Beam and solid elements were used for the primary structure and shell elements were used to model the floor, roof, and side plates of the cargo bay. On the physical structure, the panels were attached to the primary structure using spot welds at various points around the perimeter of the panels, however, the joints between the panels and the primary structure in FEM0 were modelled as continuous seam welds. These were modified to represent spot welds at various points around the perimeter of the panels as this was believed to be a significant source of error in the model updating work described by Endo and Randall [82]. This new model is referred to FEM1. Modifications were made to FEM1 to reflect the modifications made to the physical structure, as outlined in section 3.2. The different FEM configurations corresponding to each configuration of the physical structure were as follows:

Case 1 (FEM1): Helicopter-like structure with top, side and floor panels, shown in figure 3.5.

Element Types:

1. Shell63 (679 elements) – Panels
2. Solid73 (40 elements) – Mass below front floor
3. Beam4 (978 elements) – Beam sections of primary structure

Case 2 (FEM2): Helicopter-like structure with top, side and floor panels removed, shown in figure 3.6. Joints between beam elements modelled with separate elements.

Element Types:

1. Solid73 (40 elements) – Mass below front floor
2. Beam4 (688 elements) – Beam sections of primary structure
3. Beam4 (226 elements) – Joints of primary structure.

Case 3 (FEM2_m): FEM from case 2 with additional mass, bonded to central longitudinal floor member, modelled with solid elements. The FEM for case 3 is shown in figure 3.7.

Element Types:

1. Solid73 (96 elements) – Mass below front floor and steel beam bonded to central longitudinal floor member
2. Beam4 (689 elements) – Beam sections of primary structure
3. Beam4 (226 elements) – Joints of primary structure

Note that the joints of the primary structure in FEM2 and FEM2_m were modelled with small beam elements to enable the parameters of these elements to be modified independently during model updating.

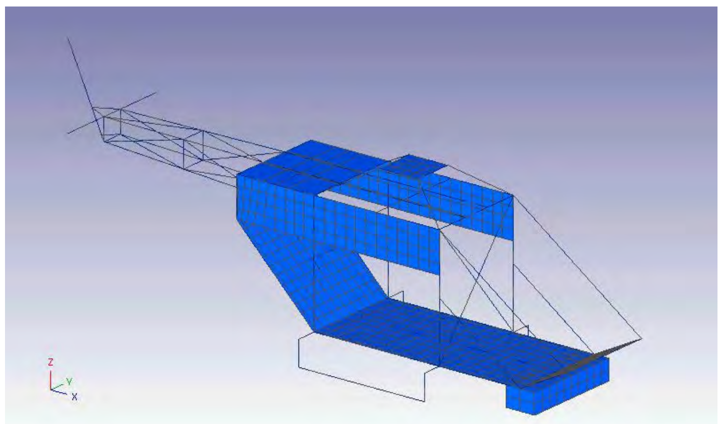

Figure 3.5 FEM of helicopter-like structure, case 1 (FEM1).

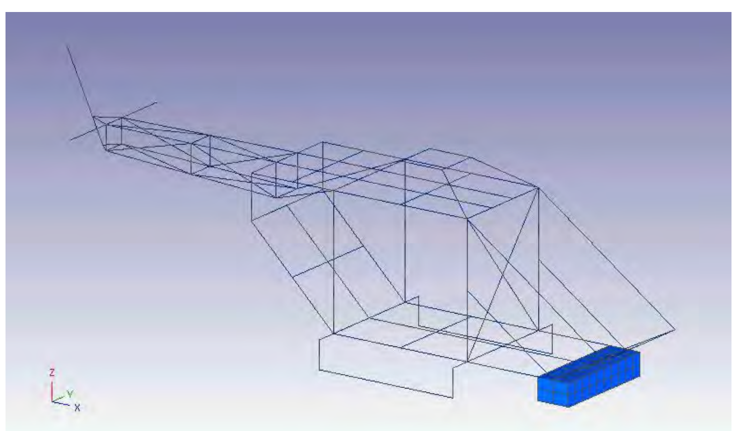

Figure 3.6 FEM of helicopter-like structure, case 2 (FEM2).

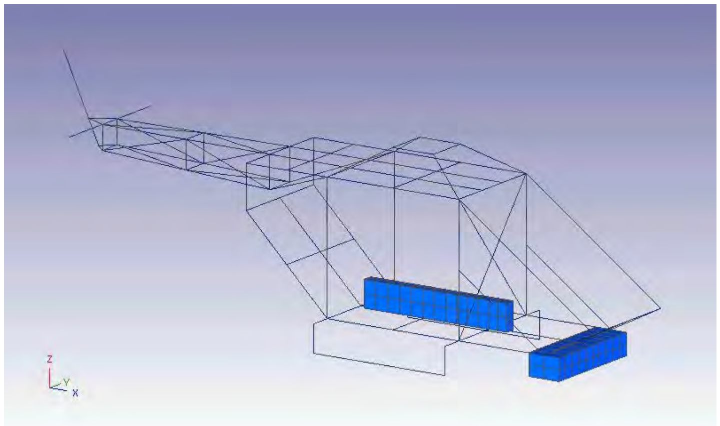

Figure 3.7 FEM of helicopter-like structure, case 3 (FEM2_m).

The initial (i.e. prior to updating) models for cases 1–3 used the same material properties for each element type: density = 7850 kg/m^3; Young's modulus = 210 *GPa*; Poisson's ratio = 0.3.

The block Lanczos solution method was used to extract modal frequencies and mode shapes for all cases.

3.4 Finite Element Model Updating

The aim of the model updating procedure is to improve the correlation of FEM and experimental modal analysis (EMA) results. The model updating software package FEMtools v2.2 was used for this process.

The model updating procedure involves a number of steps:

1. Spatial correlation of nodes and points: Nodes from the FEM are paired with measurement points used during EMA. Figure 3.8 shows FEM1 of the helicopter-like structure with coincident node/measurement-point pairs indicated by dots.

2. Shape correlation: This procedure compares the FEM and EMA mode shapes. The MAC is a simple means of numerically comparing complex mode shapes, used in addition to the comparison of modal frequencies. Automatic mode shape pairing identified mode pairs with the highest MAC value above a threshold of 20%.

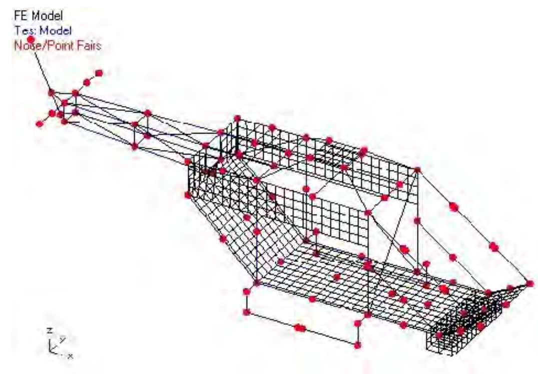

Figure 3.8 EMA model superimposed on FEM1. Coincident node/point pairs are indicated by dots.

3. Response selection: Responses are selected from any quantity measured during experimental analysis, for example, mass, displacement, modal frequencies or stress. Modal frequencies were selected as response parameters as they are functions of both mass and stiffness parameters. Modal frequencies were also considered to be estimated with the greatest accuracy.

4. Sensitivity analysis and parameter selection: Sensitivity defines the rate of change of a FEM response property, in this case modal frequency, as a function of the change of a FEM parameter. Sensitivity analysis identifies the most influential parameters to modify during model updating, and the inverse of the sensitivity matrix, the gain matrix, is used during model updating to calculate the magnitudes of parameter changes. Normalised relative sensitivities are independent of units for both the response properties and the model parameters, allowing comparison of several different parameters. Parameters identified by sensitivity analysis can be modified globally or locally; global parameter changes apply to sets of elements while local parameter changes apply to individual elements. It should be noted that sensitivity analysis identifies parameters that are most efficient to modify during model updating. These parameters are not necessarily the correct parameters to modify, or the parameters that have large errors with respect to the physical model. Therefore, parameter selection has to be tempered with engineering judgement using parameter weighting and the specification of upper and lower bounds. Parameter weighting is applied to individual parameters on the basis of expected accuracy, importance or other criteria, using confidence values. Confidence values are calculated by taking

the inverse of the estimated error of a parameter and multiplying by 100. For example, if a parameter has an estimated error of 25%, the confidence value is 400.

5. Parameter Estimation: The aim of model updating is to determine a new set of FEM parameters such that that the predicted response (natural frequencies and/or mode shapes; FRFs) correlates with the corresponding experimental response. This is approximated by a Taylor series expansion of the function relating experimental and FEM responses, and FEM parameters. The first term of this expansion is [83]

$$\{R_e\} = \{R_a\} + [S](\{P_u\} - \{P_0\}) \tag{3.1}$$

where $\{R_e\}$ is a vector of experiment responses; $\{R_a\}$ is the predicted FEM response for the set of parameter values $\{P_0\}$; $\{P_u\}$ is the set of updated FEM parameter values; and $[S]$ is the sensitivity matrix. Equation (3.1) can be expressed as [83]

$$\{\Delta R\} = [S]\{\Delta P\} \tag{3.2}$$

and for the cases considered in this study, solved by finding the pseudo-inverse of the sensitivity matrix (i.e. the gain matrix). A number of iterations are required because only the first term of the Taylor series expansion was used to derive equations (3.1) and (3.2).

6. Convergence criterion: The convergence criterion is the error function calculated during correlation analysis in model updating. The weighted absolute difference between experimental and FEM modal frequencies was used as the convergence criterion, with equal weighting assigned for all modes.

7. Model updating iterative process: Figure 3.9 shows a block diagram of the model updating procedure. Note that the internal FEM solver in FEMtools was used rather than recalculating the FEM response values for each iteration in ANSYS. No significant differences in the natural frequencies obtained from each solver were observed for FEM2. The desired number of model updating iterations is determined

by the value of the convergence criterion required to end the updating process and the minimum change of convergence criterion required to progress to the next iteration.

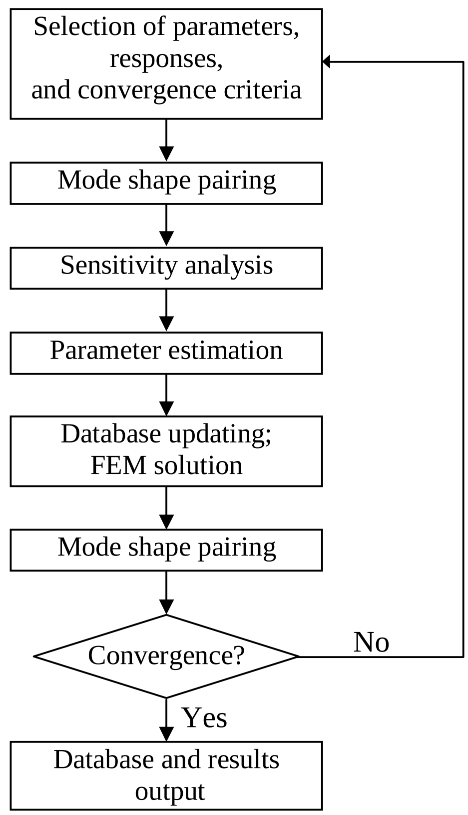

Figure 3.9 Flow chart of model updating procedure.

8. The final model updating step is the MAC contribution analysis (MCA). MCA ranks DOFs with an adverse effect on MAC values so that they can be assessed in terms of the quality of experimental data. In some cases it is beneficial to remove the deflections at particular DOFs to improve MAC values. Another reason for removal of a DOF is that experimental data could not be recorded for a particular direction at a measurement point due to physical constraints on placing accelerometers or exciting the structure.

3.5 Model Updating Results

3.5.1 Case 1

The FEM used as a basis for model updating should ideally represent the physical arrangement of structural members reasonably accurately for updating to be a success, even if FEM parameters cannot be accurately specified. Simplifications are often necessary and this can limit the effectiveness of model updating and also inhibit the use of the model for predicting the effects of structural modification. Table 3.2 (a) lists mode pairs for FEM0 and EMA1 results. FEM0 assumed continuous seam welded panels, and results are similar to those obtained reported by Endo and Randall [82].

Pair no.	EMA Mode	Frequency (Hz)	FEM Mode	Frequency (Hz)	% Error	MAC (%)
1	1	100.08	4	196.04	95.88	23.3
2	3	195.35	6	246.4	26.14	68.8
3	8	267.47	7	262.15	-1.99	63.8
4	4	197.33	8	265.33	34.46	23.3
5	12	326.49	15	318.56	-2.43	23.4
6	13	328.55	16	332.08	1.07	36.8
7	16	358.84	17	343.3	-4.33	28.3
8	15	352.95	18	345.7	-2.05	44.8
9	18	378.28	19	353.65	-6.51	41.1
Average of absolute values					19.43	39.29

Table 3.2 (a) FEM0/EMA1 mode pairs.

Pair no.	EMA Mode	Frequency (Hz)	FEM Mode	Frequency (Hz)	% Error	MAC (%)
1	1	100.08	2	100.14	0.06	19.7
2	3	195.35	3	124.48	-36.28	23
3	4	197.33	7	253.41	28.42	61.4
4	8	267.47	10	263	-1.67	66.3
5	6	237.26	11	271.74	14.53	38
6	9	273.43	13	288.14	5.38	29.4
7	13	328.55	14	308.87	-5.99	21.5
8	12	326.49	15	314.47	-3.68	27.5
9	15	352.95	20	341.11	-3.35	33.4
10	14	347.78	21	343.8	-1.15	42
11	17	371.37	23	370.53	-0.23	25.1
Average of absolute values					9.16	35.2

Table 3.2 (b) FEM1/EMA1 mode pairs.

Table 3.2 (b) lists mode pairs for FEM1/EMA1 and shows a large improvement in average frequency error accompanied by a small decrease in average MAC value compared to the results in table 3.2 (a). FEM1 was considered to be more suitable for model updating because of the improved modelling of the joints between the panels and the primary structure.

EMA1 experimental data were used to update FEM1. The updated FEM1 model is denoted FEM1_u and the details of each model updating iteration are shown in table 3.3. The results of model updating are assessed using the frequency error and MAC of paired modes from FEM1_u and EMA1. These results are compared with results from FEM1/EMA1 in figures 3.10 and 3.11. Nine mode pairs were identified for the EMA1/FEM1_u case, which was two less than the non-updated model, EMA1/FEM1. However, updating significantly improved the correlation between the identified mode pairs: less than 5% difference between modal frequencies for eight of the nine mode pairs and average absolute frequency errors decreased from 9.16% to 2.1%. Large improvements in MAC values were also achieved and the average MAC value including all mode pairs increased from 35.21% to 71.97%. These results demonstrate the effectiveness of model updating in improving the correlation between experimental and numerical models. A more practical evaluation of model updating involves assessing how well the updated FEM predicts the effects of a structural modification, compared to the predictions of a non-updated FEM. This is discussed in the following section.

Model Updating Step	Parameter Variation	Parameter Bounds and Confidence
1	Elasticity matrix scaling: D Total Iterations = 5	-10%<D<10% Confidence=400
2	Young's modulus: E Total Iterations = 5	-10%<E<10% Confidence = 400
3	Mass parameter: RHO Total Iterations = 5	-10%<RHO<10% Confidence = 400
4	Cross-sectional area: AX Total Iterations = 5	-10%<AX<10% Confidence = 400
5	Moment of inertia: I_x,I_y,I_z Total Iterations = 3	-10%< I_x,I_y,I_z <10% Confidence = 400
6	Membrane thickness: H	-10%<H<10% Confidence = 400
7	Adjusting DOFs Pairing, fine-tuning D, E, H together	-10%<X<10% Confidence = 400
8	Adjusting DOFs Pairing, fine-tuning D,E together.	-10%<X<10% Confidence = 400
9	MAC Contribution Analysis	

Table 3.3 Model updating steps for case 1: FEM1/EMA1.

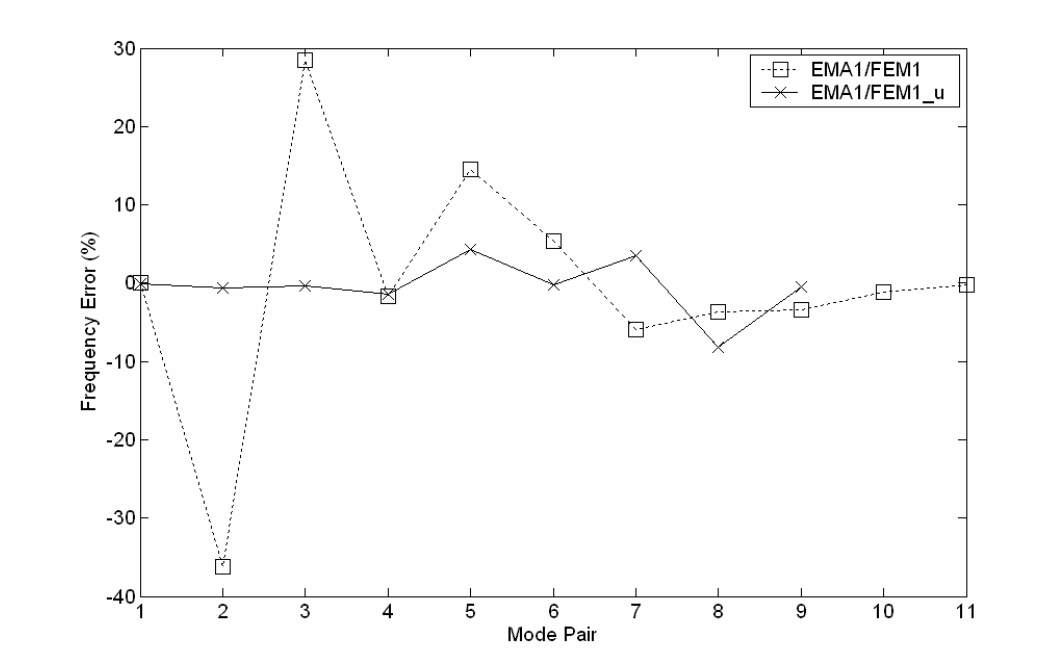

Figure 3.10 Comparison of frequency error (referenced to EMA1 results) for FEM1 (before updating) and FEM1_u (after updating).

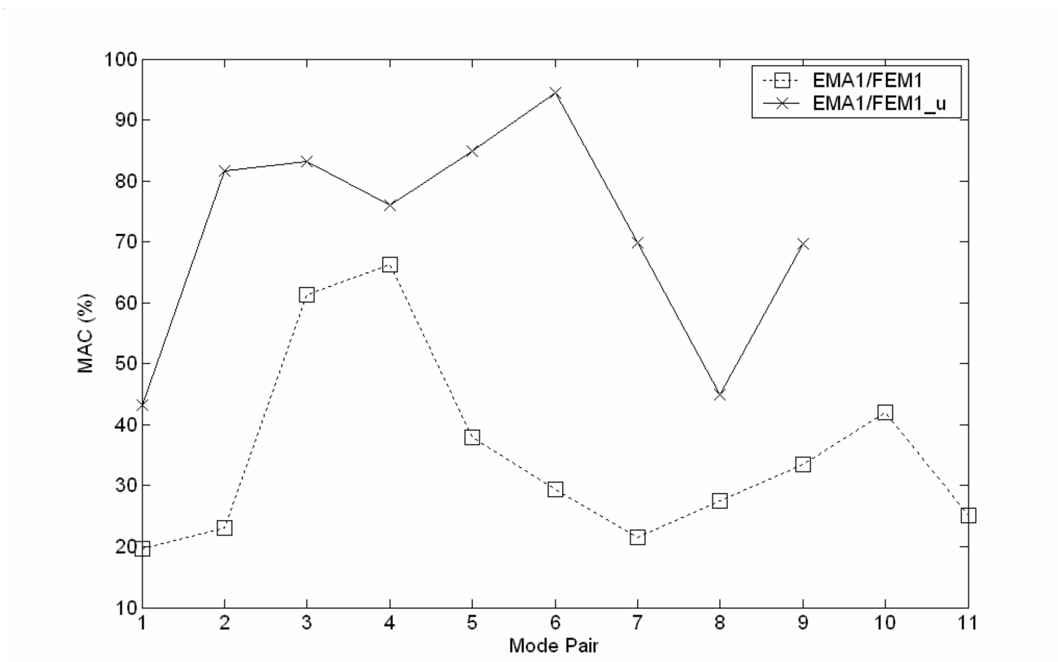

Figure 3.11 Comparison of MAC (referenced to EMA1 results) for FEM1 (before updating) and FEM1_u (after updating).

3.5.2 Case 2

The initial correlation between EMA1 and FEM1 was found to be quite poor and a number of factors were believed to account for this. Impact hammer testing of the helicopter-like structure involved exciting points on the primary structure (steel bars) as well as the spot-welded panels. It was noted that the panels rattled against the primary structure and were very compliant at some excitation points. As a result, experimental data for these points were of relatively poor accuracy and increasing numbers of averages typically failed to improve the quality of the measured FRFs, as indicated by the estimated coherence. Results in Chapter 2 suggest that the global RFLS parameter estimation algorithm would be relatively robust to these inaccuracies when estimating frequency and damping results; however, modal residues, hence mode shapes, could potentially be very poor.

Another factor that potentially reduced the accuracy of results was the modelling of the panel/primary structure joints. As discussed above, FEM0 assumed perfect coupling at the interface of the primary structure and panels, and this assumption was subsequently modified in FEM1, which modelled the spot welds between the panels and primary structure. This improved results but lead to the condition where partial or intermittent contact between the panels and the primary structure was not explicitly taken into account. Therefore, while the updated FEM, FEM1_u, showed good correlation with experimental results, it did not necessarily predict physically realisable behaviour due to the way the panels were modelled. The panels were removed from the helicopter-like structure for cases 2 and 3 to eliminate this source of uncertainty, and as a result the model updating process could be better studied.

Model updating of FEM2 using EMA2 experimental data was carried out according to the steps listed in table 3.4. Correlation between FEM2 and FEM2_u with EMA2 results is summarised in figures 3.12 and 3.13.

Removing the panels resulted in very good correlation between the initial FEM and experimental results, but this decreased the scope for improvement by model updating. Despite this, model updating increased the number of identified mode pairs from ten to fourteen and correlation between natural frequencies was typically better for the updated model. Average absolute frequency error decreased from 2.68% for EMA2/FEM2 pairs to 0.67% for EMA2/FEM2_u pairs. Average MAC values decreased marginally from 86.93% (EMA2/FEM2) to 84.36% (EMA2/FEM2_u); however, it should be remembered that four additional mode pairs were included for EMA2/FEM2_u. Figure 3.13 shows that updating produced little improvement or a marginal decrease in MAC values for the first 8 mode pairs, while frequency error for the corresponding mode pairs improves. This effect is probably due to the use of absolute difference in natural frequencies as the response property in model updating. Note that an alternative response property, for example MAC values or FRF data could be used in addition or as an alternative to natural frequencies.

Model Updating Step	Parameter Variation	Parameter Bounds and Confidence
1	Elasticity matrix scaling: D Total Iterations = 5	-10%<D<10% Confidence=400
2	Young's Modulus: E Total Iterations = 5	-10%<E<10% Confidence = 400
3	Mass parameter: RHO Total Iterations = 5	-10%<RHO<10% Confidence = 400
4	Cross-sectional area: AX Total Iterations = 5	-10%<AX<10% Confidence = 400
5	Moment of inertia: I_x,I_y,I_z Total Iterations = 3	-10%< I_x,I_y,I_z <10% Confidence = 400
6	Elasticity matrix scaling: D, Cross-sectional area: AX Total Iterations = 3	-10%<AX,D<10% Confidence = 400
7	Moment of inertia: I_z, Young's modulus: E Total Iterations = 3	-10%<I_z,E<10% Confidence = 400
8	Moment of inertia: I_y, Mass parameter: RHO Total Iterations = 3	-10%<I_y, RHO<10% Confidence = 400
9	Elasticity matrix scaling: D Moment of inertia: I_x Total Iterations = 3	-10%<D,I_x<10% Confidence = 400
10	Mass parameter: RHO Total Iterations = 3	-10%<RHO<10% Confidence = 400

Table 3.4 Model updating steps for case 2: FEM2/EMA2.

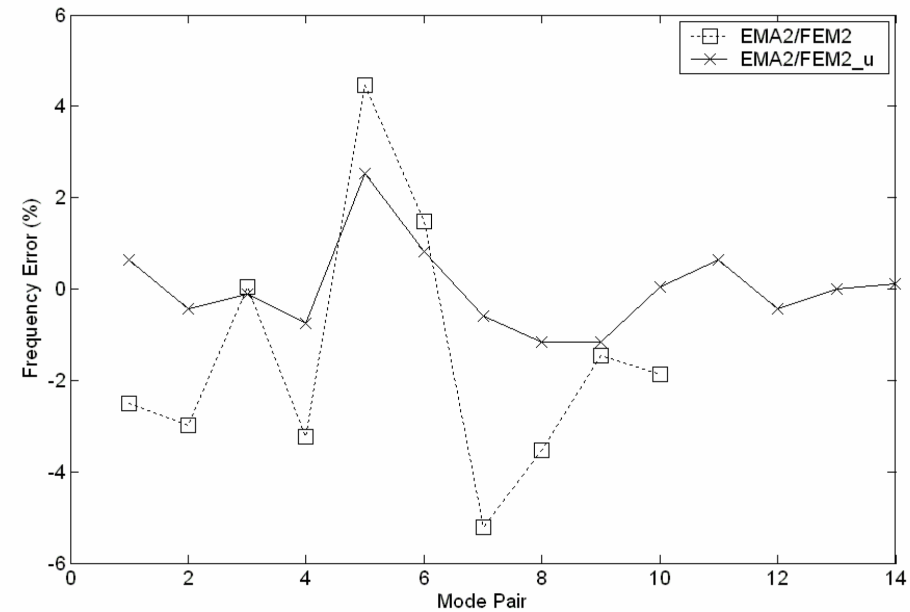

Figure 3.12 Comparison of frequency error (referenced to EMA2 results) for FEM2 (before updating) and FEM2_u (after updating).

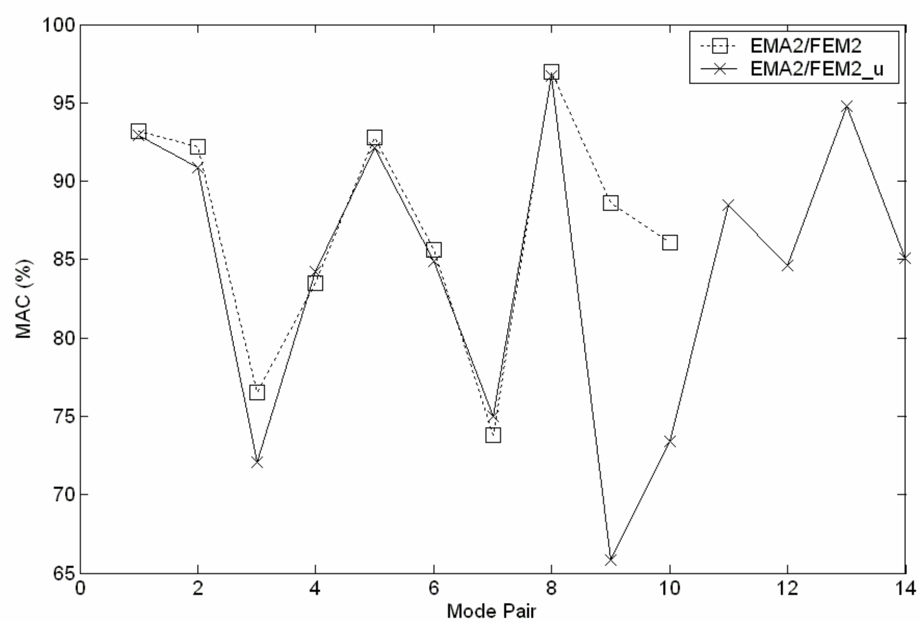

Figure 3.13 Comparison of MAC (referenced to EMA2 results) for FEM2 (before updating) and FEM2_u (after updating).

3.5.3 Case 3

The previous two cases showed that model updating improved the correlation between experimental and FEM results. Case 3 investigates whether the updated FEM can better predict the effect of structural modification than a non-updated FEM.

A steel beam was bonded to the central longitudinal floor member of the helicopter, as outlined in section 3.2.3. The steel beam could be modelled accurately and it was initially believed that the epoxy bonding would not have a significant effect on the dynamics of the structure in the frequency range of interest. The updated model FEM2_u was modified to include the added mass in a similar way to FEM2_m (the non-updated FEM with added mass) and this new model was denoted FEM2_u_m. Correlation between EMA2_m/FEM2_m and EMA2_m/FEM2_u_m is compared in figures 3.14 and 3.15.

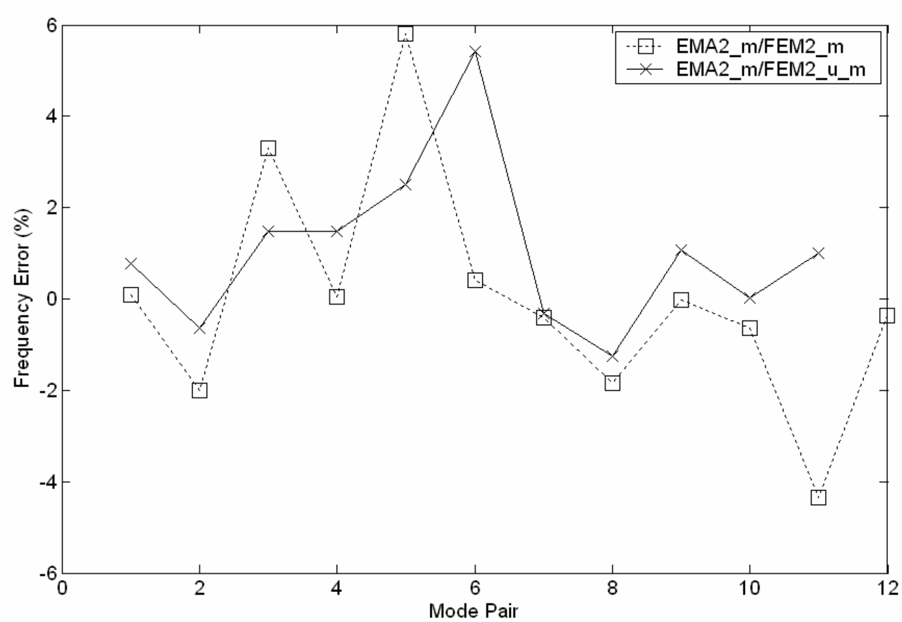

Figure 3.14 Comparison of frequency error (referenced to EMA2_m results) for FEM2_m (non-updated model with additional mass) and FEM2_u_m (updated model with additional mass).

No clear trend is seen in the frequency results, plotted in figure 3.14, however mode pairs from EMA2_m/FEM2_u_m have a marginally lower average absolute frequency error (1.45%) compared to EMA2_m/FEM2_m (1.61%). Mixed results are also indicated by the MAC values; FEM2_u_m predicts modes 6 – 9 more accurately than FEM2_m but results are poorer by varying degrees for the remaining modes. Average

MAC values decrease marginally from 71.39% (EMA2_m/FEM2 _m) to 70.77% (EMA2_m/FEM2_u_m). Note one less mode-pair was identified in EMA2_m/FEM2_u_m.

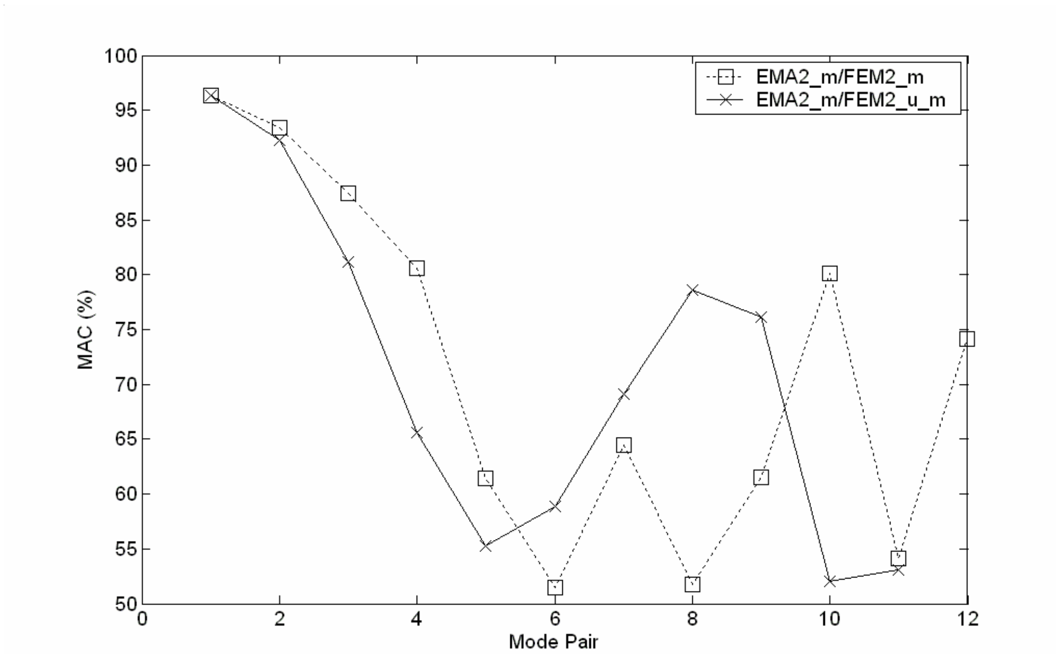

Figure 3.15 Comparison of MAC (referenced to EMA2_m results) for FEM2_m (non-updated model with additional mass) and FEM2_u_m (updated model with additional mass).

Comparison of either of the experimental/FEM model pairs considered in this case with EMA2/FEM2 illustrates the difficulties encountered in modelling the bonded steel beam. Better average absolute frequency errors are achieved: EMA2_m/FEM2_m, 1.61%; EMA2_m/FEM2_u_m, 1.45%; EMA2/FEM2, 2.68%; however, average MAC values are considerably poorer: EMA2_m/FEM2_m, 71.39%; EMA2_m/FEM2_u_m, 70.77%; EMA2/FEM2, 86.93%. This suggests that local modal parameters obtained from the experimental analysis may have adversely affected the quality of the experimental mode shapes. Removing selected DOFs in MAC contribution analysis (MCA) improved MAC values for modes with low initial MAC values but no set of problematic DOFs common to modes with low MAC were identified. For example, the MAC for mode pair five in EMA2_m/FEM2_u_m was improved from 55.29% to 70% after removing two measurement points (out of 134) from the calculation. The MAC for mode pair 10 in EMA2_m/FEM2_u_m was improved from 52.05% to 72.58% after removing ten measurement points from the calculation, but these points did not include the two points removed for mode pair five.

Explicitly modelling the epoxy joint between the added mass and the helicopter-like structure, and further updating did not lead to significant improvement of the results. This outcome raised questions about the quality of the experimental data, in particular the quality of mode shape data for some measurement points. The model updating cases considered above resulted in improvements in the agreement between natural frequencies, partly due to the use of natural frequencies as a response parameter in the objective function. On the other hand, MAC values were found to be variable and MCA identified a number of measurement points (different for each mode) that adversely affected the MAC, as noted above. The implication is that additional analysis is required to verify the accuracy of modal parameters estimated at each DOF, and to exclude problematic measurement points.

3.6 Conclusions

Finite element modelling is a powerful tool for carrying out analysis of structural dynamic behaviour. In many cases poor correlation between an initial FEM and experimental results can be improved using model updating. Three case studies have been considered to illustrate the potential of model updating. The first experimental case included non-linear behaviour in the form of contacting parts that rattled, which lead to a decrease in the quality of experimental data. Model updating significantly improved the correlation between the FEM and experimental results: average absolute frequency error between paired modes decreased from 9.16% to 2.1%, and average MAC value increased from 35.31% to 71.97%. The structural elements contributing to non-linear behaviour (i.e. the panels) were removed for the second case and this improved the initial correlation between FEM and experimental results. Model updating improved the correlation by identifying four additional mode pairs, accompanied by a marginal decrease in average MAC for mode pairs (86.93% to 84.36%), and a significant decrease in average absolute frequency error (2.68% to 0.67%). Verification of the model updating process was carried out by predicting the effects of a structural modification using the updated FEM. Results were not conclusive: average absolute frequency error was only marginally better than for the predictions using a non-updated FEM (1.61% compared to 1.45%) and average MAC values were very similar (71.39% for the non-updated FEM; 70.11% for the updated FEM). It was found that some measurement points adversely affected MAC values, though no clear trend could be identified to detect poor experimental data. The modal parameter estimation algorithm introduced in Chapter 5 is aimed at estimating accurate modal parameters in the presence of unmeasured excitation, and provides multiple estimates of global modal parameters, which allows statistical analysis of these estimates to indicate the accuracy of the results.

Chapter 4 Piezoceramic Actuators for Multi-Point Structural Excitation in Experimental Modal Analysis

4.1 Introduction

Piezoelectric actuators and sensors have been widely studied in the area of structural vibration control [84-97] and more recently non-destructive damage detection [98-100]. The experimental case studies in Chapter 2 used piezoceramic actuators to excite a beam for modal analysis, and it was shown that FRFs relating voltage (applied to the piezoceramic plates) and acceleration response could be used to extract modal parameters. The FRFs estimated in this case differ from FRFs used in classical modal analysis, which relate a measured point force to vibration response (displacement, velocity, or acceleration). The piezoceramic actuators apply a distributed excitation, and point mobilities cannot be measured as for the case of point forces. Piezoceramic actuators offer a number of advantages over other excitation methods, for example, electrodynamic shakers, impact hammers or ambient excitation. Piezoceramic actuators are relatively small, robust and cheap, and can be easily bonded to many points on a structure or be integrated into smart composite structures. Thus, piezoceramic actuators are appropriate for permanent or long term installations. They can be driven with a wide range of excitation signals and have moderate power requirements [101]. A limitation of these actuators is that determining the effectiveness of piezoceramic actuators in exciting structures is much less intuitive than for point excitation.

In this Chapter, the dynamic behaviour of piezoceramic plates bonded to a representative beam structure is discussed. The transfer function relating displacement response to the voltage applied to a pair of piezoceramic actuators bonded to a beam is derived in section 4.2, and the implications for modal parameter estimation are discussed. The approximate analytical model of the piezo-actuated beam is verified by comparison with FEM and experimental results in section 4.3. Section 4.4 presents a preliminary analysis of a cantilever beam to assess the performance of multiple actuator pairs in exciting transverse modes of the beam.

4.2 Excitation of an Aluminium Beam Using Piezoceramic Plates

An aluminium beam with pairs of piezoceramic actuators bonded to the surface is studied as this case can be treated with approximate analytical methods [85-87, 89, 90, 94, 97, 102], and has been considered in experiments discussed in Chapter 2.

Piezoelectric materials have the property that the strain and the electric field in the material are coupled. Consequently, applying an electric field to a piezoelectric material results in the deformation of the material and the material acts as a mechanical actuator. Conversely, a change in the material's electric field results from deforming the material and the material acts as a sensor. The work considered here deals with piezoceramic materials as actuators.

The coupled electro-mechanical behaviour of piezoelectric materials can be fully specified by the following set of equations [86]:

$$\varepsilon_i = S_{ij}^E \sigma_j + d_{mi} E_m \tag{4.1}$$

$$D_m = d_{mi} \sigma_i + \xi_{ik}^{\sigma} E_k \tag{4.2}$$

where $i,j = 1, \ldots, 6, k, m = 1,2,3$ refer to the principal and (shear) rotational directions; $\boldsymbol{\varepsilon}$ is a vector of strain (*m/m*); $\boldsymbol{S}^E$ is the matrix of compliance coefficients (m^2/N) measured at constant electric field; $\boldsymbol{\sigma}$ is a stress vector (N/m^2); $\boldsymbol{d}$ is the matrix of piezoelectric stain constants (*m/V*); $\boldsymbol{E}$ a vector of applied electric field (*V/m*); $\boldsymbol{D}$ a vector of electric displacement or flux density (C/m^2); and $\boldsymbol{\xi}^{\sigma}$ is the permittivity (*F/m*) under constant stress conditions.

For the case where two piezoceramic plates are bonded to an aluminium beam, a one-dimensional approximation of the coupled behaviour is used. This is justified due to the geometry of a slender beam, which leads to relatively high stiffness in the lateral-transverse direction. Figure 4.1 shows a schematic of a piezoceramic plate with a voltage applied across the poles, which are located on the top and bottom faces.

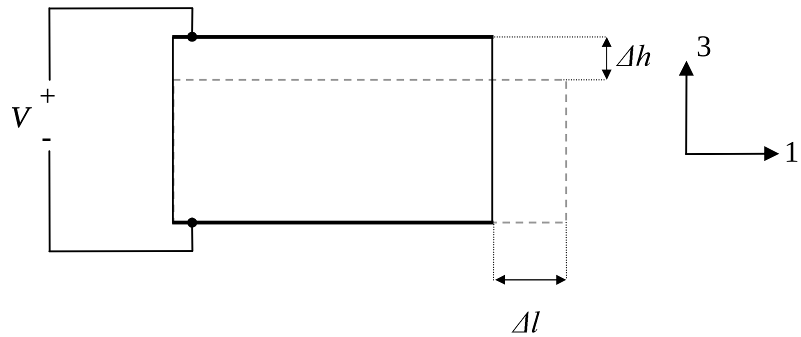

Figure 4.1 Schematic of piezoceramic actuator with voltage applied to the poles located on the top and bottom surfaces. The solid lines indicate the deformed shape and the dashed outline shows the undeformed shape.

The undeformed shape is represented by the dashed lines, and the deformed body, which results from the applied voltage, is represented by the solid lines. This two-dimensional representation is further simplified by only considering Δl; from which the strain in direction 1 can be calculated. This is termed the free strain of the piezoceramic actuator, and is denoted ε_p. Equation (4.3) is derived from equation (4.1) and describes the free strain (i.e. zero applied stress) for an actuator of thickness t_p.

$$\varepsilon_p(t) = d_{31}\frac{V(t)}{t_p} \tag{4.3}$$

Figure 4.2 shows the configuration of piezoceramic actuators bonded to a slender beam of uniform cross-section. The piezoceramic actuator is assumed to be perfectly bonded to the beam so that the strain is equal at the interface of the beam and the actuator, and the strain is considered to be a linear function of the thickness of the beam [86]. The effect of finite adhesive layer has been studied by Crawley and de Luis [89], among others [90, 94, 100]. Results suggest that for a thin and stiff bonding layer between the beam and the actuator, the assumption of perfect bonding is satisfactory. The effect of a finite adhesive layer is to limit the transfer of piezoelectric strain to the beam, through the effect of shear lag.

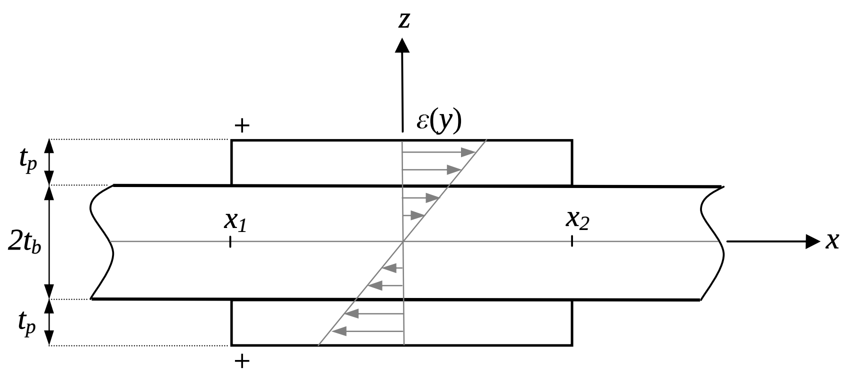

Figure 4.2 Strain distribution across top and bottom piezoceramic actuators bonded to an aluminium beam. The polarity of voltage applied to each actuator is shown, which results in a moment distributed over the contact area of the actuators being applied to the beam.

The stress in the beam and actuators is written in terms of material properties [102]

$$\sigma_b = E_b \varepsilon_b \frac{z}{t_b}, \qquad -t_b < z < t_b \tag{4.4}$$

$$\sigma_p^t = E_p \varepsilon_b \frac{z}{t_b} - E_p \varepsilon_p, \qquad t_b < z < t_b + t_p \tag{4.5}$$

where σ_b and σ_p^t is the stress in the beam and the top actuator, respectively. E is the Young's modulus and t_b is the half-thickness of the beam (figure 4.2). The stress for the bottom actuator can be defined analogously to equation (4.5). Equation (4.5) implies that the resulting stress distribution in the top actuator is due to the superposition of the actuator free strain and the strain in the beam due to mechanical loading.

The moment applied to the beam is calculated by integrating the stress distribution:

$$\int_{-t_b - t_p}^{-t_b} \sigma_p^b(z) z \, dz + \int_{-t_b}^{t_b} \sigma_b(z) z \, dz + \int_{t_b}^{t_b + t_p} \sigma_p^t(z) z \, dz = 0, \tag{4.6}$$

which yields the expression [86]

$$M_x(x,t) = \begin{cases} E_b I\, K\, \varepsilon_p(t) & x_1 < x < x_2 \\ 0 & \text{otherwise} \end{cases}, \tag{4.7}$$

where

$$K = \frac{3E_p\left((t_b + t_p)^2 - t_b^2\right)}{2\left(E_p\left((t_b + t_p)^3 - t_b^3\right) + E_b t_b^3\right)}, \tag{4.8}$$

and I is the moment of inertia about the neutral axis. Equation (4.7) shows that the moment applied by the actuators is distributed between the ends of the actuators, which can be expressed using the Heaviside step function, $H(x - a)$:

$$M_x(x,t) = E_b I\, K\, \varepsilon_p(t)\left[H(x - x_1) - H(x - x_2)\right]. \tag{4.9}$$

Equation (4.9) can be generalised to account for m pairs of actuators, as shown in equation (4.10).

$$M_x(x,t) = \sum_{i=1}^{m} M_{x_i}(x,t) \tag{4.10}$$

Transverse vibrations of a beam are well-approximated by the Euler-Bernoulli beam equation given in equation (4.11) [103]. The beam is assumed to have a uniform cross section and its length much greater than either the width or height. In addition, small transverse deformations are assumed such that the rotational inertia is ignored and the beam cross-section is assumed to remain plane as shear deformation is neglected.

The term on the RHS of equation (4.11) describes the moment applied by pairs of piezoceramic actuators.

$$E_b I \frac{\partial^4 z(x,t)}{\partial^4 x} + \rho A_b \frac{\partial^2 z(x,t)}{\partial^2 t} = \frac{\partial^2 M_x(x,t)}{\partial^2 x}. \tag{4.11}$$

ρ, A_b are the density and cross-sectional area, respectively, of a beam. Equation (4.11) is solved using separation of variables, and for general initial conditions and boundary conditions, is assumed to be of the form [102]:

$$w(x,t) = \sum_{n=1}^{\infty} W_n \phi_n(x) q_n(t). \tag{4.12}$$

$\phi_n(x)$ is the nth normal mode shape of the beam and W_n is a scaling constant to be determined from boundary conditions. $q_n(t)$ is the temporal response of the structure, and is assumed to be of the form $q_n(t) = \hat{q}e^{j\omega t}$ for a sinusoidal excitation. The time derivative is represented as $\ddot{q}_n(t) = \frac{\partial^2 q_n(t)}{\partial^2 t}$.

Equation (4.9) is substituted into equation (4.11) and evaluated using the following property of the Heaviside step function [104]: $\frac{d}{dx}H(x) = \delta(x)$;

$$\frac{\partial^2 M_x(x,t)}{\partial^2 x} = E_b I\, K\, \varepsilon_p(t) \frac{\partial}{\partial x}\left[\delta(x-x_1) - \delta(x-x_2)\right]; \tag{4.13}$$

$$\frac{\partial^2 M_x(x,t)}{\partial^2 x} = E_b I\, K\, \varepsilon_p(t) \left[\delta'(x-x_1) - \delta'(x-x_2)\right]; \tag{4.14}$$

and $\delta(x-a)$ is the Dirac Delta function, to yield

$$E_b I \sum_{n=1}^{\infty} W_n \phi_n''''(x) q_n(t) + \rho A_b \sum_{n=1}^{\infty} W_n \phi_n(x) \ddot{q}_n(t) = E_b I\, K\, \varepsilon_p(t) \left[\delta'(x-x_1) - \delta'(x-x_2)\right] \tag{4.15}$$

The mode shape function of an Euler-Bernoulli beam has the property [103]

$$\phi_n''''(x) = \beta^4 \phi_n(x), \tag{4.16}$$

where $\beta_n^4 = \omega_n^2 \frac{\rho A_b}{E_b I}$, and ω_n is the undamped natural frequency of the nth mode.

The mode shape scaling constant is evaluated using orthogonality properties of the mode shapes;

$$\int_0^L \phi_n(x)\phi_m(x)dx = \delta_{nm}\,, \tag{4.17}$$

where δ_{mn} is the Kronecker delta function. Multiplying equation (4.15) by $\phi_m(x)$ and integrating along the length of the beam uncouples the equation, and further rearranging yields

$$\omega_n^2 q_n(t) + \ddot{q}_n(t) = \frac{E_b I}{\rho A_b} K\,\varepsilon_p(t) \int_{-\infty}^{\infty} \phi_n(x)\left[\delta'(x - x_1) - \delta'(x - x_2)\right]dx\,. \tag{4.18}$$

The RHS of the preceding equation is further evaluated using fundamental properties of the Dirac Delta function [105]:

$$\int f(x)\delta^{(n)}(x)dx = -\int \frac{\partial f}{\partial x}\delta^{(n-1)}(x)dx \tag{4.19}$$

$$\int_{-\infty}^{\infty} f(x)\delta(x-a)dx = f(a) \tag{4.20}$$

such that

$$\omega_n^2 q_n(t) + \ddot{q}_n(t) = \frac{E_b I}{\rho A_b} K\,\varepsilon_p(t)\left[\phi_n'(x_2) - \phi_n'(x_1)\right]. \tag{4.21}$$

The derivation of equation (4.21) has not included any damping term, which is required to model the damping present in real systems. Therefore, an equivalent viscous damping factor, ς_{n}, is added to the LHS of equation (4.21) giving equation (4.22).

$$\ddot{q}_n(t)+2\varsigma_n\,\omega_n\,\dot{q}_n(t)+\omega_n^2\,q_n(t)=\frac{E_bI}{\rho A_b}K\,\varepsilon_p(t)\left[\phi_n'(x_2)-\phi_n'(x_1)\right]. \tag{4.22}$$

Applying the Laplace transform to equation (4.22), assuming zero initial conditions, substituting equation (4.3) and further rearranging yields

$$s^2Q(s)+2\varsigma_n\,\omega_n sQ(s)+\omega_n^2\,Q(s)=\frac{E_bI}{\rho A_b}K\,d_{31}\left[\phi_n'(x_2)-\phi_n'(x_1)\right]\frac{V(s)}{t_p} \tag{4.23}$$

Including the spatial part of the solution, $W_n\,\phi_n(x)$, and summing all modes, a transfer function between applied voltage and displacement response is

$$G_{ij}(x,s)=\frac{Q(s)}{V(s)}=\frac{E_bI}{\rho A_b}K\frac{d_{31}}{t_p}\sum_{n=1}^{\infty}\left[\phi_n'(x_2)-\phi_n'(x_1)\right]\frac{W_n\,\phi_n(x)}{s^2+2\varsigma_n\,\omega_n s+\omega_n^2} \tag{4.24}$$

or

$$G_{ij}(x,s)=\gamma\sum_{n=1}^{\infty}\frac{\chi_n W_n\,\phi_n(x)}{s^2+2\varsigma_n\,\omega_n s+\omega_n^2} \tag{4.25}$$

where

$$\gamma=\frac{E_bI}{\rho A_b}K\frac{d_{31}}{t_p} \tag{4.26}$$

$$\chi_n=\left[\phi_n'(x_2)-\phi_n'(x_1)\right] \tag{4.27}$$

Equations (4.25) - (4.27) show that the transfer function is dependent on the local slope of each mode in the contact area of the actuators. In particular, equation (4.27) describes how well the actuator pair couples to, and therefore excites, each mode. Of interest is when x_1 and x_2 are equidistant from the same node. The slope of the mode shape at x_1 and x_2 will be the same and equation (4.27) shows that coupling between the actuator pair and this mode is impossible. This is analogous to exciting a structure with a point force at a node of a particular mode. It should be noted that equations (4.25) - (4.27) may not be accurate if $x_2 - x_1$ is greater than a quarter wave length of a mode shape. In this case the effects of actuator stiffness will change the local deformation for each mode, which is not predicted by the Euler-Bernoulli beam equation.

Equations (4.25) – (4.27) can be compared to an analogous transfer function derived for the case of point excitation, given in equation (4.28) [103]. The excitation is applied at a distance *a/L* along the beam, where *L* is the length of the beam.

$$H_{ij}(x,s) = \frac{E_b I}{\rho A_b} \sum_{n=1}^{\infty} \frac{W_n \phi_n(x) \phi_n\left(\frac{a}{L}\right)}{s^2 + 2\varsigma_n \omega_n s + \omega_n^2} \tag{4.28}$$

The distributed excitation applied by piezoceramic actuators has implications for properly resolving the modal coefficients. Equation (4.28) can be written in a form typical in discussions on modal analysis of a general structure [31]:

$$H_{ij}(s) = \sum_{n=1}^{\infty} \frac{\phi_n^{(i)} \phi_n^{(j)}}{s^2 + 2\varsigma_n \omega_n s + \omega_n^2} \tag{4.29}$$

Where $\phi_n^{(i)}$ is the modal coefficient at point ***i***, the response measurement point, and $\phi_n^{(j)}$ is the modal coefficient at point ***j***, the excitation point. Extracting the modal coefficients requires taking a point receptance (mobility or inertance) measurement and computing the square root of the estimated modal residue before using this value to normalise estimated residues from transfer receptance measurements. That is,

$$H_{jj}(\omega) \rightarrow \phi_n^{(j)} \phi_n^{(j)} \rightarrow \phi_n^{(j)},$$

$$H_{ij}(\omega) \rightarrow \phi_n^{(i)} \phi_n^{(j)} \rightarrow \frac{\phi_n^{(i)} \phi_n^{(j)}}{\phi_n^{(j)}} \rightarrow \phi_n^{(i)} \tag{4.30}$$

This series of operations cannot be evaluated for distributed excitation. An alternative definition of mode shapes can, however, be used. For example, unscaled mode shapes can be defined as

$$\Phi_n = \begin{bmatrix} 1 & \dfrac{R_{2j}^{(n)}}{R_{1j}^{(n)}} & \cdots & \dfrac{R_{sj}^{(n)}}{R_{1j}^{(n)}} \end{bmatrix}^T \tag{4.31}$$

where Φ_n is the *n*th mode shape and $R_{ij}^{(n)}$ is the residue for the *n*th mode, calculated from the *ij*th element of a transfer function matrix.

4.3 Experimental and Numerical Analysis of Piezoceramic Excitation of an Aluminium Beam

The approximate model of an Euler-Bernoulli beam excited with a pair of piezoceramic actuators was verified using finite element modelling and experimental measurements. The aluminium beam used for experiments discussed in Chapter 2 was used as a representative case and the dimensions are shown in figure 4.3.

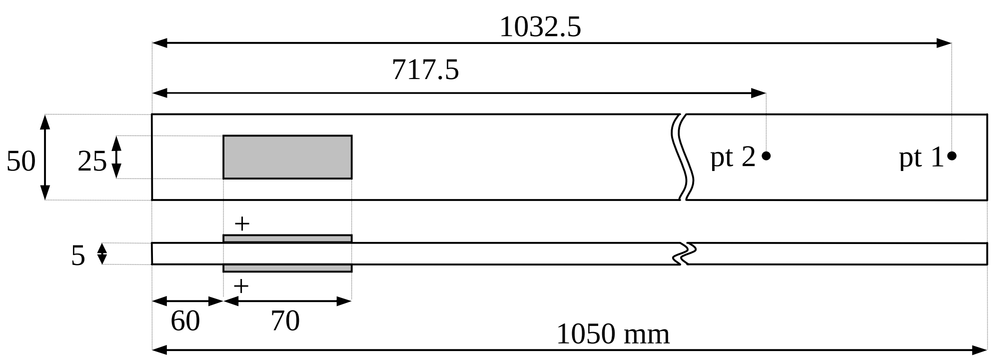

Figure 4.3 Details of free-free aluminium beam with piezoceramic actuators. The actuators are shaded grey and the polarity of the driving voltages resulted in a distributed moment being applied by the actuators. Two measurement points are also indicated.

Equations (4.25) – (4.27) were used to predict the vibration response (due to a sinusoidal excitation) at two points on the beam, which are shown in figure 4.3. The mode shape function $\phi_n(x)$ and scaling constant were evaluated using free-free boundary conditions and the modal orthogonality conditions (equation 4.17). The response for the first twenty modes was initially used in the analysis to minimise the effects of out-of-band modes. It was observed that only the first 11 modes could be calculated for the response estimate for point 1, and 15 modes for point 2. This was due to the numerical properties of the mode shape function, in particular the hyperbolic sine and cosine functions, which increase rapidly. As a consequence, the results for higher frequencies were assumed to be less accurate, and ultimately modal scaling was calculated as zero. Material properties for the aluminium beam and actuators were as follows: E_b = 62 *GPa*; ρ = 2650 kg/m^2; d_{31} = -171×10^{-12} *m/V*. The frequency range considered was 5 – 516.5Hz, with a 0.5Hz resolution. The voltage applied to each of the plates was 11 volts, to correspond with settings in experimental tests. The vibration response spectra are shown in figures 4.4 and 4.5.

4.3.1 Finite Element Model of Piezo-Actuated Beam

The finite element model of the free-free aluminium beam, discussed in Chapter 2, was modified to model the piezoelectric characteristics of the actuators. The piezoelectric actuators were modelled with a volt DOF, which allowed harmonic response due to an applied voltage to be calculated. In addition, the piezoelectric material parameters in equations (4.1) and (4.2) could be explicitly defined in the FEM analysis, and were specified as follows:

$$\mathbf{S}^E = \begin{bmatrix} 16.4 & -5.74 & -7.22 & & & \\ -5.74 & 16.4 & -7.22 & & \mathbf{0} & \\ -7.22 & -7.22 & 18.8 & & & \\ & & & 47.5 & & \\ & \mathbf{0} & & & 47.5 & \\ & & & & & 47.5 \end{bmatrix} \times \left(10^{-12}\right) \quad (m^2/N);$$

$$\mathbf{d} = \begin{bmatrix} & & -171 \\ \mathbf{0} & & -171 \\ & & 374 \\ 0 & 0 & 0 \\ & 584 & \\ 584 & & \mathbf{0} \end{bmatrix} \times \left(10^{-12}\right) \ (m/V); \qquad \xi^{\sigma} = \begin{bmatrix} 1.531 & & \mathbf{0} \\ & 1.531 & \\ \mathbf{0} & & 1.505 \end{bmatrix} \times \left(10^{-8}\right) \ (F/m);$$

$$E_b = 62\ GPa;\ \rho = 2650\ kg/m^2. \tag{4.32}$$

A modal analysis across a frequency range of 0 – 1600Hz, which included 32 modes, was carried out before the harmonic response analysis. The modal superposition solution method was used for the harmonic response with the same frequencies (5 – 516.5Hz) as used in the Euler-Bernoulli analysis. The relatively large frequency range in the modal analysis was employed to minimise the effect of out-of-band modes in the harmonic analysis. Results are plotted in figures 4.4 and 4.5.

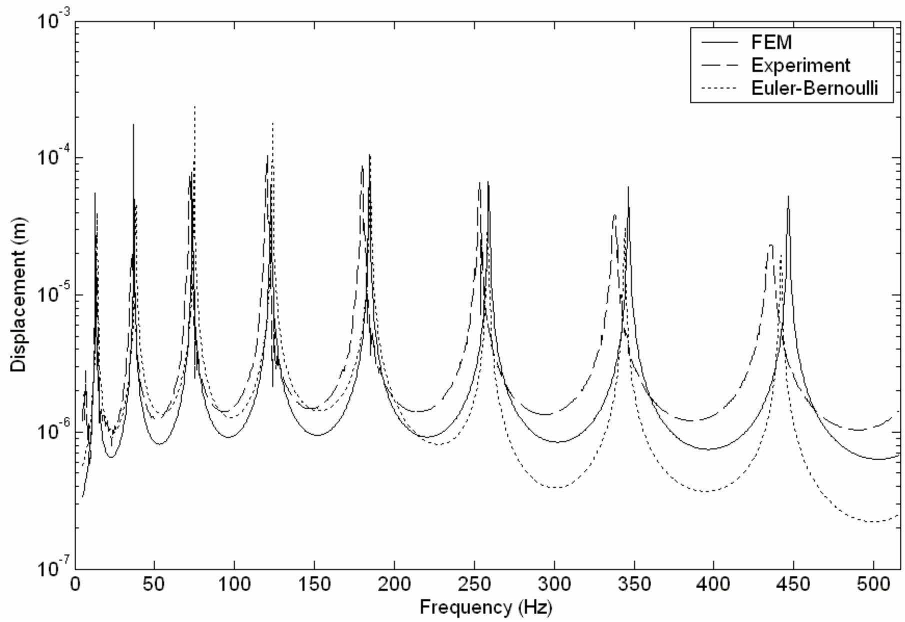

Figure 4.4 Vibration response measured at point 1 (see figure 4.3) due to an 11 volt (peak) swept sine excitation.

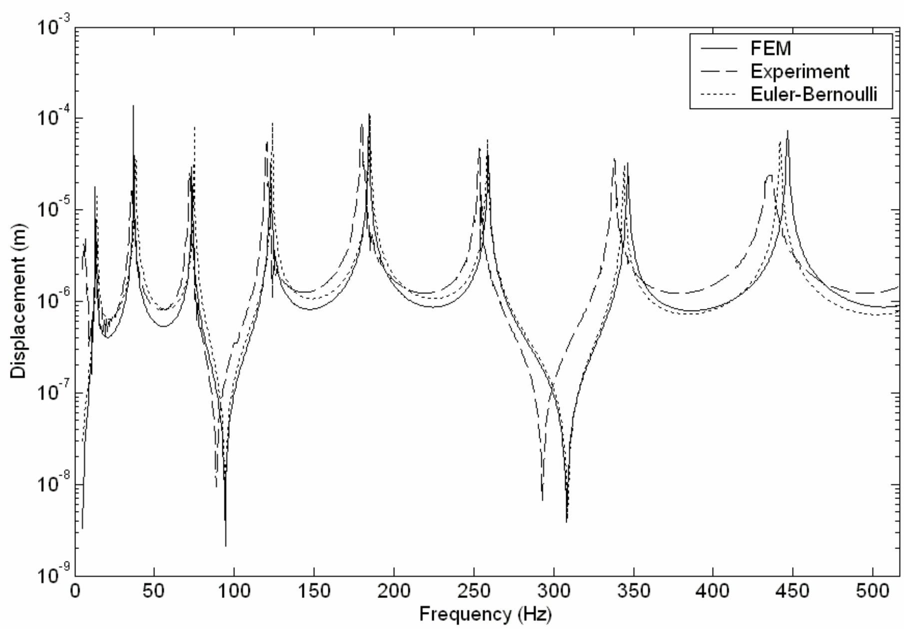

Figure 4.5 Vibration response measured at point 2 (see figure 4.3) due to an 11 volt (peak) swept sine excitation.

4.3.2 Experimental Measurements

Experimental measurements were made on the aluminium beam in a free-free configuration. An 11 volt (peak) swept sine excitation was applied to the beam in 0.5Hz steps, across a frequency range of 5 - 516.5Hz. A constant-gain voltage amplifier, which maintained a constant voltage output, was used to drive the plates. Voltage and electrical impedance measurements across each actuator verified the assumption of constant voltage excitation and only very small deviations from an ideal capacitative load (piezoceramic actuators are assumed to act like a capacitative load away from structural resonances [106]) were observed around structural resonances. Response measurements were made at two points in the transverse direction, as indicated in figure 4.3. B&K 4374 accelerometers and B&K 2635 charge amplifiers were set as for experiments discussed in Chapter 2. An HP 3566A FFT analyser was used for data acquisition and also to generate the excitation signal. The measured results at points 1 and 2 are compared with results from the Euler-Bernoulli and FEM analyses in figures 4.4 and 4.5, respectively.

4.3.3 Discussion of Results

The results from each analysis show reasonable agreement for both measurements. Natural frequencies showed greater deviation for higher frequencies. The greatest deviations, observed for the 8th mode, were under 3%. As a consequence, anti-resonances in figure 4.5 also show some deviation. Amplitudes about the resonant frequencies are affected by finite resolution; however, good correlation between each analysis is observed. Constant modal damping of 0.1% was applied in the Euler-Bernoulli and FEM analyses and results show that this was probably too low, particularly for the higher modes. Large amplitude differences at the local minima are observed in figure 4.4, especially for higher frequencies. It is believed that this is due to the limitations of the mode shape function assumed in the Euler-Bernoulli analysis, as well as the assumptions listed in section 4.2. It is interesting to note that the FEM natural frequencies at higher modes are higher than those predicted by the Euler-Bernoulli analysis. The inclusion of rotational inertia and shear deformation effects typically decreases the estimated natural frequencies [103, 107]. It is conceivable that the additional stiffness imposed by the piezoceramic actuators is increasing the natural frequencies for higher-order modes in the FEM analysis. No clear conclusions have been reached as to why the Euler-Bernoulli analysis does not agree with experimental results at the local minima in the upper-half of the frequency range for measurement point 1. However, considering the good agreement achieved for measurement point 2, the effect is more significant close to the end of the beam and may be due to the assumed mode shape function, which assumes deflection in one direction only; i.e. ignores rotation. Torsional modes (165Hz, 335Hz, and 511Hz in FEM analysis) may also have influenced the experimentally determined results. The Euler-Bernoulli model only considered transverse modes.

Figure 4.6 shows the absolute values of equation (4.27) calculated for the first fifteen modes of the free-free beam. It is clear that low order modes are not excited very effectively, relative to the higher order modes. The local minimum for mode 13 corresponds to the case where the middle of the actuator pair is located close to a node, or more specifically, an inflexion point, of the mode shape. Therefore, the applied moment of the actuators does not couple well to that mode.

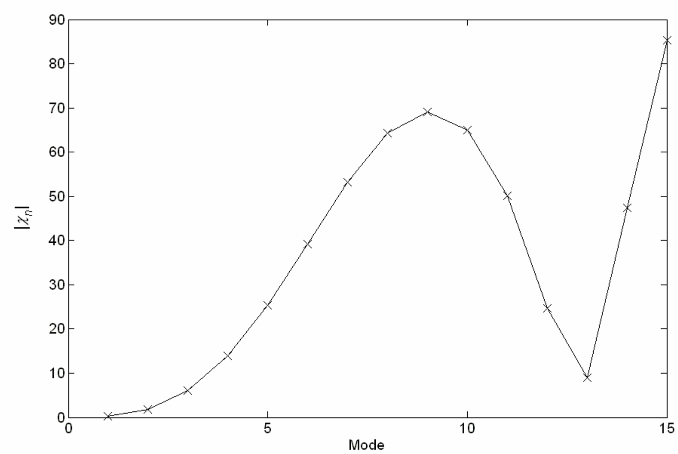

Figure 4.6 Absolute values of equation (4.27) plotted for the first fifteen modes of the free-free aluminium beam.

4.4 Preliminary Investigations of a Cantilever Aluminium Beam

The experiments considered in Chapters 6 and 8 deal with multiple sources of excitation applied to a simple structure. In order to avoid the difficulties associated with coupling multiple shakers to a light structure, piezoceramic actuators were instead chosen for structural excitation. No steps were taken to optimise the placement of the actuator pairs on the cantilever beam as the aim of this brief study was to gain insight into the performance of each actuator in exciting particular transverse modes so that modal analysis results could be better interpreted. A significant amount of literature is devoted to optimal actuator and sensor placement [84, 85, 87, 88, 91-93, 96, 108, 109].

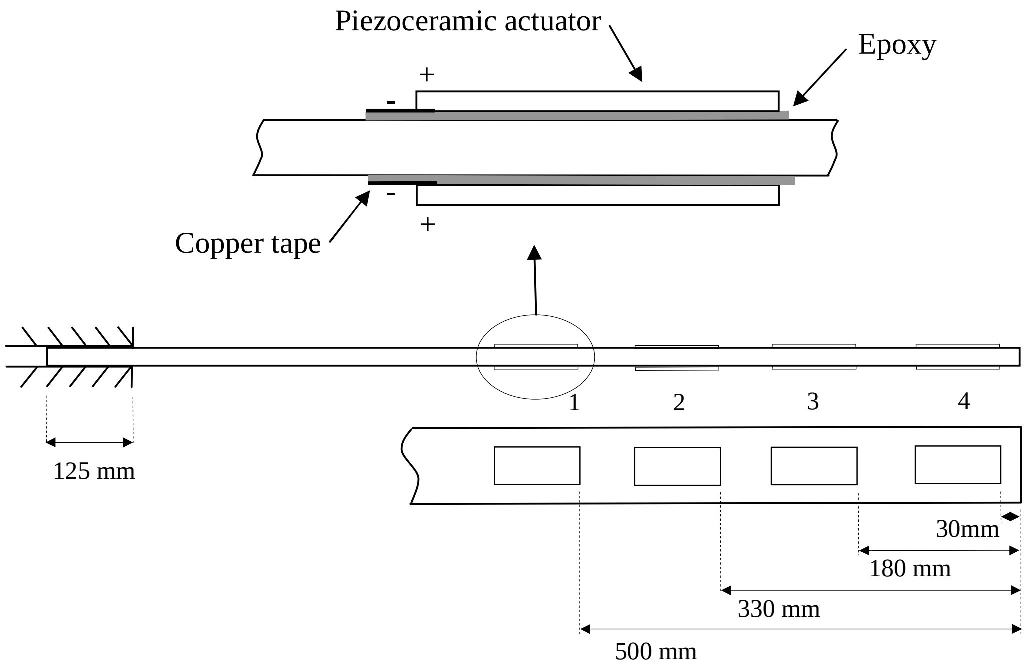

Figure 4.7 Schematic of cantilever aluminium beam showing configuration of piezoceramic actuators pairs. Note the enumeration of the actuator pairs.

Figure 4.7 shows a schematic of the cantilever aluminium beam and the configuration of actuators. The aluminium beam was 1000×50×6 mm, with 125 mm clamped between steel bars. 70×25×1mm PI ceramic PZT (lead zirconate titanate) PIC 151 piezoceramic plates were used as the actuators.

The values of equation (4.27) were calculated for the cantilever aluminium beam and are plotted in figure 4.8. The results indicate the relative effectiveness of each actuator in exciting the first ten modes. As with the free-free beam, the lower order modes are excited relatively poorly. Also of note is that mode six is also excited relatively poorly by actuators 1-3. Similar comments apply to mode 9, actuator pair 2, and mode ten, actuator pair 3. The normalised mode shapes for the cantilever beam are shown in table 4.1. Also shown are the positions of the actuator pairs. Note that for mode 6, actuator pairs 1 - 3 are located about nodes, hence explaining the results shown in figure 4.8. It is expected that identification of poorly excited modes will be a problem, as was shown in the experiments discussed in Chapter 2. Therefore, in the absence of pre-test analysis to best locate actuators, the use of multiple actuators is advantageous.

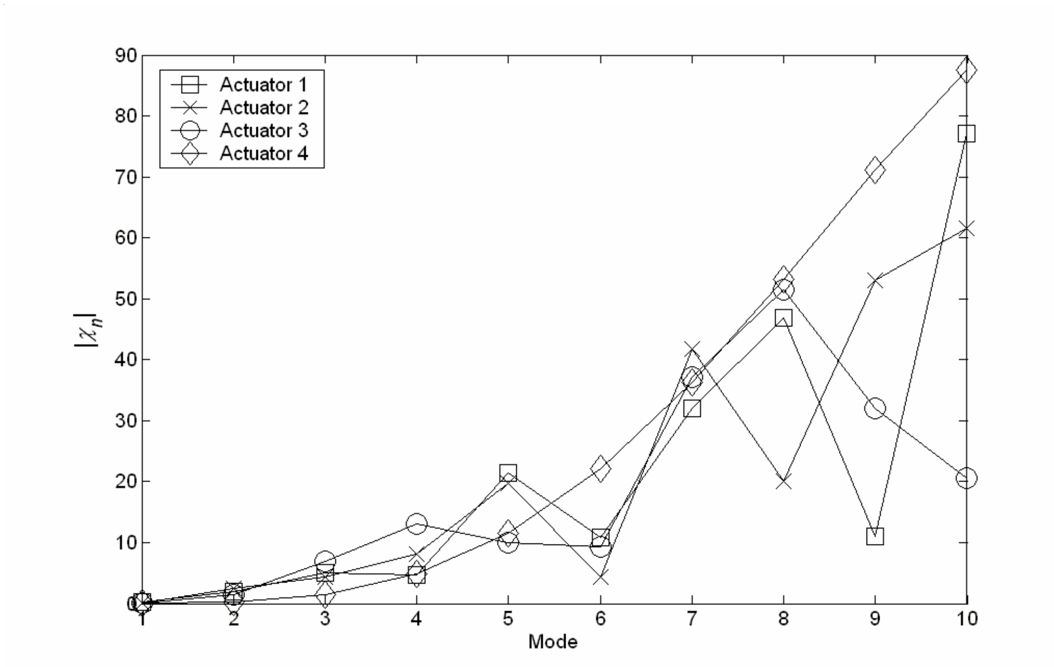

Figure 4.8 Absolute values of equation (4.27) plotted for the first ten modes of the cantilever aluminium beam.

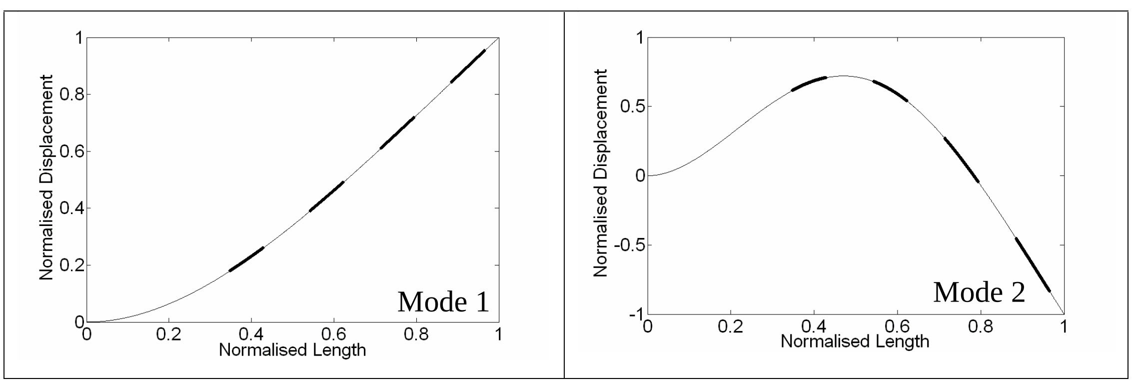

Table 4.1 (Continued over the page) Normalised mode shapes for cantilever aluminium beam. The positions of the four piezoceramic actuator pairs are indicated by the thick line.

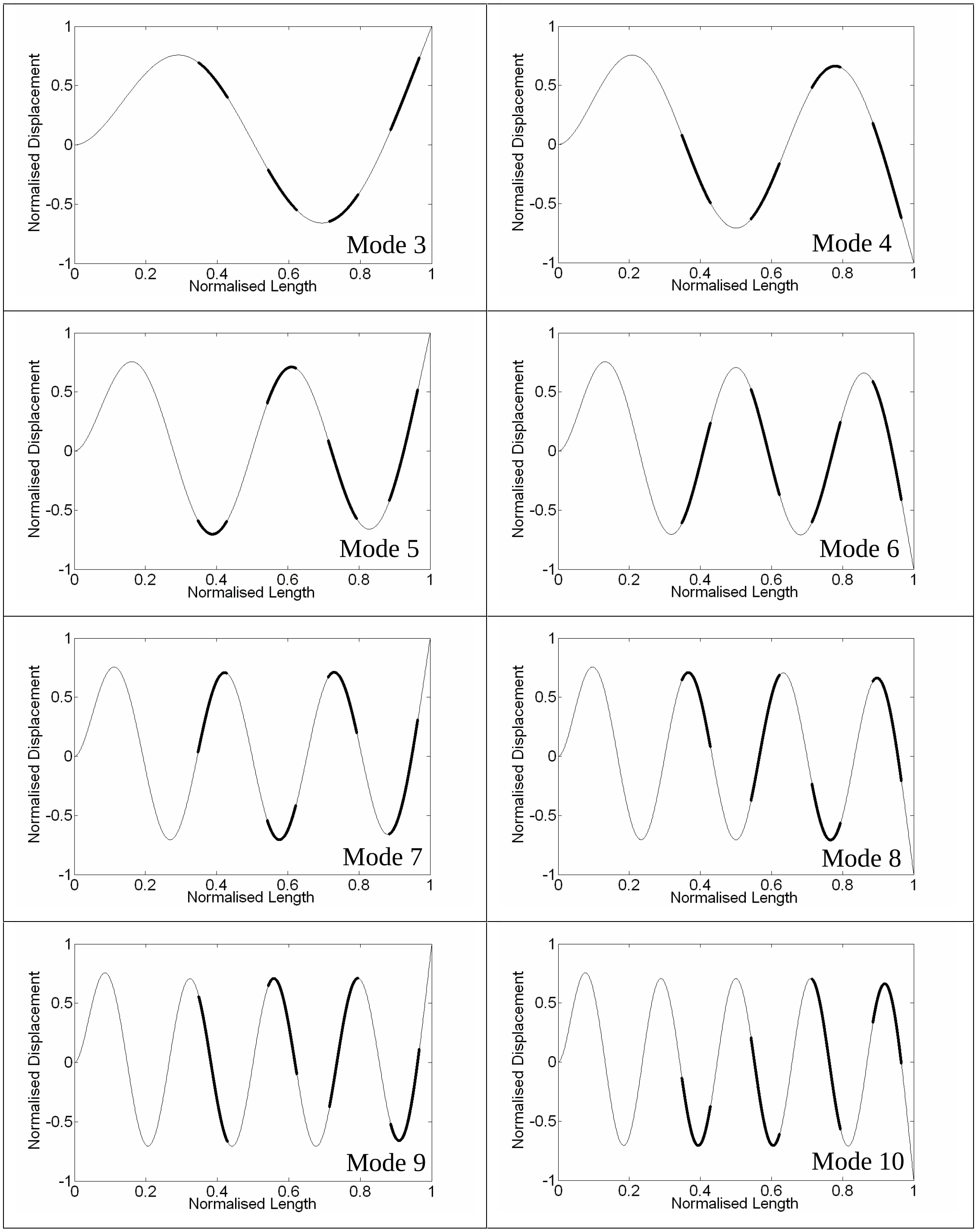

Table 4.1 (cont.) Normalised mode shapes for cantilever aluminium beam. The positions of the four piezoceramic actuator pairs are indicated by the thick line.

4.5 Conclusions

The use of piezoceramic actuators for exciting an aluminium beam has been investigated with an approximate analytical model and finite-element analysis, which are verified by experimental results. The approximate analytical model was based on Euler-Bernoulli beam theory and yielded an expression that described the effectiveness of a pair of actuators in exciting a transverse vibration mode. Reasonable agreement was shown between the analytical model, FEM harmonic analysis results, and experimental measurements on a free-free aluminium beam excited with a single pair of piezoceramic actuators. The analytical model provides a basis for explaining experimental observations discussed in Chapter 2. The distributed excitation applied by the pairs of actuators was shown to prevent scaled modes being estimated as would be possible with point excitation. Relatively scaled mode shapes can be extracted by considering residues obtained from a transfer function relating applied voltage to vibration response.

A preliminary investigation for a cantilever aluminium beam was carried out to determine the relative effectiveness of multiple pairs of actuators in exciting transverse modes. Piezoceramic actuators allow multiple excitation sources to be applied to a small structure with minimal changes to the dynamic properties of the structure. The results suggest that low order modes will be excited relatively poorly and also indicated that particular modes will not be excited well if the centre of the actuator pair is located about a node. The cantilever aluminium beam considered is used for experimental verification of a modal parameter estimation algorithm introduced in Chapter 5 and tested in Chapter 6. The discussion in this chapter allows better interpretation of the results obtained from the proposed modal parameter estimation algorithm.

Chapter 5 ARMAX Modal Parameter Identification in the Presence of Unmeasured Excitation: Theoretical Background

5.1 Introduction

The recent development and improvement of many modal analysis techniques has been aimed at extending their applications to practical situations, for example the testing of machinery and mechanical systems while in operation. In many cases, for example the testing of machines with rotating elements, it is difficult to completely isolate the structure from ambient vibration caused by the operation of the machine. This is also a key problem in the study of helicopter structural dynamics, as noted in Chapter 1. Existing modal parameter estimation techniques do not account for unmeasured sources of excitation, as discussed in Chapter 2, although pre-processing of measured data, for example using synchronous averaging can reduce the effects of unmeasured excitations.

Alternatives to input/output modal analysis include determining operational deflection shapes (ODS) [20], or the application of one of many operational (response-only) modal analysis techniques (see Brincker [65] for recent developments in theory and applications), which only require vibration response measurements. Operational modal analysis techniques generally assume that the unmeasured excitation force to be close to white noise [20, 38]; however, cases where periodic excitations of a known frequency are present in addition to broadband excitation have been investigated [110-113]. In contrast to input-output modal analysis, operational modal analysis techniques do not directly yield scaled mode shapes because the excitation force is not measured, but additional strategies, which involve the structural modification using a known mass, have recently been investigated to overcome this problem [27, 114, 115]. Operational modal analysis methods will be discussed in more detail in Chapter 8.

In this chapter, a new approach is presented to estimate modal parameters from excitation and response data obtained in the presence of significant unmeasured periodic and random excitations and also random measurement noise. This method yields scaled mode shapes and can be used with a variety of excitation signals, including periodic signals, which can be combined with synchronous (time-domain) averaging to attenuate unmeasured excitations. An autoregressive moving average with exogenous excitation (ARMAX) model is used to describe the dynamics of a structure and to take into account measurement noise and unmeasured excitation. A multistage estimation algorithm is devised to estimate the parameters of the ARMAX model, from which the modal parameters of a structure can be calculated. The ARMAX estimation algorithm includes a simple method based on the position of estimated poles on the *z*-plane to select the best model from a set of estimated models and also to distinguish between structural modes and spurious numerical poles. For moderate levels of measurement noise, modes estimated with positive damping are vibrational modes and spurious numerical modes are estimated with negative damping. The model selection criterion selects the model with the highest number of positively damped modes from a set of models of different order. A diagonal parameterisation of the autoregressive (AR) matrix, and consequently the moving average (MA) matrix, allows the MIMO ARMAX model to be estimated as a series of MISO models. In addition, the diagonal structure allows simple manipulation of the AR and MA matrices, including stabilisation, which can be achieved by reflecting unstable zeros about the unit circle. The performance of the ARMAX estimation algorithm is assessed using numerical and experimental data in Chapter 6 and further testing using a helicopter-like structure is discussed in Chapter 7.

The following section introduces the discrete-time model and the estimation algorithm is presented in section 5.3. Notes on the implementation of the algorithm are included in section 5.4 and concluding remarks are made in section 5.5.

5.2 ARMAX Model Structure

The vibration of a general continuous structure can be described by an *n* degree-of-freedom (DOF) linear differential equation [30]:

$$\mathbf{M} \cdot \ddot{\mathbf{x}}(t) + \mathbf{D} \cdot \dot{\mathbf{x}}(t) + \mathbf{K} \cdot \mathbf{x}(t) = \mathbf{f}(t) \tag{5.1}$$

$\mathbf{f}(t)$ is a vector of forces acting at each DOF and $\mathbf{x}(t)$ and its time derivatives correspond to the displacement, velocity, and acceleration at each degree DOF. **M** and **K** are the real, symmetric mass and stiffness matrices and **D** is the real, symmetric damping matrix that describes the equivalent viscous damping of the system. An alternative general representation of a linear dynamic system is an autoregressive moving average with exogenous (ARMAX) excitation model, which is described by equations (5.2) – (5.5) and shown in figure 5.1 [116].

$$\mathbf{A}(q)\cdot\mathbf{y}[t]=\mathbf{B}(q)\cdot\mathbf{f}[t]+\mathbf{C}(q)\cdot\mathbf{w}[t], \qquad (5.2)$$

where

$$\mathbf{A}(q) \equiv \mathbf{I}_s + \mathbf{A}_1 \cdot q + \cdots + \mathbf{A}_{na} \cdot q^{na}, \qquad [s \times s] \qquad (5.3)$$

$$\mathbf{B}(q) \equiv \mathbf{B}_0 + \mathbf{B}_1 \cdot q + \cdots + \mathbf{B}_{nb} \cdot q^{nb}, \qquad [s \times m] \qquad (5.4)$$

$$\mathbf{C}(q) \equiv \mathbf{I}_s + \mathbf{C}_1 \cdot q + \cdots + \mathbf{C}_{nc} \cdot q^{nc}. \qquad [s \times s] \qquad (5.5)$$

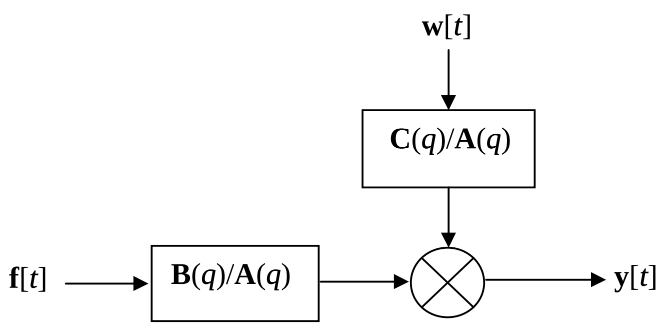

Figure 5.1 Block diagram of ARMAX model.

The ARMAX model uses rational functions to relate an *m* dimensional force vector **f**[*t*] to an *s* dimensional response vector **y**[*t*], which are both sampled at discrete times $t = k{\cdot}T_s$, $k = 0, \ldots, N-1$, and T_s is the sampling period. The response vector **y**[*t*] is assumed to be corrupted with zero-mean random measurement noise and the ARMAX model also includes an *s*-dimensional unmeasured disturbance **w**[*t*], which is assumed to be a zero-mean independent random variable (i.e. $\{\mathbf{w}[t]\}$ is white noise). **w**[*t*] is independent of **f**[*t*] but can have correlated components, i.e. a non-diagonal covariance matrix. **A**(*q*), **B**(*q*), and **C**(*q*) are the autoregressive (AR), exogenous (X) and moving average (MA) matrices respectively. The elements of these matrices are scalar polynomials in terms of *q*, the backshift operator: $\mathbf{x}[t]\cdot q^{j} = \mathbf{x}[t\text{-}j]$. The orders of the polynomial elements of the AR, X, and MA matrices are *na*, *nb*, and *nc*, respectively (equations (5.3) – (5.5)). $\mathbf{I}_s$ is the $s \times s$ identity matrix. For the single-input single-output (SISO) case, the AR, X, and MA matrices reduce to scalar polynomials. The AR matrix represents the global properties of the structure, namely, the natural frequency and damping for each mode. The X matrix is dependent on the signal type used for structural excitation [61] and also the positions of the m excitations.

The ARMAX model is adopted because it includes the stochastic component $\mathbf{w}[t]$, which accounts for noise present in the excitation and response measurements. The block diagram shown in figure 5.1 illustrates that the unmeasured disturbance is filtered by the rational function $\mathbf{C}(q)/\mathbf{A}(q)$. The significance of this is that the unmeasured disturbance is filtered not only by the MA matrix, but also by the AR matrix, which describes the global properties of the system. Therefore, the filtered unmeasured disturbance can represent the effect of unmeasured excitations.

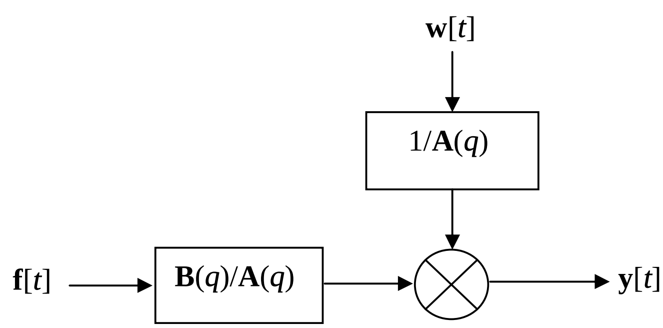

Figure 5.2 Block diagram of ARX model.

The ARMAX model is also capable of estimating modal parameters from multiple-input multiple-output (MIMO) measurements, which, compared to SISO testing, is useful for reducing measurement time, ensuring adequate excitation to all parts of large structures, and improving consistency in data sets. The autoregressive with exogenous excitation (ARX) model, which is shown in figure 5.2, can be derived from the ARMAX model by setting $nc = 0$ and the unmeasured disturbance $\mathbf{w}[t]$ corresponds to the error in a linear difference equation relating the input and output data:

$$\mathbf{y}[t] + \mathbf{A}_1 \cdot \mathbf{y}[t-1] + \cdots + \mathbf{A}_{na} \cdot \mathbf{y}[t-na] = \mathbf{B}_0 \cdot \mathbf{f}[t] + \mathbf{B}_1 \cdot \mathbf{f}[t-1] + \cdots + \mathbf{B}_{nb} \cdot \mathbf{f}[t-nb] + \mathbf{w}[t]. \tag{5.6}$$

The predictor for the ARX model corresponds to a linear regression problem, which can be efficiently solved using the least-squares criterion [116]. This will be discussed further in the next section. The deterministic case where $\mathbf{w}[t]$ is insignificant is equivalent to a discrete-time rational polynomial representation of the transfer function.

The assumptions made about the physical structure, excitation, and vibration response are as follows.

- The structure exhibits a linear, time-invariant, and causal response to an arbitrary excitation.
- The vibration response is stable; i.e. positively damped. Therefore all vibrational modes are represented by zeros of the function in equation (5.7) that fall inside the unit circle on the *z*-plane [116].

$$\mathbf{A}^*(z) = z^{na} \cdot \mathbf{A}(z^{-1}) = z^{na} + \mathbf{A}_1 \cdot z^{na-1} + \cdots + \mathbf{A}_{na} \qquad [s \times s] \tag{5.7}$$

- The MA matrix is assumed to be stable with all zeros of the function in equation (5.8) located inside the unit circle.

$$\mathbf{C}^*(z) = z^{nc} \cdot \mathbf{C}(z^{-1}) = z^{nc} + \mathbf{C}_1 \cdot z^{nc-1} + \cdots + \mathbf{C}_{nc}\,. \qquad [s \times s] \tag{5.8}$$

- The excitation is persistently exciting of order $na + nb + 1$. This implies that the spectrum of the excitation signal is non-zero for at least $na + nb + 1$ frequencies in the interval $-\pi < \omega \leq \pi$ [116]. In practice, the excitation is usually a broad-band signal, for example white noise, which satisfies the requirement for persistent excitation. It should be noted that $na \geq nb$ and specific excitation signals can be created by the superposition of a minimum of $na + 1$ summed sinusoids, which will lead to a persistently exciting signal appropriate for the estimation of an ARMAX model of order *na*. A more detailed discussion of persistent excitation can be found in [44, 116].

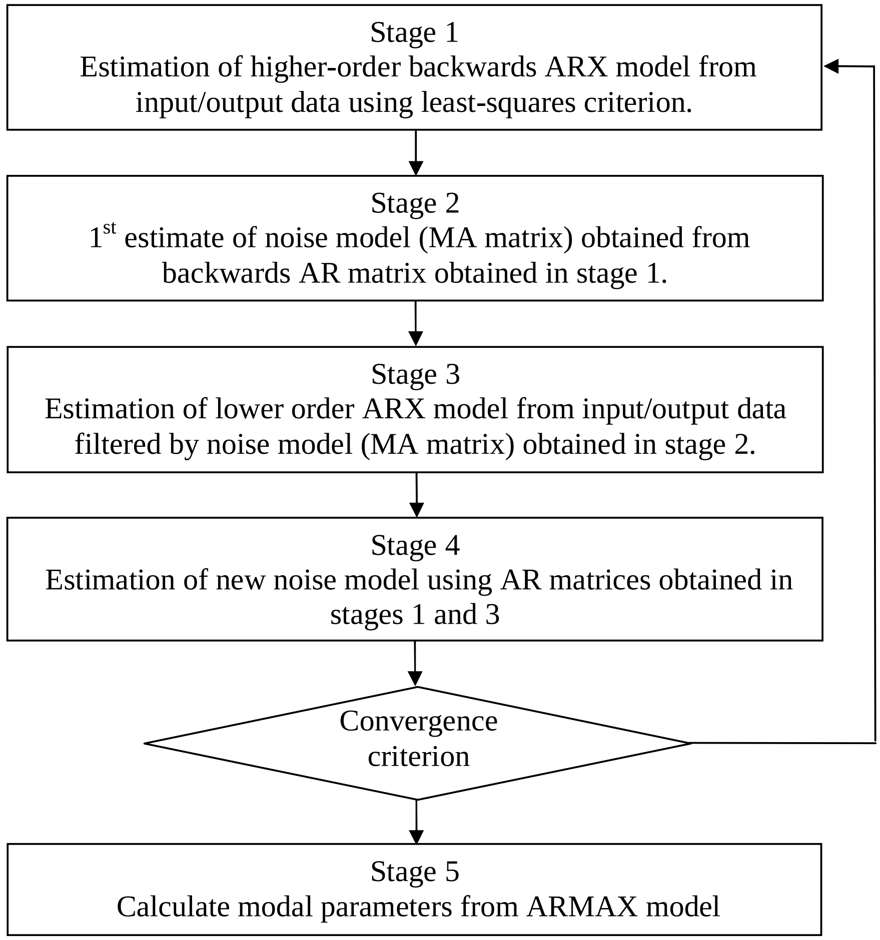

Figure 5.3 Block diagram of ARMAX estimation algorithm.

5.3 ARMAX Parameter Estimation Algorithm

As shown in Figure 5.3, the modal parameters are calculated from an ARMAX model, which is estimated by a multistage algorithm [43], implemented in an iterative loop. The first four stages are based on the work of Fassois *et al* [55, 117], with modifications to include the use of backwards ARX models, which allows spurious numerical modes and vibrational modes to be distinguished according to the position of the poles of the backwards ARX model in the *z*-plane. This is also the basis of a simple model selection criterion. A further modification is the use of a diagonal parameterisation for the AR, and consequently MA, matrices, which allows these matrices to be decomposed into scalar polynomials. The scalar polynomials can be stabilised easily by reflecting unstable zeros about the unit circle in the *z*-plane and the diagonal structure is desirable for numerical operations, such as taking the inverse.

5.3.1 Stage 1: Estimation of Higher Order ARX Model

The first stage involves estimating a higher order ARX model from the input and output data. Ljung [116] pointed out that an ARX model of order p estimated using N data points will converge to represent the true system as $N, p \rightarrow \infty$, and $N > p$. Hence, an ARX model with finite N and p will approximate a linear system relating the excitation data $\mathbf{f}[t]$ and response data $\mathbf{y}[t]$, which are corrupted with noise. Equations (5.9) – (5.11) describe an ARX model of infinite order, which can be related to the ARMAX model in equation (5.2) by pre-multiplying by the inverse of the MA matrix [55].

$$\mathbf{H}_y(q) \cdot \mathbf{y}[t] = \mathbf{H}_f(q) \cdot \mathbf{f}[t] + \mathbf{w}[t], \tag{5.9}$$

with

$$\mathbf{H}_y(q) \equiv \mathbf{I}_s + \sum_{j=1}^{\infty} \mathbf{H}_y(j) \cdot q^j = \mathbf{C}^{-1}(q) \cdot \mathbf{A}(q), \ [s \times s] \tag{5.10}$$

$$\mathbf{H}_f(q) \equiv \sum_{j=1}^{\infty} \mathbf{H}_f(j) \cdot q^j = \mathbf{C}^{-1}(q) \cdot \mathbf{B}(q). \qquad [s \times s] \tag{5.11}$$

In practice, the ARX model is limited to a finite order p, where $p > na$, and the choice of $p, na, nb,$ and nc, which is dependent on model parameterisation [44, 116], is critical to the accuracy of the estimated ARX and ARMAX models. A brief description of model parameterisation, which is concerned with the structure of the AR, MA, and X matrices, is given below.

Consider the SISO ARX model in equation (5.12).

$$y[t] + a_1 \cdot y[t-1] + \cdots + a_{na} \cdot y[t-na] = b_0 \cdot f[t] + b_1 \cdot f[t-1] + \cdots + b_{nb} \cdot f[t-nb] + e[t] \tag{5.12}$$

A set of possible models with a particular structure can be obtained by varying the values of na and nb. The parameters to be identified in each model are the coefficients a_i, $i = 1, \ldots, na$, and b_j, $j = 0, \ldots, nb$. If $f[t]$ and $y[t]$ are ideal noise-free data then an appropriate choice for na is $na = 2n$, where n is the number of modes in the frequency band $0 – 1/(2T_s)$ Hz. This is due to the $2n$ complex conjugate poles of the AR polynomial, which describe the global properties of the structure; i.e. natural frequencies and damping. The choice of nb is dependent on the type of response data used and the inter-sample behaviour of the data: for displacement response measurements, where data are assumed to be a train of impulses at the sampling instants, $nb = na - 1$ [61]. Real data typically includes components other than those caused by the structural dynamics and a higher order AR polynomial is necessary. An appropriate parameterisation of a set of SISO ARX models is therefore to set $na = (2 \times n) + k$, where $k = 2, 4, 6, \ldots, r$, and r is determined by a convergence criterion and limited by the number of samples in the input and output data records. The parameterisation of MIMO models is considerably more complex because the order of each element of the AR, MA, and X matrices has to be set. That is, for

$$\mathbf{A}(q) = \begin{bmatrix} a_{11}(q) & \cdots & a_{1s}(q) \\ \vdots & a_{ij}(q) & \vdots \\ a_{s1}(q) & \cdots & a_{ss}(q) \end{bmatrix}, \qquad a_{ij}(q) = 1 + a_{ij}^{(1)} \cdot q + \ldots + a_{ij}^{(na_{ij})} \cdot q^{na_{ij}}, \tag{5.13}$$

na_{ij} and similarly nb_{ij} have to be chosen. Setting $na_{ij} = na$, $nb_{ij} = nb$, for all i, j results in full polynomial form [44, 116] and the theoretically required order of the AR matrix is $na = 2n/s$; n is the number of modes in the frequency range of interest, s the number of response measurements, and a set of candidate models is $na = 2n/s + k$, where $k = 1, 2, \ldots, r$.

The assumption of positively damped vibrations does not always hold for noisy data. Very lightly damped structures and noisy data may lead to the estimation of negatively damped modes. In addition, very noisy data and numerical operations in subsequent stages may lead to ill-conditioning of the regression matrix used to estimate ARX-model parameters. For these reasons a diagonal structure is imposed on the AR matrix in the ARX and ARMAX models. A similar structure is also studied by Park and Kim [51]. From equation (5.13), this can be expressed as $na_{ii} = na$, $na_{ij} = 0$, $i \neq j$:

$$\mathbf{A}(q) = diag\big(a_{11}(q) \quad \cdots \quad a_{ii}(q) \quad \cdots \quad a_{ss}(q)\big). \tag{5.14}$$

This structure is a reasonable assumption for structural dynamics problems because the global properties of the structure can be modelled by the scalar polynomials that appear in the diagonal elements of the AR matrix: the AR matrix for a single-output case (SISO or MISO) is a scalar polynomial and the superposition of multiple single-output models results in a diagonal AR matrix. The diagonal structure is less sensitive to numerical operations, such as taking the inverse of the AR matrix, and a simple procedure to stabilise the AR matrix involves reflecting the poles of each scalar polynomial about the unit circle. This stabilisation procedure can also be applied to the MA matrix, which inherits a diagonal structure from the AR matrix. As the MA matrix is used in filtering operations, reflecting unstable poles about the unit circle preserves the frequency-domain properties of the filter. Alternative stabilisation strategies for matrix polynomials, see for example [55], involve more complex numerical operations such as solving systems of equations that include the correlation functions of polynomial coefficients. It has been suggested that this adversely affects the characteristics of the matrix polynomials and therefore the accuracy of parameter estimates [118]. The diagonal structure adopted in the present work also allows the MIMO ARX model to be decomposed into *s* MISO models, each with a scalar AR polynomial. The *s* estimates of the global properties can be reduced to a single estimate using weighted averaging or any other selection criterion. The order of the diagonal AR matrix is the same as for the single-output case; i.e. $na = (2n) + k$, where $k = 2, 4, 6, \ldots, r$.

The MIMO ARX model of order *p* with a diagonal AR matrix is estimated as *s* MISO ARX models using the least squares criterion. Equation (5.9) can be rewritten as

$$\mathbf{y}[t] + \sum_{j=1}^{p} \mathbf{H}_y(j) \cdot \mathbf{y}[t-j] = \sum_{j=0}^{p} \mathbf{H}_f(j) \cdot \mathbf{f}[t-j] + \boldsymbol{\varepsilon}_1[t], \tag{5.15}$$

and subsequently separated into k, $k = 1, \ldots, s$, MISO models:

$$\mathbf{y}^{(k)}[t] + \sum_{j=1}^{p} h_y^{(k)}(j) \cdot \mathbf{y}^{(k)}[t-j] = \sum_{j=0}^{p} \mathbf{H}_f^{(k)}(j) \cdot \mathbf{f}[t-j] + \boldsymbol{\varepsilon}_1^{(k)}[t], \tag{5.16}$$

where $\boldsymbol{\varepsilon}_1[t]$ is the prediction error, $\mathbf{y}^{(k)}[t]$, $\mathbf{H}_f^{(k)}(q)$ and $\boldsymbol{\varepsilon}_1^{(k)}[t]$ are the *k*th rows of $\mathbf{y}[t]$, $\mathbf{H}_f(q)$ and $\boldsymbol{\varepsilon}_1[t]$, respectively, and $h_y^{(k)}(q)$ is the *k*th diagonal element of $\mathbf{H}_y(q)$. The notation $\mathbf{H}_y(j)$, $\mathbf{H}_f(j)$, $h_y^{(k)}(j)$, etc. is used to indicate the *j*th coefficient of each (matrix) polynomial for terms that include other subscripts, as opposed to the notation

$\mathbf{A}_i$ that was used above, for example, in equations (5.3) – (5.6). The MISO ARX model can be rewritten as a linear regression problem

$$\mathbf{y}^{(k)}[t] = \mathbf{u}_k^T[t] \cdot \mathbf{h}_k + \boldsymbol{\varepsilon}_1^{(k)}[t] \tag{5.17}$$

in terms of the regression vector $\mathbf{u}_k[t]$ and parameter vector $\mathbf{h}_k$:

$$\mathbf{u}_k[t] \equiv [\,-\mathbf{y}^{(k)}[t-1] \quad -\mathbf{y}^{(k)}[t-2] \quad \cdots \quad -\mathbf{y}^{(k)}[t-p] \,\vdots\, \mathbf{f}^T[t] \quad \cdots \quad \mathbf{f}^T[t-p]\,]^T, \qquad [(p + p.m + m) \times 1] \tag{5.18}$$

$$\mathbf{h}_k \equiv \left[h_y^{(k)}(1) \quad h_y^{(k)}(2) \quad \cdots \quad h_y^{(k)}(p) \;\vdots\; \mathbf{H}_f^{(k)}(0) \quad \cdots \quad \mathbf{H}_f^{(k)}(p)\right]^T. \qquad [(p + p.m + m) \times 1] \tag{5.19}$$

The s MISO linear regression problems are solved individually using a least-squares (LS) algorithm based on QR decomposition described by Ljung [116] and outlined below.

Define

$$\mathbf{\Theta}_k = \left[\mathbf{u}_k[1] \quad \cdots \quad \mathbf{u}_k[N_1]\right]^T, \qquad [N_1 \times (p + p.m + m)] \tag{5.20}$$

$$\mathbf{Y}_k = \left[\mathbf{y}^{(k)}[1] \quad \cdots \quad \mathbf{y}^{(k)}[N_1]\right]^T, \qquad [N_1 \times 1] \tag{5.21}$$

where $N_1 = N - p - 1$ and N is the number of samples in the input and output vectors. The ARX model is then rewritten in terms of $\mathbf{Y}_k$ and $\mathbf{\Theta}_k$:

$$\mathbf{Y}_k = \mathbf{\Theta}_k \cdot \mathbf{h}_k + \mathbf{E}_{1k}, \tag{5.22}$$

and the LS criterion, which minimises the quadratic norm of the prediction error $\mathbf{E}_{1k}$, can be expressed as

$$J_{LS}^{(k)}(\mathbf{h}_k, \mathbf{y}^{(k)}, \mathbf{f}) = \left|\mathbf{Y}_k - \mathbf{\Theta}_k \cdot \mathbf{h}_k\right|^2 = \sum_{t=1}^{N_1} \left|\mathbf{y}_k[t] - \mathbf{u}_k^T[t] \cdot \mathbf{h}_k\right|^2 . \tag{5.23}$$

An orthonormal transformation preserves the length of a set of vectors and the angle between them [119] and therefore the norm in equation (5.23) is not affected by applying an orthonormal transformation $\mathbf{Q}_k\,[N_1 \times N_1]$:

$$J_{LS}^{(k)}(\mathbf{h}_k, \mathbf{y}^{(k)}, \mathbf{f}) = \left|\mathbf{Q}_k \left(\mathbf{Y}_k - \mathbf{\Theta}_k \cdot \mathbf{h}_k\right)\right|^2 , \tag{5.24}$$

where $\mathbf{Q}_k$ is chosen such that

$$\begin{bmatrix}\mathbf{\Theta}_k & \mathbf{Y}_k\end{bmatrix} = \mathbf{Q}_k \cdot \mathbf{R}_k , \qquad [N_1 \times (p + p.m + m + 1)] \tag{5.25}$$

which is a QR factorisation of $\begin{bmatrix}\mathbf{\Theta}_k & \mathbf{Y}_k\end{bmatrix}$ and

$$\mathbf{R}_k = \begin{bmatrix}\mathbf{R}_{0k} \\ \cdots \\ 0\end{bmatrix}, \qquad [N_1 \times (p + p.m + m + 1)] \tag{5.26}$$

$$\mathbf{R}_{0k} = \begin{bmatrix}\mathbf{R}_{1k} & \mathbf{R}_{2k} \\ 0 & \mathbf{R}_{3k}\end{bmatrix}. \tag{5.27}$$

($\mathbf{R}_{0k}$ $[(p + p.m + m + 1) \times (p + p.m + m + 1)]$ is upper triangular; $\mathbf{R}_{1k}$ is $[(p + p.m + m) \times (p + p.m + m)]$; $\mathbf{R}_{2k}$ is $[(p + p.m + m + 1) \times 1)]$; $\mathbf{R}_{3k}$ is scalar). The definition of an orthonormal matrix: $\mathbf{Q}_k \cdot \mathbf{Q}_k^T = \mathbf{I}$, hence $\mathbf{Q}_k^T = \mathbf{Q}_k^{-1}$ is used to rewrite equation (5.24):

$$J_{LS}^{(k)}(\mathbf{h}_k, \mathbf{y}^{(k)}, \mathbf{f}) = \left\|\begin{bmatrix}\mathbf{R}_{2k} \\ \mathbf{R}_{3k}\end{bmatrix} - \begin{bmatrix}\mathbf{R}_{1k} \cdot \mathbf{h}_k \\ 0\end{bmatrix}\right\|^2 = \left|\mathbf{R}_{2k} - \mathbf{R}_{1k} \cdot \mathbf{h}_k\right|^2 + \left|\mathbf{R}_{3k}\right| . \tag{5.28}$$

Equation (5.28) is minimised when $\mathbf{R}_{1k} \cdot \hat{\mathbf{h}}_k = \mathbf{R}_{2k}$.

The LS estimate using QR factorisation has a number of useful properties as outlined by Ljung [116]. The algorithm is appropriate for problems with a high dimension and is numerically well-conditioned when compared with techniques based on solving the normal equations, which involve computing $\mathbf{\Theta}_k^T \cdot \mathbf{\Theta}_k$. LS estimates can be obtained for models with an order smaller than that used in the initial definition of the problem by setting the appropriate elements in the parameter vector $\mathbf{h}_k$ to zero.

The model order *na* of the ARMAX model is related to the number of structural modes in a given frequency range. The order *p* of the ARX model is chosen to be greater than *na* to account for noise present in the measurements and follows from the definition of $\mathbf{H}_y(q)$ in equation (5.8). In practice the number of structural modes in a given frequency range is not known *a priori* and it is well known that over-specifying the model order reduces the bias of estimates in the presence of noise [44, 116]. Therefore, a higher-order model is desirable. Two disadvantages associated with higher order models are the increase in computation time and memory requirements, and the introduction of spurious poles that do not correspond to structural modes. The computational complexity can be justified on the basis of improved accuracy, however, distinguishing between the poles that correspond to structural modes and spurious numerical poles can be a significant problem.

A number of techniques has been developed to address this problem, for example, the use of stabilisation diagrams and dispersion analysis [57]. Stabilisation diagrams can be difficult to interpret for high order models as spurious numerical poles can exhibit only small amounts of scatter, particularly for LS estimates using singular value decomposition [47]. Dispersion analysis has been shown to be effective, but can only be calculated once the estimated ARX or ARMAX model has been estimated and factorised into pole-residue form. This can increase the computation time significantly if estimating a large number of high order models. Dispersion analysis also requires a threshold value to be defined that separates spurious numerical modes from vibration modes. An alternative method is the use of backwards ARX models, which distinguish between spurious numerical poles and vibration poles on the basis of their position on the complex *z*-plane.

Kumerasan ***et al.*** [120, 121] showed that the frequency and damping of sinusoids could be identified from the signal zeros of a linear prediction filter polynomial. If the order of the prediction filter was over-specified, the spurious numerical zeros of the linear prediction filter were shown to lie inside the unit circle if the prediction filter was a monic polynomial with coefficients chosen to have minimum Euclidean length. The result held for exponentially damped sinusoids with positive and negative damping and also for undamped sinusoids. A consequence of this result is that the frequency and damping of signals consisting of exponentially damped sinusoids could be estimated using a higher-order prediction error filter and distinguished from spurious numerical poles by first reversing the order of the signal samples. The reversal of the signal would transform the positively damped sinusoids to negatively damped sinusoids with poles that would lie outside the unit circle.

A number of studies has applied this technique to estimating modal frequencies and damping [45-47, 120-122], however, it should be noted that the prediction error approach utilises the response data only. The prediction error technique was used as the first stage of a two stage method to predict ARX models (referred to as ARMA models in the original study) by Batill & Hollkamp [45]. In a subsequent paper [46] Hollkamp & Batill proved that the minimum norm solution for backwards ARX models (again, referred to as ARMA models in the original study) resulted in the spurious numerical poles being located inside the unit circle on the complex $\boldsymbol{z}$-plane and the system poles being located outside the unit circle.

The use of backwards ARX models was adopted for the first and third stages of the ARMAX estimation algorithm. This was achieved by using forward time steps instead of backward time steps when defining the ARX model in equation (5.15) and subsequent LS estimation. An alternative approach is to simply reverse the order of the input and output data vectors. The resulting backwards AR and X matrices that are estimated are denoted $\mathbf{H}_{By}(q)$ and $\mathbf{H}_{Bf}(q)$, respectively.

5.3.2 Stage 2: 1st Estimate of Noise Model (MA matrix)

The backwards AR matrix $\mathbf{H}_{By}(q)$ estimated in the first stage contains information describing the system dynamics and the noise dynamics, as shown by equation (5.10). The second stage estimates the noise model by separating the system dynamics from noise dynamics. One approach is to simply factorise $\mathbf{H}_{By}(q)$ into two matrix polynomials; one with poles outside the unit circle and the second with poles inside the unit circle:

$$\mathbf{H}_{By}^{*}(z) = z^{p} \cdot \mathbf{H}_{By}(z^{-1}) = \mathbf{D}_1(z) \cdot \mathbf{D}_2(z). \tag{5.29}$$

$z_{D1\,i}$ and $z_{D2\,i}$ are the complex zeros of $\mathbf{D}_1(z)$ and $\mathbf{D}_2(z)$, respectively, such that

$$\left| z_{D1\,i} \right| > 1,\ i = 1, \ldots, na, \tag{5.30}$$

$$\left| z_{D2\,i} \right| \le 1,\ i = 1, \ldots, p - na. \tag{5.31}$$

Then the following assignments can be made:

$$\mathbf{A}_B(q) = \mathbf{D}_1(q) \tag{5.32}$$

$$\mathbf{C}_B(q) = \mathbf{D}_2(q) \tag{5.33}$$

Recall that the backwards ARX model will place system poles outside the unit circle, and the number of poles is related to the definition of $\mathbf{H}_y(z^{-1})$ (or the backwards equivalent $\mathbf{H}_{By}(z^{-1})$). This factorisation is easily computed because of the diagonal structure of the AR matrix and each diagonal entry can be treated as a scalar polynomial.

Another method to separate the system dynamics from noise dynamics is by deconvolution. The definition of $\mathbf{H}_y(q)$ is rewritten

$$\sum_{j=0}^{\min(i,nc)} \mathbf{C}_j \cdot \mathbf{H}_{y\,(i-j)} = \mathbf{A}_i \qquad i = 0, 1, 2, \ldots \tag{5.34}$$

and approximating $\mathbf{A}(q) = \mathbf{0}$, $q > na$, a set of equations can be written for $i = r - nc + 1, \ldots, r; \; r \geq max(na,nc) + nc$ [55]:

$$\begin{bmatrix} \hat{\mathbf{H}}^T_{y\,(r-nc)} & \hat{\mathbf{H}}^T_{y\,(r-nc-1)} & \cdots & \hat{\mathbf{H}}^T_{y\,(r-2nc+1)} \\ \hat{\mathbf{H}}^T_{y\,(r-nc+1)} & \hat{\mathbf{H}}^T_{y\,(r-nc)} & \cdots & \hat{\mathbf{H}}^T_{y\,(r-2nc+2)} \\ \vdots & \vdots & \ddots & \vdots \\ \hat{\mathbf{H}}^T_{y\,(r-1)} & \hat{\mathbf{H}}^T_{y\,(r-2)} & \cdots & \hat{\mathbf{H}}^T_{y\,(r-nc)} \end{bmatrix} \begin{bmatrix} \hat{C}_1 \\ \hat{C}_2 \\ \vdots \\ \hat{C}_{nc} \end{bmatrix} = \begin{bmatrix} \hat{\mathbf{H}}^T_{y\,(r-nc+1)} \\ \hat{\mathbf{H}}^T_{y\,(r-nc+2)} \\ \vdots \\ \hat{\mathbf{H}}^T_{y\,(r)} \end{bmatrix} \tag{5.35}$$

Both of the above methods have been used in practice and further comments on their implementation are discussed below. It should be noted that the first method yields an estimate of $\mathbf{C}^{-1}(q)$ and the second method $\mathbf{C}(q)$, which has to be taken into account in the subsequent stages. The assumption of system stability implies that the MA matrix is stable and this is the case if the first method described above is used to extract the MA matrix. The assumption of $\mathbf{A}(q)$=$\mathbf{0}$, $q > na$, used in the second method can lead to an unstable MA matrix being estimated, particularly when measurement data is corrupted with significant levels of noise. It is necessary to stabilise an unstable MA matrix for use in subsequent stages and this can be achieved by reflecting the unstable MA matrix zeros about the unit circle. Note that the diagonal structure imposed on the AR matrix leads to a diagonal MA matrix and each diagonal element can be treated as a scalar polynomial.

5.3.3 Stage 3: Filtering Input & Output Data and Estimation of Lower-Order ARX Model

The MA matrix estimated in the previous section (either as $\mathbf{C}^{-1}(q)$ or $\mathbf{C}(q)$) describes the noise dynamics of the ARMAX model. Fassois [55] showed that an ARMAX model can be expressed as an ARX model relating filtered input and output data if the MA matrix is known. The ARX model is then easily solved using least-squares estimation.

Pre-multiplying equation (5.2) by $\hat{\mathbf{C}}^{-1}(q)$ and noting that $\mathbf{A}_0 = \mathbf{I}_s$ leads to

$$\hat{\mathbf{C}}^{-1}(q)\cdot\mathbf{y}[t] = \hat{\mathbf{C}}^{-1}(q)\sum_{j=0}^{nb}\mathbf{B}(j)\cdot\mathbf{f}[t-j] - \hat{\mathbf{C}}^{-1}(q)\sum_{j=1}^{na}\mathbf{A}(j)\cdot\mathbf{y}[t-j] + \boldsymbol{\varepsilon}_2[t] \tag{5.36}$$

where $\boldsymbol{\varepsilon}_2[t]$ is the prediction error. Pre-multiplication by $\hat{\mathbf{C}}^{-1}(q)$ can be qualitatively thought of as pre-filtering the input and output data. Algebraically, Fassois [55] used the identity [44]

$$col(\mathbf{ABC}) = (\mathbf{C}^T \otimes \mathbf{A})\cdot col(\mathbf{B})\,, \tag{5.37}$$

where $col(\,\cdot\,)$ stacks the columns of a matrix into a vector with the first column at the top and $\otimes$ is the Kronecker product, to rewrite equation (5.36) in terms of a filtered input $\mathbf{F}_F$ and filtered output $\mathbf{Y}_F$:

$$\mathbf{y}_F[t] = \sum_{\mathrm{j=0}}^{\mathrm{nb}}\mathbf{F}_F[t-j]\cdot col(\mathbf{B}_j) - \sum_{j=1}^{na}\mathbf{Y}_F[t-j]\cdot col(\mathbf{A}_j) + \boldsymbol{\varepsilon}_2[t]\,, \tag{5.38}$$

where

$$\mathbf{y}_F[t] \equiv \left(\mathbf{y}^T[t]\otimes\hat{\mathbf{C}}^{-1}(q)\right)\cdot \mathrm{col}(\mathbf{I}_s) \qquad [s\times 1] \tag{5.39}$$

$$\mathbf{Y}_F[t] \equiv \mathbf{y}^T[t]\otimes\hat{\mathbf{C}}^{-1}(q) \qquad [s\times s^2] \tag{5.40}$$

$$\mathbf{F}_F[t] \equiv \mathbf{f}^T[t]\otimes\hat{\mathbf{C}}^{-1}(q) \qquad [s\times ms] \tag{5.41}$$

$$\therefore \qquad \mathbf{y}_F[t] = \mathbf{Y}_F[t]\cdot\mathrm{col}(\mathbf{I}_s) \tag{5.42}$$

Equations (5.38) – (5.42) describe a MIMO ARX model and the definition of the Kronecker product permits this model to be separated into *s* MISO ARX models. This also leads to a convenient way to calculate the filtered excitation and response data. Equation (5.40) is expanded as

$$\mathbf{Y}_F[t] = \begin{bmatrix} \mathbf{y}_1[t]\cdot\hat{\mathbf{C}}^{-1}(q) & \ldots & \mathbf{y}_k[t]\cdot\hat{\mathbf{C}}^{-1}(q) & \ldots & \mathbf{y}_s[t]\cdot\hat{\mathbf{C}}^{-1}(q) \end{bmatrix}, \tag{5.43}$$

and the *k*th element in the right hand side of equation (5.43) is

$$\mathbf{Y}_F^{(k)}[t] = \mathbf{y}_k[t]\cdot\hat{\mathbf{C}}^{-1}(q)\,, \qquad [s\times s] \tag{5.44}$$

Equation (5.44) shows that $\mathbf{Y}_F^{(k)}[t]$ is the output of $\mathbf{C}^{-1}(q)$ being applied as a finite-impulse response (FIR) filter [123] to the data series $\mathbf{y}_k[t]$ (the *k*th response measurement channel). An alternative representation can be derived by post-multiplying equation (5.44) by $\mathbf{C}(q)$:

$$\mathbf{Y}_F^{(k)}[t]\cdot\hat{\mathbf{C}}(q) = \mathbf{y}_k[t]\cdot I_s\,, \qquad [s\times s] \tag{5.45}$$

which is an infinite impulse response (IIR) implementation of the filter $\mathbf{C}(q)$. The use of equation (5.44) or (5.45) depends on the method used to obtain the estimate of the MA matrix in stage 2. A similar procedure can be applied to the force measurements, yielding the filtered input data series $\mathbf{F}_F[t]$.

The MIMO ARX model in equation (5.38) is separated into *s* MISO ARX models in terms of $\mathbf{F}_F[t]$ and $\mathbf{Y}_F^{(k)}[t]$:

$$\mathbf{y}_{Fk}[t] = \sum_{\mathrm{j=0}}^{\mathrm{nb}} \mathbf{F}_F[t-j]\cdot col(\mathbf{B}(j)) - \sum_{j=1}^{na} \mathbf{Y}_F^{(k)}[t-j]\cdot\mathbf{A}_k(j) + \boldsymbol{\varepsilon}_{2k}[t], \tag{5.46}$$

where $\mathbf{y}_{Fk}[t]$ is the *k*th row of $\mathbf{y}_F[t]$ and $\mathbf{A}_k(q)$ is the *k*th column of $\mathbf{A}(q)$.
Equation (5.46) can be rewritten as a linear regression problem:

$$\mathbf{y}_{Fk}[t] = \mathbf{U}_{Fk}[t]\cdot\boldsymbol{\theta}_{2k} + \boldsymbol{\varepsilon}_{2k}[t] \tag{5.47}$$

using the parameter vector

$$\boldsymbol{\theta}_{2\,k} \equiv \text{col}[\mathbf{A}_k(1) \cdots \mathbf{A}_k(na) \vdots \mathbf{B}(0) \cdots \mathbf{B}(nb)], \tag{5.48}$$

$$[(na.s + nb.m.s + m.s) \times 1]$$

and the regression vector

$$\mathbf{U}_{F\,k}[t] \equiv [-\mathbf{Y}_{F\,k}[t-1] \cdots - \mathbf{Y}_{F\,k}[t-na] \vdots \mathbf{F}_F[t] \cdots \mathbf{F}_F[t-nb]\,]. \tag{5.49}$$

$$[s \times (na.s + nb.m.s + m.s)]$$

The least-squares criterion is used to solve equation (5.47) using the QR factorisation algorithm described in stage 1. A backwards ARX model is also adopted for equation (5.46) using the same procedure described in stage 1 and the backwards AR and X matrices that are estimated are denoted $\mathbf{A}_B(j)$ and $\mathbf{B}_B(q)$, respectively.

The separation of the MIMO model into MISO models was initially used to overcome difficulties with forming and manipulating the very large regression matrices required for the LS solution of high-order MIMO models. The size of the regression matrix required for a MIMO model is $[s \times (na.s^2 + nb.m.s + m.s)]$ compared with $[s \times (na.s + nb.m.s + m.s)]$ for the MISO case.

5.3.4 Stage 4: Estimation of New Noise Model (MA matrix)

An improved estimate of the noise dynamics can be obtained using $\mathbf{H}_{By}(q)$ estimated in stage 1 and $\mathbf{A}_B(j)$ estimated in stage 3. Starting with the definition of $\mathbf{H}_{By}(q)$ in equation (5.10), the definition of the convolution of two polynomials (polynomial multiplication) [124]

$$\mathbf{H}_{B\,y}(k) = \sum \mathbf{C}^{-1}(j) \cdot \mathbf{A}_B(k+1-j), \qquad j = \max(1, k+1-(na+1)), \ldots, \min(k, p-na), \tag{5.50}$$

is used to set up a system of linear equations for $k = 1, \ldots, p,$ which is solved for $\mathbf{C}^{-1}(q)$.

Stages 3 and 4 can be iterated until a convergence criterion has been satisfied and then modal parameters can be calculated from the estimated ARMAX model.

5.3.5 Stage 5: Calculation of Modal Parameters from Estimated ARMAX Model

The ARMAX model estimated in stages 1 - 4 yielded the backwards polynomial matrices $\mathbf{A}_B(q)$, $\mathbf{B}_B(q)$, and $\mathbf{C}_B(q)$. Recall that the transfer function relating the input and output data is $\mathbf{A}^{-1}(q)\cdot\mathbf{B}(q)$ and this is used to determine the modal parameters of the system. Equations (5.51) – (5.52) are used to transform the backwards AR and X matrices into the forwards AR and X matrices.

$$\mathbf{A}(q)=\mathbf{A}_{B\,na}^{-1}(q)\cdot\left(\mathbf{A}_{B\,na}+\mathbf{A}_{B\,(na-1)}\cdot q^1+\mathbf{A}_{B\,(na-2)}\cdot q^2+\cdots+\mathbf{A}_{B\,(1)}\cdot q^{na-1}+I_s\cdot q^{na}\right) \tag{5.51}$$

$$\mathbf{B}(q)=\mathbf{A}_{B\,na}^{-1}(q)\cdot\left(\mathbf{B}_{B\,nb}+\mathbf{B}_{B\,(nb-1)}\cdot q^1+\mathbf{B}_{B\,(nb-2)}\cdot q^2+\cdots+\mathbf{B}_{B\,(1)}\cdot q^{nb-1}+\mathbf{B}_{B\,(0)}\cdot q^{nb}\right) \tag{5.52}$$

The poles of the transfer function can be extracted by calculating the eigenvalues of the bottom companion matrix [125] of $\mathbf{A}(q)$

$$\left\{\mu_1,\mu_1^*,\cdots,\mu_{na},\mu_{na}^*\right\}=eig\begin{bmatrix} 0 & \mathrm{I_s} & 0 & 0 & \cdots & 0 \\ 0 & 0 & \mathrm{I_s} & 0 & \cdots & 0 \\ & \cdots & & & \cdots & \\ 0 & 0 & 0 & 0 & \cdots & \mathrm{I_s} \\ -\mathbf{A}_{na} & -\mathbf{A}_{na-1} & \cdots & & \cdots & -\mathbf{A}_1 \end{bmatrix}, \tag{5.53}$$

which occur in complex conjugate pairs (μ^* denotes the conjugate of μ). Note that an alternative approach is to calculate the zeros of each diagonal element (a scalar polynomial) of the AR matrix. The system natural frequencies and damping can be estimated for each pole using the following equations [30]:

$$\omega_{n\,r}=\frac{1}{T_s}\sqrt{\ln\mu_r\cdot\ln\mu_r^*}\,, \tag{5.54}$$

$$\varsigma_r = \frac{-\ln\left(\mu_r \cdot \mu_r^*\right)}{2 \cdot \omega_{nr} \cdot T_s}, \tag{5.55}$$

($r = 1, \ldots,$ na) where T_s is the sampling period. The transfer-function zeros for each input-output channel pair can be calculated by finding the zeros of $z^{nb} \cdot b_{ij}(z^{-1})$, where $b_{ij}(z^{-1})$ is an element of the X matrix.

Alternatively, the MIMO transfer function can be separated into $s \times m$ scalar transfer functions and factorised into partial fraction form [51]:

$$\frac{b_{ij}(q)}{a_{ii}(q)} = \sum_{k=1}^{na} \left(\frac{R_{ij}^{(k)}}{1 - \mu_k \cdot q} + \frac{R_{ij}^{*(k)}}{1 - \mu_k^* \cdot q} \right). \tag{5.56}$$

The residues are used to define the kth mode shape:

$$\Phi_k = \begin{bmatrix} 1 & \dfrac{R_{2j}^{(k)}}{R_{1j}^{(k)}} & \cdots & \dfrac{R_{sj}^{(k)}}{R_{1j}^{(k)}} \end{bmatrix}^T. \tag{5.57}$$

The diagonal AR matrix yields s sets of global modal parameters and these can be averaged. The sign of the damping for each estimated mode allows the structural modes to be distinguished from the spurious numerical modes and further reduction of the estimated model can be achieved by selecting the appropriate poles and residues.

A number of subtle issues arise when using discrete models to describe continuous systems. The potential for magnification of errors when transforming the poles and residues of a discrete model into corresponding continuous-time poles and residues was discussed by Fassois *et al.* [126]. Using the definition of the z-transform, they derived the sensitivity of the global parameters to changes in the polar coordinates of the discrete-time poles as

$$\mathbf{S} \equiv \begin{bmatrix} s_r^{\omega_n} & s_\theta^{\omega_n} \\ s_r^{\varsigma} & s_\theta^{\varsigma} \end{bmatrix} = \begin{bmatrix} -\dfrac{\varsigma}{T_s \cdot \omega_n} & 1-\varsigma^2 \\ \dfrac{\varsigma^2 - 1}{\varsigma \cdot T_s \cdot \omega_n} & \varsigma^2 - 1 \end{bmatrix}, \tag{5.58}$$

where s_q^p is the sensitivity of parameter p to changes in parameter q. ω_n is the natural frequency and ς the damping of a discrete-time pole with complex modulus r and argument θ, and T_s is the sampling period. Equation (5.58) clearly shows that the sensitivity of natural frequency and damping with respect to r approaches infinity as $T_s \to 0$. The effect of this is that small estimation errors of discrete-time poles can lead to very large errors in continuous-time modal parameters for very high sampling frequencies. Modal damping is particularly sensitive to complex-modulus errors of the discrete-time pole, especially for low levels of damping. These effects should be kept in mind when estimating discrete-time models for wide-frequency ranges, as is common in vibration analysis of structures.

Fassois *et al.* [126] also noted that the transformation of discrete-time residues to the continuous residues, which are used to define mode shapes, depended on the inter-sample behaviour of the excitation signal. Two common assumptions are impulse invariance and the step approximation method. The discrete and continuous-time residues are equal (hence their errors) under the assumption of impulse invariance, which assumes that the excitation is a train of impulses occurring at the sampling instants [123]. For the case of step approximation, Fassois *et al.* [126] showed that no sensitivity issues arise, except for the case where the argument of the continuous residue approaches zero.

5.4 Implementation of ARMAX Estimation Algorithm

A number of additional points need to be addressed when implementing the ARMAX parameter estimation algorithm:

- Sampling rate and data record length;
- Model orders *na, nb, nc,* and *p*;
- Selection of 'best' model.

5.4.1 Sampling Rate and Record Length

The number of samples in the input and output data vectors is important in stages 1 and 3 where the LS criterion is used to estimate the parameters of ARX models. Equation (5.20) shows that the number of samples in the input (or output) data series determines the number of rows in the regression vector and it can be seen that this affects the level of over-determination of the regression problem. The minimum record length is determined by the size of the model, given that the regression problem should be overdetermined.

The sampling rate is also of critical importance when estimating an ARMAX model and subsequent calculation of modal parameters from the ARMAX model. Ljung [116] discussed the effect of sampling interval on bias and variance of estimated models and pointed out that very high sampling rates can lead to numerical problems in discrete-time models. Another issue is that the estimated model spreads into high frequency bands; the frequency range increases and the estimated model includes components to account for noise present in the frequency range. As $T_s \rightarrow 0$ (i.e. increasing sampling rate), low frequency signal components are misrepresented due to the finite precision of sampled data; a quantisation step becomes larger than the amplitude change of a low frequency signal component over a sampling period. On the other hand, a very slow sampling rate relative to the system time constants results in a poor representation of the system dynamics. The conclusion is that the optimal choice of the sampling period will be within the range of system time constants. Another general specification given by Söderström and Stoica [44] is to set sampling period as approximately 10% of the settling time of the system's step response. Both these specifications appear to be unsatisfactory for identifying models representing mechanical systems as the time constants (hence settling time) can become quite large due to very small damping.

Another aspect related to choice of sampling rate is the transformation of the discrete ARMAX model into modal parameters discussed in section 5.3.5.

5.4.2 Specifying Model Order (*na, nb,* and *nc*)

The theoretically required model order, *na*, was discussed in section 5.3.1 and it was noted that the order of *nb* was determined by *na* and the type of response measurements;

i.e., displacement, velocity or acceleration data. The order p of the higher order ARX model used in stage one can be set arbitrarily; Fassois & Lee [117] and Fassois [55] suggested between 2.5 and 5 times the maximum of *na, nb,* and *nc* worked well for modal analysis problems. Alternatively, a statistical model order selection criterion may be used to help identify a suitable model order. Section 5.3.1 suggests a higher order model for measurements corrupted with noise but large models increase the computation time and numerical difficulties can be encountered in subsequent stages when estimating the noise model (MA matrix) and subsequent filtering of the input and output data. The order *nc* of the MA matrix is dependent on the noise present in the system and generally no information on the nature of this disturbance is available. An approach taken by Fassois [55] involves initially setting $nc = na$, selecting the best model using a particular criterion out of a set $na = na_{min}, \ldots, na_{max}$ and then testing the effectiveness of changing *nc*. The value of *nc* also affects the separation of the noise and system dynamics in stage 2 and 4. If $nc = p - na$, the first method discussed in stage 2 (section 5.3.2) can be used where $\mathbf{H}_{By}(q)$ of order p is factorised into two polynomials, one of order *na*, the other of order *nc* (see equations (5.29) – (5.33)). If $nc \neq p - na$ the second method is used as it allows an MA matrix of any order to be estimated (equations (5.34) and (5.35)). These comments also apply to the stage 4 estimation of the noise model.

5.4.3 Model Selection

The issue of defining a set of models of different orders and then selecting the most accurate model from that set is a difficult problem and a number of approaches has been studied in literature. Tests such as the Akaike Information Criterion (AIC) [44] and Bayesian Information Criterion (BIC) have been used in literature and are simple to implement once the innovations sequence (model error) $\mathbf{w}[t]$ (see equation (5.2)) has been computed. The BIC is defined as [55]

$$\mathbf{BIC} = \ln\left(\det\left|\hat{\Sigma}\right|\right) + d\left(\frac{\ln(N)}{N}\right), \tag{5.59}$$

where d is the number of scalar parameters in the ARMAX model, N the number of samples in the input (or output) data and

$$\hat{\Sigma} = \frac{1}{N}\sum_{t=1}^{N}\hat{\mathbf{w}}[t]\cdot\hat{\mathbf{w}}^{T}[t] \qquad [s \times s] \tag{5.60}$$

is the covariance matrix of the innovations sequence. The diagonal terms in the covariance matrix are the estimates of variance (or mean square value for a zero-mean sequence) of each element of the innovations and the non-diagonal terms estimate the covariance between elements. The BIC examines the magnitude of the innovations and the correlation between elements, and also includes a penalty for large models weighted by the number of data samples used in the estimation; a larger number of samples reduces the sensitivity of the BIC to the number of estimated parameters.

Other tests can be applied to the innovations sequence to test the assumption that it is a random sequence (that can have correlated components) independent of all inputs to the system [44]. For example, testing the autocorrelation of each element of the innovations and also the cross-correlation between the innovations sequence and the input can help select the most accurate model.

Another method is the use of stabilisation diagrams, which plot the estimated modal frequencies and damping for each model order. The consistency or stability of vibration modes helps distinguish between spurious numerical modes and vibration modes and also allows the model of minimum order with stable global parameters to be selected. In practice, stability diagrams can be difficult to interpret, particularly for higher order models with high modal density. Also, as mentioned in section 5.3.1, the LS estimation of ARX models can lead to spurious numerical poles being uniformly spread around the unit circle with little variation for different model sizes, which also contributes to the difficulty in interpreting stabilisation diagrams. A related method is to check the number of estimated modes with positive damping and select the smallest model that has the largest number of positively damped poles. This method is discussed further in Chapter 6.

Estimating a large number of models with varying order (*na* and *nc*) improves the chance of identifying a model that describes the behaviour of the structure accurately. A compromise has to be reached where a number of models can be estimated in a reasonable time and still describe the behaviour of the structure accurately. A subset of data may be used to estimate a number of models and then the full set of data may be used to estimate a smaller number of models of appropriate order. Examining the power spectra of response data can also provide further information, for example, a rough estimate of the number of expected modes in a frequency band, which will aid the determination of model order. These issues will be discussed in more detail in Chapter 6, which describes numerical testing of the ARMAX estimation algorithm and the analysis of experimental data.

5.5 Conclusions

An algorithm to estimate an ARMAX model from data that includes measurement noise and also unmeasured periodic and random excitations has been introduced. This addresses a case that has not been widely considered as was revealed in the review of modal parameter estimation methods in Chapter 2. Cases where unmeasured sources of excitation are present are likely to arise when analysing structures in their operating environments, for example investigating the structural dynamics of helicopters in-flight. The estimation algorithm is an iterative multistage method, which incorporates the estimation of backwards ARX models, estimation of a noise model, filtering of the excitation and response data and estimation of a lower-order ARX model. The use of backwards ARX models allows vibrational modes and spurious numerical poles to be distinguished on the basis of the sign of modal damping. The number of positively damped poles has also been introduced as a method to select the best model from a set of estimated models. A diagonal parameterisation of the AR matrix, and consequently the MA matrix allows the MIMO ARMAX model to be estimated as a set of MISO models. The diagonal structure also allows simple manipulation and stabilisation of the AR and MA matrices. Numerical and experimental testing of the algorithm and model selection criterion is discussed in the following chapter and further experimental tests using the helicopter-like structure are described in Chapter 7.

Chapter 6 ARMAX Modal Parameter Identification in the Presence of Unmeasured Excitation: Numerical and Experimental Verification

6.1 Introduction

Chapter 2 revealed that existing experimental modal analysis techniques usually require excitation and response data with a high signal-to-noise (s/n) ratio and that all sources of excitation be measured and uncorrelated. In practice, unmeasured sources of excitation are likely to be present when analysing structures in their operating environment, for example helicopters in flight. Hence, a modal parameter estimation scheme based on the identification of parameters in an ARMAX model, which explicitly modelled sources of unmeasured excitation, was introduced in the previous chapter. In this chapter, numerical tests using data simulating the response of a two degree-of-freedom (DOF) system are used to assess the performance of the ARMAX estimation algorithm when data is corrupted with random measurement noise and unmeasured periodic and random excitations. Tests include the effect of unmeasured random and periodic excitations applied to systems with lightly damped modes, closely spaced modes, as well as a case with high levels of damping. A new model selection criterion based on the number of positively damped modes is also investigated and compared with the Bayesian Information Criterion (BIC) [55].

Further testing of the ARMAX estimation algorithm is carried out using experimental data obtained from a cantilever aluminium beam. Initial experiments applied independent random excitation using electrodynamic shakers. Subsequent experiments investigated the effect of unmeasured periodic and random excitations and employed pairs of piezoceramic plates to excite the beam as described in Chapter 4. Results obtained from the ARMAX estimation algorithm are compared with results obtained from frequency domain curve fitting of SIMO data and results from least-squares estimation of ARX models.

6.2 Numerical Testing

A two degree-of-freedom system was used for numerical testing of the ARMAX algorithm. Figure 6.1 shows a schematic of the simulated system and three sets of mass, damping, and stiffness parameters used to simulate 3 systems; the first system having well-spaced, lightly damped modes; the second system having lightly-damped modes separated by 0.345 Hz; and the third system having well-spaced highly damped modes. The physical and modal parameters for each system are listed in table 1. Equation (6.1) is the time domain differential equation for the system and transfer function matrices are given in equations (6.2), (6.3), and (6.4) for systems 1, 2, and 3, respectively.

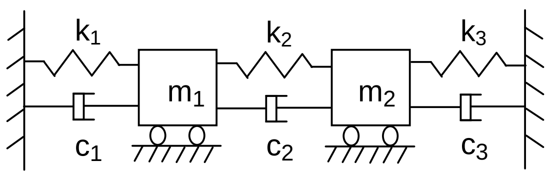

Figure 6.1 Two DOF damped spring mass system.

$$\begin{bmatrix} m_1 & 0 \\ 0 & m_2 \end{bmatrix}\ddot{\mathbf{v}}(t) + \begin{bmatrix} c_1+c_2 & -c_2 \\ -c_2 & c_2+c_3 \end{bmatrix}\dot{\mathbf{v}}(t) + \begin{bmatrix} k_1+k_2 & -k_2 \\ -k_2 & k_2+k_3 \end{bmatrix}\mathbf{v}(t) = \mathbf{f}(t) \tag{6.1}$$

$$\mathbf{H}(s) = \frac{1}{2s^4+1.6s^3+1900.08s^2+260s+150000}\begin{pmatrix} 2s^2+0.4s+300 & 0.4s+300 \\ 0.4s+300 & s^2+0.6s+800 \end{pmatrix} \tag{6.2}$$

$$\mathbf{H}(s) = \frac{1}{s^4+0.8s^3+680.14s^2+264s+114000}\begin{pmatrix} s^2+0.3s+340 & 0.1s+40 \\ 0.1s+40 & s^2+0.5s+340 \end{pmatrix} \tag{6.3}$$

$$\mathbf{H}(s) = \frac{1}{2s^4+18s^3+1912s^2+2900s+150000}\begin{pmatrix} 2s^2+4s+300 & 4s+300 \\ 4s+300 & s^2+7s+800 \end{pmatrix} \tag{6.4}$$

The displacement response at each DOF was generated using the Matlab function `lsim()` to simulate the response of the system's continuous-time transfer function when excited with independent random noise applied to each DOF. The function `lsim()` discretises the continuous-time transfer function using a zero-order-hold assumption. Ten seconds of excitation and response data sampled at 50 Hz was used for all tests except those investigating the effect of record length and sampling rate, described in sections 6.2.6 and 6.2.8, respectively. Frequency response functions (FRFs) for each system are shown in figures 6.2 (a), (b), and (c). A range of tests included unmeasured excitations added to the measured random excitations, and measurement noise could be applied by adding a zero-mean random sequence of appropriate mean-square amplitude to each of the response measurements. A summary of the noise conditions and unmeasured excitations used for each numerical test is listed in table 6.2.

System	Physical Parameters	Mode	Frequency (Hertz)	Damping (%)	Magnitude (DOF 2)	Phase° (DOF 2)
1	$m_1 = 1$; $m_2 = 2$; $c_1=0.2$; $c_2= 0.4$; $c_3= 0$; $k_1=500$; $k_2= 300$; $k_3= 0$	1	1.485	0.4180	2.377	0.3211
		2	4.676	1.229	0.2104	179.0
2	$m_1 = 1$; $m_2 = 1$; $c_1=0.4$; $c_2= 0.1$; $c_3= 0.2$; $k_1=300$; $k_2= 40$; $k_3= 300$	1	2.757	0.8658	1.002	2.479
		2	3.102	1.283	0.9982	177.2
3	$m_1 = 1$; $m_2 = 2$ $c_1=3$; $c_2= 4$; $c_3= 0$; $k_1=500$; $k_2= 300$; $k_3=0$	1	1.485	4.613	2.371	2.518
		2	4.673	13.86	0.2160	172.3

Table 6.1 Physical and modal parameters of 2 DOF systems. Magnitude and phase is listed for DOF 2, relative to a unit displacement of DOF 1.

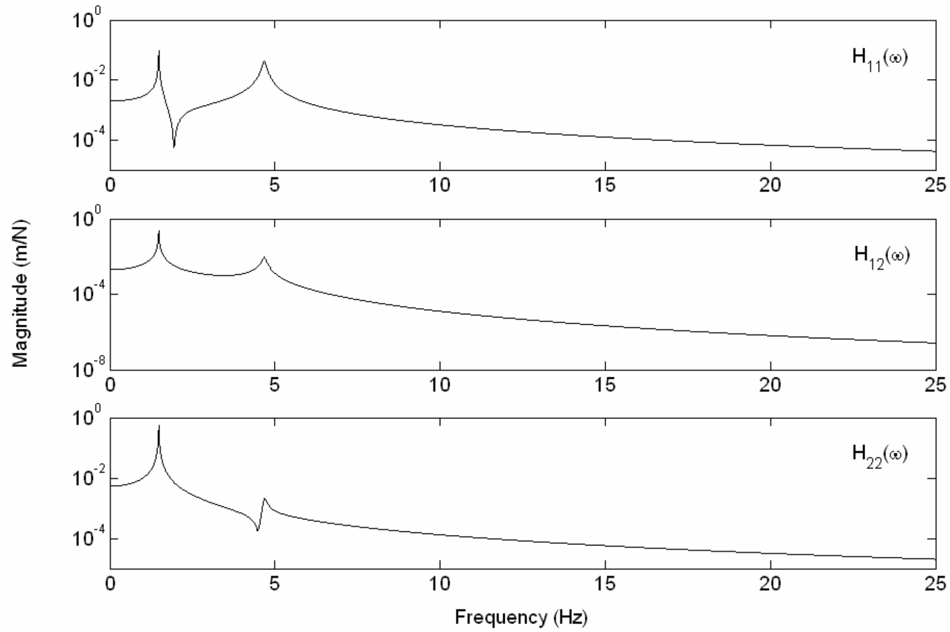

Figure 6.2 (a) Frequency response functions relating each degree-of-freedom for 2 DOF system 1, calculated using the transfer function matrix in equation (6.2).

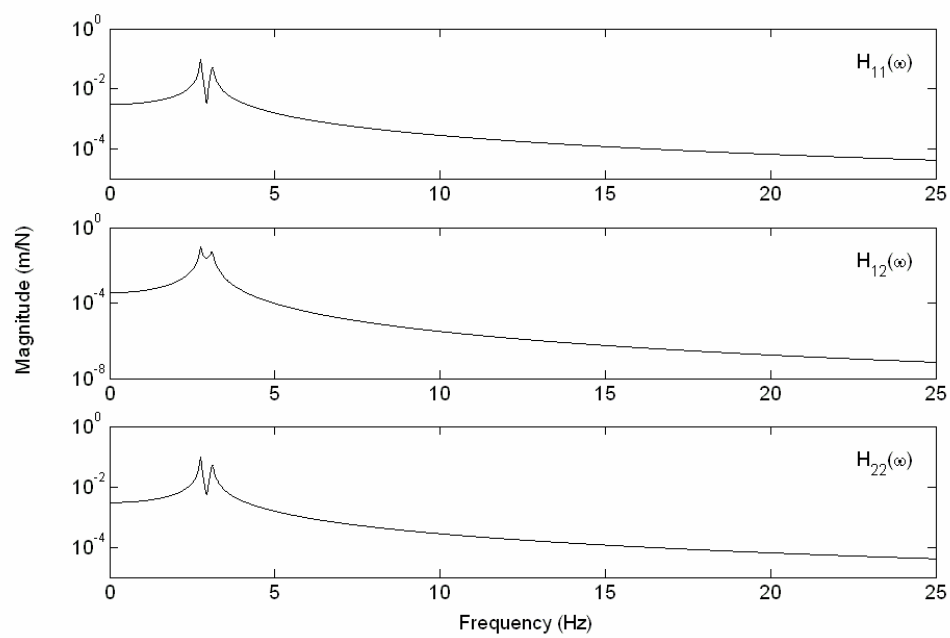

Figure 6.2 (b) Frequency response functions relating each degree-of-freedom for 2 DOF system 2, calculated using the transfer function matrix in equation (6.3).

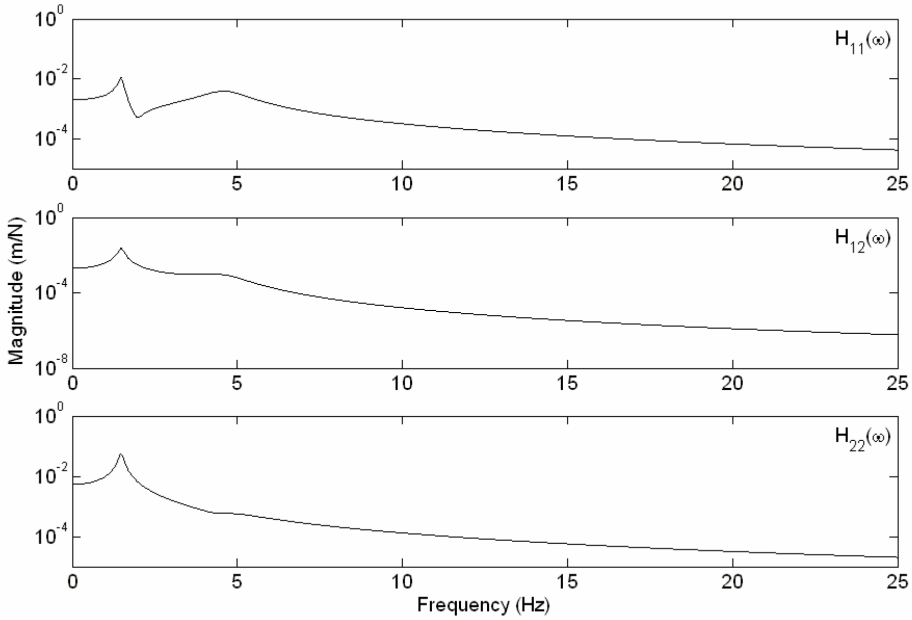

Figure 6.2 (c) Frequency response functions relating each degree-of-freedom for 2 DOF system 3, calculated using the transfer function matrix in equation (6.4).

Fifty tests using independent realisations of excitation data and measurement noise were run to enable the mean and standard deviation of estimated modal parameters to be calculated. In addition, the unmeasured periodic excitations used for each test were generated using summed sinusoids with a random phase relationship. The selected model was often of higher order than theoretically necessary and the frequency response function of each estimated ARMAX model was used in addition to the sign of the damping to help identify the correct modal parameters. Figure 6.3 shows an example of the average of FRFs synthesised from the 50 ARMAX models from test 1 data, and the average of the exact FRFs for all DOFs is also plotted. Two peaks can be clearly identified and these were assumed to represent vibration modes. ARMAX model poles with a natural frequency within 5% of the selected peaks were assumed to represent structural modes, and were further assessed using the sign of the damping. The 5% tolerance was chosen on the basis of the resolution of the FRFs synthesised from the ARMAX models. Figure 6.4 plots the FRFs from all selected ARMAX models for a case where some models fail to identify the second mode, as indicated by the arrow in the figure.

Test	System	Noise conditions
1	1	• 10% random noise added to the response measurements.
2	1	• 100% unmeasured periodic signals at 1, 2, & 4 Hz used to excite DOF 1 in addition to measured random excitation. • 10 % random noise added to the response measurements.
3	1	• 20% unmeasured random noise used to excite each DOF in addition to the measured random excitation. • 10% random noise added to the response measurements.
4	1	• 100% unmeasured periodic signals at 1, 2, & 4 Hz used to excite DOF 1. • 20% unmeasured random noise applied to each DOF in addition to the measured random excitation. • 10% random noise added to the response measurements.
5	2	• 10% random noise added to the response measurements.
6	2	• 100% unmeasured periodic signals at 1, 2.50, & 4 Hz used to excite DOF 1 in addition to measured random excitation. • 10 % random noise added to the response measurements.
7	2	• 20% unmeasured random noise used to excite each DOF in addition to the measured random excitation. • 10% random noise added to the response measurements.
8	2	• 100% unmeasured periodic signals at 1, 2.50, & 4 Hz used to excite DOF 1. • 20% unmeasured random noise applied to each DOF in addition to the measured random excitation. • 10% random noise added to the response measurements.
9	3	• 10% random noise added to the response measurements.
10	3	• 100% unmeasured periodic signals at 1, 2, & 4 Hz used to excite DOF 1 in addition to measured random excitation. • 10 % random noise added to the response measurements.
11	3	• 20% unmeasured random noise used to excite each DOF in addition to the measured random excitation. • 10% random noise added to the response measurements.
12	3	• 100% unmeasured periodic signals at 1, 2, & 4 Hz used to excite DOF 1. • 20% unmeasured random noise applied to each DOF in addition to the measured random excitation. • 10% random noise added to the response measurements.

Table 6.2 Summary of noise conditions and unmeasured excitations for numerical tests. Listed noise (or unmeasured excitation) levels are the ratio of the RMS values of the noise and clean signals to which the noise is added.

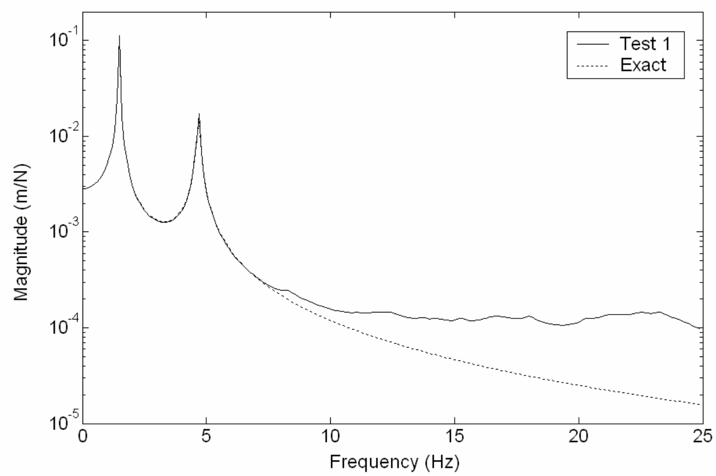

Figure 6.3 Averaged frequency response functions of estimated ARMAX models for test 1 data (Test 1) compared with averaged exact FRFs (Exact).

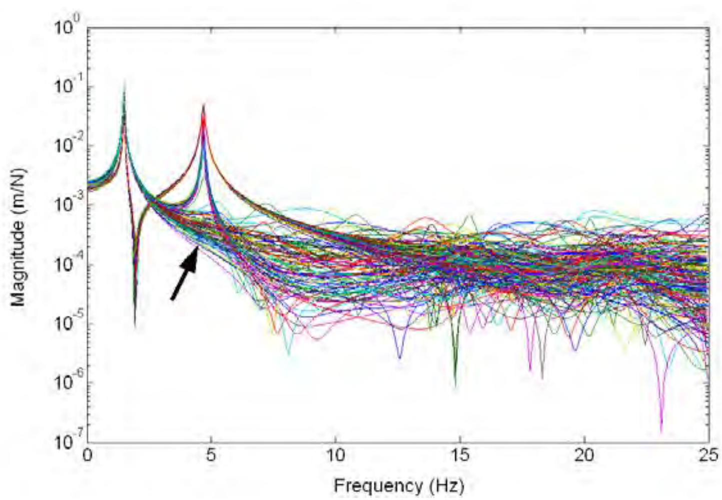

Figure 6.4 Frequency response functions of 50 estimated ARMAX models for test 1 data. The arrow indicates models that have not correctly identified mode 2.

Note that *s* estimates (*s* is the number of response measurement points) of the global modal parameters, and *m* estimates (*m* is the number of excitation points) are obtained from each ARMAX model as the excitation and response measurements were taken at each DOF. The minimum set of measurements required corresponds to either a row or column of the transfer function matrix: in this case either one excitation and two response (SIMO) measurements or two excitation and one response (MISO) measurements.

6.2.1 Model Selection Using BIC and NPDP Criterion

The performance of the BIC and number of positively damped poles (NPDP) model selection criteria were compared using sets of ARMAX models estimated as discussed above from data generated under the conditions described by test 1 and test 2 (table 6.2).

The NPDP model selection criterion was implemented with the following rules:

1. Select the model of smallest order with the greatest number of positively damped poles estimated with the minimum number of iterations over a particular threshold. This rule automatically penalises higher order models with large numbers of iterations.
2. The iteration threshold is set to at least one depending on the variation of numbers of positively damped poles. Experience showed that approximately five iterations of stages 3 and 4 were beneficial for the accuracy of modal parameters. Therefore a minimum number of iterations can be imposed if no variation of the number of positively damped poles is observed in the set of estimated models.
3. A subset of model orders can be used if little or no variation of the number of positively damped poles is observed.

The mean and standard deviation were calculated for modal parameters obtained from the ARMAX models selected by the BIC and NPDP criterion. Results for models estimated from test 1 data are shown in figure 6.5 and results for models estimated from test 2 data are shown in figure 6.6. Figure 6.5 shows that the ARMAX algorithm is successful in identifying modal parameters from data corrupted with 10% random measurement noise. In particular, modal frequencies are very accurately estimated with results within 1% of their true value. Modal frequency results obtained by BIC and NPDP criterion are very similar. Modal damping results illustrate the negative bias on damping peculiar to backwards ARX models estimated from data corrupted with noise.

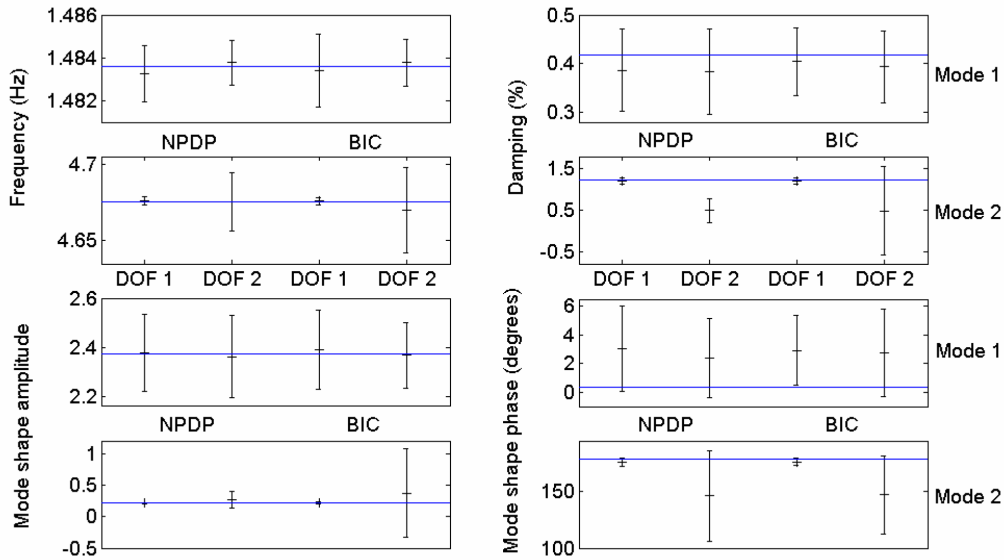

Figure 6.5 Modal parameters obtained from ARMAX models selected by BIC and NPDP criterion for test 1 data. The true value of each parameter is indicated by the horizontal lines in each plot.

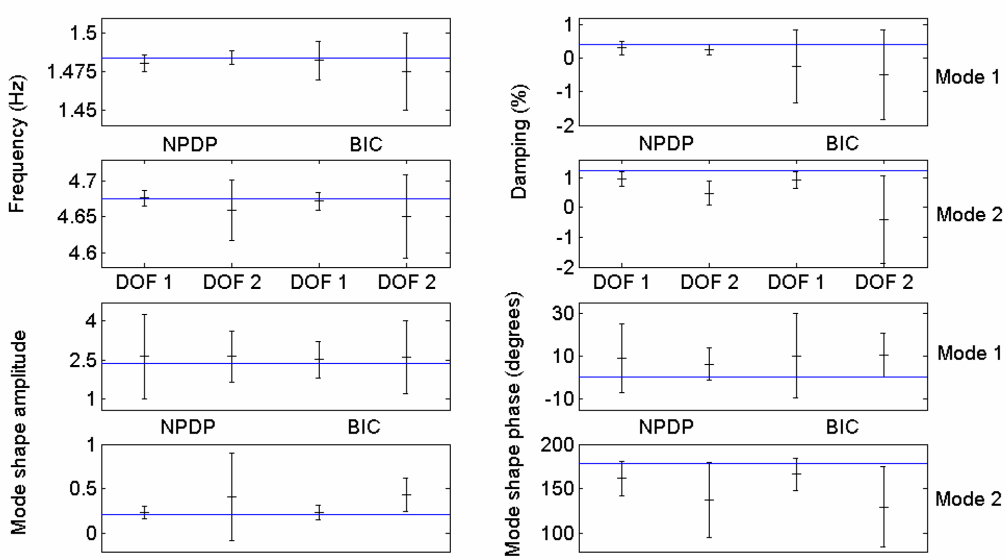

Figure 6.6 Modal parameters obtained from ARMAX models selected by BIC and NPDP criterion for test 2 data. The true value of each parameter is indicated by the horizontal lines in each plot.

Mode 1 damping values are within 10% of their true values and similar results are obtained for both model selection criteria. Mode 2 damping values show the effect of noise present in measurements obtained from DOF 2. Damping values obtained from the MISO model with DOF 2 as reference are poorer than those obtained from the MISO model with DOF 1 as reference. This pattern is reflected in the standard deviation of mode shape magnitude and phase results for mode 2. Mode shape results obtained from each model selection criterion are of acceptable accuracy, noting that the phase values are particularly sensitive to noise and unmeasured excitations, especially for mode 2, DOF 2. It should be emphasised that the BIC results were obtained for a subset of models $na \geq 8$, estimated with 4 more iterations, because the BIC consistently estimated low-order models, which often did not identify modes. The NPDP was applied to the set of models with $na \geq 4$ estimated with 4 more iterations.

Figures 6.7 (a) and (b) show the 1-sided power spectra of clean response measurements and the added random noise for each DOF. The signal power at frequencies just below 5 Hz (corresponding to the natural frequency of the second mode) measured at DOF 2 is less than an order of magnitude above the random noise. This explains the relatively poor results obtained for mode 2 obtained from models with DOF 2 as reference.

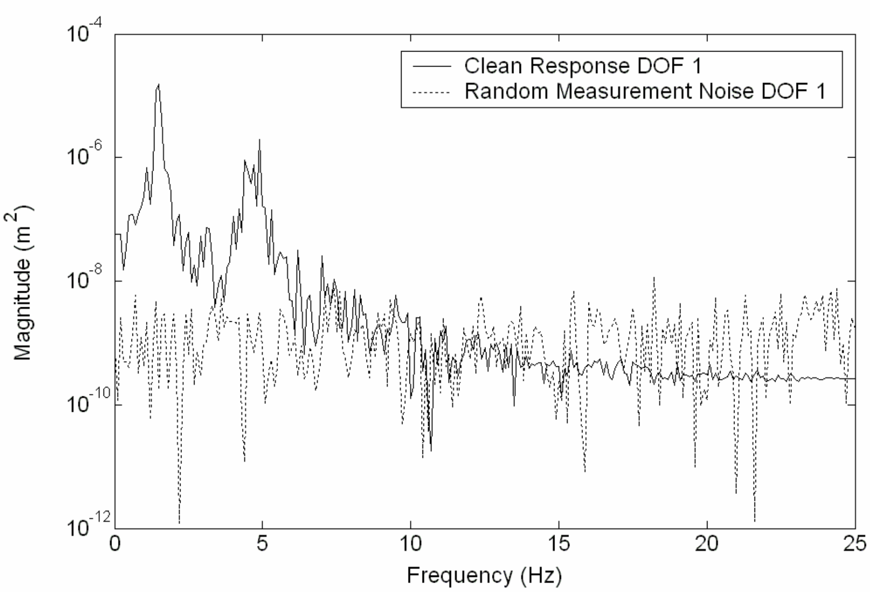

Figure 6.7 (a) 1-sided power spectrum of clean response (no added noise) and random noise added to response measurement at DOF 1, system 1.

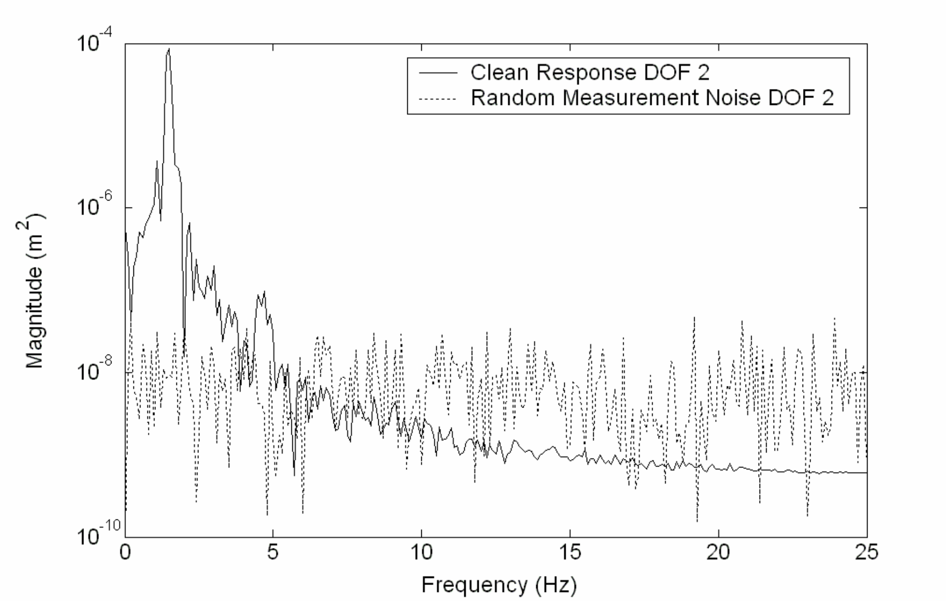

Figure 6.7 (b) 1-sided power spectrum of clean response (no added noise) and random noise added to response measurement at DOF 2, system 1.

A similar pattern of results is obtained for test 2 data (figure 6.6), where DOF 1 was excited by unmeasured periodic excitations in addition to the measured random excitations. The unmeasured periodic excitation leads to many instances of modes being estimated with negative damping. The NPDP model selection criterion performs better than the BIC; the BIC damping results for mode 1 DOFs 1, 2 and mode 2 DOF 2 are negative, whereas NPDP damping results are all positive. The multiple estimates of global parameters can be reduced by averaging, ignoring negatively damped modes, and the relative standard deviation of parameters obtained for each response measurement point indicates the quality of the response for each mode at that particular measurement point. The addition of unmeasured periodic excitations reduces the effectiveness of the ARMAX estimation algorithm, however, accuracy remains acceptable.

A limitation of the BIC is its poor sensitivity to different model orders and the effect of iterations in stages 3 and 4 of the ARMAX estimation algorithm. Figure 6.8 shows the BIC values corresponding to ARMAX models obtained for each model order and iteration for a typical realisation of data under test 1 conditions. The BIC decreases after the first iteration for all model orders but stabilises quickly after the second iteration. Models with a highly over-specified order have higher initial BIC values and take more iterations to stabilise, which is probably due to the effect of the higher number of

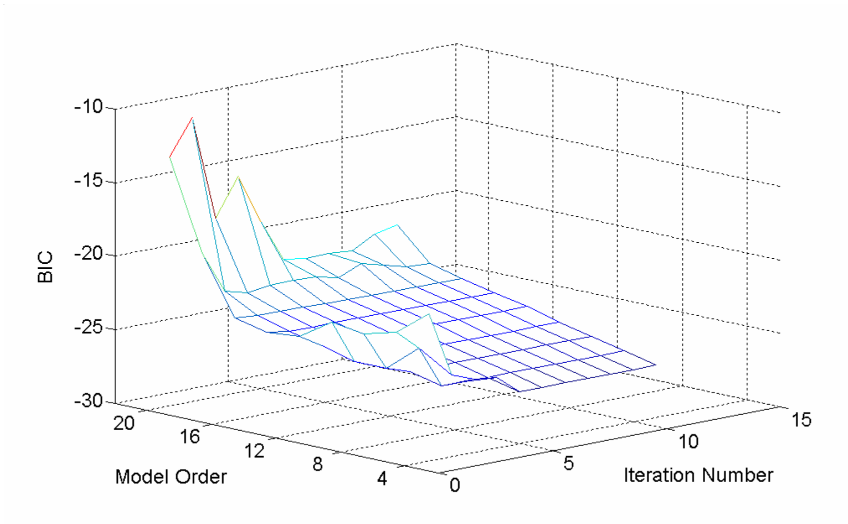

Figure 6.8 BIC calculated for each model and iteration for a typical realisation of test 1 data.

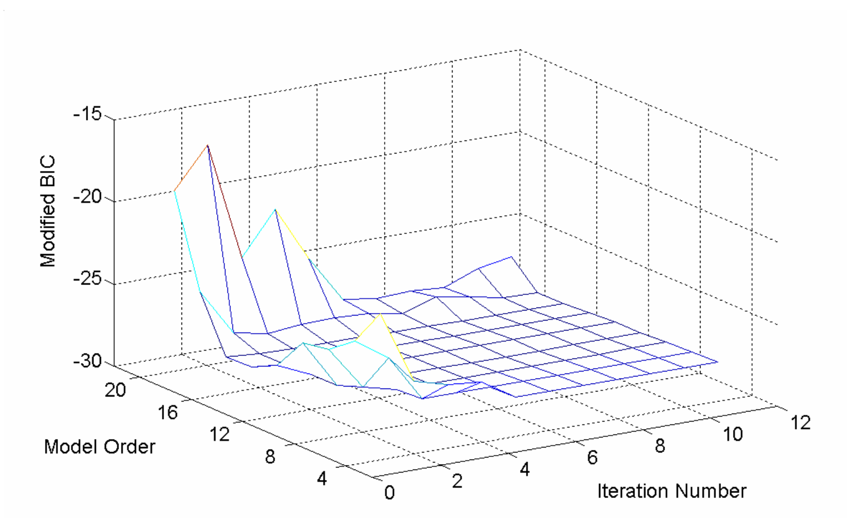

Figure 6.9 Modified BIC calculated for each model and iteration for a typical realisation of test 1data. The modified BIC does not include the term penalising larger models.

spurious numerical poles. It was found that low-order models estimated after a few iterations were typically selected by the BIC but estimated modal parameters increased in accuracy for higher-order models and after a greater number of iterations. More accurate results were obtained by searching for the minimum BIC in a subset of models with $na \geq 8$ with a minimum of four iterations, and this was adopted for all tests using the BIC. The effect of the second term in equation (5.59), which penalises higher-order models, is illustrated by plotting a modified BIC value without that term in figure 6.9 for the same set of models as those used to generate figure 6.8. The positive slope along the model order axis has been removed, which increases the likelihood of higher order models being selected by the modified BIC. Results showed that the modified BIC value was still not sufficiently sensitive to the effect of iterating stages 3 and 4, and subsequent results show that the number of positively damped poles (NPDP) criterion addressed this problem.

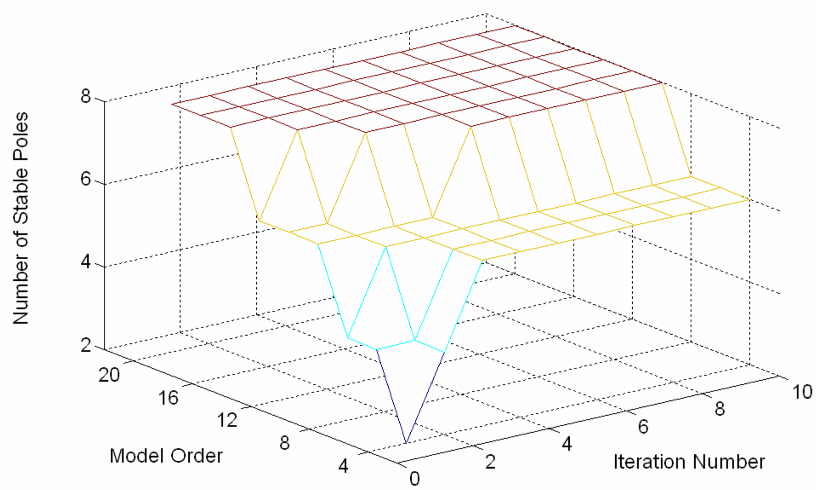

Figure 6.10 Number of positively damped poles estimated for each model and iteration for a typical realisation of test 1 data.

Figure 6.10 shows a plot of the number of positively damped poles estimated for each model order and iteration for a typical realisation of test 1 data. It can be seen that low-order models only select a subset of the 8 possible positively damped modes. The maximum number is eight due to complex conjugate poles for two modes being estimated for 2 MISO models: 2×2×2=8. It is likely that the modes that are not identified correspond to the second mode in models using DOF 2 as a reference, due to the poor signal-to-noise ratio, as discussed above. Models of order 10, 12, and 14 initially have only six modes identified with positive damping but further iterations improve the accuracy of the model and the maximum eight modes are estimated with positive damping. The BIC and NPDP are shown in figures 6.11 and 6.12 for typical realisations of test 2 data. The bias of the BIC towards lower-order models can clearly be seen and the plot of NPDP shows that low-order models fail to identify positively damped poles. All 8 positively damped poles are identified in an ARMAX model of order 16, after 9 iterations of stages 3 and 4, and this model is selected by the NPDP criterion.

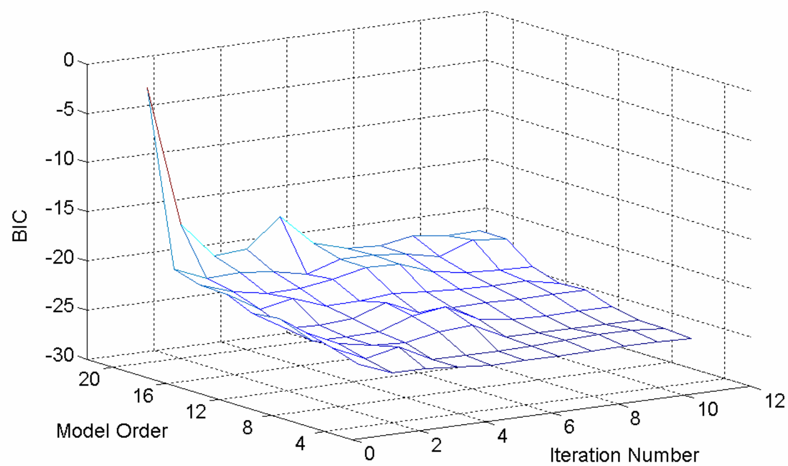

Figure 6.11 BIC calculated for each model and iteration for a typical realisation of test 2 data.

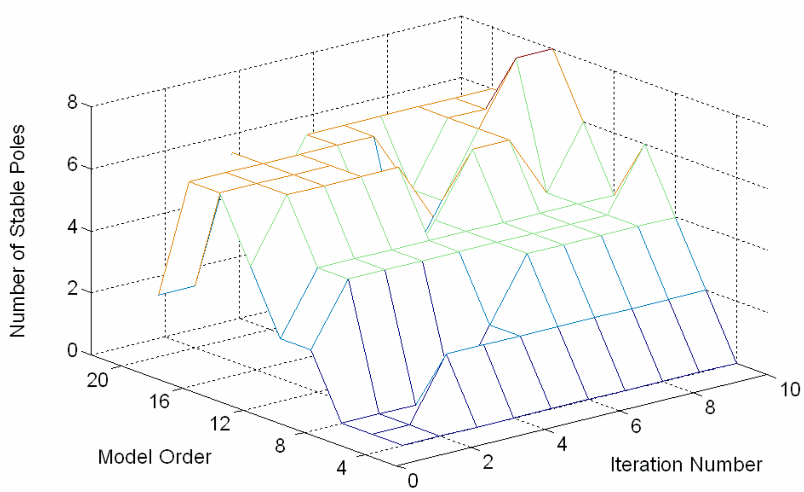

Figure 6.12 Number of positively damped modes estimated for each model and iteration for a typical realisation of test 2 data.

The second and third rules of the NPDP criterion outlined above can be imposed if extra iterations or larger models do not increase the number of positively damped poles as it is expected that to a certain extent larger models and a moderate number of iterations will improve the accuracy of the estimated modal parameters. As shown in figure 6.13, no model correctly identifies all eight positively damped poles. Note that both modes have still been correctly identified with positive damping and in this case these were probably identified for the MISO model with DOF 1 as a reference. Experience suggests that using a moderate number of iterations, say between 4 and 10, and avoiding the models with lower order would improve the accuracy of the estimated modal parameters. Therefore, for sets of models like that shown in figure 6.13, the second and third rules of the model selection criterion could be imposed. Analysis of synthesised FRFs and pole-zero diagrams from models estimated from a representative set of data is useful in determining a suitable range of model orders.

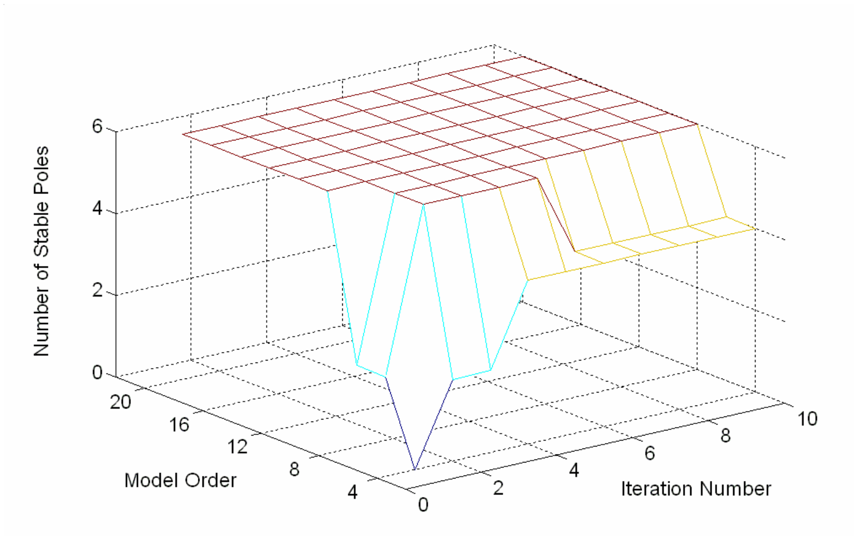

Figure 6.13 Number of positively damped poles estimated for each model and iteration for a different realisation of test 1 data.

The advantage of using the NPDP criterion is that it directly assesses the sign of modal damping and this appears to be a good indicator of the accuracy of the other modal parameters of vibration modes. If the ARMAX model was intended for prediction of the vibration response, the BIC, modified BIC, or the correlation-based model selection criteria [44, 116] may be a better choice, as they assess the model prediction error or innovations sequence. A further benefit of using the NPDP criterion is that it avoids calculating the innovations sequence, which is calculated recursively using the estimated ARMAX model and the measured excitation and response data. Problems can be encountered during this operation if the estimated ARMAX model is unstable. The number of positively damped poles can be determined by calculating the roots of each scalar AR polynomial directly after the ARX model in stage 3 is estimated. Other model selection criteria based on testing the assumptions made about the innovations sequence and the correlation between the innovations sequence measured excitations were tested. Results are discussed in Appendix A, and show that the performance was comparable to that of the BIC. Conditioning of the regression matrices used in the estimation scheme is also included in the discussion in Appendix A.

6.2.2 Unmeasured Random and Periodic Excitation – 2DOF System 1

The performance of the ARMAX estimation algorithm and NPDP criterion was assessed for the noise conditions described in tests 1 – 4 (table 6.2) and the mean and standard deviation of results are plotted in figures 6.14 and 6.15. Modal frequencies are estimated very accurately for all tests and all modal damping values are positive, but the negative bias is evident, especially for mode 2, DOF 2 estimates. Accuracy decreases and greater scatter is seen in damping results for higher levels of unmeasured excitation. Mode shape magnitudes are accurately estimated; the large standard deviation values for some results arising from residues corresponding to spurious poles, which are more prevalent for tests 2 and 4, which include unmeasured periodic excitations. Mode shape phase values for mode 2, DOF 2 are sensitive to measurement noise and unmeasured excitations.

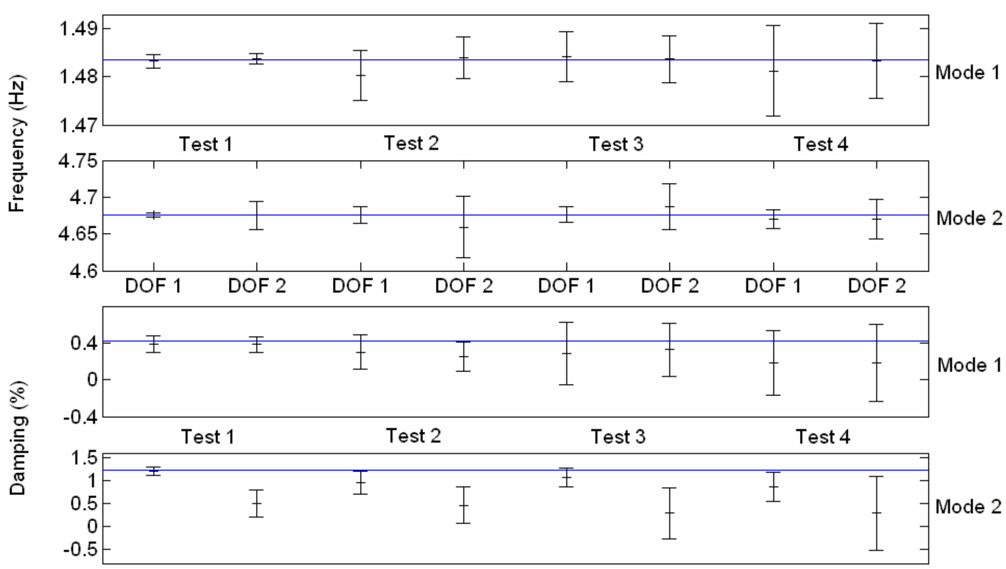

Figure 6.14 Modal frequency and damping obtained from ARMAX models selected by NPDP criterion for tests 1-4. The true value of each parameter is indicated by the horizontal lines in each plot.

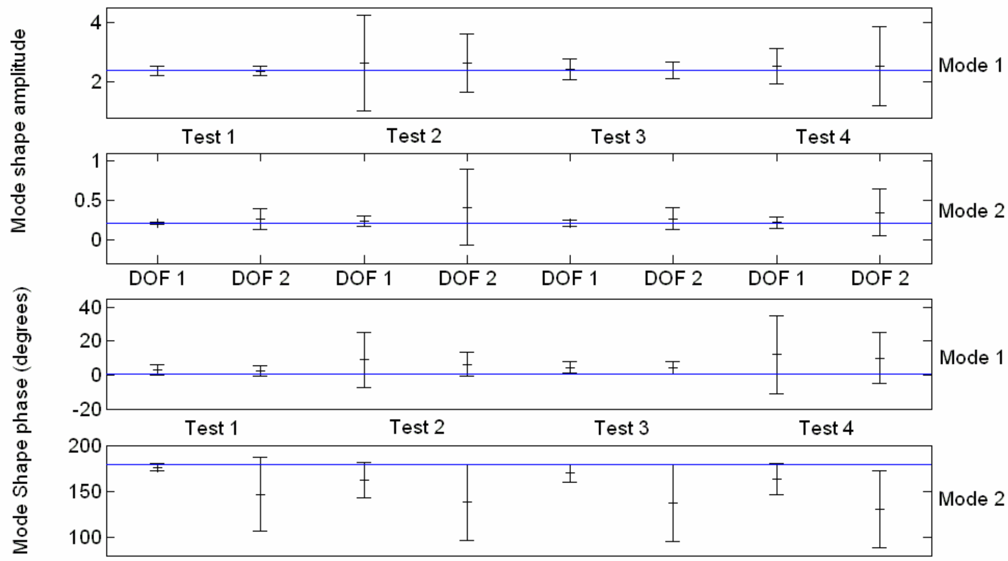

Figure 6.15 Mode shape amplitude and phase obtained from ARMAX models selected by NPDP criterion for tests 1-4. The true value of each parameter is indicated by the horizontal lines in each plot.

The results show that the ARMAX parameter estimation algorithm and NPDP model selection criterion achieve acceptable accuracy for the 4 noise cases presented here noting that reasonable results are estimated for each mode using at least one DOF as a reference.

6.2.3 Unmeasured Random and Periodic Excitation – 2DOF System 2

The ARMAX algorithm was also tested using simulated data from 2 DOF system 2 under noise conditions summarised in table 6.2, tests 5 - 8. System 2 exhibited modes separated by 0.345 Hz, and the unmeasured periodic noise used in tests 6 and 8 included a component at 2.50 Hz; 0.257 Hz below the first modal frequency. The number of models estimated was increased from 20 up to 30 for tests 6 and 8, which included unmeasured periodic excitation and unmeasured periodic and random excitation, respectively. Modal parameters estimated from tests 5 – 8 are summarised in figures 6.16 and 6.17. Similar to tests 1 – 4, modal frequencies for both modes are the most accurately estimated modal parameters but the closely spaced modes lead to more scatter in the results. Unmeasured periodic excitations used in tests 6 and 8 lead to greater uncertainty in modal frequencies estimated at DOF 1; the DOF where the unmeasured periodic excitation was applied, and also affect the mean frequency value estimated for mode 1 at DOF 1.

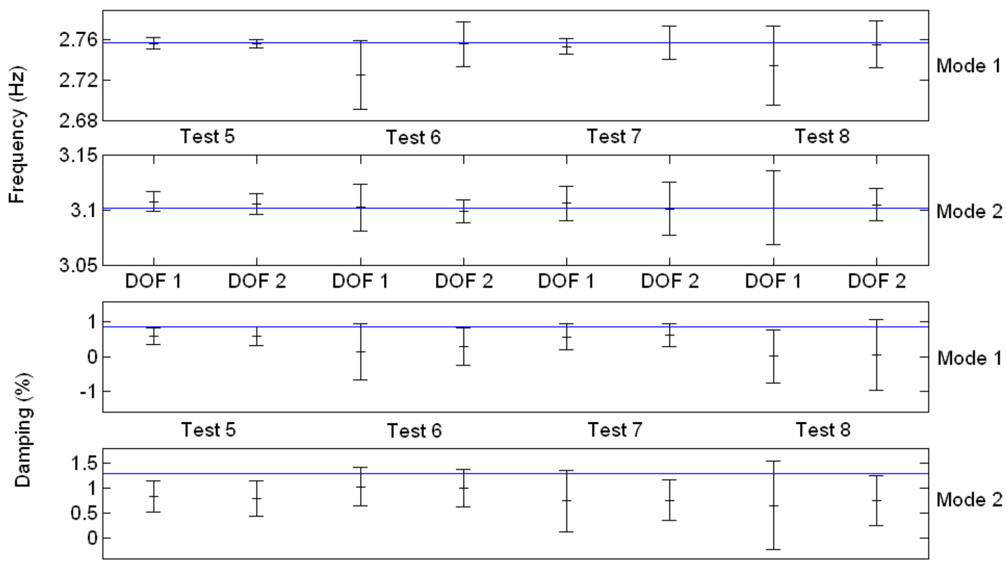

Figure 6.16 Modal frequency and damping obtained from ARMAX models selected by NPDP criterion for tests 5-8. The true value of each parameter is indicated by the horizontal lines in each plot.

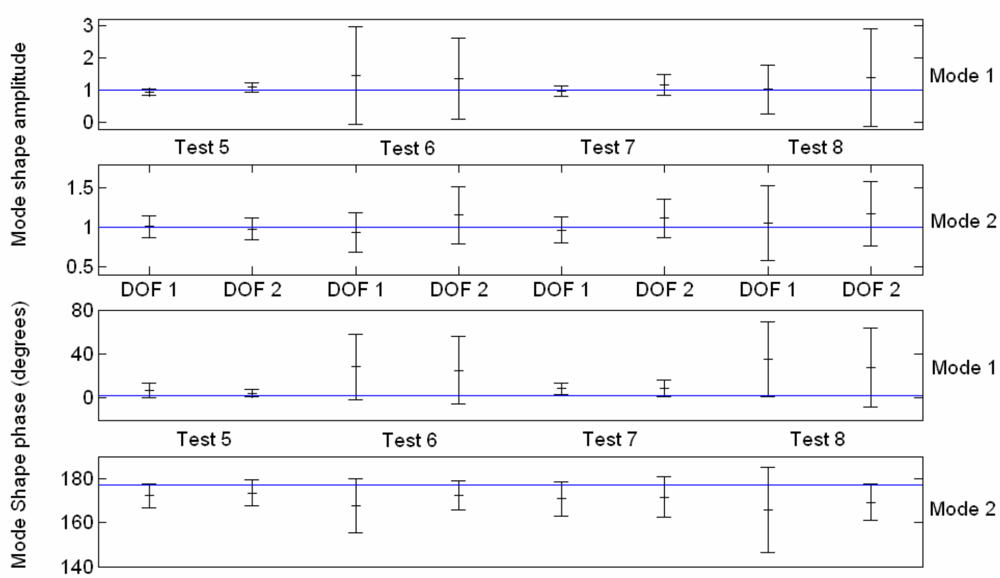

Figure 6.17 Mode shape amplitude and phase obtained from ARMAX models selected by NPDP criterion for tests 5-8. The true value of each parameter is indicated by the horizontal lines in each plot.

This pattern is also reflected in the estimates of the other modal parameters; unmeasured periodic excitations generally lead to poorer estimates. Results also show that the negative bias on the damping estimates due to noise is more evident for systems with closely spaced modes. Standard deviation results suggest mode shape estimates are quite sensitive to the unmeasured periodic excitation for this system. Overall, acceptable frequency and mode shape magnitude results are obtained for each mode using at least one DOF as reference.

6.2.4 Unmeasured Random and Periodic Excitation – 2DOF System 3

High levels of modal damping were imposed on system 3; 4.61% and 13.86% for modes 1 and 2, respectively. Figure 6.2 (c) shows that the response for mode 2 is relatively low amplitude, especially for DOF 2. The estimated modal parameters, plotted in figures 6.18 and 6.19 again show the increased uncertainty of results for increasing levels of unmeasured excitation. There is significant negative bias on damping estimates for mode 2 DOF 2, and it was noted that many models failed to identify mode 2 for the DOF 2 reference point. Mode 2 DOF 1 results are relatively good; however, there is still close to 50 % error for tests with unmeasured periodic excitations added. Mode shape results are of acceptable accuracy, but with higher standard deviations for mode 2 DOF 2.

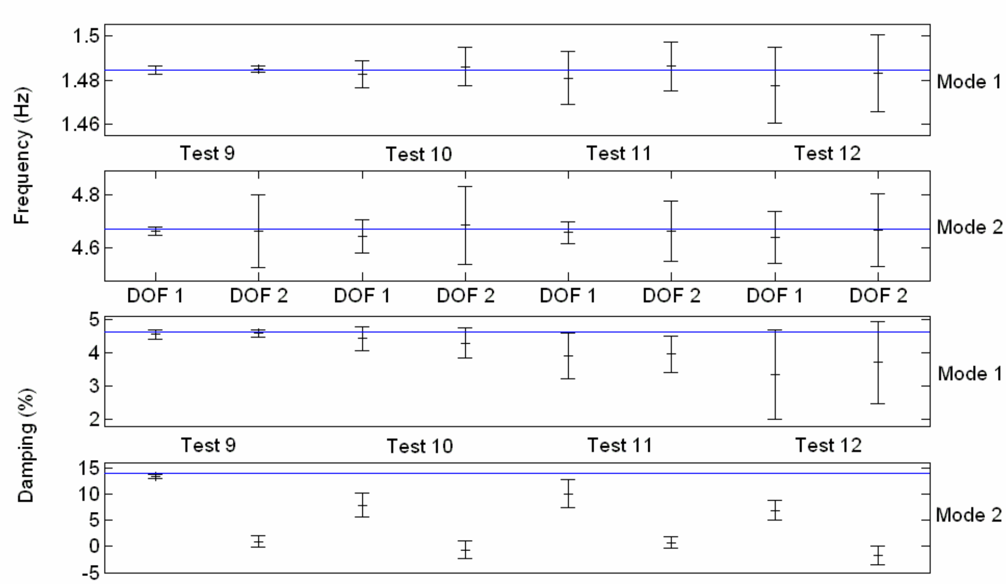

Figure 6.18 Modal frequency and damping obtained from ARMAX models selected by NPDP criterion for tests 9-12. The true value of each parameter is indicated by the horizontal lines in each plot.

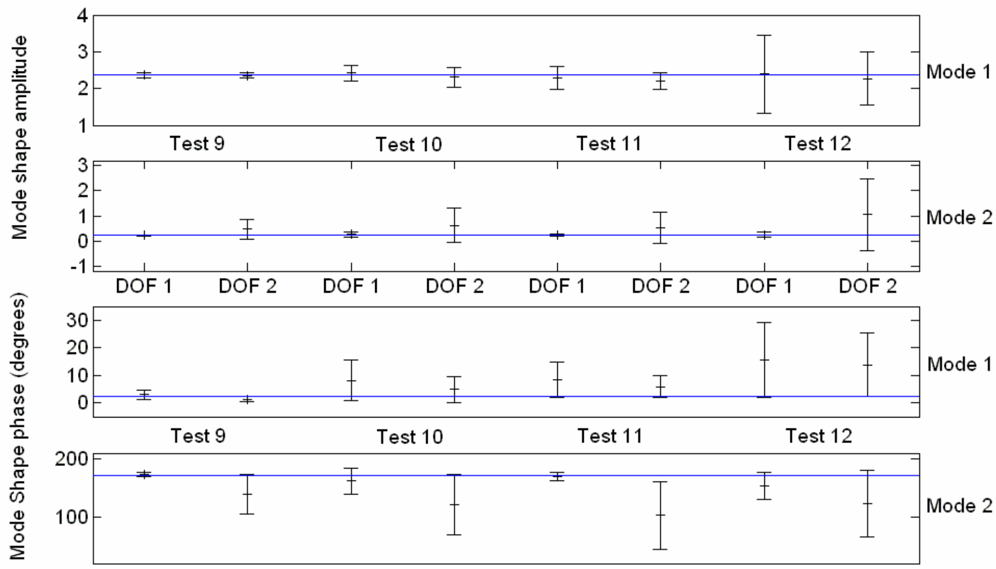

Figure 6.19 Mode shape amplitude and phase obtained from ARMAX models selected by NPDP criterion for tests 9-12. The true value of each parameter is indicated by the horizontal lines in each plot.

The results for tests 1 - 12 show that the ARMAX algorithm performs reasonably well for cases with unmeasured excitations. Higher model orders are required to account for the unmeasured excitations, particularly when they include periodic components. The importance of selecting measurement points with good vibration response is illustrated by the relatively poor results obtained for mode 2, DOF 2. Closely spaced modes and high levels of damping increase the sensitivity of the ARMAX algorithm to measurement noise and unmeasured excitations.

6.2.5 Effect of Data Record Length

The role of the length of the data record was discussed in section 5.3.1. Three sets of tests were carried out to investigate whether increasing the number of samples used for estimating ARMAX models resulted in improved accuracy of modal parameters.

The ARMAX estimation algorithm was used to estimate the modal parameters for 50 realisations of the data generated for each of the tests. Settings for the estimation algorithm were as follows:

- System 1 used to generate response data for random excitations;
- Sampling period 0.02 seconds;
- Record length:
    - Test 13: 10 seconds;
    - Test 14: 20 seconds;
    - Test 15: 40 seconds.
- 10% random noise added to the response measurements.
- $na = 4, 6, \ldots, 20$; $nb = na - 1$; $p = 5 \cdot na$; $nc = p - na$;
- Ten iterations of stages 3 and 4;
- Models were saved after stage 1 and each of the 10 iterations of stages 3 and 4 resulting in ninety-nine models being estimated for data realisation;
- NPDP criterion used for model selection.

The mean and standard deviations of the estimated modal parameters are shown in figures 6.20 and 6.21.

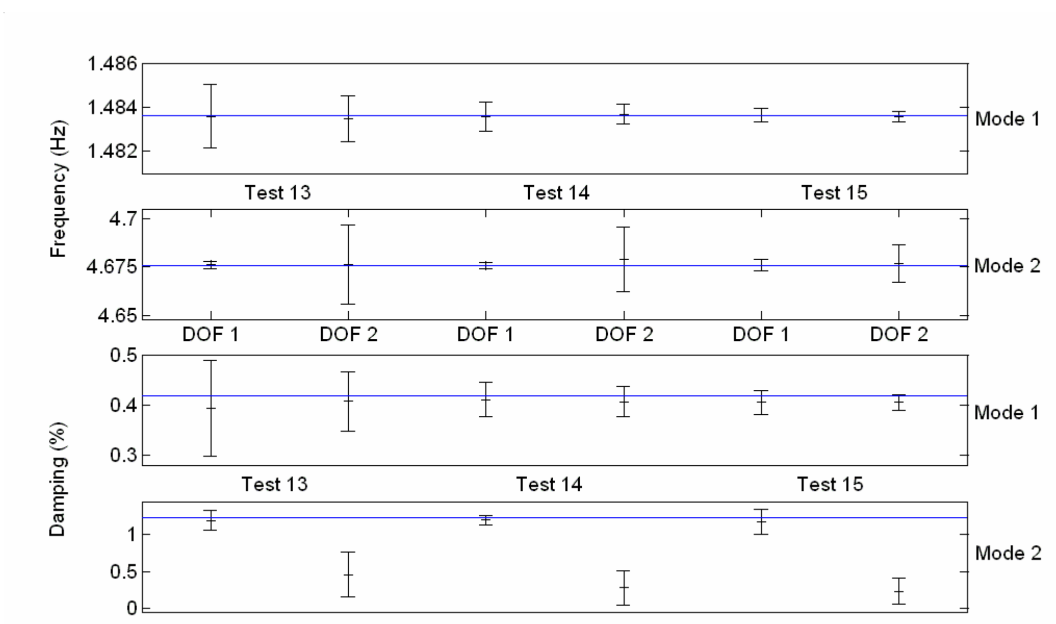

Figure 6.20 Modal frequency and damping obtained from ARMAX models selected by NPDP criterion for tests 13-15. The true value of each parameter is indicated by the horizontal lines in each plot.

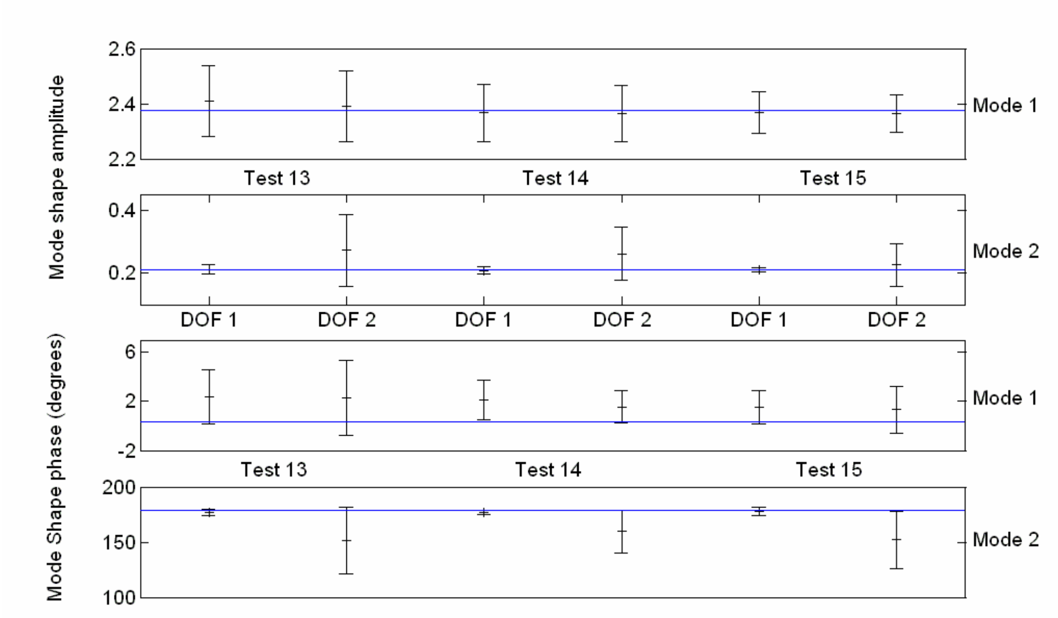

Figure 6.21 Mode shape amplitude and phase obtained from ARMAX models selected by NPDP criterion for tests 13-15. The true value of each parameter is indicated by the horizontal lines in each plot.

Improvement in the standard deviation of modal frequencies, damping, and mode shape amplitude and phase for mode 1 can be seen for increasing record length. This trend is not as evident in the results for mode 2; the poor results obtained for DOF 2 marginally improve for increasing record length. The results suggest that increasing record length is beneficial although this is accompanied by an increase in computational load. Ten seconds (500 samples) of data has been used for all other numerical tests because the mean value of modal parameters does not significantly improve for increased numbers of samples.

6.2.6 Effect of Sampling Rate

Specification of an appropriate sampling rate was discussed in section 5.4.1. Nine tests estimating modal parameters from data corrupted with random measurement noise were carried out to investigate the effect of sampling rate on the accuracy of estimated modal parameters and to verify that the sampling rate used for all other numerical tests (0.02 seconds) would not adversely affect the performance of the estimation algorithm.

The ARMAX estimation algorithm was used to estimate the modal parameters for 50 realisations of the data generated for each of the nine tests. Settings for the estimation algorithm were as follows:

- System 1 used to generate response data for random excitation;
- 10% random noise added to the response measurements;
- Sampling rate, record length, and the number of samples as listed in the table 6.3.
- $na = 4, 6, \ldots, 20$; $nb = na - 1$; $p = 5 \cdot na$; $nc = p - na$;
- Ten iterations of stages 3 and 4;
- Models were saved after stage 1 and each of the 10 iterations of stages 3 and 4 resulting in ninety-nine models being estimated for each set;
- NPDP criterion used for model selection.

Test	16	17	18	19	20	21	19a	20a	21a
Sampling Period (seconds)	0.1	0.05	0.025	1/80	1/160	1/320	1/80	1/160	1/320
Record Length (seconds)	50	25	12.5	6.25	3.125	1.5625	10	10	10
Number of Samples	500	500	500	500	500	500	800	1600	3200

Table 6.3 Sampling period, record length, and number of samples used for tests 16 – 21.

Tests 16 – 21 involved fixing the number of samples for increasing sampling frequency. As a consequence, the record length (in seconds) decreased for increasing sampling rate. Tests 19a, 20a, and 21a used the same sampling rate as for tests 19 – 21 and employed a fixed record length (in seconds), hence the number of samples in a record increased for increasing sampling frequency. It was therefore expected that the trend identified in tests 13 – 15, i.e. higher numbers of samples improve accuracy of modal parameters, would affect tests 19a – 21a.

Mean and standard deviation for estimated modal parameters are plotted in figures 6.22 and 6.23 for tests 19 – 21. Increasing frequency and damping standard deviation is observed for increased sampling rate, however, this trend is not reflected in the mode shape results, which are relativity insensitive to changes in sampling rate. The results of these tests do not allow the errors due to the estimation algorithm to be distinguished from the magnification of errors caused by the discrete-to-continuous transformation. According to literature [126] discussed in section 5.3.5, the error contributed by both will increase for higher sampling rates. It is also conceivable that the constant number of samples used lead to the increased standard deviations observed in frequency and damping results, due to the decreasing record length (in seconds). This argument is reinforced by the results in figures 6.24 and 6.25, which show estimated modal parameters for tests 19 – 21 and 19a – 21a. Increasing the record length (in seconds) appears to compensate for the decrease in accuracy observed in tests 19 – 21 for increasing sampling frequency. The results for tests 19a – 21a are reasonably consistent for increasing sampling frequency, although the accuracy of the frequency and damping obtained for DOF 2 show small decreases in accuracy for increasing sampling frequency.

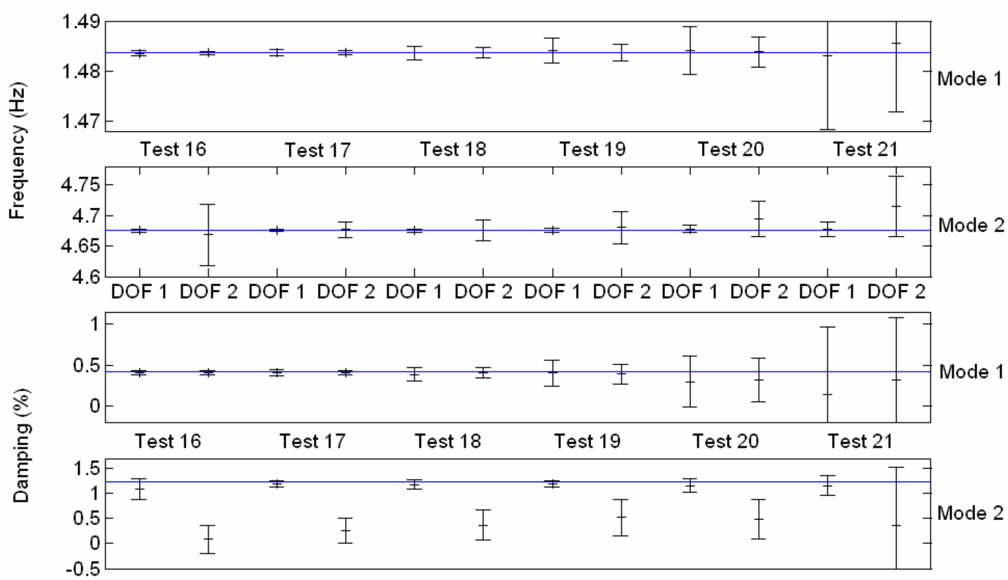

Figure 6.22 Modal frequency and damping obtained from ARMAX models selected by NPDP criterion for tests 16 - 21. The true value of each parameter is indicated by the horizontal lines in each plot.

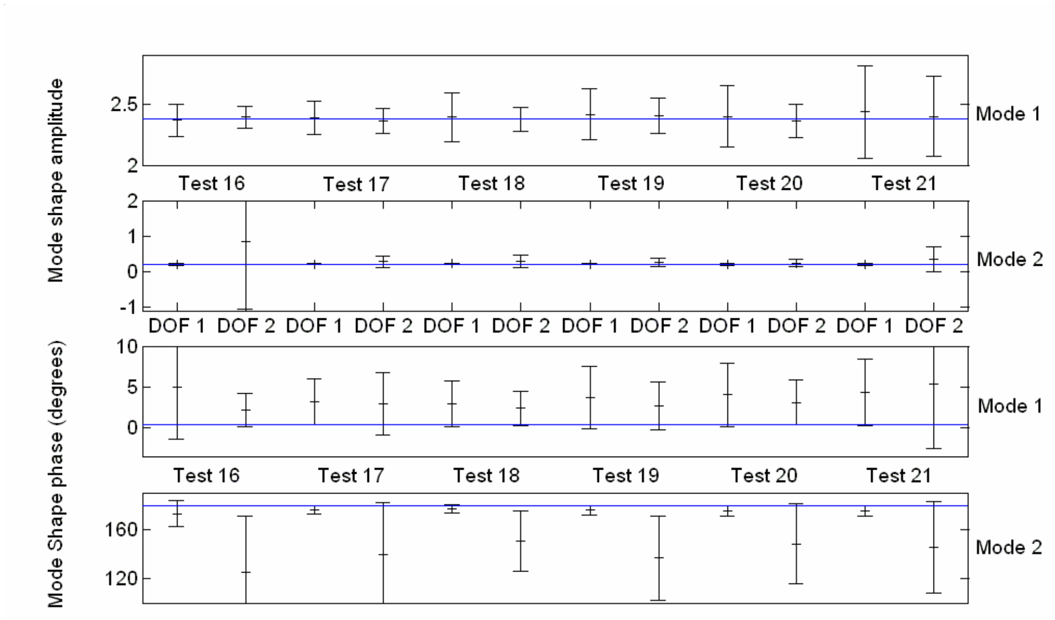

Figure 6.23 Mode shape amplitude and phase obtained from ARMAX models selected by NPDP criterion for tests 16 - 21. The true value of each parameter is indicated by the horizontal lines in each plot.

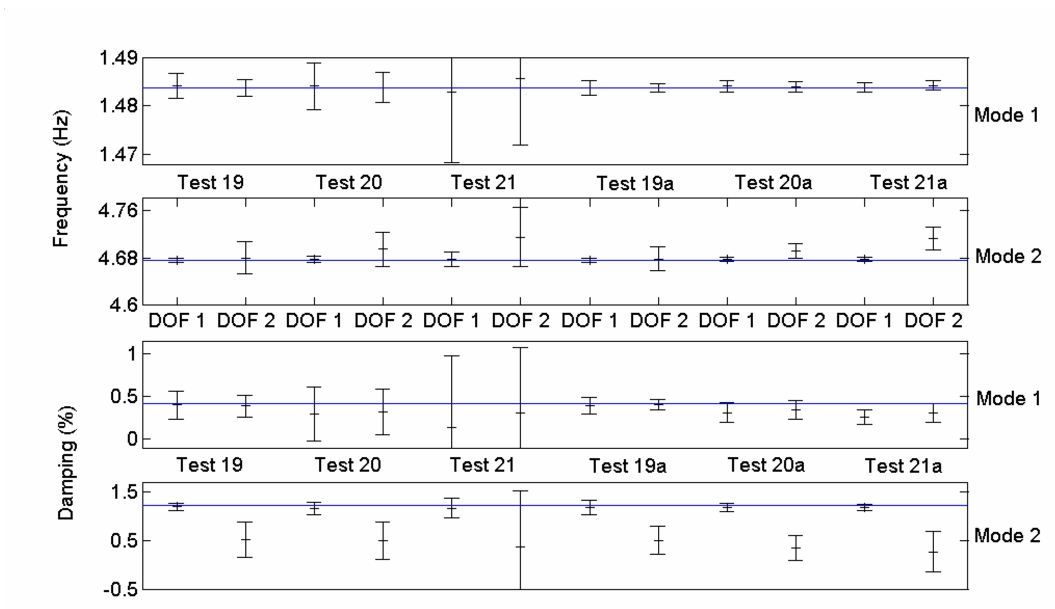

Figure 6.24 Modal frequency and damping obtained from ARMAX models selected by NPDP criterion for tests 19 - 21 & 19a - 21a. The true value of each parameter is indicated by the horizontal lines in each plot.

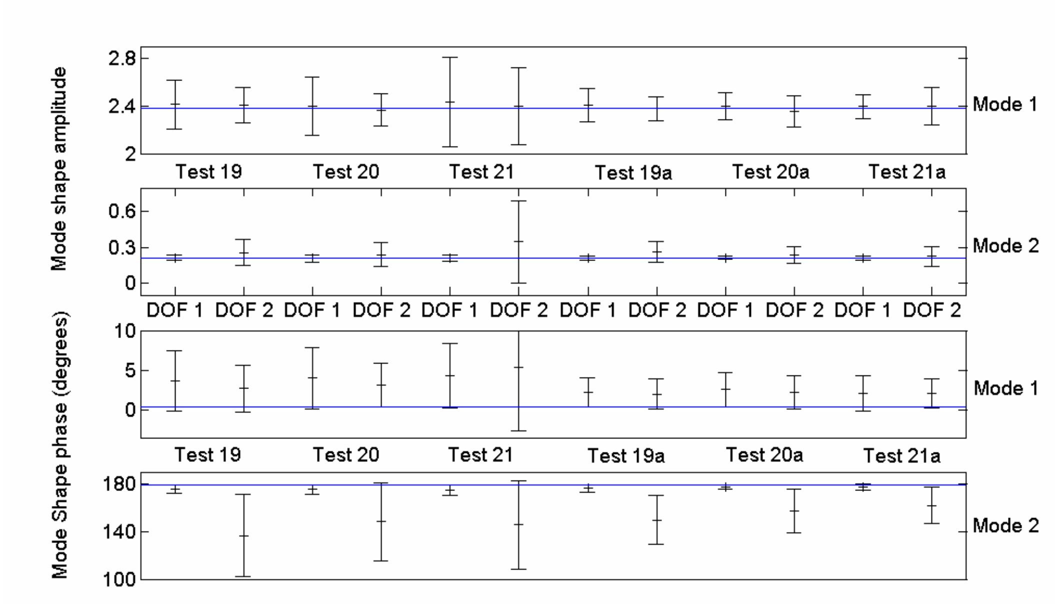

Figure 6.25 Mode shape amplitude and phase obtained from ARMAX models selected by NPDP criterion for tests 19 - 21 & 19a - 21a. The true value of each parameter is indicated by the horizontal lines in each plot.

The results of these tests suggest that the sampling frequency chosen for all other numerical tests (0.02 seconds) is a reasonable compromise between sampling frequency and record length and is sufficient for testing the performance of the ARMAX estimation algorithm.

6.2.7 Known Noise Properties

Results for tests 2, 4, 6, 8, 10, and 12 showed that the unmeasured periodic excitations affected the accuracy of the estimated modal parameters. The iteration of stages 3 and 4 is aimed at reducing the effect of unmeasured excitations and measurement noise; however, results show that often selected models include poles with frequencies close to those of unmeasured periodic excitations. In many practical situations the frequency of rotating components causing periodic excitations is known or can be measured accurately and this information can be used in the ARMAX estimation algorithm. The tests described in this section investigate whether this improves the accuracy of the modal parameters obtained from the ARMAX estimation algorithm.

Figure 6.26 displays poles of the AR matrix obtained from stage 1 of the ARMAX estimation algorithm, when processing data from test 2 (100% unmeasured periodic excitations at 1, 2, and 4 Hz and 10% random measurement noise).

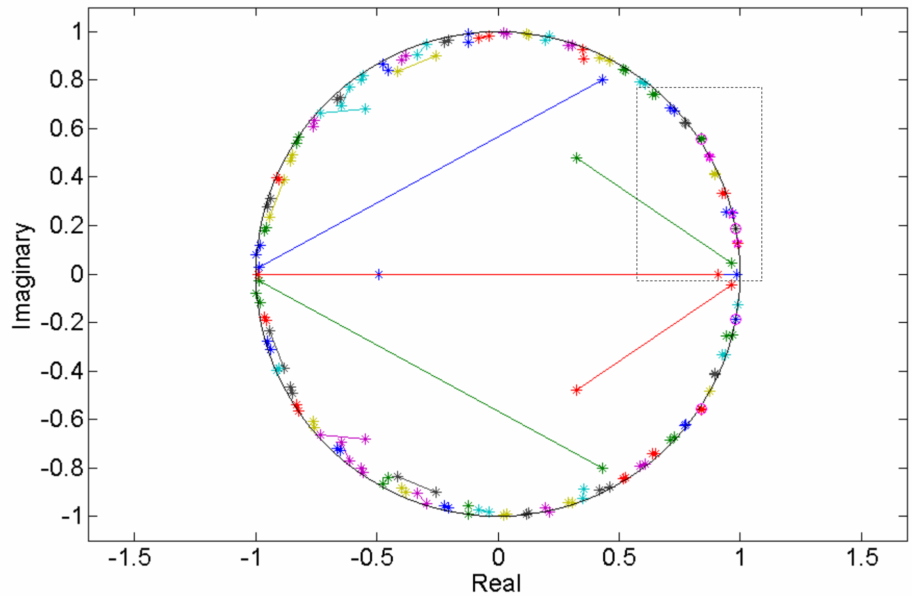

Figure 6.26 AR matrix poles of stage 1 ARX model estimated from test 2 data. The dashed rectangle indicates the area shown in figure 6.27.

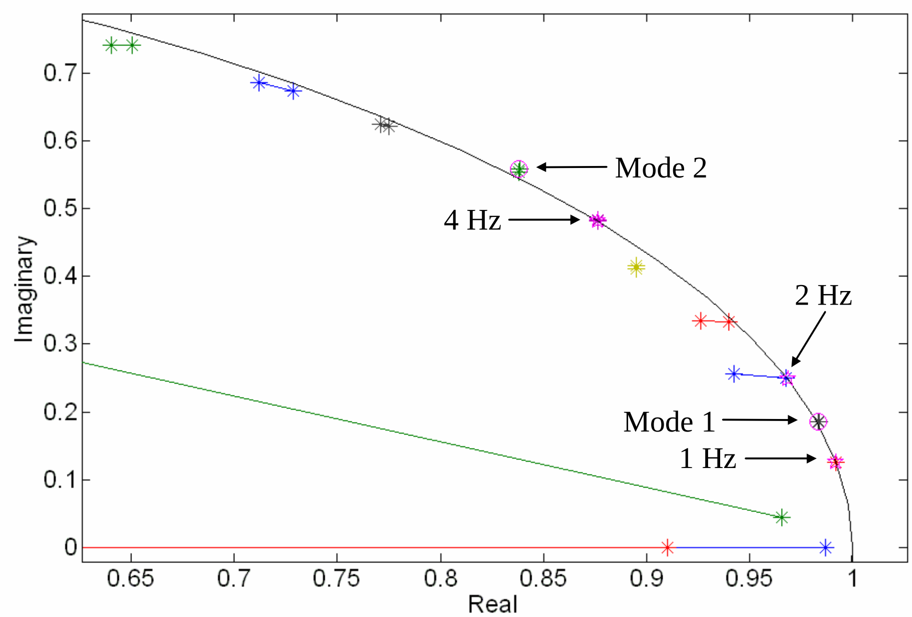

Figure 6.27 AR matrix poles of stage 1 ARX model estimated from test 2 data. This figure corresponds to the area enclosed by the dashed rectangle shown in figure 6.26.

Poles have been paired according to their proximity on the ***z***-plane and most of the poles are inside the unit circle (i.e. stable or positively damped). A subset of the poles is plotted in figure 6.27. The position of poles corresponding to modes 1 and 2 and also the unmeasured periodic excitations are marked and remaining poles correspond to noise components in the response signal. The poles corresponding to the noise components are inside the unit circle; the poles corresponding to the vibration modes are outside the unit circle (due to the ***backwards*** ARX model), but this is not always true for noisy data. The poles close to unmeasured periodic excitations are very close to the unit circle and can sometimes appear inside.

The iteration of stages 3 and 4 applies the MA matrix as a filter to the excitation and response data and this attenuates signal components that do not have a strong linear relationship (in terms of the ***q*** operator) with the excitation. Figure 6.28 shows zeros of the MA matrix FIR filter obtained from stage 4 after a number of iterations of stage 3 and 4, for the same set of data used to generate figures 6.26 and 6.27.

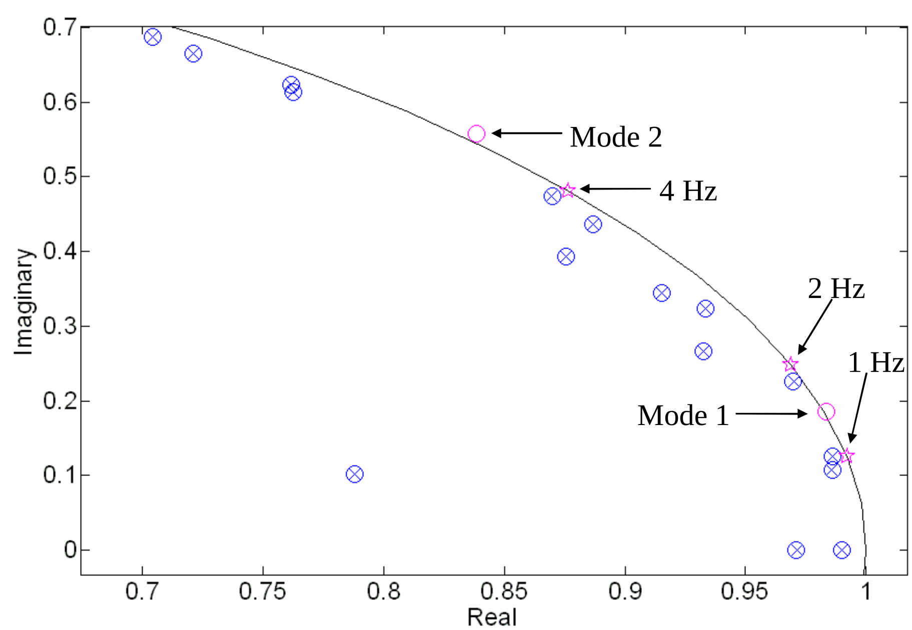

Figure 6.28 Zeros of MA matrix FIR filter estimated in stage 4 from test 2 data.

The MA matrix zeros are all inside the unit circle (i.e. the filter is stable) and there are zeros close to the poles corresponding to the unmeasured periodic excitations, which are marked. Note also that there are not any MA matrix zeros close to the vibration-mode poles. The fact that the MA matrix zeros are all inside the unit circle is a consequence of the backwards ARX model used in the estimation algorithm. As a result the MA matrix doesn't have to be stabilised, although this could easily be carried out because of the diagonal structure of the MA matrix.

Figure 6.29 shows the poles of the lower order AR matrix estimated in stage 3 after the excitation and response data has been filtered by the MA matrix. A subset of these poles is plotted in figure 6.30. All the spurious numerical poles are inside the unit circle (see figure 6.29) and there is one pole that is very close to the unit circle at approximately 4 Hz (figure 6.30). This corresponds to one component of the unmeasured periodic excitation, which the MA matrix did not successfully attenuate. Three of the four vibration mode poles are outside the unit circle (i.e. one pole for mode 2, figure 6.30, is inside the unit circle), which shows the effect of noisy measurements. The poles in figures 6.29 and 6.30 have been paired according to their proximity in the *z*-plane. Vibration modes are typically very close together, as are poles corresponding to unmeasured periodic excitations. The remaining poles are distributed around the unit circle and their positions vary, although this is not always true for high order models, which has been observed in the higher-order ARX model estimated in stage 1 of the algorithm.

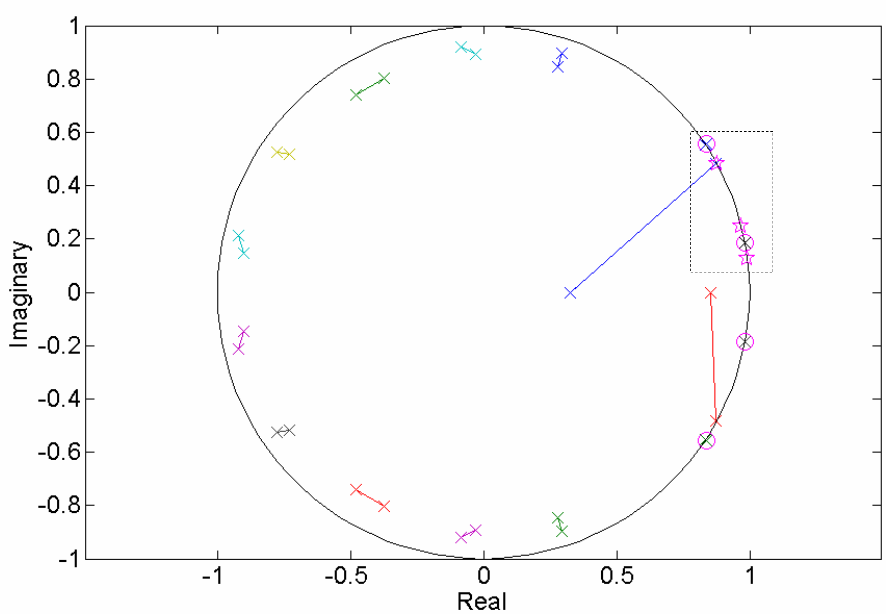

Figure 6.29 AR matrix poles of stage 3 ARX model estimated from test 2 data. The dashed rectangle indicates the area shown in figure 6.30.

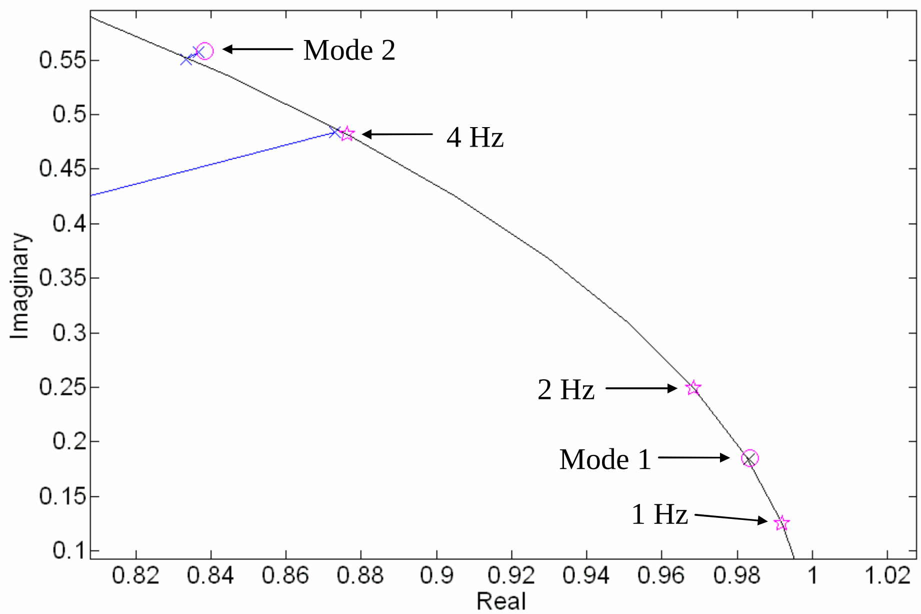

Figure 6.30 AR matrix poles of stage 3 ARX model estimated from test 2 data. This figure corresponds to the area enclosed by the dashed rectangle shown in figure 6.29.

Poles that correspond to the unmeasured periodic excitations will appear as peaks in the synthesised FRFs and can be mistaken for vibration modes. Figure 6.31 shows summed FRFs from the 50 ARMAX models estimated from test 2 data.

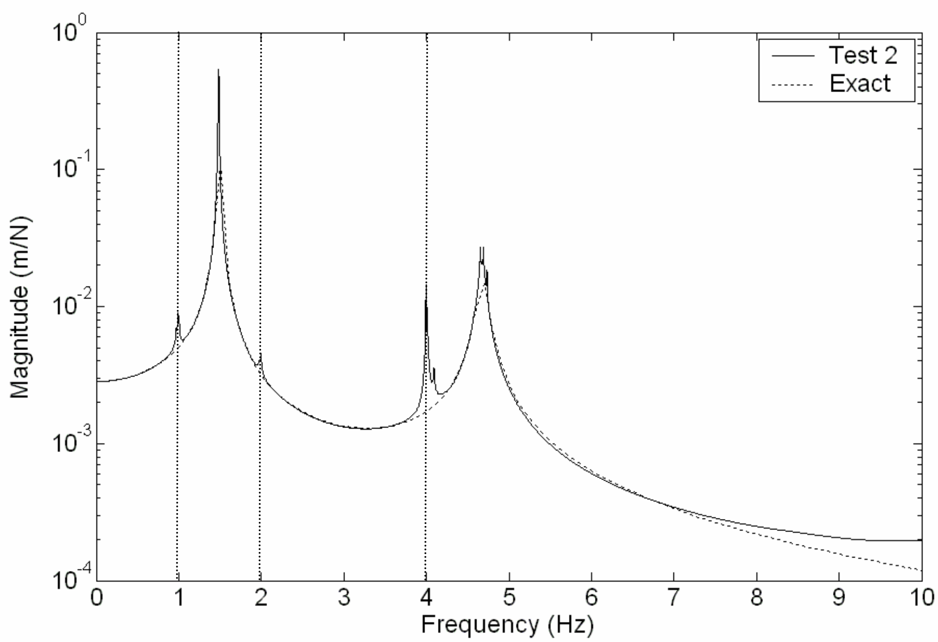

Figure 6.31 Averaged FRFs synthesised from the 50 ARMAX models estimated from realisations of test 2 data (Test 2), compared with averaged exact FRFs (Exact).

The two major peaks correspond to the two vibration modes at 1.48 Hz and 4.67 Hz. The three other peaks at 1, 2 and 4 Hz are due to the unmeasured periodic excitations. In practice, the modal parameters estimated at poles that do not correspond to structural modes will typically have negative damping. The frequency and damping results in table 6.4 were obtained from the 50 ARMAX models estimated from realisations of test 2 data. Many models did not identify any modes at these frequencies (see for example ~ 2 Hz, DOF 1), while some models identified modes at these frequencies with very small positively damping values.

Average Frequency		Average Damping	
DOF 1	DOF 2	DOF 1	DOF 2
0.988161	0.99658	-1.34075	-1.68461
-	1.987136	-	-0.60574
4.0129	4.007796	-0.29705	-0.64746

Table 6.4 Modal parameters identified at frequencies corresponding to unmeasured periodic excitations from test 2 data.

Prior knowledge of the frequencies of any unmeasured periodic excitations allows zeros of the MA matrix to be placed close to those frequencies and this can improve the attenuation of these components in the stage 3 estimation of a lower-order ARX model. Equation (5.50) is rewritten as

$$\mathbf{H}_{By}(k) = \sum \left(\left[\mathbf{C}(j) \cdot \mathbf{C}_{pn}(j) \right]^{-1} \mathbf{A}_B (k+1-j) \right), \quad j = max(1, k+1-(na+1)), \ldots, min(k, p-na) \tag{6.5}$$

where

$$\mathbf{C}_{pn}(q) = \prod_{i=1}^{r} \left(1 - \alpha (2 \cos o_i) q^{-1} + \alpha^2 q^{-2} \right), \tag{6.6}$$

$\mathbf{C}_{pn}(q)$ is a diagonal matrix polynomial describing the unmeasured periodic excitation and its form is taken from Fernandes et al [127]. r is the number of sinusoids in the unmeasured excitation; α is the damping factor; and o_i is the frequency of the sinusoid normalised by the sampling frequency. Equation (6.5) is solved by setting up a system of equations in terms of the unknown $\mathbf{C}^{-1}(q)$, which is of order nc - $2r$. Equation (6.6) describes a notch filter, and the damping factor sets the width of the notches.

The ARMAX estimation algorithm with a modified MA matrix, which included information about the unmeasured periodic excitations, was used to estimate the modal parameters for 50 realisations of the data generated under the conditions outlined in tests 2 and 3 above. Settings for the estimation algorithm are as follows:

- Test 22 used data simulated for conditions described for test 2:
  - 100% unmeasured periodic signals at 1, 2, & 4 Hz used to excite DOF 1 in addition to measured random excitation.
  - 10 % random noise added to each response measurement.
- Test 23 used data simulated for conditions described for test 4:
  - 100% unmeasured periodic signals at 1, 2, & 4 Hz used to excite DOF 1.
  - 20% unmeasured random noise applied to each DOF in addition to the measured random excitation applied to each DOF.
  - 10% random measurement noise added to the response measurements.
- $na = 4, 6, \ldots, 20$; $nb = na - 1$; $p = 5 \cdot na$;
- $nc = p - na - 6$;
- $o_1 = 1/50$; $o_2 = 2/50$; $o_3 = 4/50$;
- $\alpha = 0.999$;
- Ten iterations of stages 3 and 4;
- Models were saved after stage 1 and each of the 10 iterations of stages 3 and 4 resulting in ninety-nine models being estimated for each set;
- NPDP criterion used for model selection;
- Estimation algorithm applied to 50 independent realisations of the data for each test.

The damping factor for tests 22 and 23 was chosen based on a number of preliminary tests in which the damping factor α was varied from 0.90 to 0.9999. The damping factor resulted in a different notch width at different frequencies and the modified algorithm was found to be less effective for lower values of α, and also very high values. The value $\alpha = 0.999$ was found to yield the best results, which are plotted in figures 6.32 and 6.33. Also shown in the figures are the results estimated for tests 2 and 4, which estimated modal parameters from data generated under the same conditions as tests 22 and 23, respectively, using the standard ARMAX algorithm. The frequency and damping results obtained for the known noise algorithm (tests 22 and 23) are quite similar to those obtained by the standard ARMAX algorithm. There is a marginal improvement in the estimated mode shapes for the known-noise algorithm.

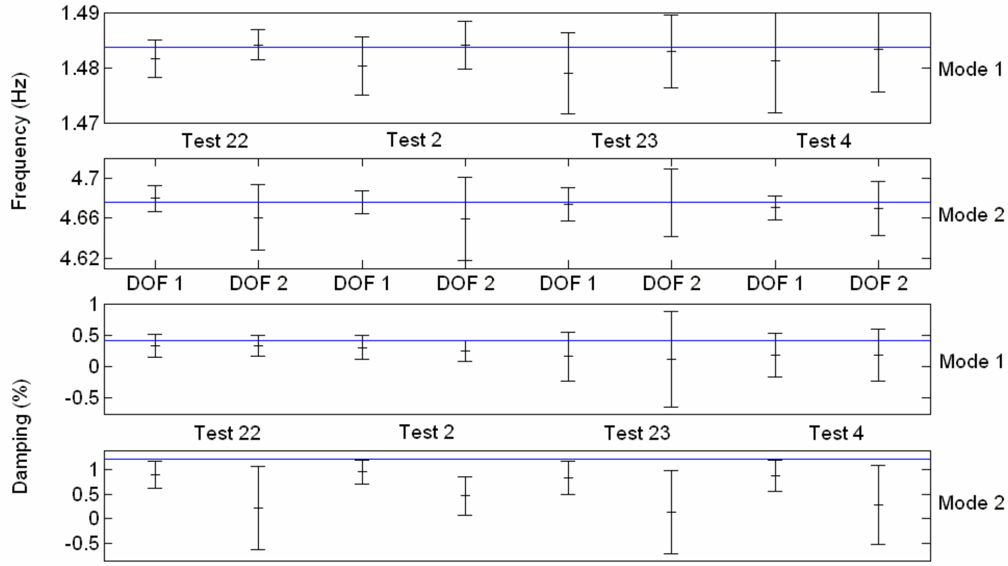

Figure 6.32 Modal frequency and damping obtained from ARMAX models selected by NPDP criterion for tests 2 and 4 (standard ARMAX algorithm) and tests 22 and 23 (known noise properties algorithm). The true value of each parameter is indicated by the horizontal lines in each plot.

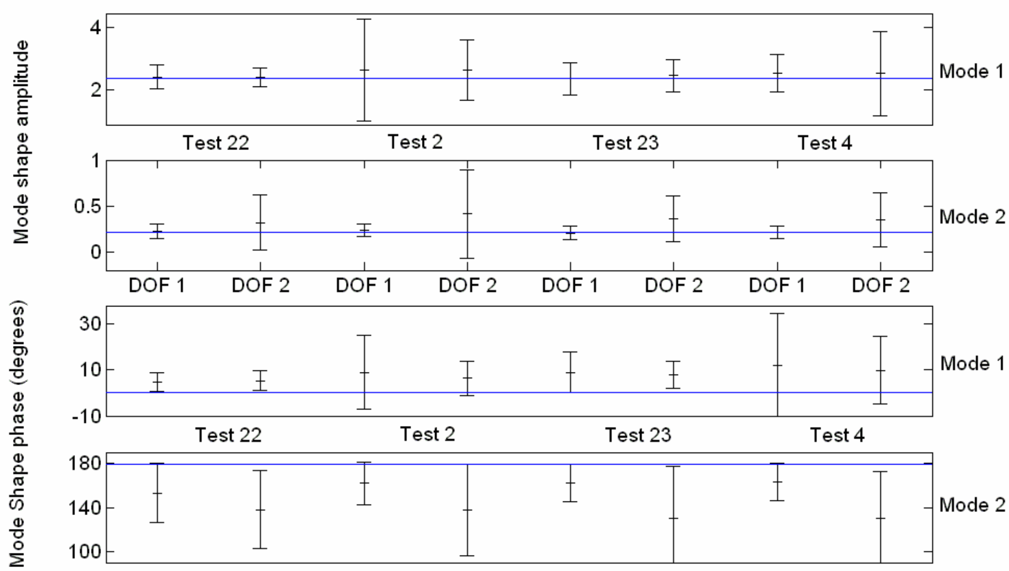

Figure 6.33 Mode shape magnitude and phase obtained from ARMAX models selected by NPDP criterion for tests 2 and 4 (standard ARMAX algorithm) and tests 22 and 23 (known noise properties algorithm). The true value of each parameter is indicated by the horizontal lines in each plot.

A potential benefit of the known noise algorithm is that it reduces the number of spurious modes corresponding to unmeasured periodic excitations. This is illustrated in figure 6.34, which plots the average FRFs from tests 2, 22, and the exact analytical results. Similarly, figure 6.35 is produced for tests 4 and 23.

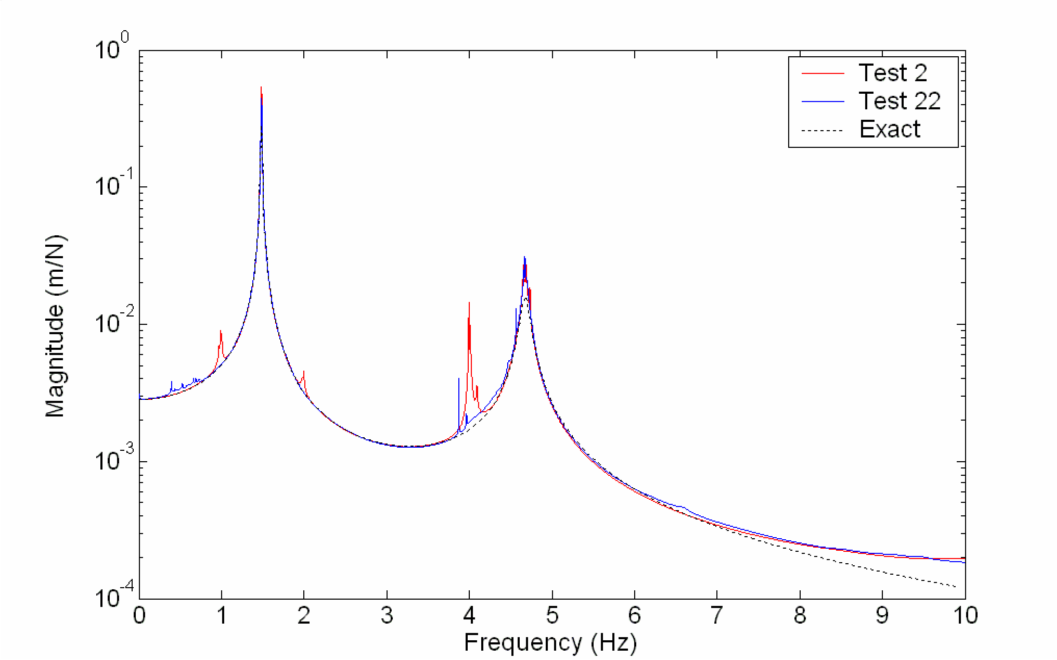

Figure 6.34 Averaged synthesised FRFs from tests 2 and 22, as well as the averaged exact FRFs.

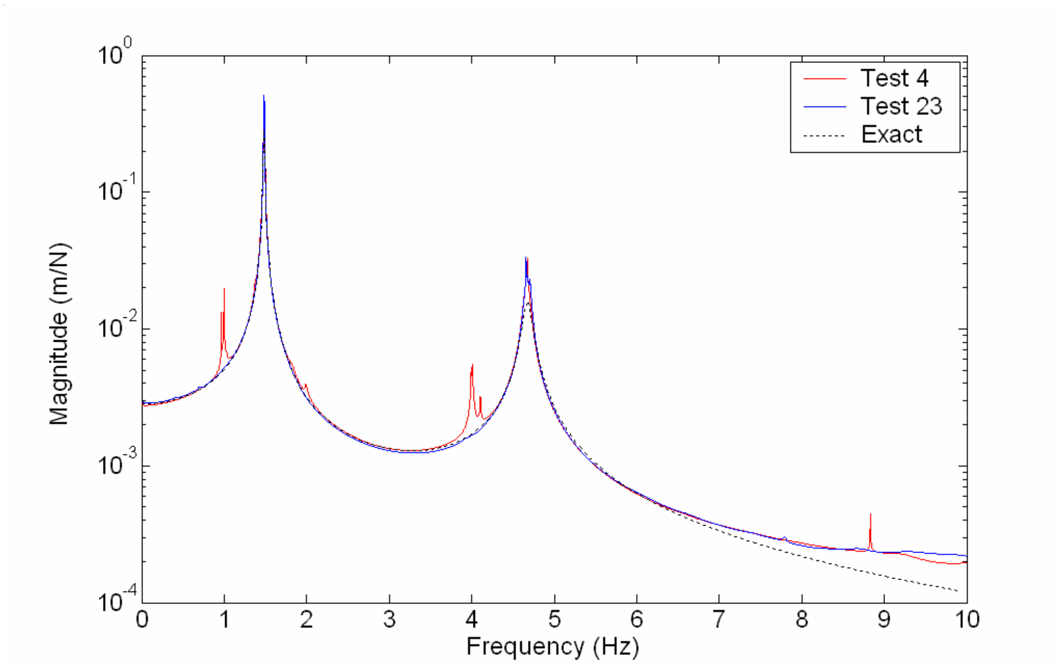

Figure 6.35 Averaged synthesised FRFs from tests 4 and 23, as well as the averaged exact FRFs.

The averaged FRFs for tests 22 and 23 clearly show that no modes are present at 1, 2 or 4 Hz, which is not the case for results obtained from tests 2 and 4. Therefore, the models with known noise properties would be more appropriate for prediction of the vibration response; however, the same results could be achieved by producing a reduced model from vibrational modes, as the spurious modes due to noise and unmeasured periodic components can be easily identified and removed, based on the sign of the estimated damping.

6.2.8 Conclusions from Numerical Tests

This section has described numerical tests carried out to assess the performance of the ARMAX estimation algorithm. Model selection criteria were investigated and the BIC and NPDP criteria were directly compared for a range of different noise conditions. Both criteria selected models with similar accuracy, although fewer instances of negative modal damping were present in NPDP-selected models. The NPDP also has the advantage that it can be calculated directly from the ARX parameters compared with the BIC, which requires recursive calculation of the innovations sequence using the estimated ARMAX model. The ARMAX algorithm successfully estimated modal parameters in the presence of measurement noise for each mode using at least one DOF as reference, although damping values were the least accurate. The sign of the damping was found to be useful in distinguishing vibration modes from numerical poles and provided an indication of the signal-to-noise ratio for each measurement point when comparing sets of estimated global parameters. Standard deviation of global parameters also reflected relative accuracy for each reference DOF. Unmeasured periodic and random excitations decreased the accuracy of modal parameters; however, modal parameters were still accurately estimated at DOFs with a high vibration response. The effect of data record length and sampling rate were investigated and results verified that a record length of 10 seconds and sampling rate of 50 Hz, used in all other tests, was appropriate for testing the performance of the ARMAX algorithm. The ARMAX estimation algorithm can be modified to account for unmeasured periodic excitation when the frequency of excitation is known. This modified algorithm yielded results of similar accuracy to the standard algorithm while preventing spurious modes corresponding to unmeasured periodic excitations being estimated.

6.3 Experimental Tests

Experiments were carried out on a cantilever beam to further test the performance of the ARMAX estimation algorithm. The experiments included unmeasured random and periodic excitation, and the use of piezoceramic plates for structural excitation was investigated in addition to the more typical method of using electromagnetic shakers for excitation.

6.3.1 Experiment 1: Single Input Using Electromagnetic Shaker

A 1000×50×6 mm aluminium beam was securely clamped to a heavy steel structure, with 125mm of the beam being constrained by rectangular steel bars as shown in figure 6.36. The aluminium beam was the same as that described in Chapter 4 before the piezoceramic actuators were bonded. A Brüel & Kjær (B&K) 4810 shaker was used to excite the beam at measurement point 5; the excitation signal was band-limited (0 – 1600 Hz) random noise amplified by a B&K 2706 power amplifier. The excitation force was measured using a B&K 8001 impedance head and acceleration measurements were made with four B&K 4374 accelerometers at 34 equally spaced points along the beam. B&K 2635 charge amplifiers were used for signal preconditioning: high-pass filter cut-off at 2 Hz, low-pass filter cut-off at 3 kHz. As the excitation point was fixed and response measurements were made at 34 points along the beam, 9 sets of SIMO data were used for modal analysis of the beam. A Hewlett-Packard 3566A FFT analyser was used for acquiring time records used by the ARMAX estimation algorithm and also for calculating averaged frequency response functions (FRFs), which were required for frequency domain curve fitting.

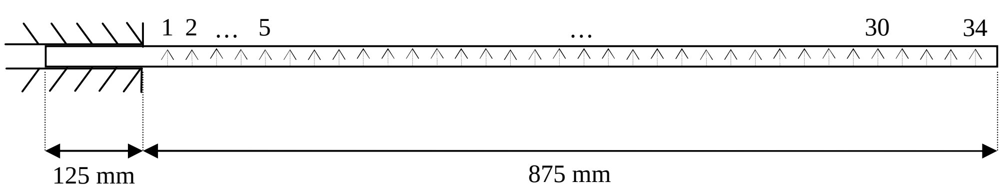

Figure 6.36 Diagram of cantilever beam showing positions of 34 equally-spaced measurement points. Excitation was applied at point 5 for experiment 1, and points 5 and 30 for experiment 2.

Modal parameters for the cantilever beam were first calculated using frequency-domain curve fitting available in the STAR Modal v5.23 software package from Spectral

Dynamics. A rational fraction least squares (RFLS) method was used to fit the FRFs and the results were used as a basis for comparison with the modal parameters obtained from the ARMAX algorithm and also least-squares estimated ARX models. FRFs over a frequency range of 0 – 1600 Hz and a resolution of 0.5 Hz were calculated from averaged time record data with 50 % overlap and scaled with a Hanning window. Up to 10 averages were used based on the quality of the FRF and coherence results for each measurement.

The ARMAX estimation algorithm used time record data sampled at 4096 Hz with 2048 samples for each record. One set of SIMO data was first used to estimate a large set of models of order $na = 40, 42, \ldots, 80$ and these results were then used to choose a smaller set of models that would yield acceptable results for all sets of SIMO data. The settings for the ARMAX estimation algorithm used to process all sets of data were as follows:

- $na = 60, \ldots, 80$, $nb = na$, $p = 5 \cdot na$, $nc = p - na$;
- Ten iterations of stages 3 and 4;
- NPDP criterion used for model selection.

Table 6.5 shows that modal frequencies estimated by FRF curve fitting and the ARMAX algorithm are within 1% of each other, except for the first mode. The poor results for the first mode are due to a number of factors. Firstly, the low response of the first mode, which was approximately 47 dB below the peak response in the FRF relating the response at the free end of the beam to the excitation point, is a consequence of the excitation location. Excitation of the transverse modes could be improved by moving the excitation point closer to the free end of the beam. The MIMO experiments discussed in the following section address this point by adding an additional shaker closer to the free end of the beam. The frequency resolution of 0.5 Hz in the FRFs was not ideal for identifying modal parameters at such low frequencies using the RFLS method, and similar problems arise in the ARMAX results, as the frequencies of the low order modes are small compared to the sampling frequency, which contributes to the poor accuracy [126]. Coupling between the shaker and the beam was indicated by peaks and troughs in the excitation power spectrum around modal frequencies, however, no other significant features were observed across the analysis frequency range.

	STAR Modal Results		ARMAX Results		Percentage Error		
Mode	Frequency (Hz)	Damping (%)	Frequency (Hz)	Damping (%)	Frequency (Hz)	Damping (%)	MAC (%)
1	5.76	-0.081	-	-	-	-	-
2	37.6	0.007	37.32	-	-0.748	-	6.94
3	106.06	0.299	105.94	0.137	-0.116	-54.16	97.26
4	207.19	0.114	206.98	0.199	-0.104	74.58	99.30
5	344.21	0.173	343.82	0.279	-0.114	60.95	99.78
6	511.85	0.194	511.91	0.235	0.011	20.88	98.71
7	731.73	0.343	733.36	0.323	0.222	-5.84	99.43
8	971.19	0.177	970.61	0.211	-0.060	19.41	99.36
9	1240	0.168	1242.81	0.135	0.227	-20.05	96.96
10	1550	0.260	1544.80	0.232	-0.336	-11.00	96.08

Table 6.5 Comparison of curve-fitted and ARMAX results estimated from experiment 1 data.

Differences are seen in damping results obtained from each estimation method and greater differences are seen at lower frequencies suggesting the influence of the sampling rate, but there is no clear higher or lower bias in the damping results. The RFLS results might not be accurate, because it could be argued that the frequency resolution is insufficient to accurately determine modal damping for the lower order modes. This is shown by the negative damping value estimated for mode 1 and the very low damping value of 0.007 % estimated for mode 2 by FRF curve fitting. The MAC values comparing mode shapes obtained from each estimation method are satisfactory for modes 3 to 10.

Least-squares estimation of SIMO ARX models was also carried out. A set of models of order p_{arx} = 5,6, …, 28 were estimated from 2048 samples of excitation and response data using the Matlab `idarx()`function. Since each data set included 4 response channels, a 4-dimensional ARX model was estimated for each data set, which lead to $2{\cdot}p_{arx}$ modes being estimated. Both the BIC and final prediction error (FPE) criterion [44] were used for model order selection. It was found that the BIC consistently selected models of order 5 – 8, which failed to identify many vibration modes. The FPE criterion typically selected models of order 25 – 28, which were found to be inaccurate due to the sensitivity of high-order multi-dimensional polynomial models to numerical operations. The problems with the ARX models were identified by pole-zero placement in the complex z-plane as well as FRFs synthesised from the estimated ARX models. In the absence of a numerical criterion for model selection, the highest order ARX model that did not suffer from obvious scattering of poles and zeros around the low and high frequency ranges of the unit circle (on the *z*-plane) was chosen. The subset of vibration modes was selected on the basis of peaks in synthesised FRFs.

Table 6.6 compares results from ARX models with FRF curve-fitted results. Similar to the ARMAX results, the ARX models failed to identify the first mode but frequency and mode shape results for modes 3 – 10 show very good agreement with the curve-fitted results: MAC values are above 98 % except for mode 4 (89%) which was affected by a small number of poorly estimated points. Damping results show reasonable agreement for modes 6 – 10, but much poorer results were estimated for modes 2 – 5.

	STAR Modal Results		ARX Results		Percentage Error		
Mode	Frequency (Hz)	Damping (%)	Frequency (Hz)	Damping (%)	Frequency (Hz)	Damping (%)	MAC (%)
1	5.76	-0.081	-	-	-	-	
2	37.6	0.007	37.68	4.3512	0.206	63794	3.40
3	106.06	0.299	105.86	0.0966	-0.192	-67.68	98.59
4	207.19	0.114	206.99	8.5857	-0.097	7432	89.74
5	344.21	0.173	343.33	1.8477	-0.256	965.9	99.41
6	511.85	0.194	511.82	0.1789	-0.007	-7.94	99.89
7	731.73	0.343	733.00	0.3587	0.174	4.57	99.62
8	971.19	0.177	970.91	0.1873	-0.029	5.85	99.94
9	1240	0.168	1242.6	0.1655	0.210	-1.70	99.33
10	1550	0.260	1545.1	0.2348	-0.318	-9.81	99.92

Table 6.6 Comparison of curve-fitted and ARX results estimated from experiment 1 data.

6.3.2 Experiment 2: Two Inputs Using Electromagnetic Shakers

A B&K 4809 shaker was added to the experimental apparatus described above, and excited the cantilever beam at point 30 using independent band limited (0 – 1600 Hz) random noise. A B&K 8200 force transducer measured the excitation force applied by the second shaker and a B&K 2635 charge amplifier was used for signal preconditioning with the same settings described in experiment 1.

	ARMAX Results		Percentage Error		MAC (%)	
Mode	Frequency (Hz)	Damping (%)	Frequency (Hz)	Damping (%)	Excitation Point 5	Excitation Point 30
1	-	-	-	-	-	-
2	39.22	0.430	4.309	6218	38.55	0.84
3	105.70	0.138	-0.339	-53.90	98.29	3.62
4	205.68	0.191	-0.730	67.91	98.51	98.33
5	341.66	0.144	-0.740	-16.76	99.40	99.51
6	509.50	0.191	-0.459	-1.97	99.57	99.57
7	735.88	0.188	0.567	-45.19	98.91	98.83
8	967.81	0.173	-0.348	-2.46	99.13	99.58
9	1233.1	0.204	-0.557	21.11	73.32	83.75
10	1531.4	0.494	-1.200	89.71	83.32	79.80

Table 6.7 Comparison of ARMAX results estimated from experiment 2 data with curve-fitted results from experiment 1 data.

The ARMAX algorithm was implemented as for experiment 1 to estimate the modal parameters from the sets of MIMO data. The results listed in table 6.7 show similar trends to those obtained from experiment 1 data: frequencies and mode shapes are quite similar for all except the low order modes; however, damping estimates differ significantly. The larger negative error of modal frequencies estimated by the ARMAX algorithm for experiment 2 data, compared to results from experiment 1 possibly reflect mass loading on the beam by the additional shaker. The fact that the first mode was not identified and the second mode was identified poorly in both experiments 1 and 2 suggests that the ARMAX algorithm cannot adequately estimate modes for such a large frequency range. Over eight octaves separate the first modal frequency and the Nyquist frequency. Other studies of time-series system identification methods applied to modal analysis have limited the analysis frequency range to 5 octaves or less [39, 56, 117]. An alternative strategy is therefore to apply the ARMAX estimation algorithm over limited frequency ranges using appropriately filtered and sampled data. A number of applications of the algorithm could be employed when considering dynamic behaviour over a wide frequency range.

An advantage of having multiple shakers, especially for large structures, is that excitation energy can be applied to the structure at different points to excite all modes. However, the use of two shakers to excite such a small structure in one direction resulted in mechanical coupling between the measured excitation signals, particularly around modal frequencies. It is typical to assume that excitation sources are completely independent when applying a MIMO modal parameter estimation technique and the results presented in this section demonstrate that the ARMAX algorithm achieves satisfactory accuracies (except for lower-order modes) even when this condition is not met. The ARMAX algorithm yields mode shape estimates for each excitation point and it is interesting to note that the MAC value for mode 3, excitation point 30 is quite poor and that point 30 is very close to a node for the third transverse mode. Slightly lower MAC values for modes 9 and 10 are due to poorly estimated residues at a small number of measurement points.

Further tests using three shakers for exciting the beam were carried out, in particular using the third shaker to impose an unmeasured excitation on the beam. It was found that the addition of the third shaker lead to coupling of excitation forces and that the shakers affected the dynamics of the cantilever beam. Hence, experiments using three measured sources of excitation and one additional unmeasured excitation were carried out using piezoceramic plates and are described in the next section.

6.3.3 Excitation Using Piezoceramic Plates

Experiments discussed in Chapter 2, and work reported in Chapter 4 investigated the use of piezoceramic plates for exciting structures and showed that FRFs calculated from the voltage applied to the piezoceramic plates and the acceleration response could be used to extract modal parameters. An advantage of using piezoceramic plates is that they can be bonded to the structure and do not significantly change the structure's dynamic characteristics if the dimensions of the plates are small compared to the structure under investigation. A disadvantage with using piezoceramic plates is that their ability to excite a particular vibration mode is related to the deflection of the mode shape where the piezoceramic patch is located. Modes that have little deflection are not effectively excited, as discussed in Chapter 4.

Four experiments were carried out to assess the performance of the ARMAX estimation algorithm for different types of unmeasured excitation. Three pairs of piezoceramic plates were used to excite the beam using independent band-limited (0-1600 Hz) random noise and a fourth pair of plates were used to impose unmeasured excitation on the beam. Figure 6.37 shows the apparatus used and the schematic shown in figure 4.7 shows detail of the actuator positions and applied voltages. The eight piezoceramic (PI

Ceramic, lead zirconate titanate (PZT), PIC 151) actuators, each 70×25×1 mm, were bonded to the aluminium beam used in the shaker experiments. The electrodes of the plates were on each major face and etch-primer was applied to coat the aluminium beam where the plates were bonded.

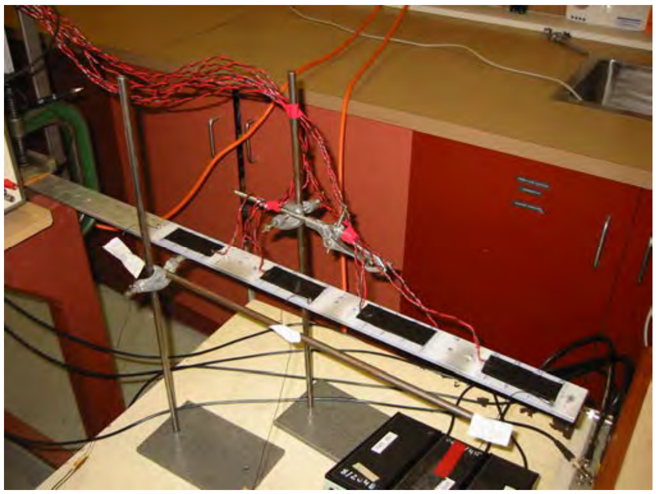

Figure 6.37 Cantilever aluminium beam with four pairs of piezoceramic actuators used for excitation. The top actuator of each pair is covered by black tape.

The plates were bonded to the beam with epoxy and a small piece of copper tape was used as a conductor to the bottom electrode of each plate. The combination of etch primer and epoxy formed an insulating layer between the piezoceramic plate and the aluminium beam. Excitation signals were amplified with a constant gain (0 – 1600 Hz frequency range) high-voltage amplifier and the typical peak-to-peak voltage applied to each plate was approximately 80 volts. The pairs of plates were connected in parallel with opposite polarity so that a distributed moment was applied between the ends of the plates. Note that applying the same polarity to each plate would result in axial excitation of the beam.

6.3.4 Experiment 3: Single Measured Input

This experiment was carried out to obtain a set of SIMO measurements for estimating the beam modal parameters using frequency-domain curve fitting. Band limited (0 – 1600 Hz) random excitation was applied to actuator pair 1 and response measurements were taken using 3 B&K 4374 accelerometers with signal preconditioning using B&K 2635 charge amplifiers as for the previous experiments. Response measurements were made at 34 points (as for experiments 1 and 2) along the aluminium beam resulting in

12 sets of SIMO data. The piezoceramic actuators applied a distributed moment to the beam and the voltage of the excitation signals fed into the voltage amplifier driving the actuators was recorded to represent this moment excitation. FRFs over a frequency band of 0 – 1600 Hz and with a resolution of 0.5 Hz were calculated using the HP3566A FFT analyser. A Hanning window and up to 10 averages (50% overlap) were used when calculated in the FRFs.

The modal parameters were estimated from the FRFs using a RFLS curve-fitting method. These results were used to assess the results obtained by the ARMAX estimation for MIMO sets of data obtained from experiments described below.

	STAR Modal Results Experiment 1		STAR Modal Results Experiment 3		Percentage Error		
Mode	Frequency (Hz)	Damping (%)	Frequency (Hz)	Damping (%)	Frequency (Hz)	Damping (%)	MAC (%)
1	5.76	-0.081	-	-	-	-	0
2	37.6	0.007	39.94	-0.163	6.223	-2497	88.36
3	106.06	0.299	106.57	0.451	0.481	51.01	98.89
4	207.19	0.114	210.64	0.317	1.665	178.51	97.68
5	344.21	0.173	350.06	0.329	1.700	89.99	99.06
6	511.85	0.194	520.92	0.270	1.772	38.88	99.65
7	731.73	0.343	729.26	0.559	-0.338	62.83	96.81
8	971.19	0.177	987.3	0.272	1.659	53.90	97.85
9	1240	0.168	1260	0.276	1.613	63.88	96.1
10	1550	0.260	1600	0.323	3.226	23.97	98.21

Table 6.8 Comparison of estimated modal parameters from curve-fitting of experiment 1 (electrodynamic shaker excitation) and experiment 3 (piezoceramic excitation) data.

Frequency results for modes 3 - 10 obtained from experiment 3, listed in table 6.8, are up to 3.3% different from those obtained from experiment 1 data and typically higher frequency, which is probably due to the mass loading of the electromagnetic shaker and the additional stiffness of the piezoceramic plates. Note that experiments 1 and 2 were carried out before the piezoceramic plates were bonded to the beam. Some differences in damping values are observed; values for experiment 3 were typically higher than those for experiment 1. These differences may be due to the additional damping imposed on the structure by the piezoceramic plates, but it is also conceivable that electromagnetic shakers used in experiments 1 and 2 may have introduced some damping to the system. Mode shapes are similar for modes 2 to 10. As discussed in Chapter 4, the piezoceramic plates apply a distributed moment between parallel edges of each plate and the action of a pair of plates as used for these experiments can be approximated by two point moments acting in opposing directions at the ends of the plates. This differs from the point force which is applied by an electromagnetic shaker. Because the piezoceramic plates apply a distributed moment, the ability of a pair of plates to excite a particular mode is related to the change in slope of the mode in the region of the piezoceramic plates. The effect of this is seen in the poor results obtained for experiment 3, modes 1 and 2 where there is not significant change in slope in the contact area of actuator pair 1. This is discussed further in section 6.3.6.

It should also be noted that the FRFs obtained from experiment 3 data have units $m.s^2/v$ instead of $m.s^2/N$, which are the units for FRFs in experiment 1 data. Mode shapes are normalised by the residue obtained at a particular measurement point, and this cancels out the differences in FRF scaling if the moment applied by the piezoceramic actuators is proportional to the applied voltage. MAC values in table 6.8 suggest good correlation between mode shapes obtained from shaker excitation and piezoceramic plate excitation. However, as noted above, MAC values are not affected by mode shape scaling. For the purpose of this work, the piezoceramic plates were considered acceptable for exciting modes 3 – 10 and therefore could be used to apply multiple sources of excitation to the cantilever beam without the difficulties associated with coupling relatively large electromagnetic shakers to the beam.

6.3.5 Experiment 4: Three Measured Inputs

Three independent sources of band-limited random excitation were applied to actuators pairs 1, 2 and 3. Twelve sets of 3-input, 3-output time signals were recorded using the HP3566A FFT analyser at a sampling frequency of 4096 Hz. The ARMAX estimation algorithm was used to estimate a large set of models for one set of data. From these results a smaller range of model orders could be specified when the ARMAX algorithm was used to estimate modal parameters from all sets of data, with the following settings:

- $na = 60, \ldots, 80$, $nb = na$, $p = 5 \cdot na$, $nc = p - na$;
- Ten iterations of stages 3 and 4;
- NPDP criterion used for model selection;

- Record length 2048 samples.

	ARMAX Results		Percentage Error		MAC (%)		
Mode	Frequency (Hz)	Damping (%)	Frequency (Hz)	Damping (%)	Actuator Pair 1	Actuator Pair 2	Actuator Pair 3
1	-	-	-	-	-	-	-
2	37.27	-	-6.686	-	29.26	5.93	27.74
3	106.13	0.168	-0.415	-62.80	5.29	1.03	1.53
4	209.87	0.281	-0.366	-11.43	21.62	60.43	27.46
5	349.63	0.161	-0.122	-51.21	97.64	90.85	64.43
6	521.38	0.186	0.089	-31.01	93.79	2.86	42.43
7	736.00	0.389	0.924	-30.43	98.47	98.36	97.73
8	986.31	0.229	-0.100	-15.80	98.59	97.53	98.68
9	1260.93	0.249	0.074	-9.72	94.89	95.26	94.74
10	1587.90	0.230	-0.756	-28.68	85.20	84.03	14.38

Table 6.9 Comparison of ARMAX results estimated from experiment 4 data with curve-fitted results from experiment 3 data.

Modal frequencies estimated by the ARMAX algorithm from experiment 4 data, listed in table 6.9, are similar to those identified by curve fitting experiment 3 data, except for the first two modes. Mode 1 is not identified by either method due to the limitations of the piezoceramic actuator pair, discussed above. Mode 2 results are also poor, and no positive damping values were identified for this mode. Damping values for all other modes are positive, however, comparison with curve-fitted results shows a negative bias on the ARMAX damping values. Numerical tests results suggested that negative bias of damping values resulted from noisy data. Three sets of mode shapes are estimated because three actuators were used to excite the structure but the ARMAX algorithm does not identify the first four mode shapes accurately. Given that the ARMAX algorithm yielded high MAC values for modes 3 – 10 using experiment 1 data (single input using shaker) and also experiment 2 data (two inputs using shaker excitation), these results suggest that resolving modes at low frequencies from data with a high sampling rate is more difficult when using this configuration of piezoceramic actuators. This limitation is important when considering the effect of unmeasured excitations, which is discussed below.

6.3.6 Experiments 5, 6 and 7: Three Measured Inputs with Unmeasured Periodic and Random Excitations.

These experiments used the same configuration as experiment 4 with the addition of unmeasured excitations applied by the 4th pair of piezoceramic actuators. The unmeasured excitations were not included in the data set used in the estimation of modal parameters. The RMS levels of the measured and unmeasured excitation signals and the resulting signal-to-noise ratios for each experiment are listed in table 6.10. Experiment 6 employed unmeasured periodic and random excitations and figure 6.38 shows the 1-sided power spectrum of the summed random excitations and the unmeasured excitations. The relative levels of the unmeasured periodic and random excitations can be seen in the lower part of the figure.

Experiment		Actuator Pair			
		1	2	3	4
5 • Unmeasured periodic excitation at 200, 500, 900, and 1200 Hz	RMS Level (volts)	0.6492	0.5103	0.4105	3.4471
	Noise Level 4/(1+2+3)	2.1956			
6 • Unmeasured periodic excitation at 200, 500, 900, and 1200 Hz. • Unmeasured random excitation	RMS Level (volts)	0.6468	0.5147	0.4159	3.2660
	Noise Level 4/(1+2+3)	2.0705			
7 • Unmeasured random excitation	RMS Level (volts)	0.6372	0.5203	0.4144	1.4087
	Noise Level 4/(1+2+3)	0.8962			

Table 6.10 RMS levels of un-amplified excitation signals applied to piezoceramic actuator pairs and resulting unmeasured excitation level for experiments 5, 6, and 7. Note that a fixed gain high voltage amplifier was used to drive the piezoceramic actuators.

The ARMAX algorithm was used to estimate modal parameters from the measured data as described for experiment 4. Estimated modal parameters from experiments 4-7 are compared with those obtained from experiment 3 in figures 6.39 – 6.43.

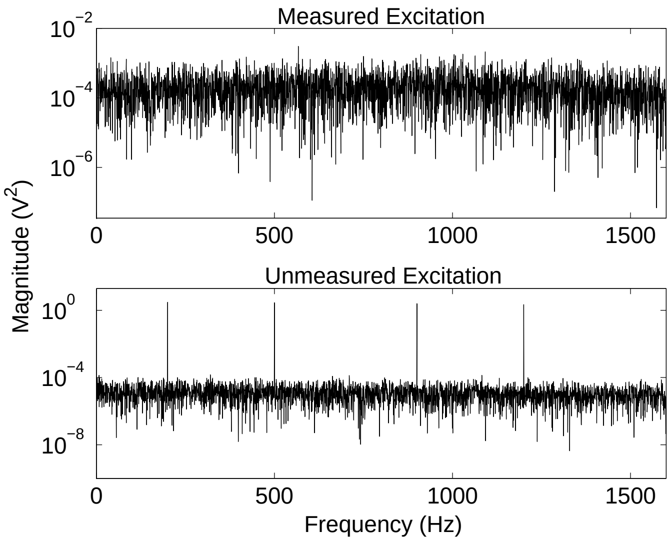

Figure 6.38 1-sided power spectra of excitation signals used in experiment 6. The top plot shows the power spectrum for the summed measured excitation. Bottom plot shows the power spectrum for the unmeasured periodic excitation.

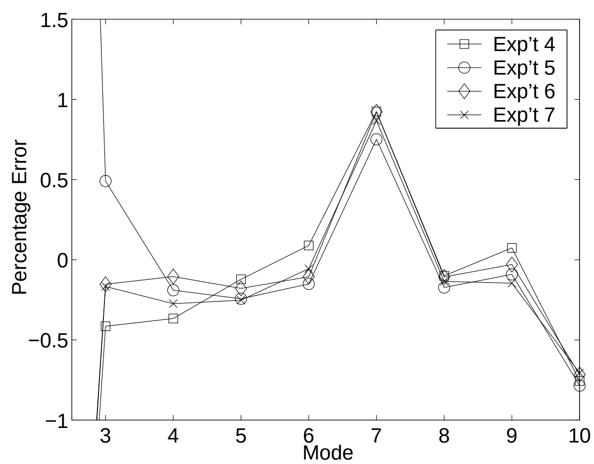

Figure 6.39 Modal frequency error for ARMAX results from experiments 4 – 7 compared to curve-fitted results for experiment 3.

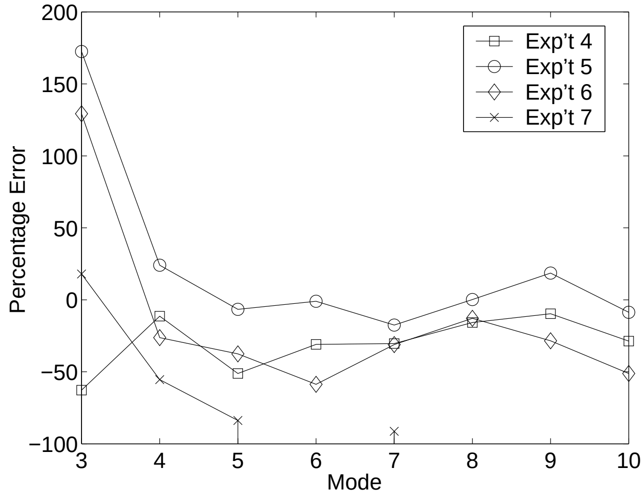

Figure 6.40 Modal damping error for ARMAX results from experiments 4 – 7 compared to curve-fitted results for experiment 3.

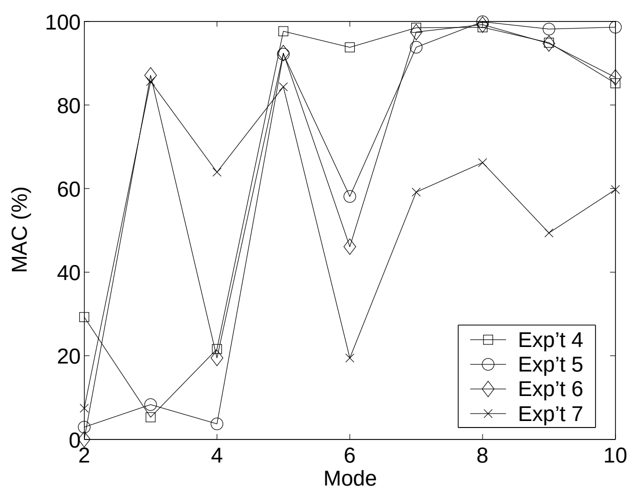

Figure 6.41 MAC comparing ARMAX mode shapes from experiments 4 – 7 (actuator pair 1) to curve-fitted mode shapes from experiment 3.

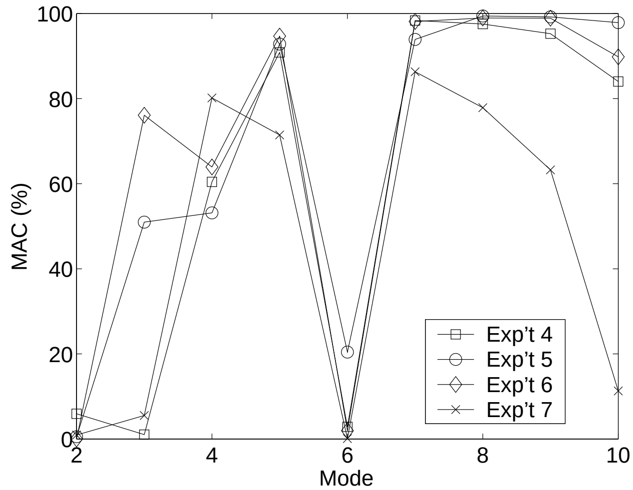

Figure 6.42 MAC comparing ARMAX mode shapes from experiments 4 – 7 (actuator pair 2) to curve-fitted mode shapes from experiment 3.

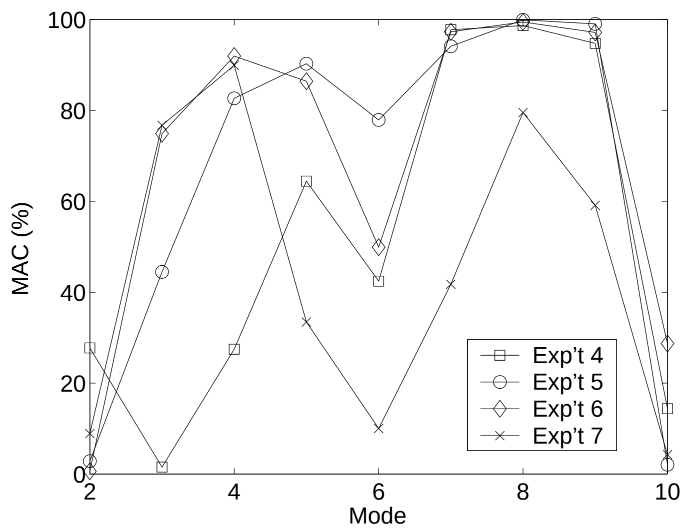

Figure 6.43 MAC comparing ARMAX mode shapes from experiments 4 – 7 (actuator pair 3) to curve-fitted mode shapes from experiment 3.

Comparison of ARMAX results for experiments 4, 5, 6 and 7 shows that the addition of unmeasured excitations has very little effect on the accuracy of estimated modal frequencies (see figure 6.39). Modal damping (figure 6.40) and mode shape results (figures 6.41 – 6.43) indicate that the unmeasured periodic excitation (test 5) and the unmeasured periodic and random excitation (test 6) only lead to a marginal decrease in accuracy although a clear trend is hard to identify. Modal damping and mode shape results for experiment 7 data are significantly less accurate; 5 of the ten modes were estimated with negative damping and mode shapes are quite poorly estimated. The nature of the unmeasured excitation is clearly important and the high levels of periodic excitation do not affect the accuracy of the ARMAX estimation algorithm. The ARMAX algorithm is much more sensitive to broad-band unmeasured excitations and results are unsatisfactory for unmeasured excitation levels approaching 100% of the measured excitation level.

The MAC values plotted in figures 6.41 – 6.43 further illustrate some of the limitations associated with using piezoceramic plates. The mode shapes for mode six, actuator pairs 1 and 2 (figures 6.41 and 6.42), are poorly identified for all tests and similarly for modes six and ten, actuator pair 3 (figure 6.43). This was found to be due to the location of actuators with respect to the deflection of the modes in question: the middle of actuator pairs 1, 2 and 3 were located at nodes of mode 6, and similarly, the middle of actuator three was very close to a node of mode 10 (cf. table 4.1 for analytical results). The piezoceramic actuators do not effectively excite these modes as shown by figure 4.8, which results in poorly estimated mode shapes. The ARMAX results from experiments 1 and 2 show that the ARMAX algorithm performs no worse for MIMO data than for SIMO data using electromagnetic shaker excitation. However, the ARMAX algorithm clearly has difficulty identifying mode shapes for a number of modes for noise-free data, compared to the curve fitted results using 1 pair of piezoceramic actuators. This suggests that multiple piezoceramic actuators may reduce the accuracy of some estimated mode shapes; however, MIMO data sets are still advantageous because of the multiple estimates of modal parameters.

ARX models were estimated from experiment 5, 6, and 7 data as for experiment 1 data, described in section 6.3.1. As with the ARMAX results discussed above, modal parameters from ARX models are compared with curve-fitted results from experiment 3 data. Modal frequency error is plotted in figure 6.44 and shows reasonable agreement for modes 3 – 10; however, frequency error is typically larger than ARMAX results shown in figure 6.39. The ARX models failed to identify the first mode and large errors were observed for frequency, damping and mode shape results for mode 2. Figure 6.45 shows that ARX models suffer from positive bias on damping estimates in the presence of unmeasured excitations. The actual damping estimates were often above 3%. The ARMAX algorithm incorporates estimation of backwards ARX models, which suffer from a negative bias on damping estimates but ARMAX damping estimates were typically under 1% for modes 3 – 10. MAC values indicate that the ARX models fail to adequately estimate mode shapes for a large number of modes. MAC results are generally worse than those obtained by the ARMAX algorithm (cf. figures 6.41 – 6.43). Note that both methods show poor results for mode six in experiments 5, 6 and 7. Mode six included anti-nodes in the contact area of actuators 1, 2, and 3, as discussed above.

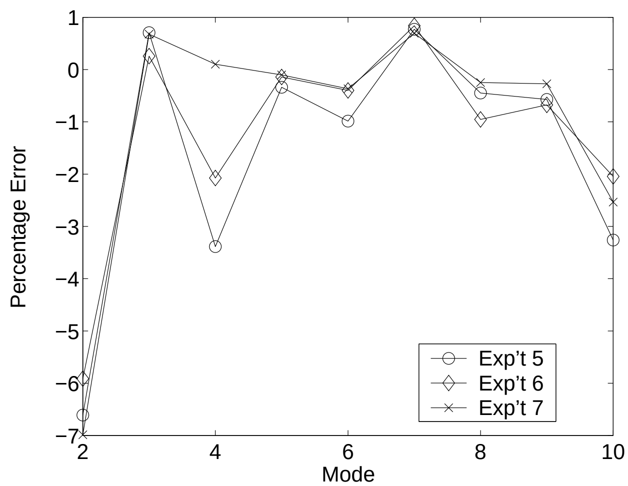

Figure 6.44 Modal frequency error for ARX results from experiments 5 – 7 compared to curve-fitted results for experiment 3.

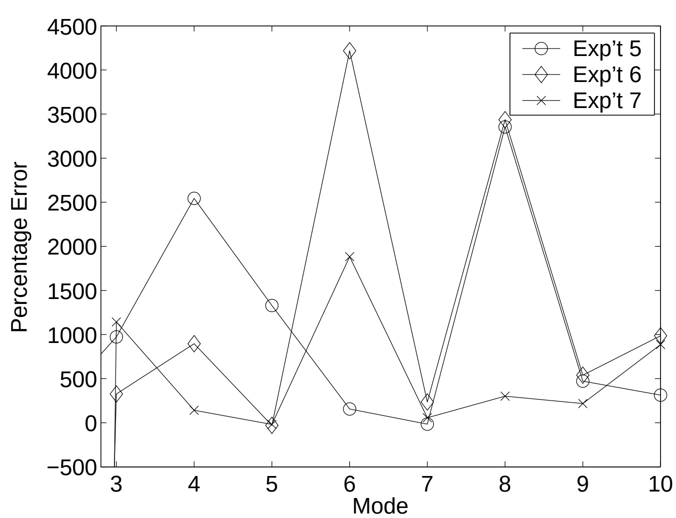

Figure 6.45 Modal damping error for ARX results from experiments 5 – 7 compared to curve-fitted results for experiment 3.

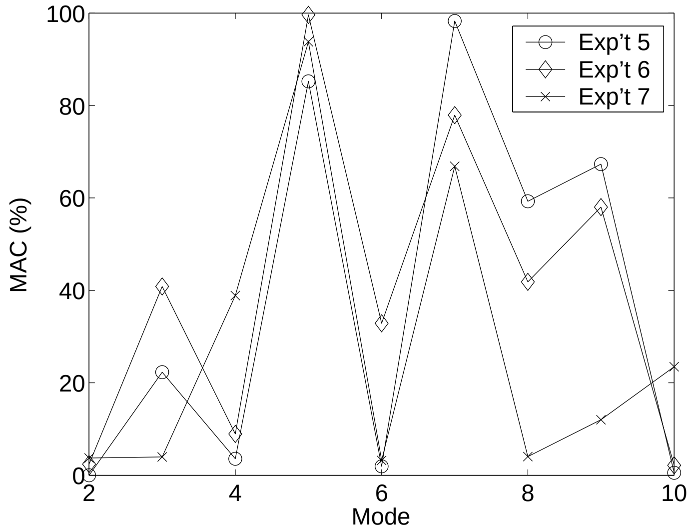

Figure 6.46 MAC comparing ARX mode shapes from experiments 5 – 7 (actuator pair 1) to curve-fitted mode shapes from experiment 3.

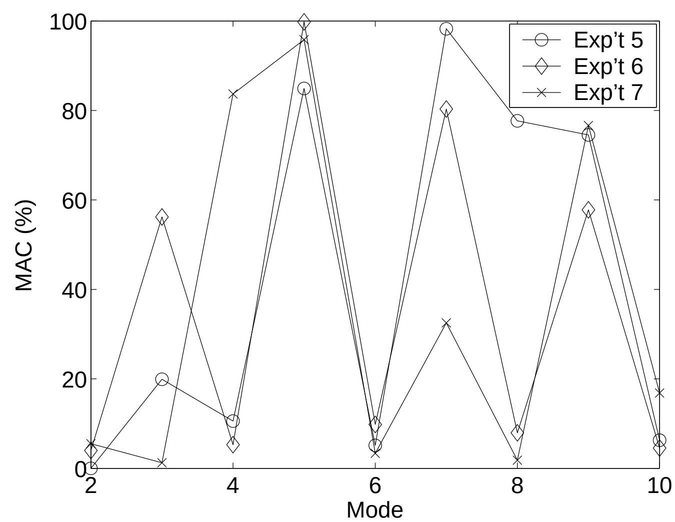

Figure 6.47 MAC comparing ARX mode shapes from experiments 5 – 7 (actuator pair 2) to curve-fitted mode shapes from experiment 3.

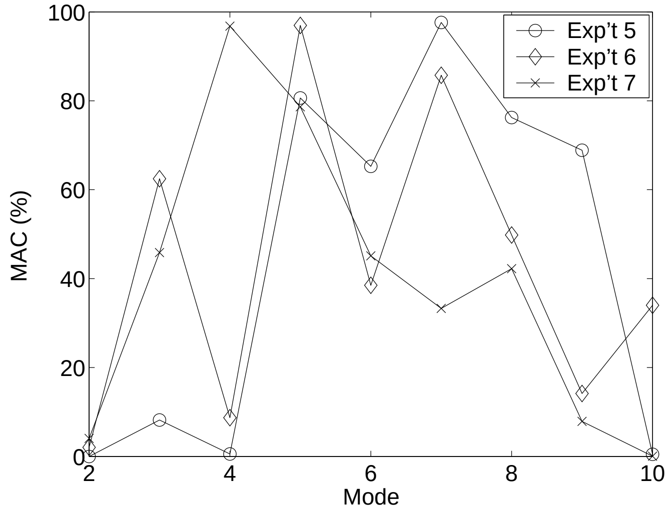

Figure 6.48 MAC comparing ARX mode shapes from experiments 5 – 7 (actuator pair 3) to curve-fitted mode shapes from experiment 3.

6.3.7 Discussion

The large frequency range considered in the experiments highlighted a number of limitations of the ARMAX algorithm. The high sampling frequency relative to the natural frequencies of the low order modes has contributed to the poor accuracy of low order modes in experiments described above. This is in addition to the limited ability of piezoceramic plates to excite low order modes. A further problem that arises when dealing with large frequency ranges or large numbers of modes in a frequency range is the order of the ARMAX model required to adequately describe the behaviour of the structure. Very large models are time-consuming to estimate, which is a problem for complex structures or if a large range of model orders are to be tested. In addition, larger models are required to accurately describe the noise or unmeasured excitations and the resulting high-order MA matrix filter can introduce numerical problems. A solution is to limit the order of the MA matrix, however, choosing the best order for the MA matrix requires estimating larger sets of models. Experience has shown that the accuracy of the modal parameters is only marginally sensitive to MA matrix order and limiting the frequency range of interest, hence the number of modes, is a reasonable approach as it addresses all the issues described above.

6.4 Conclusions

An algorithm to estimate modal parameters from excitation and response measurements obtained in the presence of unmeasured excitations was introduced in Chapter 5. The ARMAX estimation algorithm incorporates a model selection criterion based on the number of positively damped poles. The performance of the ARMAX estimation algorithm and model selection criterion was investigated using data simulating the behaviour of a two degree-of-freedom system as well as data obtained from experimental tests on a cantilever aluminium beam. Numerical test results demonstrated the effectiveness of the ARMAX algorithm in estimating modal parameters from data corrupted with 10% measurement noise, and also for cases where up to 100% unmeasured periodic excitations and 20% unmeasured random excitations were applied to the system. Accuracy of modal parameters decreased with increasing levels of unmeasured excitations, particularly for DOFs with a relatively low response. The ARMAX algorithm was more sensitive to noise and unmeasured excitations when estimating modal parameters of a simulated 2 DOF system with closely-spaced modes (separated by 0.345Hz), with a component of unmeasured periodic excitation 0.257Hz below the first modal frequency. Results for a highly damped 2 DOF system were also marginally less accurate than results for a lightly damped 2 DOF system.

Experimental results verified the operation of the ARMAX estimation algorithm for SIMO and MIMO data sets obtained using electrodynamic shakers for excitation and modal parameter results were found to compare well with those from FRF curve fitting, except for the first two modes. Tests using electrodynamic shakers for excitation reflected numerical test results, which showed that the ARMAX algorithm has difficulty identifying low frequency modes when data is sampled at a high sampling rate. Numerical tests indicated that increasing the data record length could compensate for this, but with an associated increase in computational load. Over eight octaves separated the first modal frequency and Nyquist frequency and results suggest that between four and five octaves is a more appropriate frequency range. Piezoceramic actuators were used for MIMO tests including unmeasured periodic and random excitation. The ability to excite different modes was observed to be related to the position of the actuator pairs and the delflection of a particular mode over the contact area of the piezoceramic plates. Up to 200% unmeasured periodic excitations did not significantly reduce the accuracy of the modal parameters estimated by the ARMAX estimation algorithm. Ninety percent unmeasured random excitations was observed to significantly reduce the capacity to accurately estimate modal damping and mode shapes. The ARMAX algorithm was found to yield more accurate modal parameters than ARX models estimated using the least-squares criterion in experiments that included unmeasured excitation.

The cantilever beam used for experimental tests was characterised by well-spaced transverse vibration modes with light damping. In addition, the unmeasured periodic excitations were at frequencies away from modal frequencies. In the following chapter, the ARMAX estimation algorithm is applied to a more complex structure, which includes closely spaced modes and unmeasured periodic excitations close to modal frequencies.

Chapter 7 ARMAX Modal Parameter Estimation in the Presence of Unmeasured Excitation: Experimental Case Study

7.1 Introduction

Experimental tests carried out on a cantilever aluminium beam, discussed in Chapter 6, demonstrated the performance of the ARMAX algorithm for estimating modal parameters in cases where there were unmeasured excitations. In this chapter, the ARMAX estimation algorithm is applied to a more complex structure—a helicopter-like structure, which includes closely spaced modes and modes with poor responses at some measurement locations. The effect of unmeasured periodic and random excitations is investigated with unmeasured periodic excitation frequencies close to the structure's natural frequencies. The performance of the ARMAX estimation algorithm is compared with the performance of a frequency domain RFLS curve fitting algorithm. In addition, periodic excitation and synchronous averaging, discussed in Chapter 2, is used as a means of improving signal-to-noise ratio (s/n) of measured time series data.

Details of the experimental apparatus are outlined in the following section. In section 7.3, the analysis of SIMO data using both the ARMAX and RFLS algorithms is described. Estimation of modal parameters in the presence of unmeasured excitation using the ARMAX algorithm is discussed in Section 7.4, and results are compared with those obtained from the RFLS algorithm in Section 7.5. A discussion of the coupling between excitation sources is contained in Section 7.6, and concluding remarks are made in Section 7.7.

7.2 Modal Analysis of Helicopter-Like Structure

The helicopter-like structure was suspended from a heavy steel frame using elastic cords to approximate free-free conditions. In this configuration, natural frequencies for the six rigid body modes were checked to be less than 10 Hz. Electromagnetic shakers were used to excite the structure: a single shaker was coupled to the tail boom of the structure for single-input experiments; a second shaker was coupled to the rotor-head area for two-input experiments. The experimental setup is shown in figure 7.1. Response measurements were taken at 30 points over the structure at positions indicated in figure 7.2. The set of axes in figure 7.2 show the global coordinate directions used for the analysis, and table 7.1 lists the position and direction of each measurement.

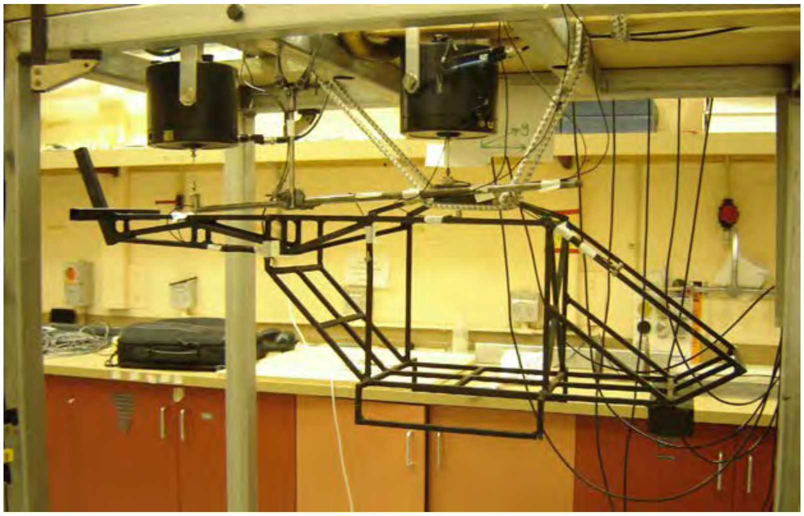

Figure 7.1 Helicopter-like structure suspended with elastic cord to approximate free-free conditions. Two shakers were used to excite the structure in this experiment.

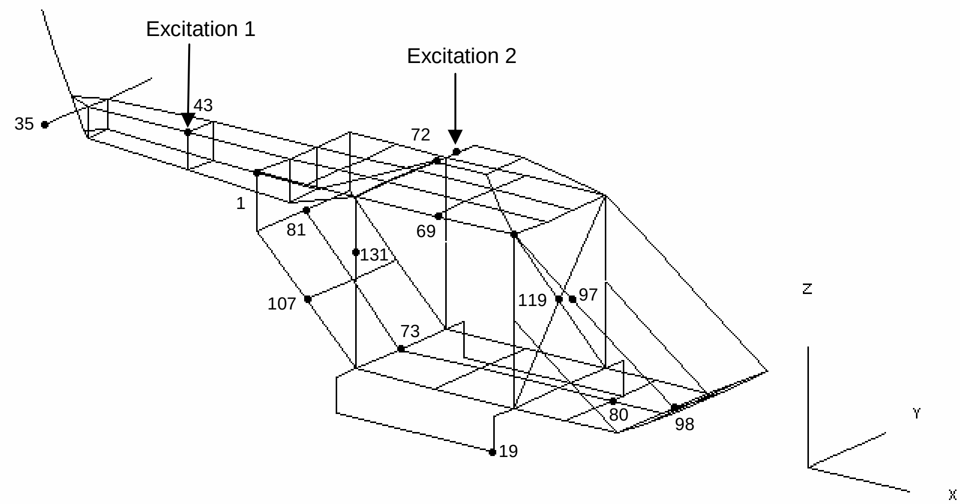

Figure 7.2 Helicopter-like structure excitation and measurement points.

Measurement Number	Coordinate	Measurement Number	Coordinate	Measurement Number	Coordinate
1	35 +z	11	72 -y	21	73 +z
2	35 +x	12	97 +z’	22	81 -x’
3	43 -y	13	97 -y’	23	81 +z’
4	1 -x	14	98 +x’	24	49 -y
5	1 -y	15	98 -z’	25	49 +z’
6	1 +z	16	98 -y’	26	131 -y
7	69 -y	17	19 +x	27	107 -y’
8	69 +z	18	19 -y	28	107 +z’
9	72 +z	19	19 -z	29	43 -z’
10	72 -x	20	80 +z	30	119 +x’

Table 7.1 Measurement coordinates for helicopter-like structure experiments. Coordinates marked with an apostrophe indicate a local set of axes rotated with respect to the axes shown in figure 7.2.

The experimental set up employed for this range of experiments was similar to that discussed in Chapters 2 and 3. The dynamic properties of the free-free helicopter structure included a number of difficult-to-measure characteristics including very lightly damped modes, closely spaced modes, as well as local modes, which had a limited response at some measurement points.

7.3 Single-Input Multiple-Output Experiments

The SIMO experiments were carried out to enable an initial comparison between frequency domain curve fitting and the ARMAX estimation algorithm under conditions of minimal noise. A Hewlett Packard 3566A 8 channel FFT analyser was used for data acquisition, calculation of spectral data (FRFs, coherence, auto- and cross-spectral densities), and as a signal generator for band-limited random noise. Response measurements were made with B&K 4374 and 4393 accelerometers and the acceleration and applied force at the excitation point was measured by a B&K 8001 impedance head. B&K 2635, 2626, and 2650 charge amplifiers conditioned the excitation and response signals with high-pass (2 or 3 Hz) and low-pass (1 kHz) filtering. A B&K 2706 power amplifier was used to drive a B&K 4809 electrodynamic shaker, which was securely clamped to the heavy steel structure supporting the helicopter-like structure. Continuous random excitation was applied to the tail boom of the helicopter-like structure at the position indicated by ‘Excitation 1’ in figure 7.2. Six sets of 5 or 6 response measurements were made, which included one fixed reference measurement point (to allow data to be used for response-only modal analysis) at point 43 –z. 180 seconds of time series data were measured. The shaker constrained the structure in the ***x-y*** plane, and to a lesser extent in the ***z*** direction.

7.3.1 Modal Parameter Estimation by FRF Curve Fitting

The STAR Modal software estimated modal parameters of the helicopter-like structure using a rational fraction least squares (RFLS) method to model the measured FRFs. FRFs were calculated from time series data under the following conditions: f_s = 1024Hz; frequency range 0 – 400Hz; Δf = 0.5Hz; Hanning window applied to segments of time record with 66% overlap; 20 averages. A global implementation of the RFLS technique was used, which first calculated an estimate of the frequency and damping values from all FRFs, and then used these frequency and damping values when calculating modal residues. A key part of this curve fitting technique is the identification of frequency bands containing resonant peaks. Examination of the measured FRFs and the averaged, squared imaginary part of all FRFs helped identify modal peaks and appropriate frequency bands required by the fitting process. Knowledge of the modal frequencies from experiments described in Chapters 2 and 3 helped verify the presence of modes; however, a more thorough analysis identified extra modes in this case study. The different boundary conditions applied to the structure and shakers are likely to have affected the dynamic properties. A plot of the squared, averaged imaginary part of the FRFs is shown in figure 7.3.

Figure 7.3 shows that there are a number of closely spaced sets of modes, for example around 75, 160, 280, and 315Hz. The lower peaks, for example around 113Hz and 185Hz represent modes with a low response at many of the measurement points. Results from RFLS curve fitting are compared with those obtained from the ARMAX algorithm in Section 7.3.3. It should be noted that another curve fitting algorithm included in the STAR Modal software was used to verify the RFLS results. The second algorithm was based on the Polyreference Time Domain Method. No significant difference was observed in the estimated modal parameters.

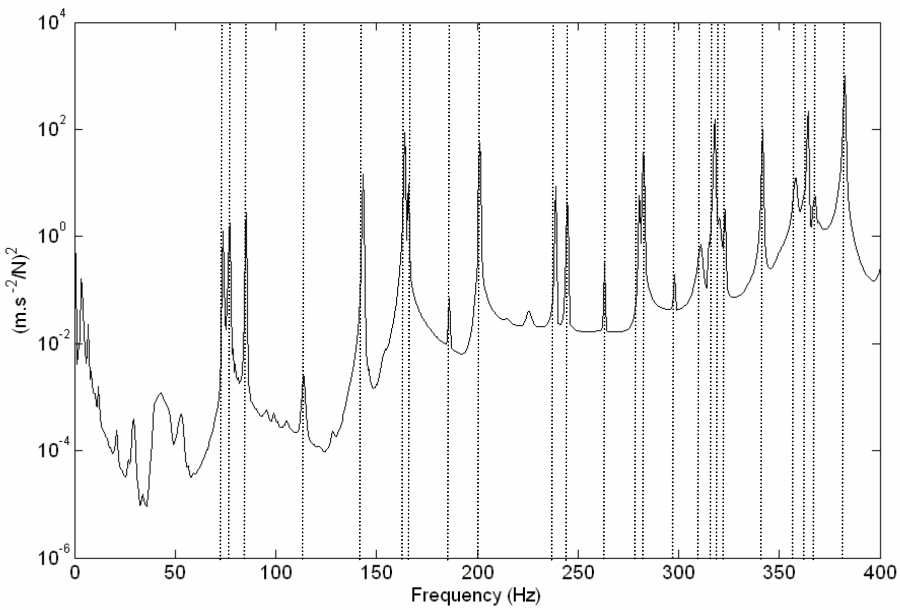

Figure 7.3 Mean-square imaginary part of measured FRFs. The dotted lines indicate the peaks that were selected in the curve fitting processing.

7.3.2 ARMAX Modal Parameter Estimation

Time series data from the SIMO experiment were first filtered and then decimated before application of the ARMAX algorithm. These steps were carried out to reduce the frequency range, hence the number of modes to be estimated, which would therefore limit the size of the required ARMAX model. The data were low-pass filtered in the forward and reverse directions using an eighth-order Chebyshev Type 1 filter, cut-off at 300 Hz, which resulted in zero phase-shift and effectively doubled the order of the filter. The Matlab `resample()` reduced the sampling rate to 600Hz and also applied a low pass FIR filter. As this filter is sensitive to the initial and final conditions of the data series (it assumes data before and after are zero) the filtering and resampling steps were applied to a long segment of the data before 2048 samples were extracted away from the end points for use with the ARMAX algorithm.

The ARMAX algorithm was first applied to one set of single-input 2-output data to estimate a large range of models of order 40 – 90. Based on the results of this initial test, the ARMAX algorithm was applied to all data sets (grouped as single-input 2-output data sets) with the following conditions: *na* = 80, 82, …, 90; eight iterations of stages 3 and 4; NPDP criterion used for model selection; record length 2048 samples. Vibration modes were selected by identifying modal peaks in individual and averaged FRFs synthesised from the fifteen (fifteen sets of single-input 2-output data) estimated ARX models. Figure 7.4 shows the averaged FRFs. The sign of estimated damping was used to verify that a selected mode was a structural vibration mode. ARMAX results are compared with RFLS results in the following section.

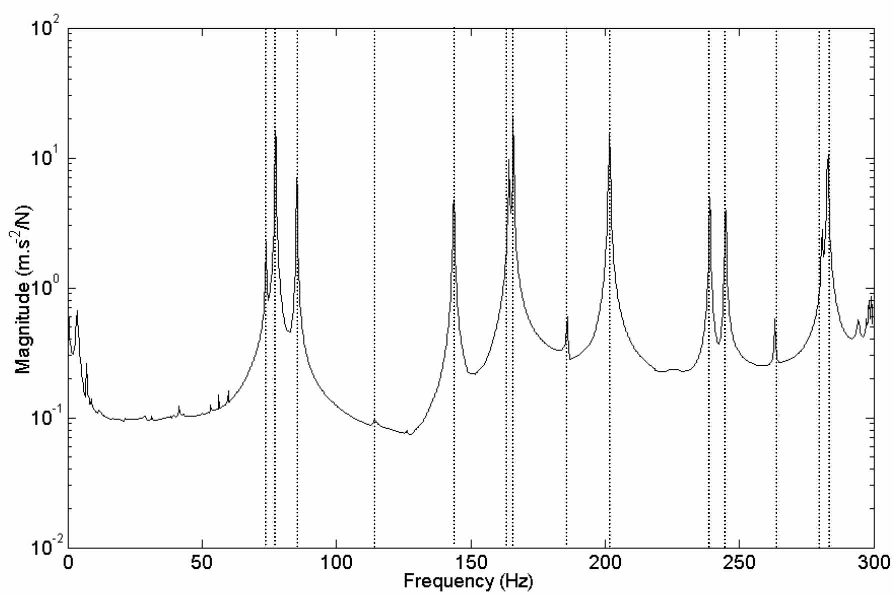

Figure 7.4 Averaged FRFs synthesised from estimated ARX models. The dotted lines indicate modes selected as vibration modes.

7.3.3 SIMO Experimental Results

Modal frequencies estimated by the ARMAX algorithm are listed in table 7.2.

Mode	1	2	3	4	5	6	7
Frequency (Hz)	73.89	77.30	85.36	114.0	143.8	165.4	165.7
Mode	8	9	10	11	12	13	14
Frequency (Hz)	186.0	201.7	239.1	244.8	263.2	281.1	282.9

Table 7.2 Estimated modal frequencies obtained by ARMAX algorithm from SIMO data.

Percentage difference between RFLS and ARMAX modal frequencies are plotted in figure 7.5, which shows the very good agreement between the two sets of results.

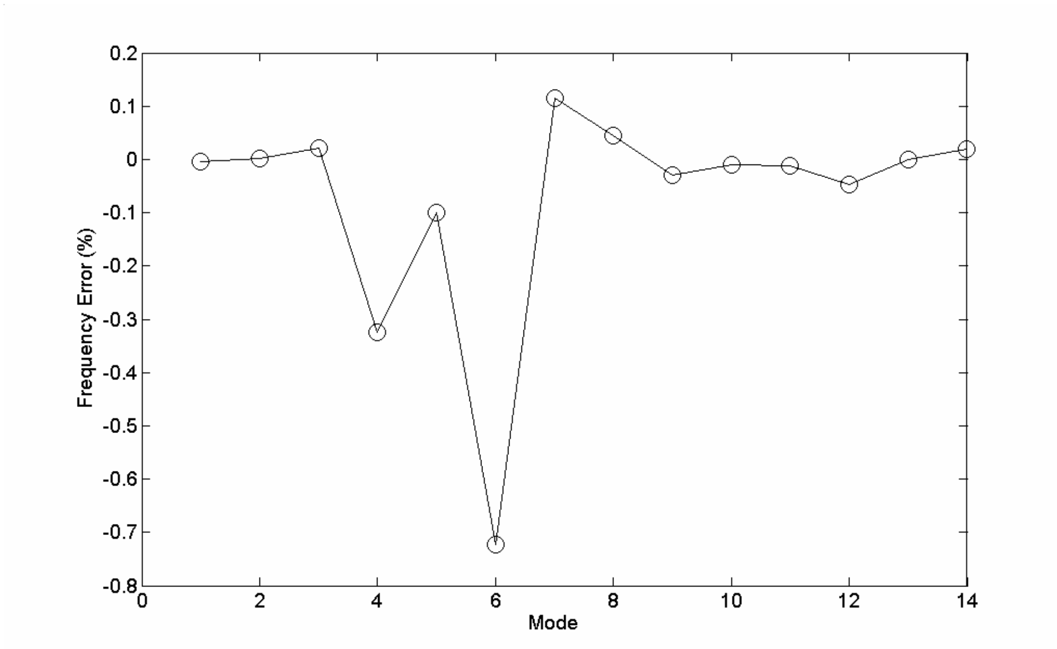

Figure 7.5 Frequency error of RFLS results compared to ARMAX results.

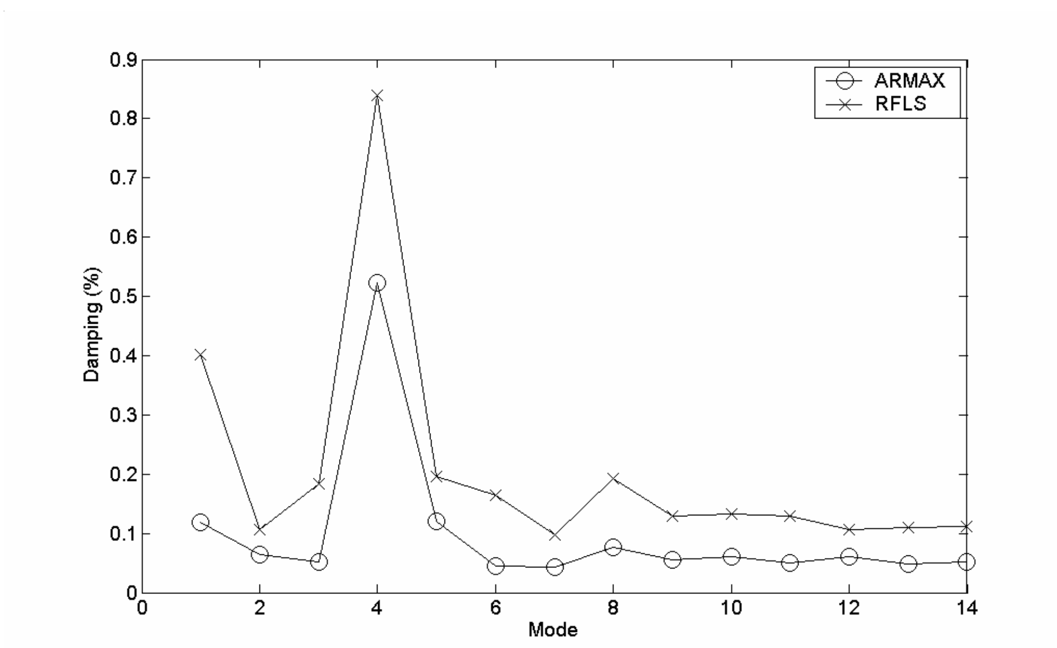

Figure 7.6 Modal damping estimated from SIMO experiments using ARMAX and RFLS methods.

Figure 7.6 compares the modal damping obtained by each estimation method. A systematic difference between the two sets of estimates is evident, and reflects the limitations of each method. The RFLS technique models FRF data, which is affected by the well-known limitations of the FFT, namely leakage and finite resolution (picket fence effect). These effects place a positive bias on damping results. It was suggested in Chapter 6 that the ARMAX estimation algorithm suffers from negatively biased damping results for non-ideal data; in extreme cases the damping is estimated as negative. Note that for the ARMAX algorithm, global modal parameters are averaged from estimates obtained for each measurement point, and in the case of damping, negative values are omitted.

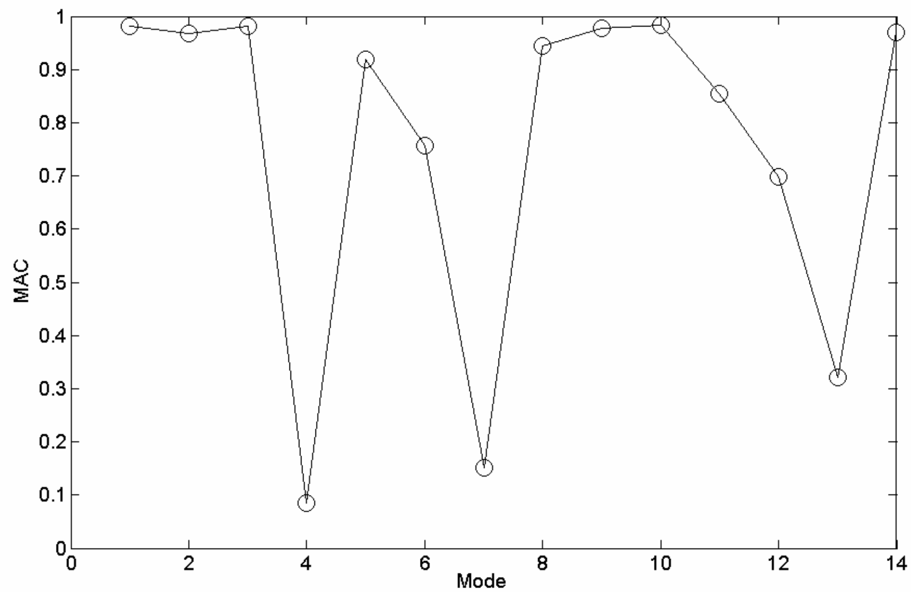

Figure 7.7 MAC value comparing modes obtained from ARMAX and RFLS algorithms.

Figure 7.7 shows MAC values comparing corresponding modes from the RFLS and ARMAX results. Eight of the 14 mode pairs have MAC values of greater than 90%. The remaining modes that do not have high MAC values were found to have low-level responses at many of the measurement points. For example, mode 4 (114.0 Hz) was found to have no clear resonant peak in most of the measured FRFs. As a consequence, significant errors could be present in the RFLS curve fit results. Similarly, the ARMAX algorithm did not identify poles around 114 Hz for many of the measurement points. Both methods did show good agreement for a limited number of measurement points, as shown in figure 7.8, which compares normalised residues for mode 4.

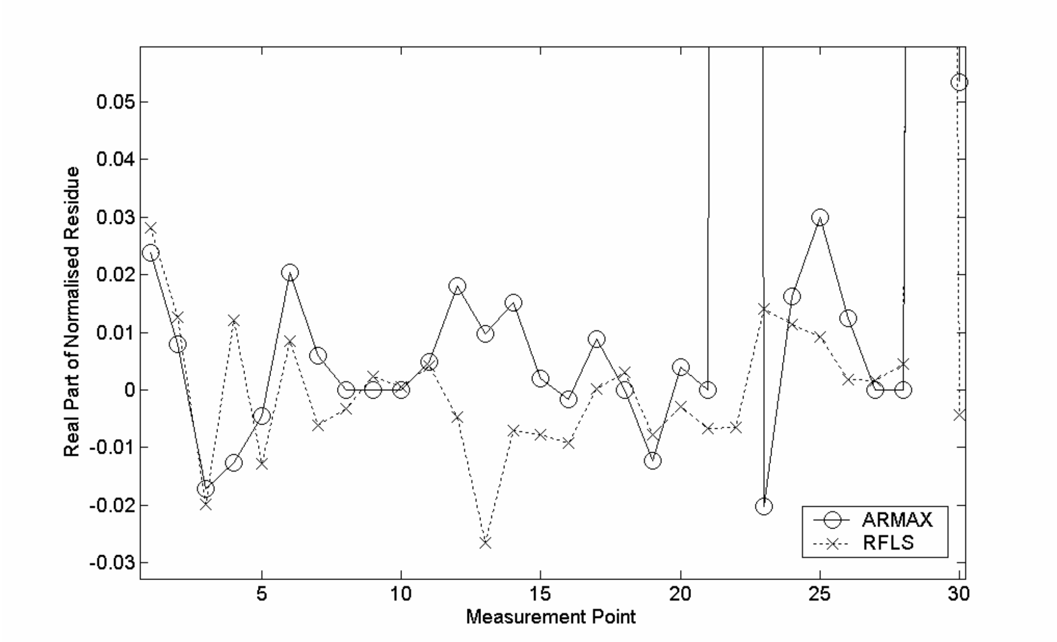

Figure 7.8 Comparison of mode 4 mode shape estimated by ARMAX and RFLS algorithms. The calculated residues have been normalised by the residue calculated for point 29. Note the agreement between values for measurement points 1, 2, 3, 10, 11, 18, 19 and 27.

It is worth noting that earlier tests carried out on the helicopter structure, in particular the impact hammer test described in Chapter 2, did not identify the mode at 114 Hz, or the presence of closely spaced modes at around 164 Hz, where similar comments apply.

While there was good agreement between modal parameters estimated by the ARMAX and RFLS algorithms, the ARMAX algorithm estimated models that fitted the measured FRF much more closely. This is illustrated in figures 7.9 – 7.12, which compare measured FRFs with those synthesised from the estimated RFLS and ARMAX models. An explanation of these results is that the STAR Modal software fits modes taking into account out-of-band modes, i.e. using residual terms; however, only in-band modes are used to synthesise FRFs. The ARMAX model fits all signal components in a frequency band, for example rigid body modes (seen below 10 Hz), and noise components. Figures 7.9 - 7.12 reflect this with very good agreement between ARMAX and measured FRFs.

Both the ARMAX and the RFLS FRFs have been plotted with the same resolution as the measured FRFs. The lower modal damping estimated by the ARMAX models is evident in the modal peaks, which are typically higher than the peaks in the measured

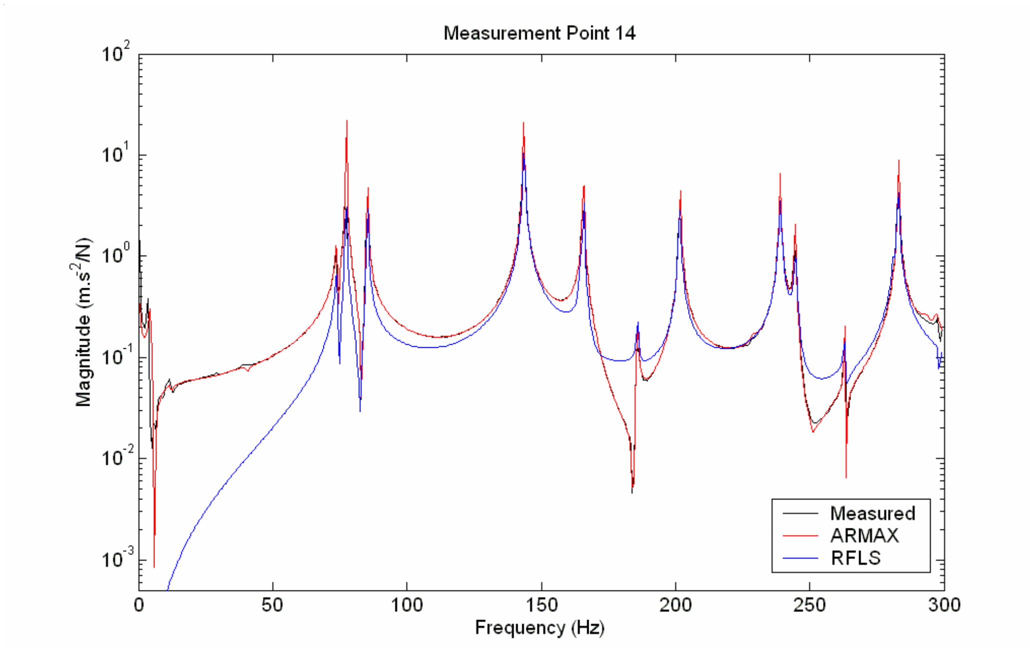

Figure 7.9 Comparison of measured and synthesised FRFs for measurement point 14.

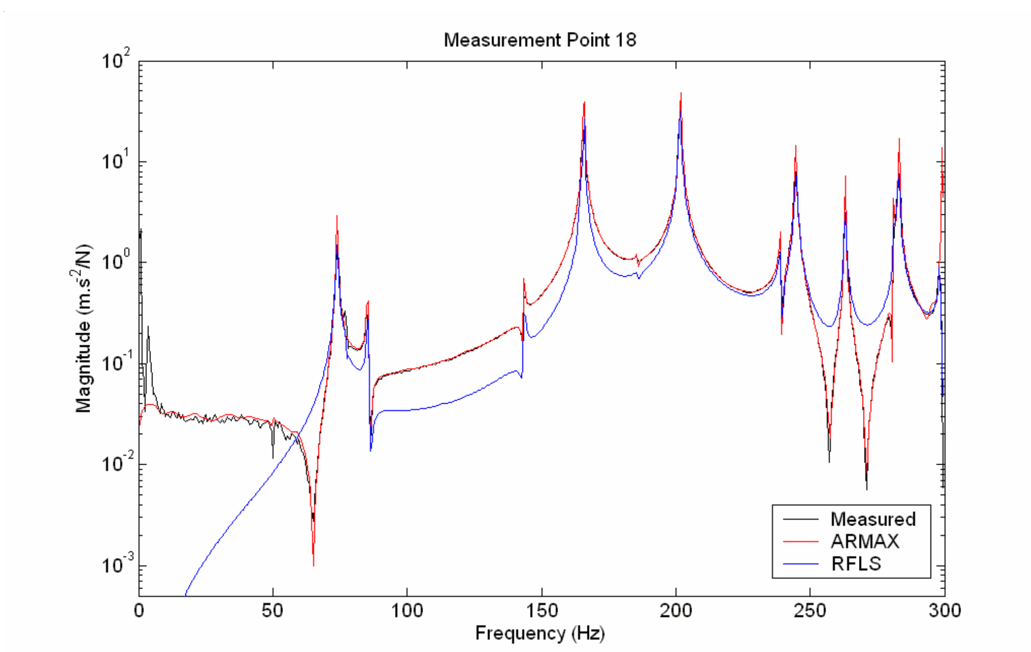

Figure 7.10 Comparison of measured and synthesised FRFs for measurement point 18.

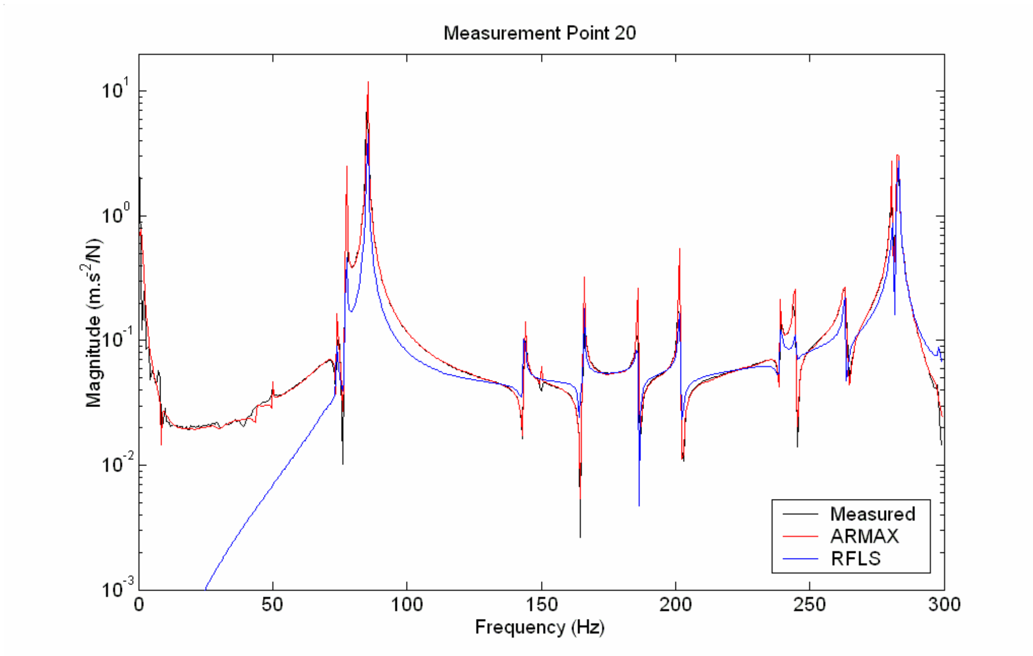

Figure 7.11 Comparison of measured and synthesised FRFs for measurement point 20.

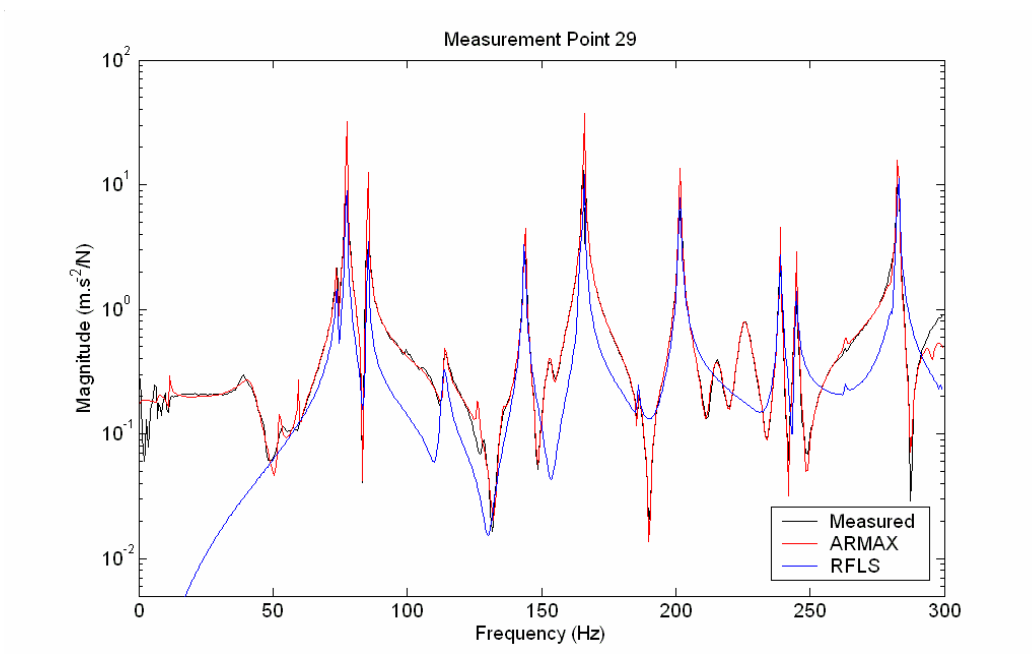

Figure 7.12 Comparison of measured and synthesised FRFs for measurement point 29.

and RFLS FRFs. Also of note is that a resonant peak corresponding to mode 4 (114 Hz) is only present in the point-inertance measurement (measurement point 29), shown in figure 7.12.

In this section, the performance of the ARMAX and RFLS algorithms has been compared. It has been shown that there is good agreement between modal parameters estimated by the two different methods. The FRFs synthesised from the estimated ARMAX models compare very well with measured FRFs. The following section discusses the performance of both algorithms for experiments with two sources of excitation, one of which is unmeasured.

7.4 Multiple Excitation Experiments

A second source of excitation was added to assess the performance of the ARMAX algorithm when measurements were made in the presence of unmeasured excitation. The experimental apparatus was the same as that used for the SIMO experiments with an additional B&K 4809 shaker coupled to the helicopter-like structure. Applied force was measured with a B&K 8200 force transducer; a B&K 2626 charge amplifier was used to condition and filter the signal with settings used for the SIMO experiment. Response measurements were made with four B&K 4393 accelerometers and the accelerometer integrated into the B&K 8001 impedance head. 180 seconds of excitation and response data were measured in each experiment and the three experiments were carried out with different combinations of excitation signals.

Experiment 1:

- Pseudo-random sequence of length 2048 samples applied by excitation 1;
- Periodic signal with summed sinusoidal components at 75.5, 120, 200, and 281Hz applied by excitation 2;
- Ratio of RMS levels of excitation 2 to excitation 1 (noise/signal ratio) = 2.04.

Experiment 2:

- Pseudo-random sequence of length 2048 samples applied by excitation 1;
- Continuous random noise applied by excitation 2;
- Ratio of RMS levels of excitation 2 to excitation 1 (noise/signal ratio) = 0.83.

Experiment 3:

- Pseudo-random sequence of length 2048 samples applied by excitation 1;
- Continuous random noise plus sinusoidal components at 75.5, 120, 200, and 281Hz applied by excitation 2; i.e. the sum of the unmeasured excitation signals used in experiments 1 and 2.
- Ratio of RMS levels of excitation 2 to excitation 1 (noise/signal ratio) = 2.11.

Note that the frequencies of the unmeasured periodic excitations were close to the natural frequencies of modes 1, 2, 9, 6, and 7. In addition, the pseudo-random measured excitation signal allowed synchronous averaging of excitation and response records. One-sided power spectra of the excitation signals are plotted in figures 7.13 – 7.15. Some coupling between the two excitation signals used in experiments 1 and 3 can be seen around 75Hz, which is the frequency of the first sinusoidal component of excitation 2 and between the natural frequencies of the first two vibration modes (74Hz and 77Hz, respectively). The implications of coupling between the excitation signals will be discussed more in Section 7.5. Note that excitation 2 used in experiment 3 was the sum of the signals used for excitation 2 in experiments 1 and 2; i.e. periodic and random noise.

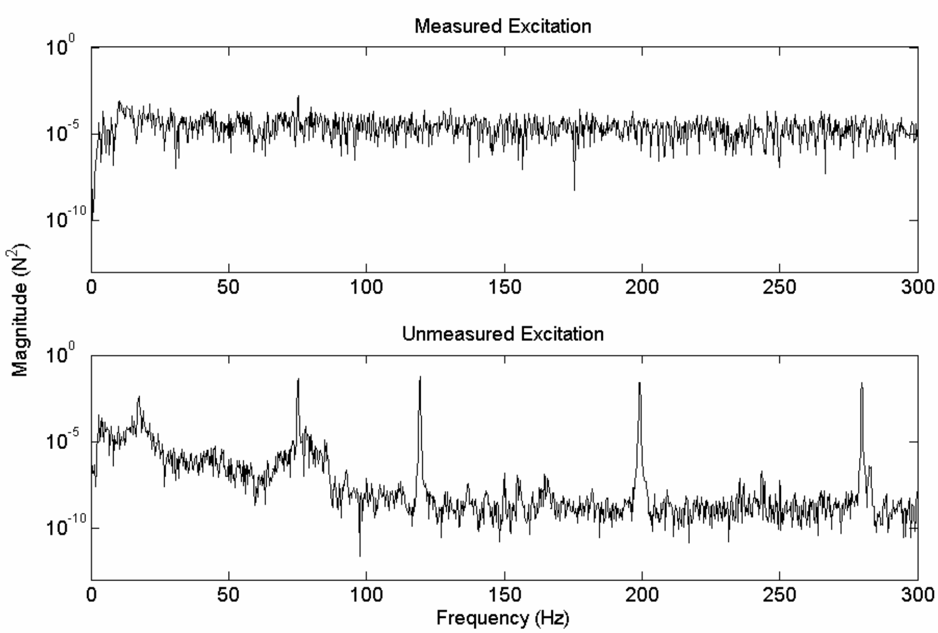

Figure 7.13 1-sided power spectrum of excitation 1 (measured excitation) and excitation 2 (unmeasured excitation) used in experiment 1.

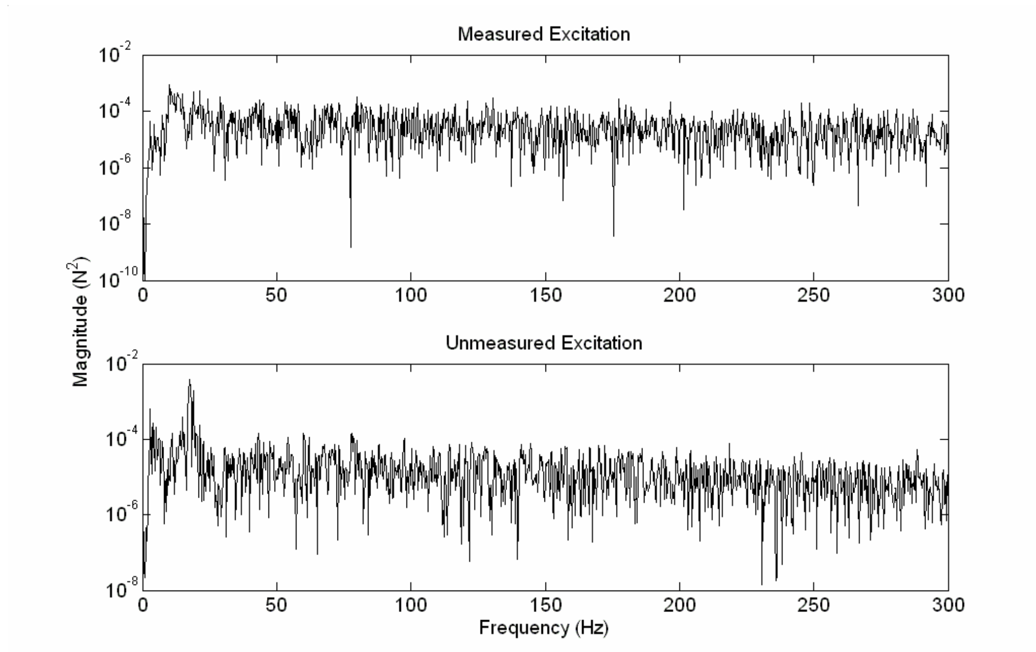

Figure 7.14 1-sided power spectrum of excitation 1 (measured excitation) and excitation 2 (unmeasured excitation) used in experiment 2.

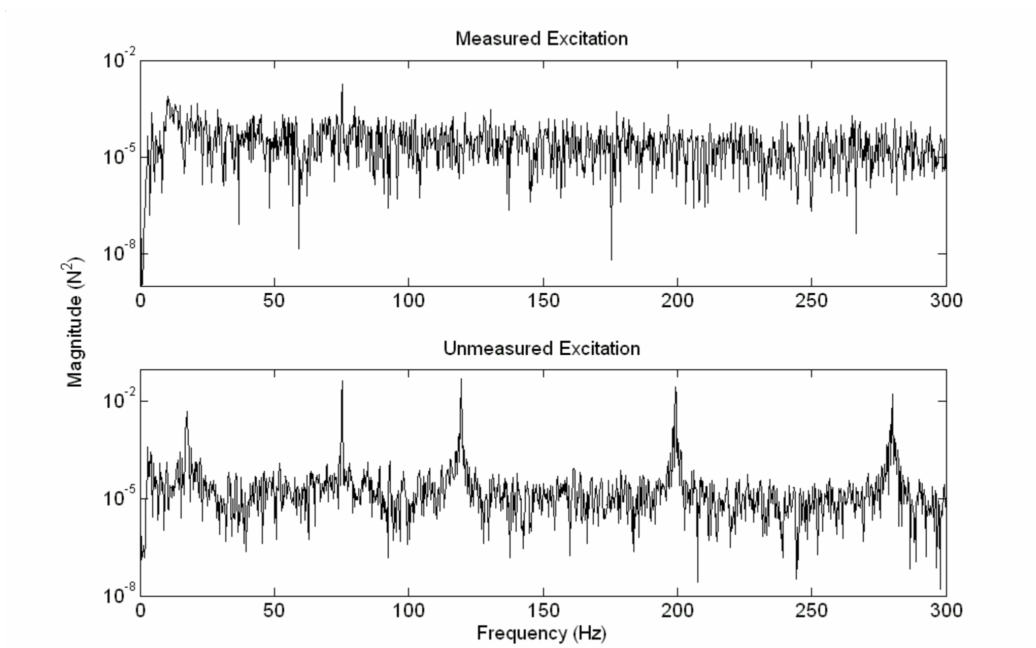

Figure 7.15 1-sided power spectrum of excitation 1 (measured excitation) and excitation 2 (unmeasured excitation) used in experiment 3.

7.4.1 Comparison of MIMO Experiment 2 and SIMO ARMAX Results

Comparison of SIMO results discussed in the previous section and Experiment 2 results obtained by the ARMAX algorithm was carried out to assess whether the addition of the second shaker imposed constraints on the helicopter-like structure, which may have affected the estimated modal parameters. The ARMAX algorithm was used to estimate modal parameters from the Experiment 2 data using ***both*** excitation signals in the estimation. Details of the ARMAX algorithm setup are as follows: fifteen 2-input 2-ouput data sets; *na* = 80, 82, …, 90; eight iterations of stages 3 and 4; NPDP criterion used for model selection; record length 2048 samples. An example of the Matlab code used for these tests is given in Appendix F. The results from this analysis of data are denoted ‘MIMO ARMAX E2’ to emphasise that both sources of excitation were used in the ARMAX estimation algorithm applied to Experiment 2 data.

Figure 7.16 compares frequencies from SIMO ARMAX analysis (discussed in the previous section) and MIMO ARMAX E2 results and shows that the agreement is very good.

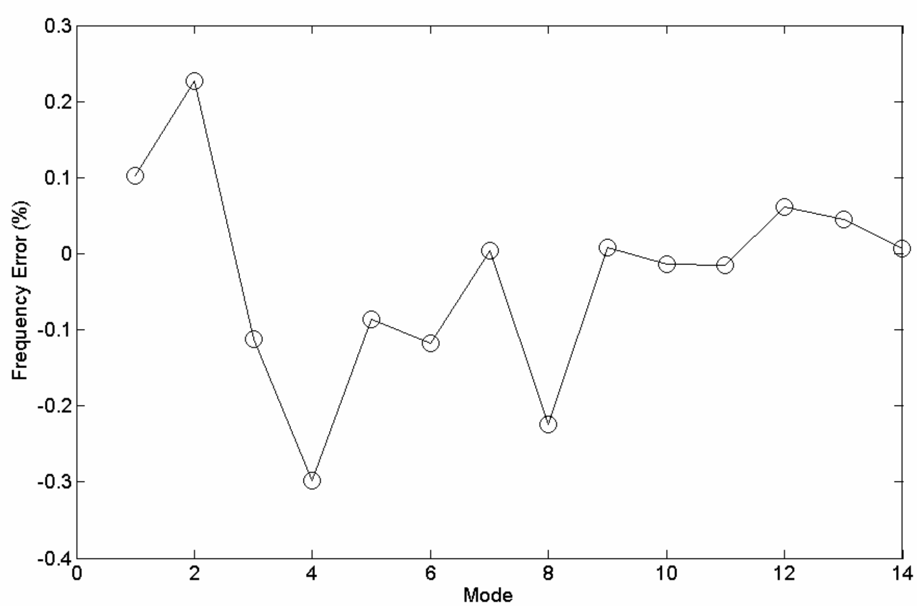

Figure 7.16 Percentage difference between modal frequencies estimated from SIMO ARMAX and MIMO ARMAX E2 analyses.

Similarly, modal damping values estimated from the same analyses are very close, as shown in figure 7.17.

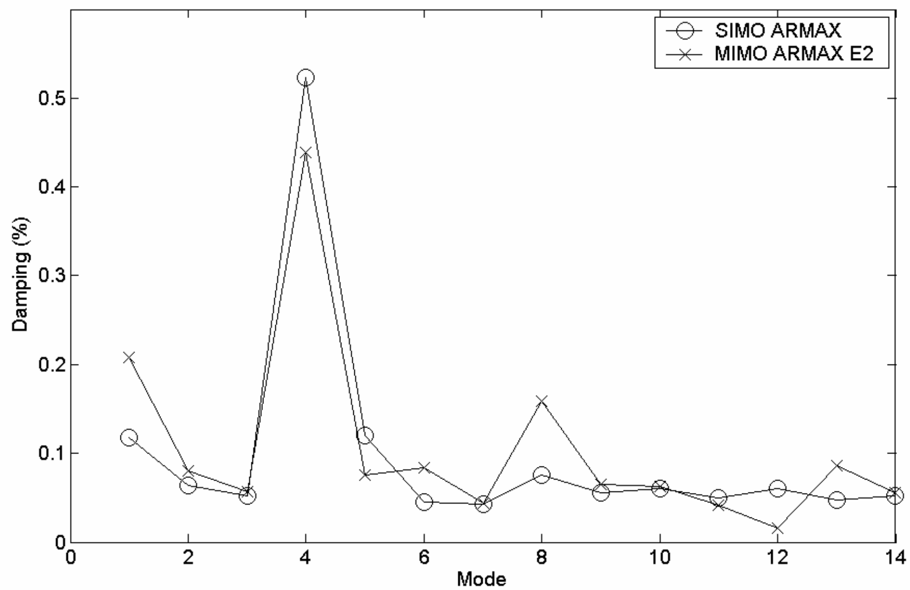

Figure 7.17 Modal damping estimated from SIMO ARMAX and MIMO ARMAX E2 analyses.

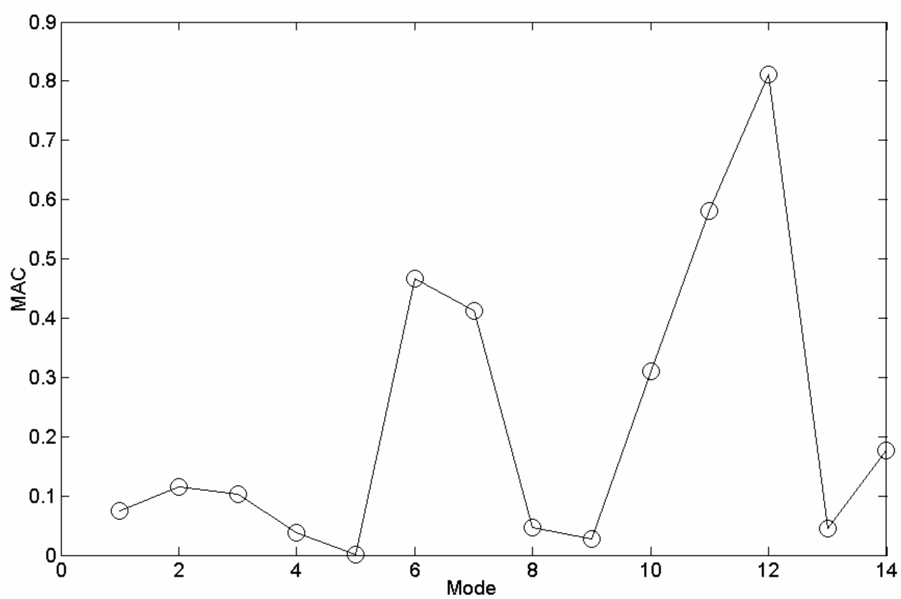

Figure 7.18 MAC for mode pairs estimated from SIMO ARMAX and MIMO ARMAX E2 analyses.

Agreement between mode shapes is relatively poor, as shown by the MAC values plotted in figure 7.18. This shows the effect of constraints applied by coupling the second shaker: both shakers theoretically apply no constraints in the axial direction (the global z direction shown in figure 7.2), but they do constrain the helicopter-like structure in the x-y plane, which clearly affects the mode shapes. The MIMO ARMAX E2 results were believed to be a satisfactory basis for comparison with results obtained from experiments 1 and 3, which were carried out with the same configuration as experiment 2. Comparison of results obtained from analysis of data from experiments 1, 2 and 3 are discussed in the following section.

7.4.2 Unmeasured Excitations

Data from experiments 1, 2, and 3 were processed using the ARMAX algorithm to assess its performance when significant unmeasured excitations were present. The signals applied by excitation 2 were used to simulate unmeasured excitation and therefore were not used by the ARMAX estimation algorithm. The ARMAX algorithm estimated modal parameters for each experiment using the following conditions: fifteen single-input (excitation 1) 2-ouput data sets; na = 80, 82, …, 90; eight iterations of stages 3 and 4; NPDP criterion used for model selection; record length 2048 samples. Results are denoted SIMO E1, SIMO E2, and SIMO E3, for results obtained from experiments 1, 2, and 3, respectively. The analysis names 'SIMO E1' etc. are used to emphasise that only a single excitation signal (excitation 1) was used for modal parameter estimation, but it should be noted that unmeasured excitations were applied by the second shaker (excitation 2).

7.4.3 Synchronous Averaging

The pseudo-random sequence used for excitation 1 in Experiments 1, 2, and 3 was two seconds in length and enabled synchronous averaging of the measured excitation and response data. Recall that 180 seconds of data were measured in each experiment resulting in a maximum of 90 synchronous averages. The averaging operations were found to be adversely affected by prior re-sampling, which reduced the sampling rate to 600Hz (described in section 7.3.2), most likely due to sample jitter resulting from application of the FIR filter. Furthermore, re-sampling the averaged data resulted in a time-series with an insufficient number of samples for estimating high-order ARMAX models. A solution to this problem, which still applied the maximum number of averages (90), involved synchronously averaging the data and then re-sampling a new time series created by concatenating the averaged time series. This solution allowed a 2048 sample segment of re-sampled data to be used for the ARMAX algorithm, and this segment of data could be selected to avoid the inaccuracies at the end points of the re-sampled data series (inaccuracies due to the FIR filter used in the re-sampling process). The 2048 samples of data used in the ARMAX algorithm spanned approximately 1.7 periods of the pseudo-random excitation. The ARMAX algorithm was applied to the averaged, re-sampled data from Experiments 1, 2, and 3 with the following conditions: fifteen single-input (excitation 1) 2-ouput data sets; na = 80, 82, …, 90; eight iterations of stages 3 and 4; NPDP criterion used for model selection; record length 2048 samples. Results are denoted SIMO E1 av, SIMO E2 av, and SIMO E3 av, for results obtained from Experiments 1, 2, and 3, respectively. The analysis names 'SIMO E1 av' etc. are used to emphasise that only a single excitation signal was used for modal parameter estimation and that synchronous averaging was used to pre-process the data. Recall that unmeasured excitations were applied by the second shaker (excitation 2) in Experiments 1, 2, and 3.

7.4.4 Experiment 1 Results: Unmeasured Periodic Excitation

Modal parameters from SIMO E1 and SIMO E1 av are compared with the MIMO E2 results in figures 7.19 – 7.23.

Estimated modal frequencies show very good agreement with those obtained from the MIMO E2 experiments. No significant change is observed after synchronous averaging is applied to the data. Numerical and experimental results discussed in Chapter 6 suggested that unmeasured periodic excitations do not significantly affect the ARMAX modal parameter estimates. Therefore, the effect of synchronous averaging in attenuating responses due to the unmeasured periodic excitations would not be clearly represented in the modal parameter results. These comments are reflected in the standard deviations for the modal frequencies estimated from each set of data (figure 7.20), with an increase in standard deviation apparent in only a few modes estimated from data with unmeasured excitations.

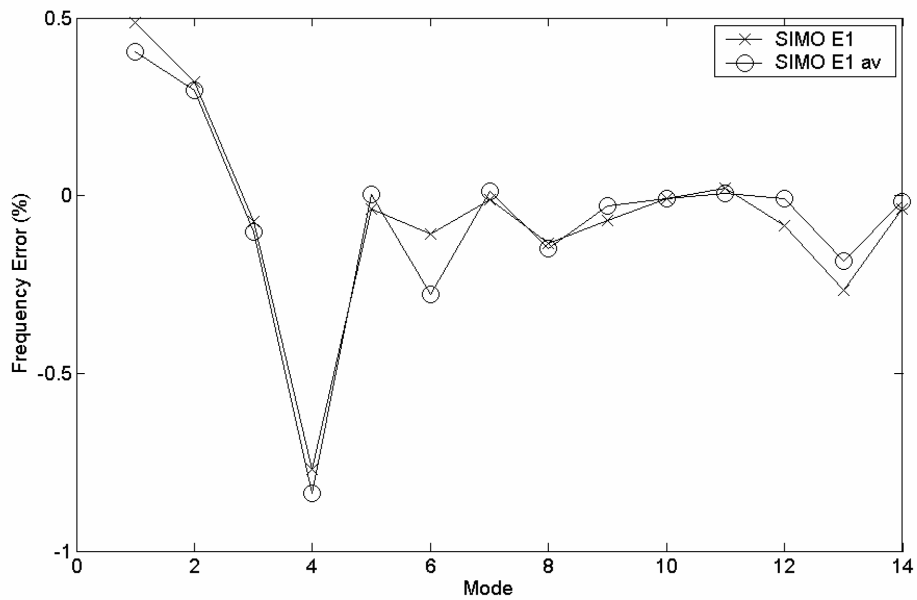

Figure 7.19 Modal frequencies estimated from SIMO E1 and SIMO E1 av analyses compared with modal frequencies estimated from MIMO E2 analysis.

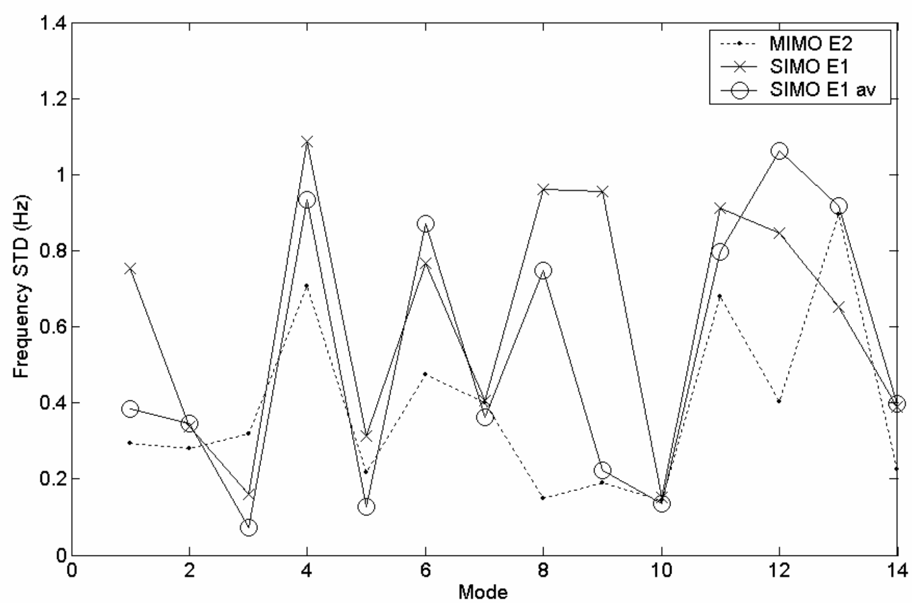

Figure 7.20 Modal frequency standard deviation for SIMO E1, SIMO E1 av, and MIMO E2 analyses.

As discussed in chapter 6, modal damping is more sensitive to the effects of unmeasured periodic excitation. Variation in damping estimates (figure 7.21) is seen to occur for modes where there is a poor response at a number of excitation points, for

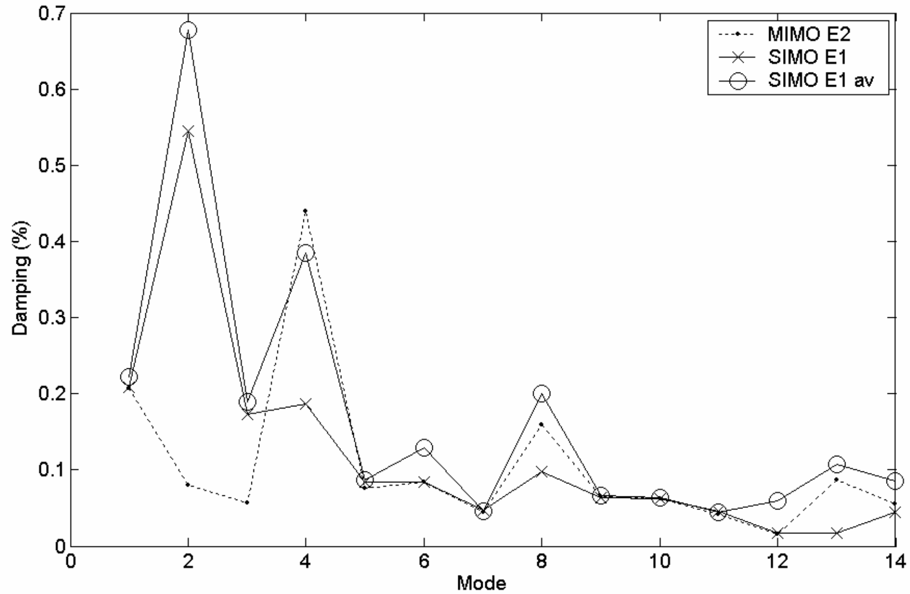

Figure 7.21 Modal damping estimated from SIMO E1 and SIMO E1 av analyses compared with modal damping estimated from MIMO E2 analysis.

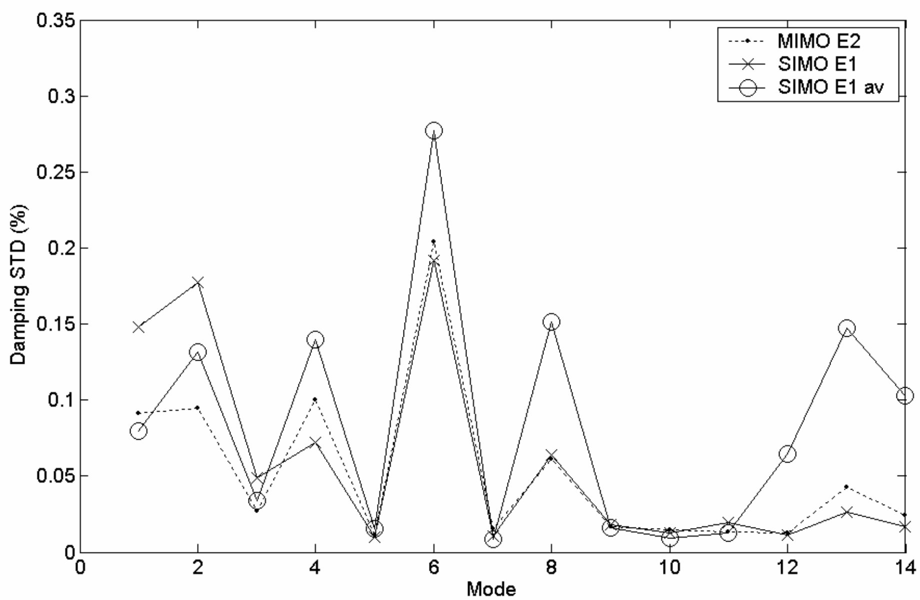

Figure 7.22 Modal damping standard deviation for SIMO E1, SIMO E1 av, and MIMO E2 analyses.

example, modes 4 and 8; closely spaced modes, for example mode 6 (which is < 1 Hz below mode 7); and closely spaced modes with a unmeasured periodic excitation close by, as in the cases of modes 2 and 13. This is also reflected in the standard deviation for modal damping values estimated from each data set, shown in figure 7.22. It is interesting to note that the unmeasured periodic excitation at 200Hz does not significantly affect the damping estimates at mode 9 (201.7Hz), which was found to have a strong response at most measurement points. Overall, the ARMAX algorithm is observed to be effective in estimating modal damping from data obtained in the presence of unmeasured periodic excitations, even if the frequencies of unmeasured excitation are close to natural frequencies of the structure. This also accounts for the similarity between SIMO E1 and SIMO E1 av results as the averaging process will attenuate the unmeasured periodic excitations, which are not synchronous with the averaging period, and this will not be clearly reflected in the estimated modal parameters.

The MAC values (figure 7.23) comparing mode shapes obtained from the SIMO E1 and SIMO E1 av analyses with mode shapes obtained from the MIMO E2 analysis show a similar pattern to the results obtained in the SIMO analysis, described in Section 7.2.

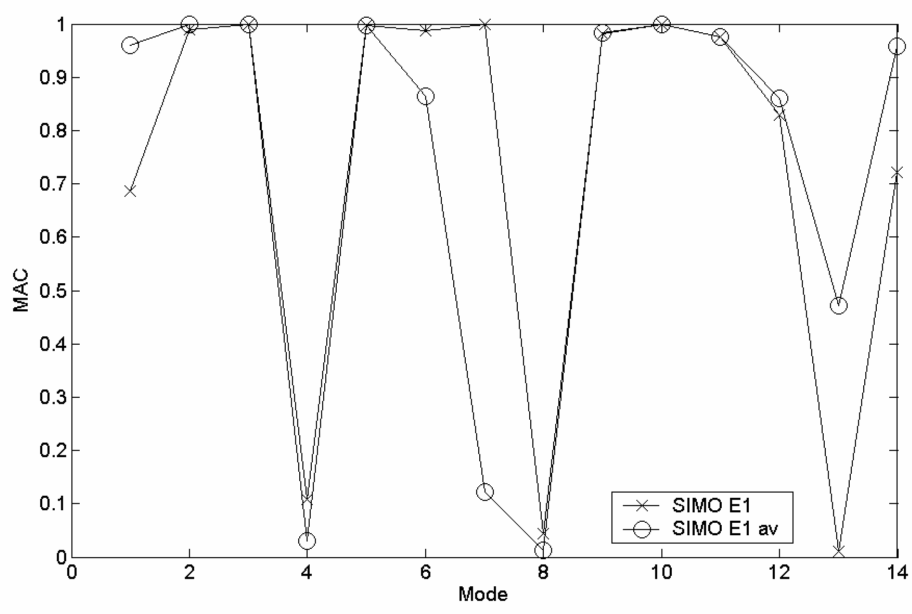

Figure 7.23 MAC comparing mode shapes estimated from SIMO E1 and SIMO E1 av analyses with mode shapes estimated from MIMO E2 analysis.

This further highlights the difficulty with using the MAC to compare modes where some measurement points have very poor response and therefore large amounts of uncertainty in mode shape estimates. Nine out of fourteen modes have been estimated with MAC values higher than 0.9 and the differences between the SIMO E1 and SIMO E1 av results are typically due to a small number of measurement points with an inaccurate result. This is illustrated for mode 7, where the SIMO E1 MAC value is very close to 1, and the SIMO E1 av MAC value is just over 0.1. The normalised residue for mode 7 obtained from the SIMO E1 av analysis is compared with that from the MIMO E2 analysis in figure 7.24. There is a clear discrepancy at measurement points 1 and 18. The MAC value for mode 7 omitting points 1 and 18 was 0.99.

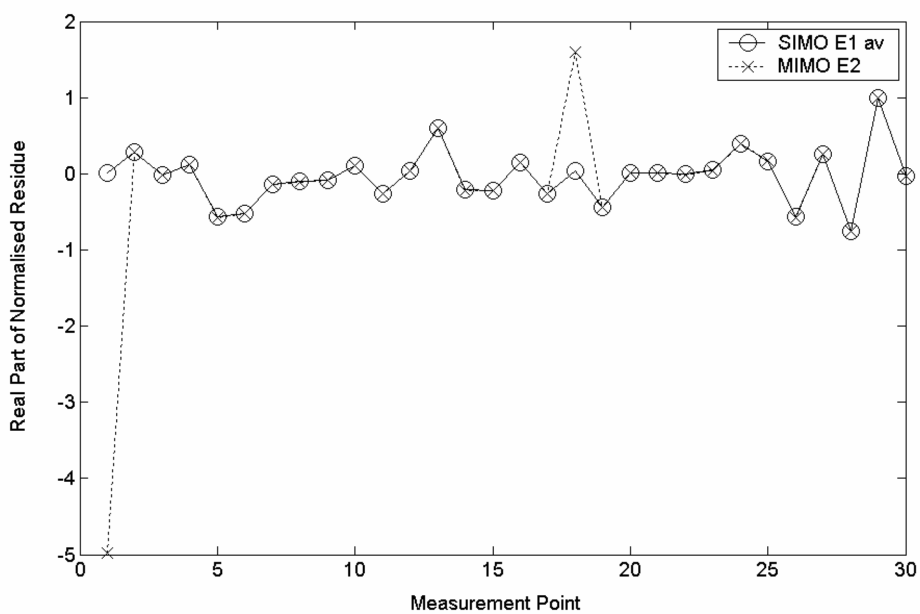

Figure 7.24 Comparison of mode 7 mode shapes estimated from SIMO E1 av and MIMO E2 analyses.

7.4.5 Experiment 2 Results: Unmeasured Random Excitation

The estimated modal parameters from the SIMO E2 and SIMO E2 av analyses are compared with those from the MIMO E2 analysis in figures 7.25 – 7.29. As for the Experiment 1 results discussed in the previous section, modal frequencies are in good agreement with the MIMO E2 results. Synchronous averaging has no significant effect on the estimated natural frequencies. Similarly, no clear trend is seen in the standard deviation of the estimated modal frequencies, shown in figure 7.26.

Unmeasured random excitation has a more significant effect on the modal damping than was observed for unmeasured periodic excitation. Figure 7.27 shows reasonable agreement between damping values except for modes 4, 8, and 12 where negative damping has been estimated in the SIMO E2 analysis. Synchronous averaging improves the damping for modes 4 and 12; however, mode 8 is still estimated with negative damping. Similarly, the damping standard deviation values are relatively large for modes 4, 8, and 12 and synchronous averaging decreases the values for modes 4 and 12.

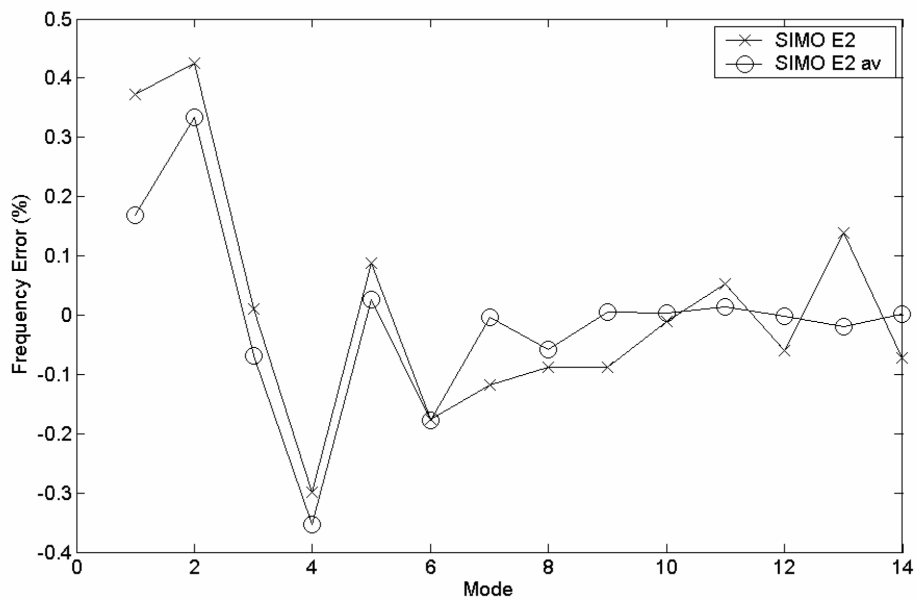

Figure 7.25 Modal frequencies estimated from SIMO E2 and SIMO E2 av analyses compared with modal frequencies estimated from MIMO E2 analysis.

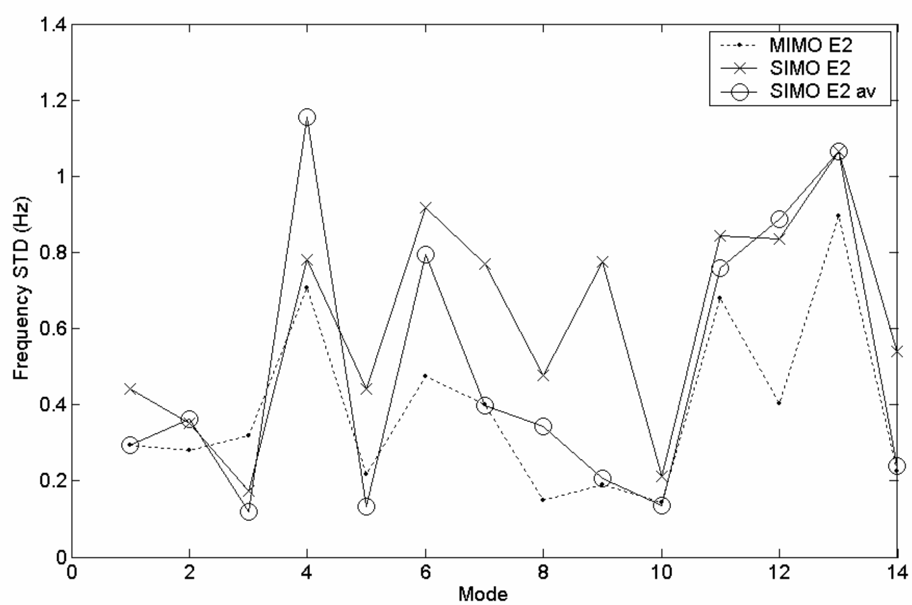

Figure 7.26 Modal frequency standard deviation for SIMO E2, SIMO E2 av, and MIMO E2 analyses.

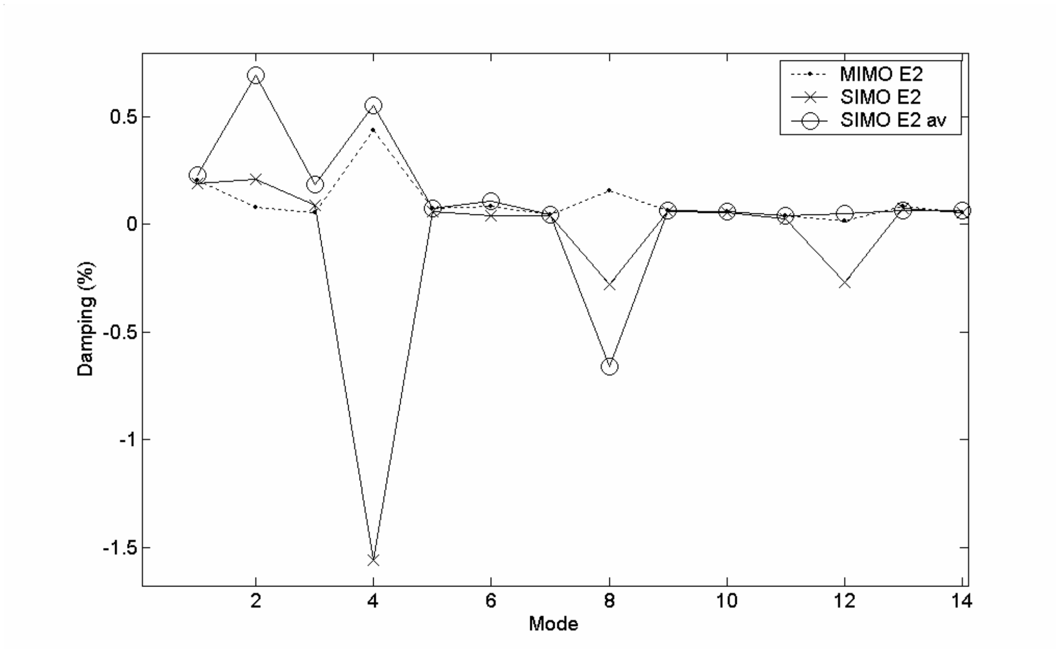

Figure 7.27 Modal damping estimated from SIMO E2 and SIMO E2 av analyses compared with modal damping estimated from MIMO E2 analysis.

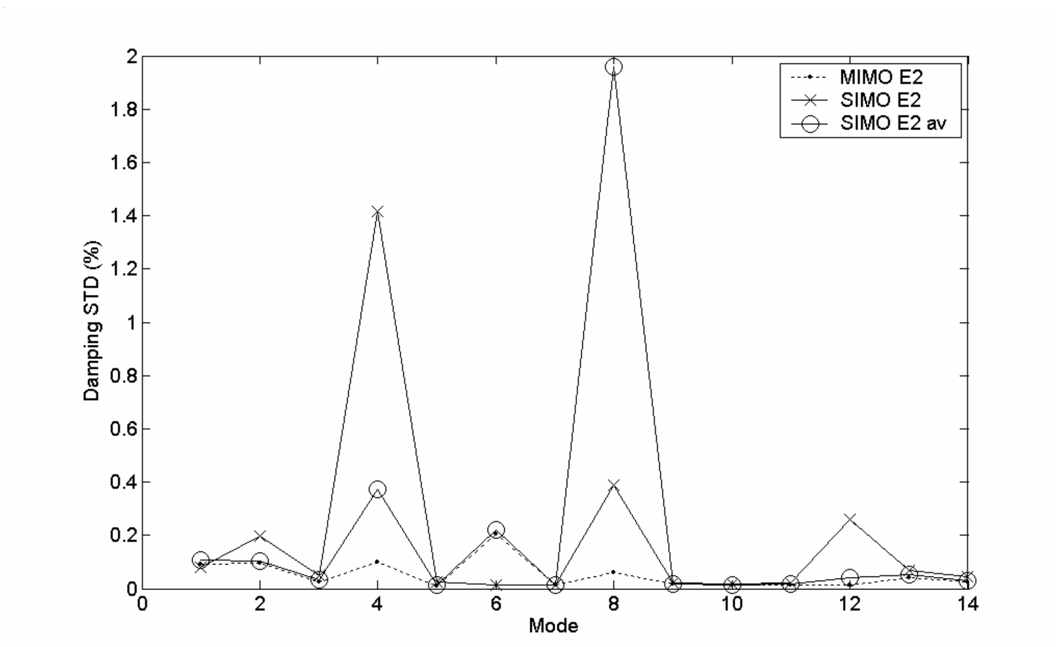

Figure 7.28 Modal damping standard deviation for SIMO E2, SIMO E2 av, and MIMO E2 analyses.

Referring to figure 7.4, modes 4, 8, and 12 (114, 186, and 263Hz, respectively) have relatively low peaks, indicating that the responses are relatively poor at a number of measurement points. The signal-to-noise ratio around these frequencies is likely to be lower than modal frequencies with a larger response due to measurement noise, and this adds to the poor signal-to-noise ratio due to the unmeasured excitations.

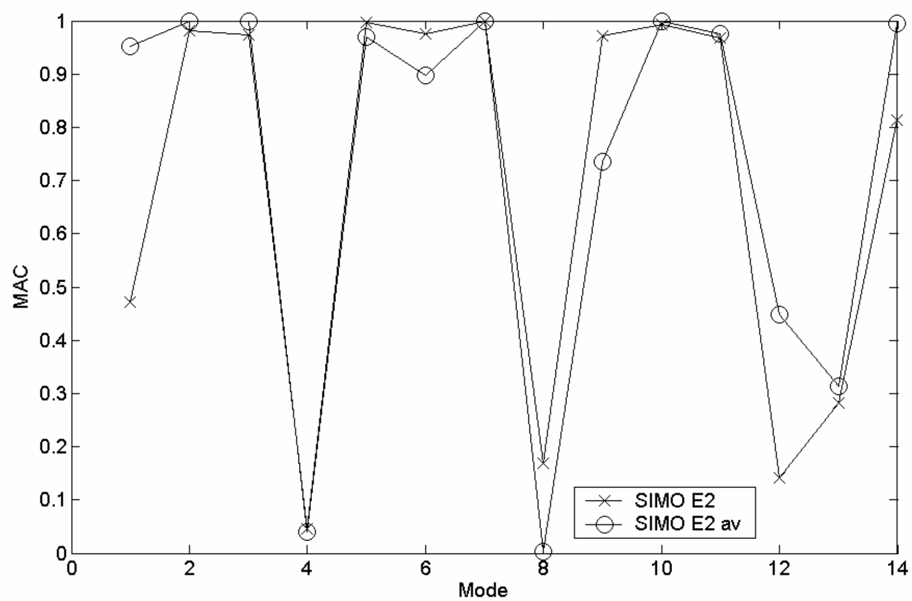

Figure 7.29 MAC comparing mode shapes estimated from SIMO E2 and SIMO E2 av analyses with mode shapes estimated from MIMO E2 analysis.

MAC values in figure 7.29 show a similar pattern to those obtained for unmeasured periodic noise discussed in the last section, that is, modes 4, 8, and 12 show the poorest agreement. The unmeasured random excitations were found to affect mode shape estimates uniformly across measurement points for modes with low MAC values, as opposed to a small number of poorly estimated points as was illustrated by the example discussed in section 7.4.4 (see figure 7.24).

7.4.6 Experiment 3 Results: Unmeasured Periodic and Random Excitation

Modal parameters from SIMO E3 and SIMO E3 av are compared with the MIMO E2 results in figures 7.30 – 7.34. As expected, the estimated modal frequencies are not significantly affected by the unmeasured periodic and random excitations, as shown in figure 7.30 and similar comments apply to the standard deviation for modal frequency plotted in figure 7.31.

Modal damping results show a similar trend to that observed for unmeasured random excitations, discussed in the previous section. Synchronous averaging improves the accuracy of damping for modes 4 and 12, which were estimated with negative damping in the SIMO E3 analysis.

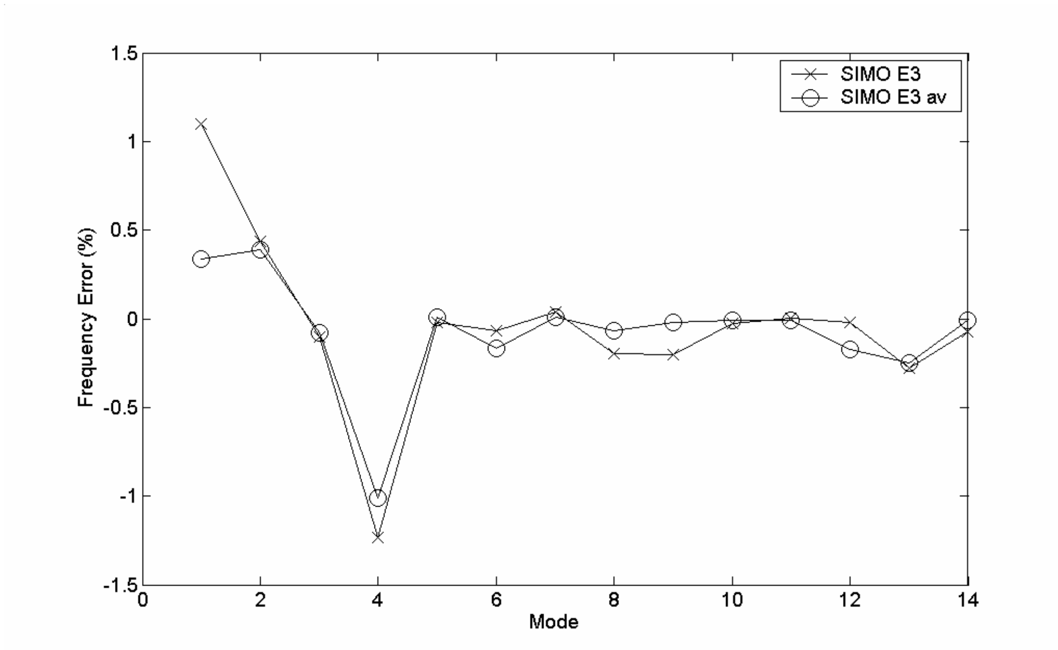

Figure 7.30 Modal frequencies estimated from SIMO E3 and SIMO E3 av analyses compared with modal frequencies estimated from MIMO E2 analysis.

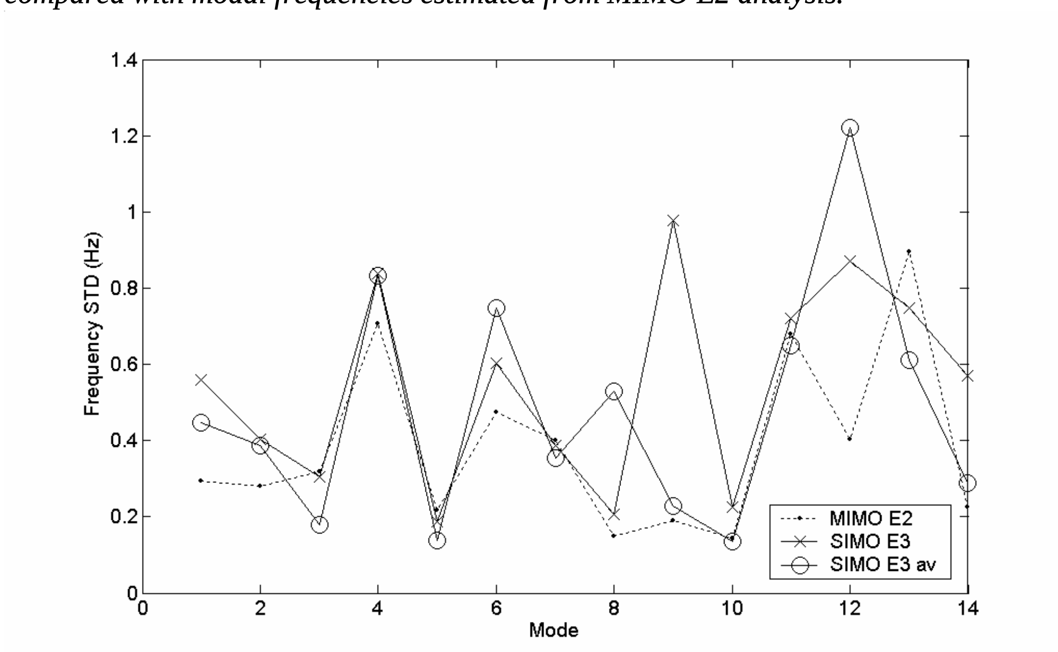

Figure 7.31 Modal frequency standard deviation for SIMO E3, SIMO E3 av, and MIMO E2 analyses.

The large standard deviation value for mode 8, SIMO E3 av, reflects the poor damping estimate for that mode. This is due to a pole with a frequency very close to the natural frequency of mode 8, but with a high value of negative damping. The mode-selection method used for the analyses discussed in this chapter is based only on modal frequency; alternatively, damping could be considered and modes with very large negative damping could be easily identified and removed.

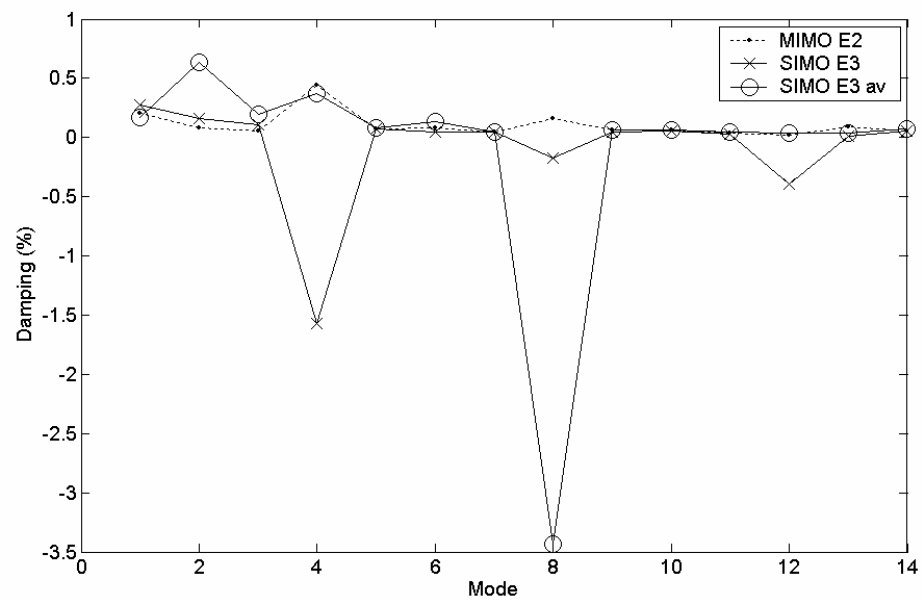

Figure 7.32 Modal damping estimated from SIMO E3, SIMO E3 av, and MIMO E2 analyses.

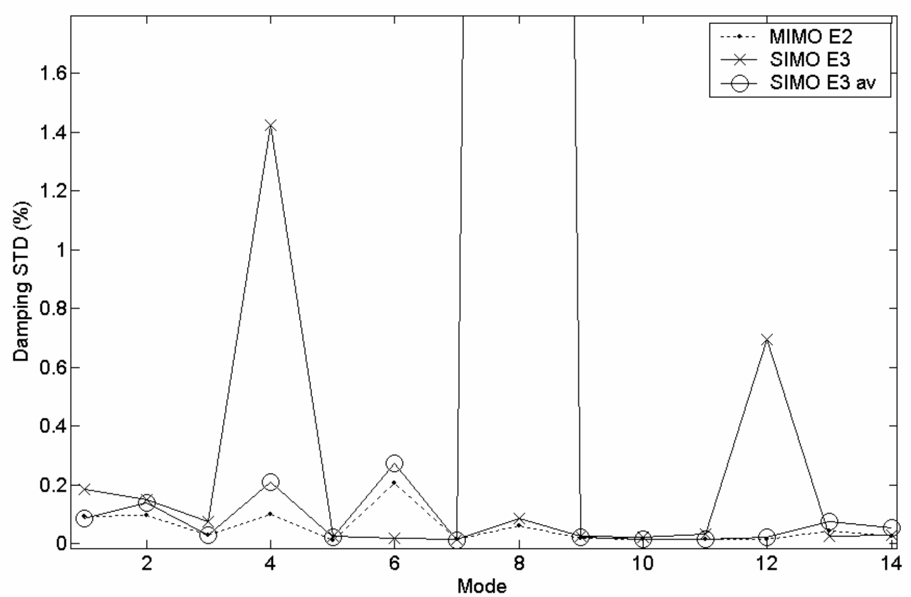

Figure 7.33 Modal damping standard deviation for SIMO E3, SIMO E3 av, and MIMO E2 analyses.

MAC values for the SIMO E3 and SIMO E3 av analyses are very similar to those obtained for the SIMO E2 and SIMO E2 av analyses, which was expected due to the limited effect of unmeasured periodic excitations. Synchronous averaging leads to a significant improvement in the MAC values for modes 1, 12 and 13, however, little or no improvement is seen for the modes with very poor correlation, namely, modes 4, 7, and 8.

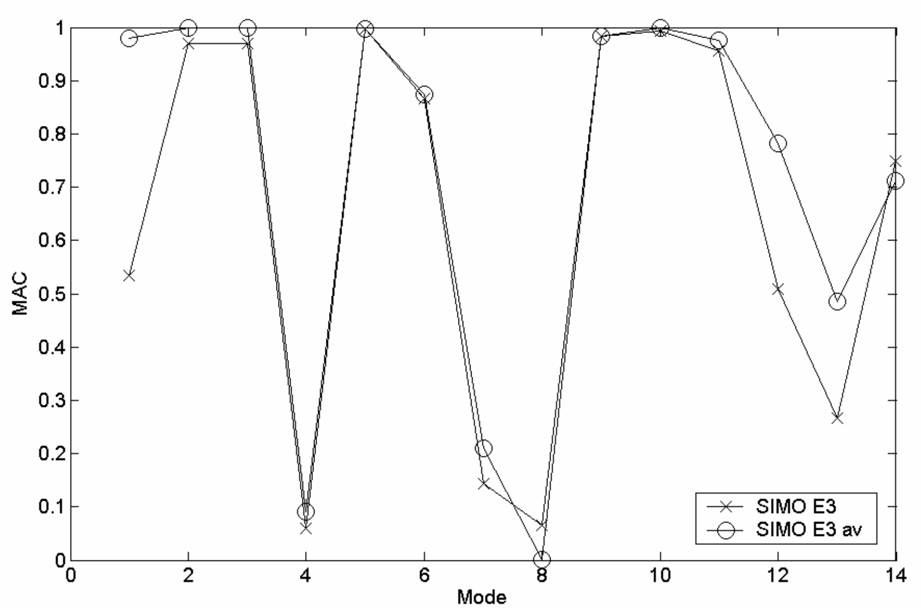

Figure 7.34 MAC comparing mode shapes estimated from SIMO E3 and SIMO E3 av analyses with mode shapes estimated from MIMO E2 analysis.

Mode shape correlation between different tests has been consistently poor for modes 4 and 8, and as noted above, these modes have a limited response at a number of measurement points. The poor mode shape estimates at a number of measurement points will contribute to low MAC values. These comments also apply to the results from the SIMO experiments obtained using the ARMAX and RFLS algorithms, discussed in section 7.3.

Closely spaced modes were also more sensitive to the presence of unmeasured excitations, for example modes 6 and 7, which were separated by approximately 0.5 Hz or less, and modes 13 and 14, which were separated by less than 2 Hz. This is in agreement with conclusions from numerical tests discussed in Chapter 6. The presence of an unmeasured periodic excitation at 280 Hz further affected the mode shape estimates of mode 13 in the analysis of data from experiment 1 and 3.

In terms of estimated modal parameters, the most significant effect of synchronous averaging was the improvement in damping values for modes 4 and 12, which were estimated with negative damping in the SIMO E2 and SIMO E3 analysis. The review in section 2.3 showed that synchronous averaging attenuates signal components that are not synchronous with the averaging period, and the quality of the FRFs synthesised from the estimated ARMAX models more clearly illustrate this. Plots of synthesised FRFs at measurement points 14, 18, 20 and 29 are shown in Appendix B for all analyses discussed in this section. The models synthesised from averaged data are in much better agreement with results from the MIMO E2 analysis (i.e. 2-input 2-output with no noise, see section 7.4.1) and peaks due to poles modelling the unmeasured periodic excitation are less prominent. As discussed in section 7.4.4, the ARMAX algorithm produces accurate modal parameters in the presence of purely unmeasured periodic excitations, therefore the effect of averaging is not as obvious when analysing frequency, damping, and mode shape results.

The ARMAX algorithm successfully identifies the modal frequencies of all modes in the presence of significant unmeasured periodic and random excitation, while modal damping and mode shapes are less accurate for modes with a poor response at many measurement points. The ARMAX algorithm achieves acceptable accuracy for very short data records; in this case study 2048 samples, and synchronous averaging improves damping estimates for modes with low responses at many measurement points. Modes where poor accuracy is achieved are common to all the analyses, including noise-free conditions and this reflects a significant limitation of the ARMAX algorithm, namely, that it cannot properly identify modes at measurement points with a poor response. Synchronous averaging has the greatest impact on modal parameters estimated in the presence of unmeasured random excitations (see for example Experiment 2 and Experiment 3 results), as the ARMAX algorithm is most sensitive to unmeasured random excitations, as opposed to unmeasured periodic excitations. The following section compares the performance of the ARMAX algorithm with the RFLS algorithm for Experiments 1- 3.

7.5 Comparison of ARMAX and RFLS Modal Parameter Estimation in the Presence of Unmeasured Excitations

The RFLS FRF curve fitting method was used to process data measured in Experiments 1, 2, and 3. FRFs were calculated between response measurements and excitation 1. Excitation 2 was treated as an unmeasured excitation as for the ARMAX analyses discussed in the previous section. Modal parameters were estimated using the RFLS method for experiments 1, 2 and 3 under the following conditions: f_s = 1024 Hz; frequency range 0 - 400 Hz; Δf = 0.5 Hz; uniform window (i.e. no weighting) applied to segments of time record 2048 samples long synchronised to the pseudo-random excitation. Two sets of modal parameters were estimated from data processed using different numbers of averages: RFLS E1, RFLS E2, and RFLS E3, refer to RFLS curve fitting of Experiment 1, 2 and 3 data, respectively, using 20 synchronous averages; RFLS E1 av, RFLS E2 av, and RFLS E3 av, refer to RFLS curve fitting of Experiment 1, 2 and 3 data, respectively, using 89 synchronous averages. Estimated modal parameters for each of the tests are compared with modal parameters from the MIMO ARMAX E2 analysis in Appendix C. The higher numbers of averages generally produced marginally better results for all combinations of unmeasured excitations. Frequency results are typically within 1% of the values estimated in the MIMO ARMAX E2 analysis. Negative damping is estimated for at least one mode in each analysis, and synchronous averaging does lead to an improvement in one negative damping value for unmeasured periodic excitation in RFLS E1 av analysis. For the case where unmeasured random excitation is present, synchronous averaging does not improve negative damping estimates. Results from the RFLS FRF curve fitting are compared with the ARMAX results in the following sections.

7.5.1 Comparison of ARMAX and RFLS Results for Experiment 1 Data: Unmeasured Periodic Excitation

Results from the SIMO E1 analysis (ARMAX estimation, 2048 samples, unmeasured periodic noise) were compared with those obtained from the RFLS E1 av analysis (RFLS estimation, unmeasured excitation, 89 synchronous averages). Note that because a higher number of averages yielded slightly better results for the RFLS algorithm, RFLS E1 av results were compared with the SIMO E1 results to illustrate that the

ARMAX algorithm can use significantly less data. The results from the MIMO E2 analysis (MIMO ARMAX estimation) were used as a basis for calculating frequency error and MAC values, as well as providing an estimate of damping in noise-free conditions. Figure 7.35 shows that there is no significant difference in the estimated modal frequencies, while modal damping estimates (figure 7.36) are also quite similar for most of the modes except mode 4, which had a poor response at many measurement points. Note that no standard deviation data is produced by the RFLS algorithm for the frequency and damping estimates. The MAC values in figure 7.37 indicate good correlation between RFLS E1 av and MIMO E2 mode shapes for only modes 2 and 3, while the SIMO E1 analysis shows much better agreement for a greater number of modes.

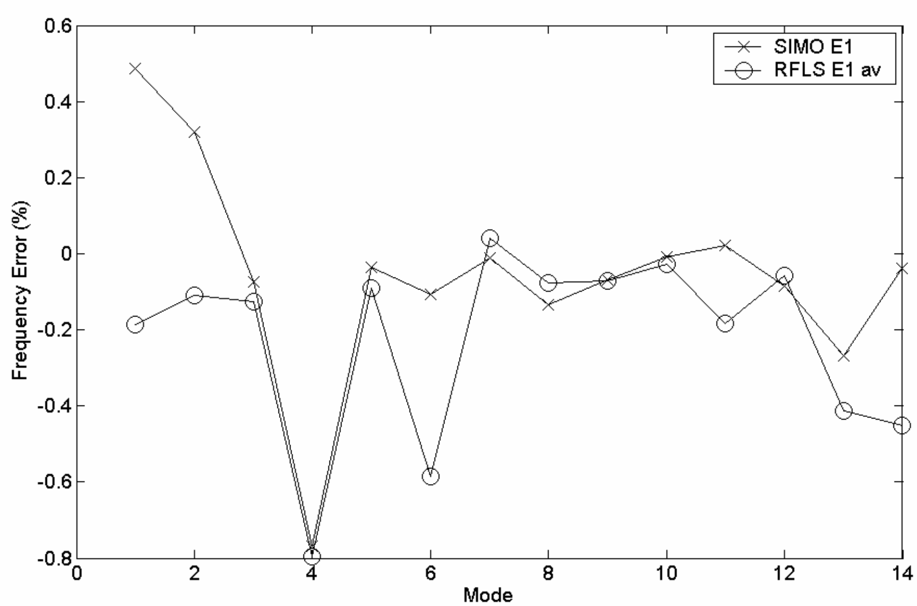

Figure 7.35 Comparison of modal frequencies from RFLS FRF curve fitting of Experiment 1 data and SIMO E1 analysis with modal frequencies from ARMAX MIMO E2 analysis.

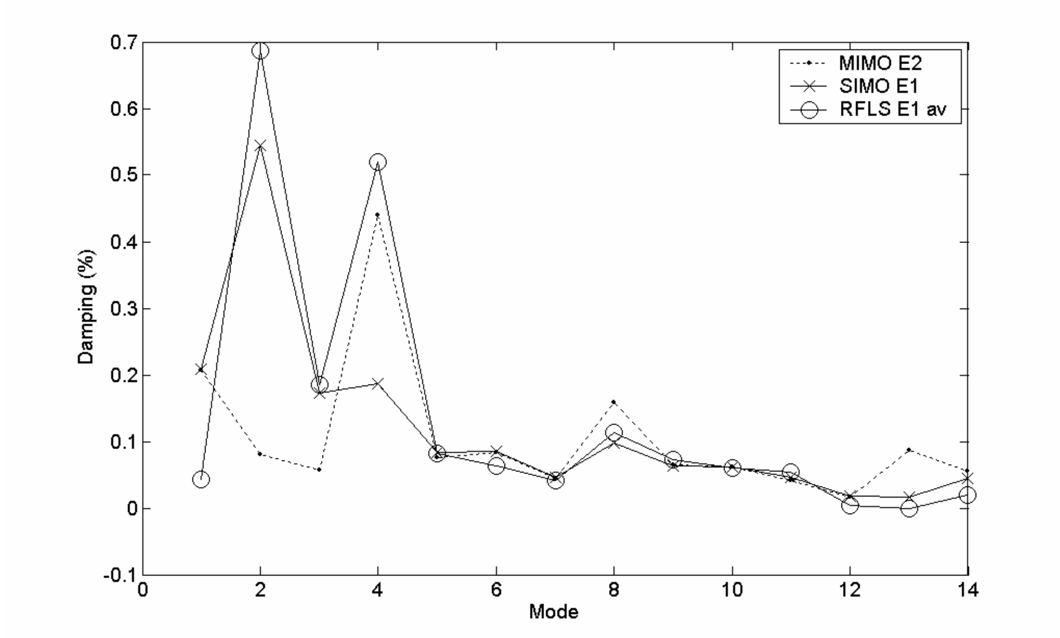

Figure 7.36 Comparison of modal damping from RFLS FRF curve fitting of Experiment 1 data, SIMO E1 analysis, and ARMAX MIMO E2 analysis.

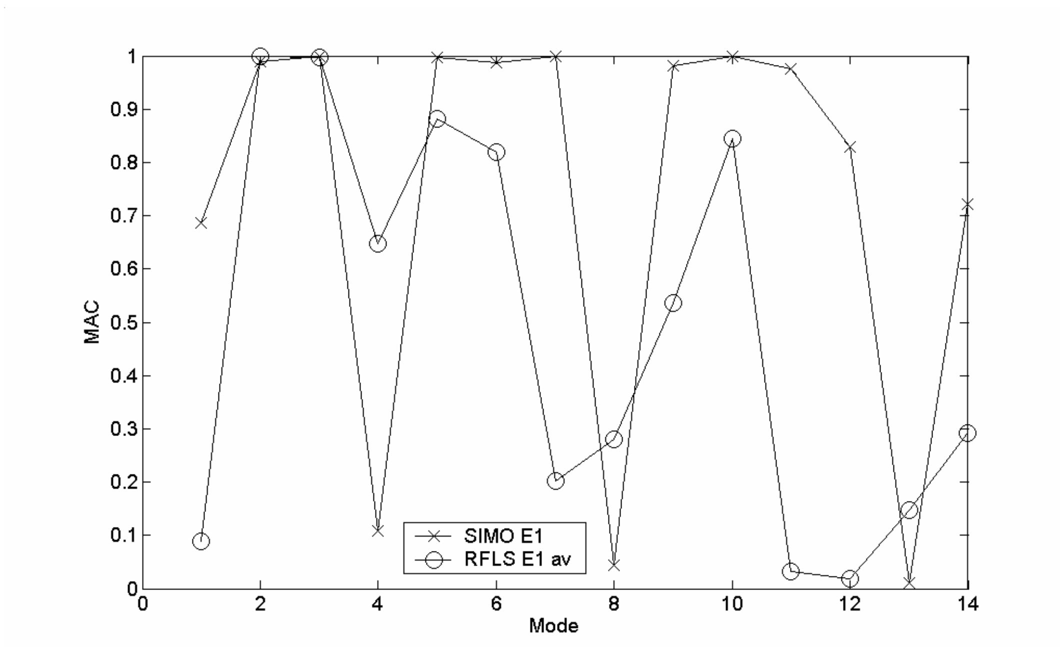

Figure 7.37 MAC comparing mode shapes from RFLS FRF curve fitting of Experiment 1 data and SIMO E1 analysis with mode shapes from ARMAX MIMO E2 analysis.

7.5.2 Comparison of ARMAX and RFLS Results for Experiment 2 Data: Unmeasured Random Excitation

Modal parameters from SIMO E2 and RFLS E2 av analyses are compared with the noise-free results from the MIMO E2 analysis and plotted in figures 7.38 – 7.40. As with the results presented in the previous section, SIMO E2 and RFLS E2 av results were compared to illustrate that the ARMAX algorithm can perform well using short data records. The pattern of results is also quite similar to those discussed in the previous section; however, the unmeasured random excitation has a greater effect on the accuracy of both estimation methods when compared with unmeasured periodic excitation. While the ARMAX algorithm estimates negative damping for three modes, it was shown in section 7.3.5 that averaging improved the results for two of the three modes. It is interesting to note the ARMAX and RFLS algorithms estimate negative damping for different modes using synchronously averaged data: mode 8 (186Hz) for the ARMAX algorithm, and mode 13 (280Hz) for the RFLS algorithm. Mode 13 is separated from mode 14 by approximately 1 Hz, while mode 8 had relatively low-level response at many measurement points.

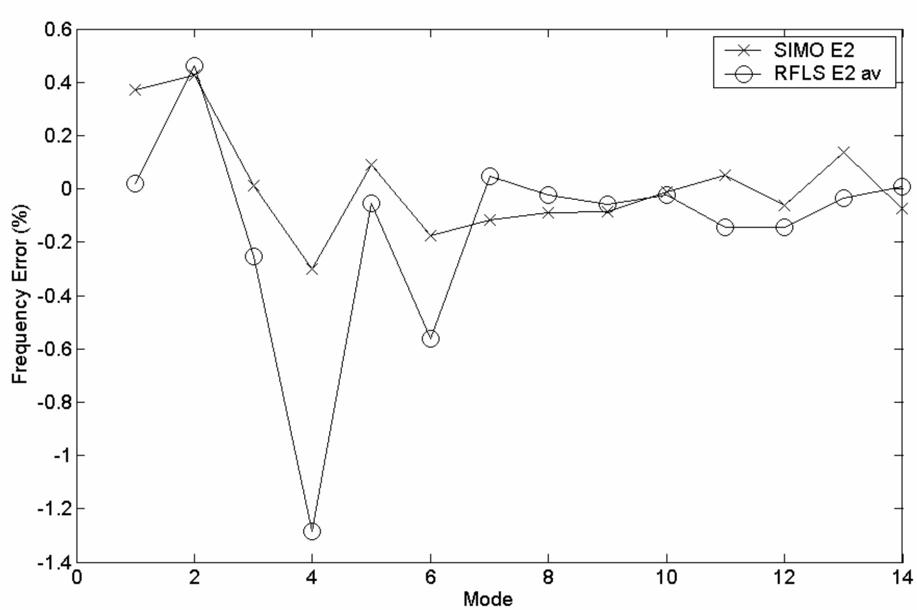

Figure 7.38 Comparison of modal frequencies from RFLS FRF curve fitting of Experiment 2 data and SIMO E2 analysis with modal frequencies from ARMAX MIMO E2 analysis.

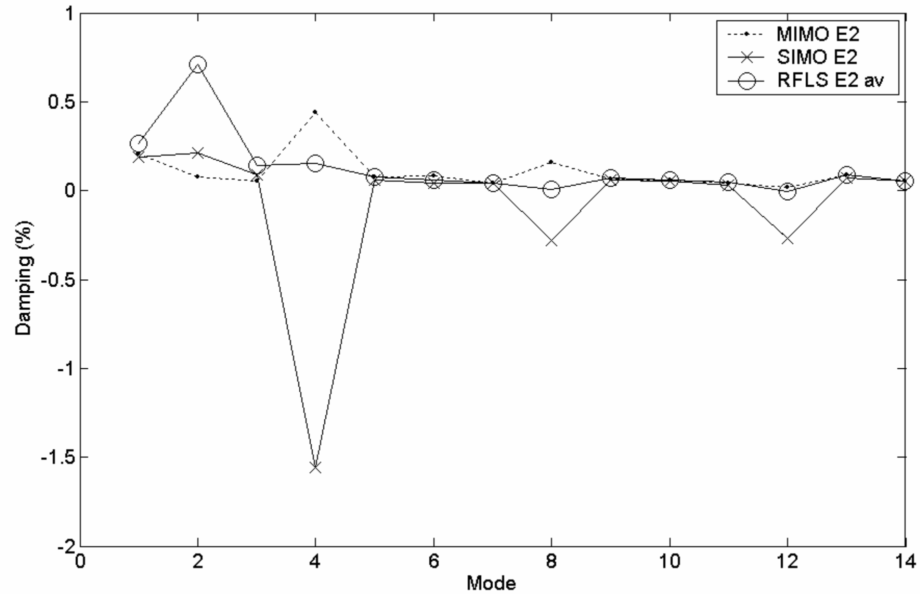

Figure 7.39 Comparison of modal damping from RFLS FRF curve fitting of Experiment 2 data, SIMO E2 analysis, and ARMAX MIMO E2 analysis.

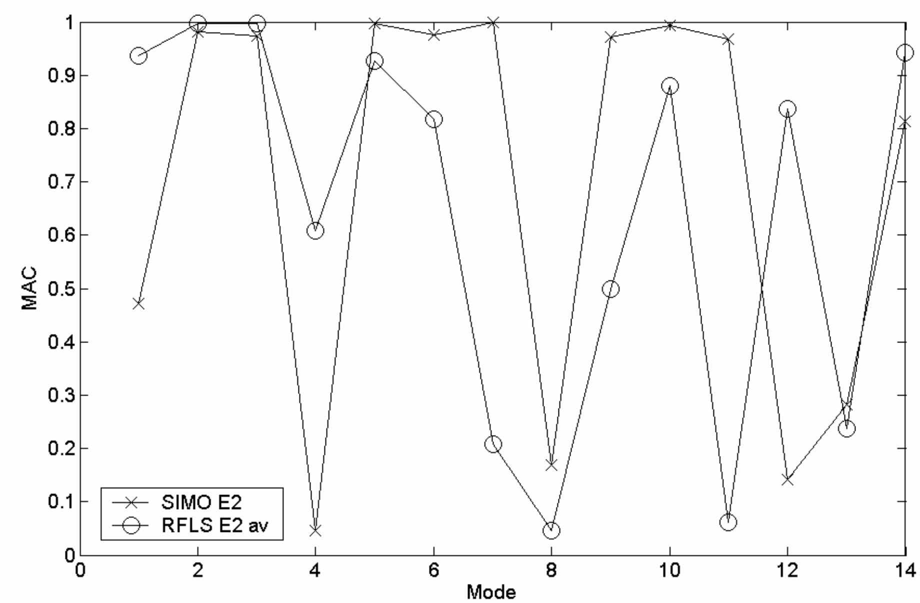

Figure 7.40 MAC comparing mode shapes from RFLS FRF curve fitting of Experiment 2 data and SIMO E2 analysis with mode shapes from ARMAX MIMO E2 analysis.

7.5.3 Comparison of ARMAX and RFLS Results for Experiment 3 Data: Unmeasured Periodic and Random Excitation

Comparison of results from the SIMO E3 and RFLS E3 av analyses reflect comments made in the previous two sections and are shown in figures 7.41 – 7.43, using results from MIMO E2 analysis as a basis for calculating frequency error and MAC value. Both the ARMAX and RFLS algorithms have difficulty with low amplitude modes and share a similar pattern of MAC values.

The results in this section have shown that ARMAX algorithm typically yielded a more accurate set of modal parameters in conditions where unmeasured periodic and/or random excitations were present. The ARMAX algorithm also required less measurement data to achieve these results; 2048 samples, as opposed to 89×2048 samples used in the RFLS analyses that included synchronous averaging. It should be noted when drawing conclusions from the MAC values that comparison of the two algorithms for noise-free data, discussed in section 7.3.3, showed large differences in the mode shape results for modes 4, 7, and 13.

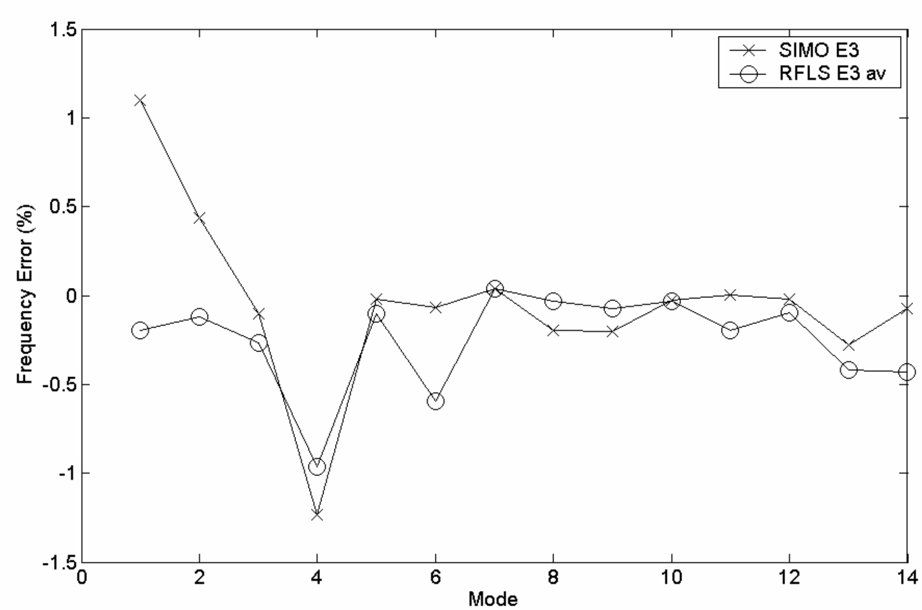

Figure 7.41 Comparison of modal frequencies from RFLS FRF curve fitting of Experiment 3 data and SIMO E3 analysis with modal frequencies from ARMAX MIMO E2 analysis.

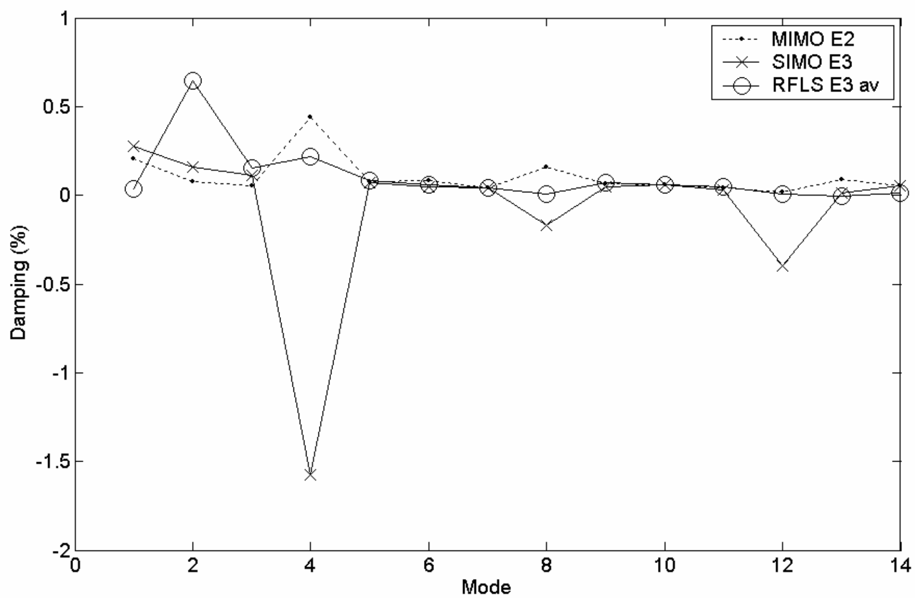

Figure 7.42 Comparison of modal damping from RFLS FRF curve fitting of Experiment 3 data, SIMO E3 analysis, and ARMAX MIMO E2 analysis.

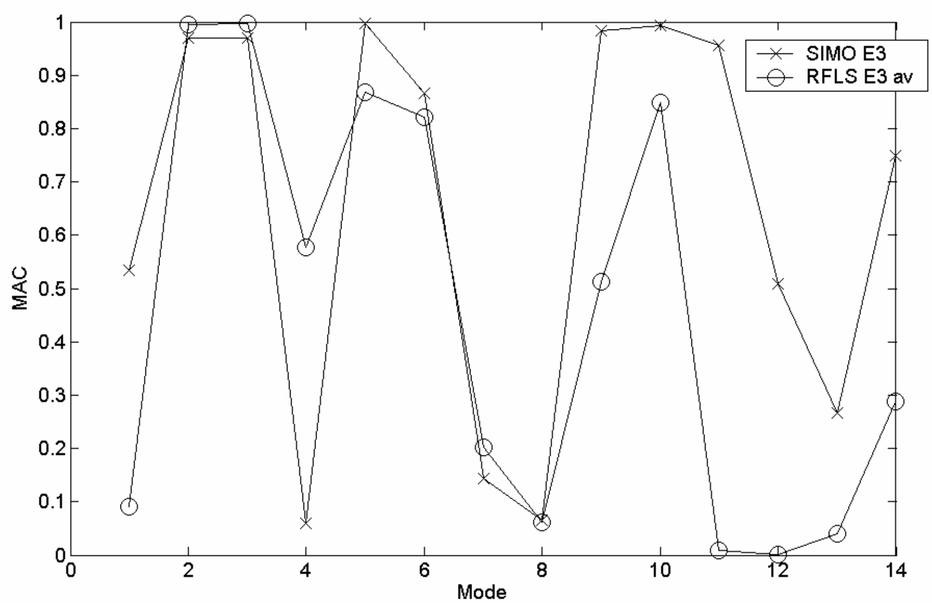

Figure 7.43 MAC comparing mode shapes from RFLS FRF curve fitting of Experiment 3 data and SIMO E3 analysis with mode shapes from ARMAX MIMO E2 analysis.

7.5.4 Comparison of Mode Selection for ARMAX and RFLS Algorithms

An important distinction can be made between the roles of mode selection in the two estimation algorithms. The ARMAX algorithm fits a model to the time-series data and mode selection involves identifying poles of the model that represent vibration modes. The true vibration modes are typically a subset of modes modelled by the ARMAX model due to model order over-specification. The RFLS method fits a model to bands of the measured FRF, which are selected on the basis of some mode selection criteria. Figure 7.44 shows the averaged, squared imaginary part of the measured FRFs obtained from the RFLS E3 av analysis. The dotted lines in the figure mark the modal frequencies of the identified vibration modes, which were based on the results of the noise free analysis. There are many additional peaks in the plot, which are due to measurement noise and unmeasured excitations, even after 89 averages. In the case where no prior knowledge of the structure was available, mode selection would be a time consuming task. Figure 7.45 shows the averaged synthesised FRFs from the ARMAX results selected by the NPDP model selection criterion, for the SIMO E3 analysis (estimated using 2048 samples). The dotted lines indicate the natural frequencies of the selected modes, which are clearly represented, except for mode 4 at approximately 114 Hz, which had a poor response at a number of measurement points. It is emphasised that these results were estimated from 2048 data points in contrast to the 89 × 2048 samples used by RFLS algorithm with synchronous averaging.

A peak at 120 Hz is evident in both figure 7.44 and 7.45, and could easily be mistaken for a structural mode without the knowledge that the peak is due to the unmeasured periodic excitation. The use of backwards ARX models in the ARMAX estimation algorithm provides a means to help distinguish between spurious modes and vibration modes, based on the sign of the damping. Figure 7.46 shows the damping estimated for a mode at 119.5 Hz (SIMO E3 analysis), which corresponds to a frequency present in the unmeasured periodic excitations.

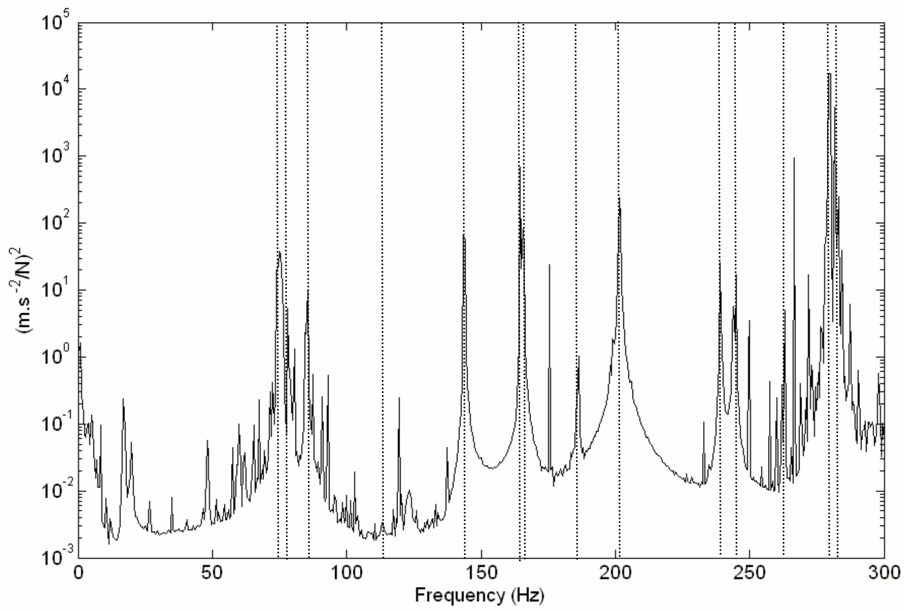

Figure 7.44 Averaged, squared imaginary part of measured FRFs from the RFLS E3 av analysis. The dotted lines indicate the peaks that were selected in the curve fitting processing.

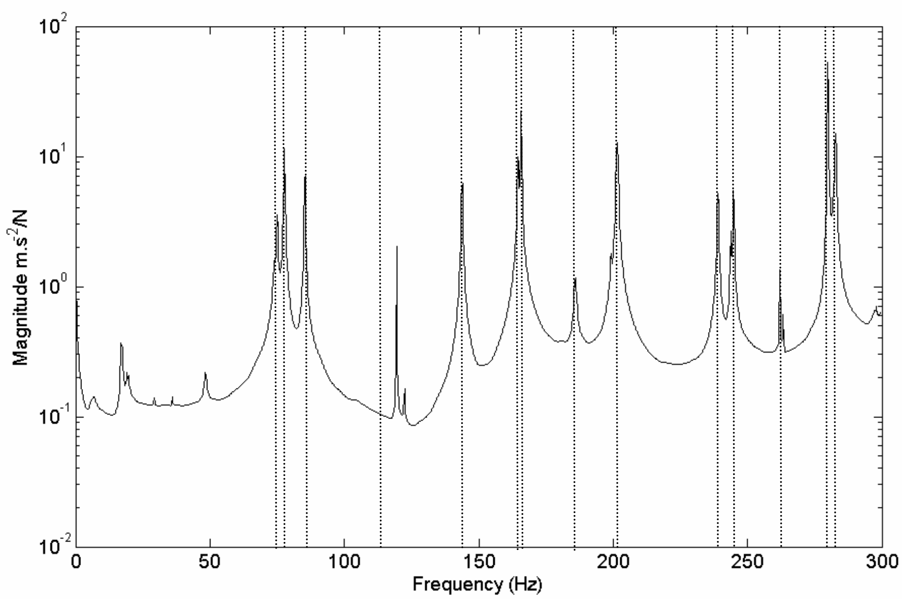

Figure 7.45 Averaged FRFs estimated in the SIMO E3 analysis. The dotted lines indicate the peaks that were selected as vibration modes.

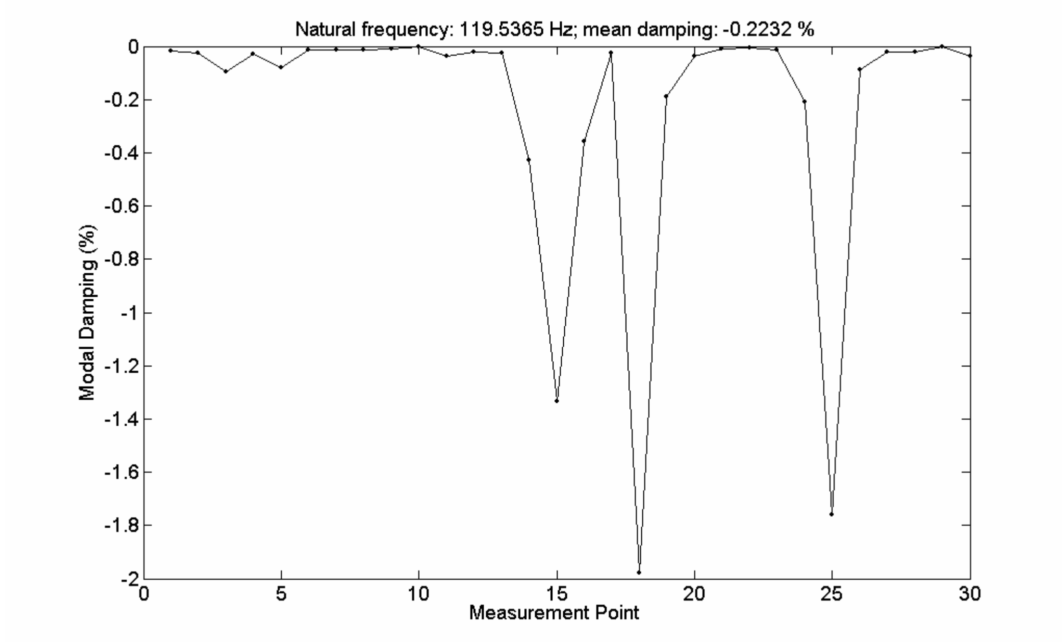

Figure 7.46 SIMO E3 analysis damping estimates at each measurement point for a spurious mode at 120 Hz, which corresponds to a component of the unmeasured periodic excitation.

The damping estimated at every measurement point is negative, which indicates that either the estimation is heavily biased by noise, or the mode is not a true vibration mode. FRFs synthesised from the estimation ARMAX model show a very narrow peak around 119 Hz for most measurement points. The sign of the damping is not a strong criterion when used in isolation, as SIMO E3 analysis yielded three vibration modes with negative damping (averaging reduced the number of negatively damped vibration modes to two). Synthesised FRFs revealed that the vibration modes estimated with negative damping had relatively poor responses at some measurement points, which contrasts to the way the unmeasured periodic excitations are modelled by the ARMAX model, i.e. with prominent narrow peaks. An advantage with using the ARMAX algorithm is that FRFs can be synthesised with any resolution. However, measured FRFs, used by the RFLS algorithm, have resolution determined by the experimental set-up, and can be subject to leakage effects, which would increase the difficulty of distinguishing between a vibration mode and a spurious mode on the basis of the shape of the peak in the FRF. Effectively distinguishing between spurious modes and vibrational modes requires a number of different tools. The ARMAX algorithm estimates a model that accurately fits the measured data and the mode selection process is aided by the sign of the modal damping, smooth synthesised FRFs and multiple estimates of global parameters allowing statistical analysis of the results.

7.6 Coupling of Structural Excitation Sources

In Chapter 6, the performance of the ARMAX algorithm was tested under a similar set of noise conditions using experimental data obtained from an aluminium beam. It was shown that the addition of unmeasured random noise had a significant effect on the accuracy of damping values. A major difference between the tests discussed in Chapter 6 and those carried out on the helicopter-like structure was the source of excitation and the measurement of the excitation signal. Applied voltage was used as the excitation signal for the beam experiments and applied force was measured for the helicopter-like structure testing. The beam experiments using piezoceramic actuators for excitation satisfied the requirement that the excitation sources were uncorrelated, therefore the unmeasured excitation sources were truly unmeasured. This was not the case for the helicopter-like structure, which involved coupling between the structure and the shakers as well as between the measured excitation signals. The coupling was due to the rigid mounting of the shakers and because the shakers were not small compared with the helicopter-like structure.

Figures 7.47 – 7.49 plot an estimate of the coherence function for the two excitation signals used in Experiments 1 – 3, respectively. The coherence function is defined as [128]

$$\gamma_{12}^2(f)=\frac{\left|G_{12}(f)\right|^2}{G_{11}(f)\cdot G_{22}(f)}\ , \qquad\qquad 0\le\gamma_{12}^2(f)\le 1, \tag{7.1}$$

where $G_{11}(f), G_{22}(f)$ are the estimates of the auto-spectra for excitation 1 and excitation 2, respectively, and $G_{12}(f)$ is an estimate of the cross-spectrum between excitation 1 and excitation 2. The coherence functions were calculated using a Hanning window, 66% overlap, and 268 averages.

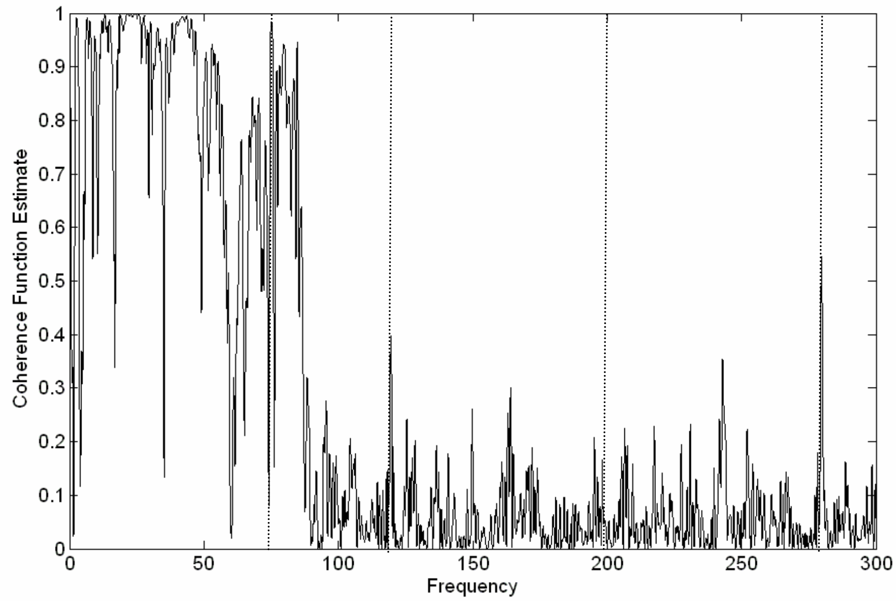

Figure 7.47 Estimated coherence function between excitation 1 (pseudo-random excitation) and excitation 2 (periodic excitation, 75.5Hz, 120Hz, 200Hz, and 281Hz), for Experiment 1. Vertical dotted lines mark frequencies of periodic excitation.

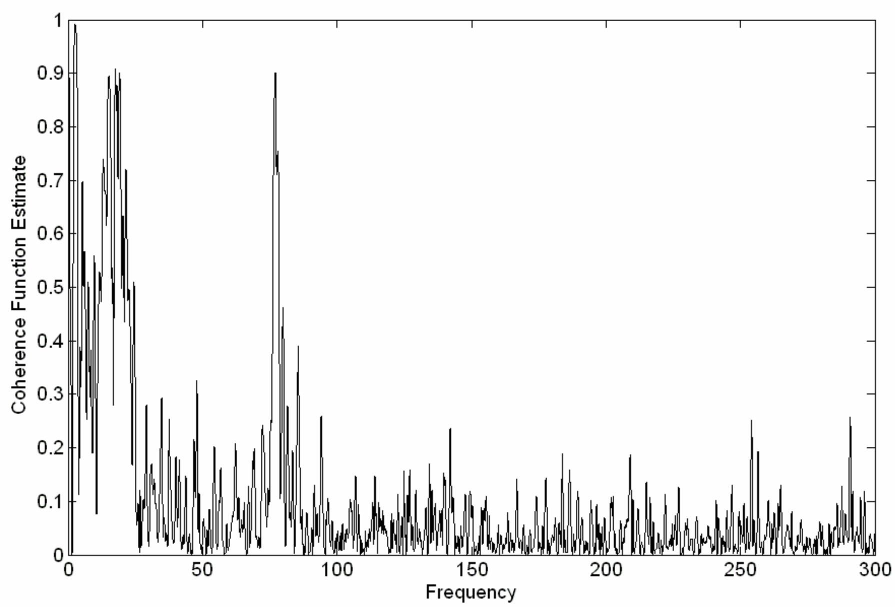

Figure 7.48 Estimated coherence function between excitation 1 (pseudo-random excitation) and excitation 2 (continuous random excitation), for Experiment 2.

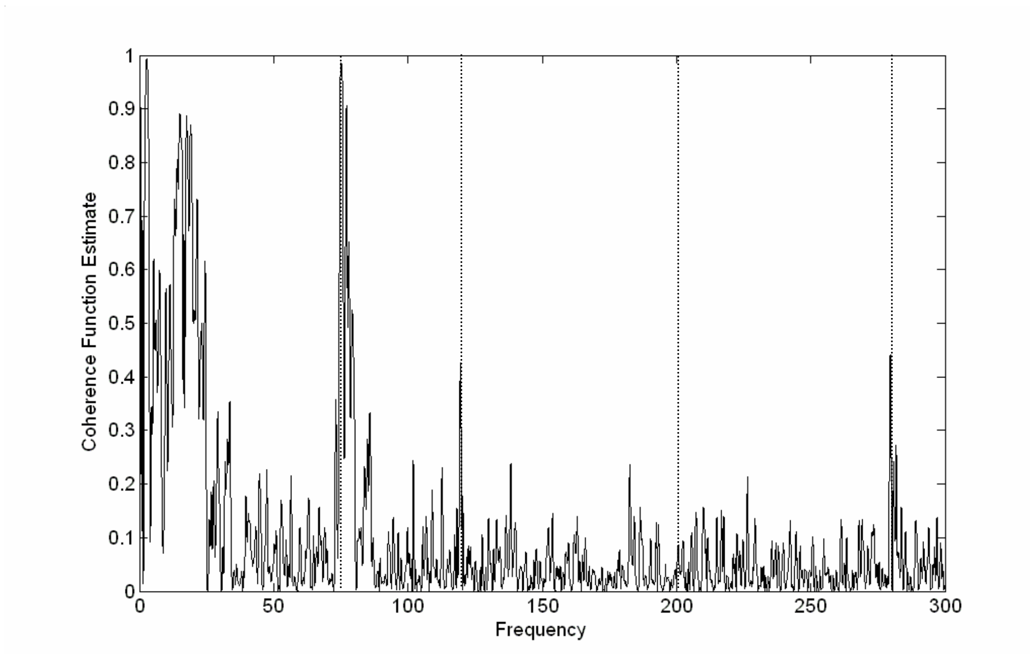

Figure 7.49 Estimated coherence function between excitation 1 (pseudo-random excitation) and excitation 2 (continuous random and periodic excitation, 75.5Hz, 120Hz, 200Hz, and 281Hz), for Experiment 3. Vertical dotted lines mark frequencies of periodic excitation.

Coupling between the shakers and structure is indicated by peaks in the coherence functions, and a number of peaks can be seen in figure 7.47. These are located at the frequencies of the unmeasured periodic excitation, especially at 75.5 Hz. In addition to these peaks, there is significant coupling at low frequencies in the experiment 1 data, and also around the first two modes (74Hz & 77Hz). This can clearly be seen in figure 7.48, as Experiment 2 used unmeasured random noise, and little correlation between the excitation signals can be seen at other frequencies. While some correlation between the excitation signals exists, in particular around the frequencies of the unmeasured excitation, the assumption of unmeasured excitation is still considered to be valid.

7.7 Conclusions

Experimental tests on a helicopter-like structure were carried out in order to test the performance of the ARMAX estimation algorithm for a structure with a more complex dynamic behaviour. Closely spaced modes, DOFs with poor vibration responses for at a number of measurement points, and significant unmeasured excitations including periodic components close to natural frequencies were characteristics of the tests discussed in this chapter. The ARMAX algorithm was shown to achieve acceptable accuracy under noise-free conditions and results were in agreement with a RFLS estimation algorithm except for three of the fourteen modes, which were found to have poor mode shape correlation. The ARMAX algorithm also estimated reasonably accurate results in the presence of 200% periodic excitation, 89% random excitation, and the superposition of random and periodic excitation. Systematic inaccuracies were observed in all tests for modes with low vibration response at a number of measurements points, and the MAC value, which was used to compare mode shape results, was found to be sensitive to poor results at a small number of measurement points. The use of a pseudo-random excitation signal allowed excitation and response-measurements to be synchronously averaged. Synchronous averaging improved ARMAX damping estimates for modes estimated with negative damping for cases with unmeasured excitation; though little improvement was observed in other modal parameters. Similarly, the RFLS curve-fitting algorithm did not appear to significantly benefit from increased numbers of averages (20 to 89). The ARMAX algorithm was found to obtain more accurate mode shape results for cases with unmeasured excitations, compared to the RFLS algorithm; however this is qualified by the results for noise-free data, where three of the fourteen modes showed poor mode shape correlation. The accuracy of frequency and damping results was comparable for cases with unmeasured excitation, although the ARMAX algorithm used 2048 data samples to achieve these results, compared with the 89×2048 samples used by the RFLS algorithm applied to synchronously averaged data.

The following chapter presents a preliminary study of an adapted ARMAX algorithm aimed at identifying modal parameters from response measurements. This work is carried out with the broad aim of developing a general modal parameter estimation algorithm that utilises vibration response data obtained under any condition: with measured excitation data; with measured and unmeasured excitation; and using response measurements exclusively.

Chapter 8 Modal Parameter Identification from Vibration Response Measurements

8.1 Introduction

In chapter 5, an ARMAX-based algorithm was introduced to estimate modal parameters from excitation and response measurements in the presence of significant unmeasured excitation. The testing of the algorithm was discussed in Chapter 6 and it was demonstrated that the algorithm performed reasonably well in the presence of unmeasured excitation, although the accuracy of estimated modal parameters decreased for increasing levels of unmeasured excitation. It is therefore expected that for very high levels of unmeasured excitation, the ARMAX algorithm would yield inaccurate results. An algorithm that estimates modal parameters from response measurements could potentially be of benefit in these cases, and may provide insight into, or lead to improvements for the I/O algorithm. Therefore, a preliminary investigation of the adaptation of the ARMAX algorithm for use with response measurements is presented in this chapter. Two different algorithms are adapted from the ARMAX I/O algorithm and their performance is assessed using simulated vibration data from a 2 DOF system and experimental data obtained from a cantilever aluminium beam.

In the following section, a range of existing response-only modal analysis algorithms are reviewed. Issues which arise in adapting the ARMAX algorithm for use with response measurements are discussed in section 8.3 and two adapted algorithms are presented in section 8.4. Numerical and experimental tests are discussed in section 8.5 and section 8.6, respectively, and concluding remarks are made in section 8.7.

8.2 Review of Response-Only Modal Analysis Algorithms

Response-only modal analysis methods estimate modal natural frequencies, damping and mode shapes from vibration response data measured from a structure without any explicit knowledge of the excitation. Many of the techniques have been adapted from classical input/output modal analysis methods and assume the excitation applied to the structure approximates white noise.

The most basic method is the peak-picking method [38, 128, 129], which involves identifying resonant peaks in a spectrum and subsequently identifying modal parameters. As discussed in section 2.2, the peak picking method was originally applied to frequency response function (FRF) data (cf. equations (2.5) and (2.8)). The response-only version of the peak-picking method is applied to the matrix of auto- and cross-spectra of the response measurements,

$$\mathbf{S}_y(j\omega) = \mathbf{H}(j\omega)\mathbf{R}_u\mathbf{H}^T(-j\omega), \qquad [s \times s] \tag{8.1}$$

where $\mathbf{S}_y$ is the matrix of auto- and cross-spectra of the response measurements, **H** is the transfer function matrix, and $\mathbf{R}_u$ is the spectral density matrix of the unmeasured white-noise excitations. Natural frequency and damping estimates can be obtained from the peaks in the response spectra and at these points equation (8.1) can be approximated as [38]

$$\mathbf{S}_y(j\omega_i) \approx \alpha_i \Phi_i \Phi_i^H, \tag{8.2}$$

and is used to determine Φ_i, the mode shape of the *i*th mode. $(\cdot)^H$ is the conjugate transpose of a matrix and α_i is a constant determined by the natural frequency, damping, modal participation factor, and excitation spectral density matrix. Note that proper scaling of mode shapes cannot be resolved because the contribution of the excitation spectral density matrix is unknown.

The peak picking method can be applied very quickly, particularly as FFT analysers, which are widely used in I/O modal analysis, typically calculate auto- and cross-spectra. Bendat & Piersol [128] demonstrate that the phase and coherence data associated with cross-spectra may be used to confirm the presence of modes: the coherence around resonant peaks should approach 1, reflecting the high signal-to-noise ratio and the linear relationship between response measurements; the phase of lightly damped modes will be close to zero or 180°.

The peak-picking method is limited by the resolution of the spectra, and results will be poor if the assumptions of lightly-damped and well-spaced modes are not valid. Operational deflection shapes, as opposed to mode shapes, will be estimated at frequencies where more than one mode contributes to the response. Cases where the excitation is not white will also cause problems. It is noted by Bendat and Piersol [128] that narrow band excitation may be identified by peaks in the cross-spectra that have phases other than zero and 180°. A further issue is the subjective nature of picking resonant peaks; however, good knowledge of the system under test is a critical factor and an advantage for all modal analysis techniques.

A variation of the peak picking method is the frequency domain decomposition (FDD) method [38, 129-131], which identifies modal parameters from the singular value decomposition (SVD) of the spectrum matrix. Peeters & De Roeck [38] noted that the FDD method is a renamed version of the complex modal indicator function (CMIF), which has been applied to both response measurements and FRF data (see section 2.2), and is useful for identifying the presence of closely spaced vibrational modes.

The SVD of the spectrum matrix (equation (8.1)), is written as [38]

$$\mathbf{S}_y(j\omega) = \mathbf{U}(j\omega)\boldsymbol{\Sigma}(j\omega)\mathbf{U}^H(j\omega), \tag{8.3}$$

where $\mathbf{U}(j\omega)$ ($s \times s$) is the matrix of singular vectors, which correspond to the singular values that are the elements of the diagonal matrix $\boldsymbol{\Sigma}(j\omega)$. The singular values indicate the rank of the spectrum matrix at a particular frequency, and the rank is determined by the number of modes that significantly contribute to the response at that frequency. A resonant frequency of a well-spaced mode will be indicated by a local maximum of one singular value at the resonant frequency. Closely spaced modes will be indicated by local maxima in separate singular values. This characteristic addresses a limitation of the classical peak-picking method described above, which assumes well-spaced modes. Re-writing equation (8.3) as

$$\mathbf{S}_y(j\omega) = \sum_{r=1}^{s} \mathbf{u}_r(j\omega)\sigma_r(j\omega)\mathbf{u}_r^H(j\omega) \tag{8.4}$$

and comparing with equation (8.2) shows that the singular vector for a dominant singular value at a resonant peak is an estimate of the mode shape vector.

The basic version of the FDD method determines modal frequencies to the resolution of the spectrum matrix and does not directly yield damping values. As with the classical peak-picking method, SDOF curve-fitting techniques can be applied to a region around the local maximum of a singular value spectrum to yield an improved frequency estimate and modal damping. The enhanced frequency domain decomposition (EFDD), outlined by Gade et al [131], isolates a SDOF 'bell function' in the singular value spectrum using the modal assurance criterion (MAC) to ensure mode shapes at frequencies within the frequency band correlate with a given threshold value. The isolated bell function is transformed into the time-domain to yield a correlation function and the damped natural frequency is estimated by counting zero-crossings per unit time. Modal damping is estimated by curve-fitting the logarithmic envelope of the correlation function. The FDD and EFDD techniques have been implemented in the ARTeMIS operational modal analysis software package produced by Structural Vibration Solutions. Numerous applications of both techniques are discussed by Brincker & Møller [65].

Correlation functions between response measurements are the starting point for a number of other methods, broadly referred to as the Natural Excitation Technique (NExT) [19, 20, 113, 132, 133], which involves calculating auto- and cross-correlation functions between response measurements, estimating global modal parameters from correlation functions using time-domain modal parameter identification, and finally estimating mode shapes. The basis of the technique is that the correlation functions between response measurements are a sum of decaying sinusoids with the same natural frequencies and damping ratios as the system's impulse response functions. A summary of the derivation by James et al [132] is given below.

The impulse response of a system measured at point *k* due to an input at point *i* can be written

$$x_{ik}(t) = \sum_{r=1}^{n} \frac{\phi_i^r \phi_k^r}{m^r \omega_d^r} \exp\left(-\varsigma^r \omega_n^r t\right) \sin\left(\omega_d^r t\right), \tag{8.5}$$

where ω_n^r, ς^r, are the natural frequency and damping of the rth mode, respectively; $\omega_d^r = \omega_n^r \sqrt{1-(\varsigma^r)^2}$; m^r the rth modal mass; and ϕ_i^r is the rth, mode shape at point $\boldsymbol{i}$. The response due to an arbitrary force applied at point $\boldsymbol{k}$, f_k, is

$$x_{ik}(t) = \sum_{r=1}^{n} \phi_i^r \phi_k^r \int_{-\infty}^{t} f_k(\tau) g^r(t-\tau) d\tau \, , \tag{8.6}$$

where

$$g^r(t) = \frac{1}{m^r \omega_d^r} \exp\left(-\varsigma^r \omega_n^r t\right) \sin\left(\omega_d^r t\right). \tag{8.7}$$

The cross correlation between response measurements at points $\boldsymbol{i}$ and $\boldsymbol{j}$, due to an input at point $\boldsymbol{k}$ is

$$R_{ijk}(T) = E\left[\; x_{ik}(t+T)\, x_{jk}(t) \;\right], \tag{8.8}$$

where E is the expectation operator. Substituting equation (8.6) into (8.8) gives

$$R_{ijk}(T) = \sum_{r=1}^{n} \sum_{s=1}^{n} \phi_i^r \phi_k^r \phi_j^s \phi_k^s \int_{-\infty}^{t} \int_{-\infty}^{t+T} g^r(t+T-\sigma) g^s(t-\tau) E\left[f_k(\sigma) f_k(\tau)\right] d\sigma \, d\tau \, , \tag{8.9}$$

which can be further simplified noting that the autocorrelation for a white noise input is

$$R_{ff}^k(\tau-\sigma) = E\left[f_k(\tau) f_k(\sigma)\right] = \alpha_k \, \delta(\tau-\sigma). \tag{8.10}$$

The last equality in the above equation is a scaled Dirac Delta function; the scaling constant α_k can be pulled outside the integrals in equation (8.9) and the delta function evaluated by the first integral:

$$R_{ijk}(T) = \sum_{r=1}^{n} \sum_{s=1}^{n} \alpha_k \phi_i^r \phi_k^r \phi_j^s \phi_k^s \int_{-\infty}^{t} g^r(t+T-\tau) g^s(t-\tau) \, d\tau \, . \tag{8.11}$$

Equation (8.11) is written as a definite integral by substituting $\lambda = t - \tau$ and changing the variable of integration

$$R_{ijk}(T) = \sum_{r=1}^{n} \sum_{s=1}^{n} \alpha_k \phi_i^r \phi_k^r \phi_j^s \phi_k^s \int_0^\infty g^r(\lambda + T) g^s(\lambda)\, d\lambda \,. \tag{8.12}$$

Expanding $g^r(\lambda + T)$ using the trigonometric addition formulas gives

$$g^r(\lambda + T) = \left[\exp\left(-\varsigma^r \omega_n^r T\right)\cos\left(\omega_d^r T\right)\right]\frac{\exp\left(-\varsigma^r \omega_n^r \lambda\right)\sin\left(\omega_d^r \lambda\right)}{m^r \omega_d^r}$$

$$+ \left[\exp\left(-\varsigma^r \omega_n^r T\right)\sin\left(\omega_d^r T\right)\right]\frac{\exp\left(-\varsigma^r \omega_n^r \lambda\right)\cos\left(\omega_d^r \lambda\right)}{m^r \omega_d^r} \tag{8.13}$$

and the expressions for $g^r(\lambda)$ and $g^r(\lambda+T)$ are substituted into equation (8.12) and functions of T are separated from those of λ:

$$R_{ijk}(T) = \sum_{r=1}^{n} \left[G_{ijk}^r \exp\left(-\varsigma^r \omega_n^r T\right)\cos\left(\omega_d^r T\right) + H_{ijk}^r \exp\left(-\varsigma^r \omega_n^r T\right)\sin\left(\omega_d^r T\right)\right], \tag{8.14}$$

where

$$\begin{Bmatrix} G_{ijk}^r \\ H_{ijk}^r \end{Bmatrix} = \sum_{s=1}^{n} \frac{\alpha_k \phi_i^r \phi_k^r \phi_j^s \phi_k^s}{m^r \omega_d^r m^s \omega_d^s} \int_0^\infty \exp\left(-\varsigma^r \omega_n^r - \varsigma^s \omega_n^s\right)\lambda \sin\left(\omega_d^s \lambda\right) \begin{Bmatrix} \sin\left(\omega_d^r \lambda\right) \\ \cos\left(\omega_d^r \lambda\right) \end{Bmatrix} d\lambda \,. \tag{8.15}$$

Equation (8.14) shows that the correlation function between two response measurements is a sum of scaled sinusoidal functions in terms of the natural frequencies and damping of the system. Evaluating the integral in equation (8.15) and further manipulation yields

$$R_{ij}(T) = \sum_{r=1}^{n} \frac{\phi_i^r A_j^r}{m^r \omega_d^r} \exp\left(-\varsigma \omega_n^r T\right)\sin\left(\omega_d^r T + \Theta^r\right), \tag{8.16}$$

which clearly shows the summation of damped sinusoidal components. A_j^r and Θ^r are the scaling and phase factors.

A number of studies has shown that correlation functions between response measurements can be used as inputs into existing I/O modal analysis algorithms. James et al. [132] applied the Polyreference technique and Eigensystem Realisation Algorithm (ERA) to correlation functions calculated form simulated and experimental data obtained from a wind turbine. Details of the Polyreference technique and ERA can be found in [30]. Results were generally good; however, some difficulty was encountered when trying to identify closely spaced modes. Estimates of some modal parameters were less accurate when amplitudes of correlation functions at particular modes were low compared to the noise level. It was demonstrated that NExT successfully identified total damping due to structural and aero-elastic effects while the wind turbine was in operation. This is a key feature of operational modal analysis. In a subsequent study investigating the dynamic properties of a bridge excited by traffic loading, Farrar and James [19] first isolated peaks in the cross-spectrum by zero-padding the remaining spectrum before calculating the filtered correlation function using the inverse Fourier transform. The filtered correlation functions were curve fitted for frequency and damping results using the complex exponential curve fitting method, which could also be set to fit multiple modes for cases where closely spaced modes were present. Mode shapes were determined from amplitude and phase data in the cross-spectra.

Hermans and Van der Auweraer [20] applied the NExT using least squares exponential (LSCE) modal parameter estimation to three industrial cases: analysis of the rear suspension of a car; flight flutter data from a commercial aircraft; and data obtained from a bridge under ambient excitation. Results from the first case identified a problematic mode in the rear suspension and comparison of NExT and I/O modal analysis results showed good correlation of the mode shape, a small decrease in natural frequency but a significant increase in damping, which reflected the role of mounting the suspension and operating test conditions. The second case analysed response data from the wing tip of a commercial aircraft. The test utilised burst swept sine excitation and modal parameters obtained from NExT were compared with a maximum-likelihood frequency domain algorithm applied to both the excitation and response data. The NExT results showed moderate variability compared to the I/O results and state-space response-only modelling (discussed below). The final case considered in this study was vibration response data obtained from a bridge. The results of the NExT were apparently sensitive to the number of reference measurements used when calculating the correlation functions; results were less accurate for a larger number of references, but overall a reasonable correlation between synthesised auto-spectra and measured auto-spectra was achieved.

Peeters and De Roeck [38] noted that autoregressive (AR) modelling of correlation functions is one method in the class of instrumental variable (IV) methods. The correlation-driven polyreference time domain technique is another IV method, which also includes the LSCE and Ibrahim Time Domain (ITD) techniques as special cases.

An AR model describing the correlation functions of vibration response measurements can be derived from an autoregressive moving average (ARMA) model describing the vibration of a structure [38]:

$$\mathbf{y}[t]+\mathbf{A}_1\mathbf{y}[t-1]+\ \cdots\ +\mathbf{A}_{na}\mathbf{y}[t-na]=\mathrm{e}[t]+\mathbf{B}_1\mathbf{e}[t-1]+\ \cdots\ +\mathbf{B}_{nb}\mathrm{e}[t-nb]\,, \tag{8.17}$$

where $\mathbf{y}[t]$ is the s dimensional response vector and $e[t]$ is an s dimensional white noise sequence representing the unmeasured excitation. The coefficients of the response vector are $s \times s$ matrices and termed the AR coefficients. Similarly, those of the white noise sequence are termed MA coefficients. $nb = na$ for a vibrating structure and na is the order of the ARMA model; $na = n/s$ for ideal white noise excitation and noise-free response data, where n is the number of modes to be modelled. IV methods reformulate a model in terms of a new data vector, termed the instruments, which are assumed to fulfil certain conditions. For the case considered here, $e[t]$ is assumed to be uncorrelated with past response data, i.e. $\mathbf{y}[t-i]$, $i > na$, which means that post-multiplying equation (8.17) by $\mathbf{y}^T[t-na-i]$ and taking the expectation yields

$$R_{na+i}+\mathbf{A}_1R_{na+i-1}+\ \cdots\ +\mathbf{A}_{na}R_i=\mathbf{0}\,. \qquad i > 0 \tag{8.18}$$

Equation (8.18) is solved by writing an over-determined system of equations for all possible time lags and finding the least-squares (LS) solution. The modal parameters of the system are calculated from eigenvalue decomposition of the bottom companion matrix of AR coefficients [38]:

$$\begin{pmatrix} \mathbf{0} & \mathbf{I}_s & \cdots & \mathbf{0} \\ \mathbf{0} & \mathbf{0} & \cdots & \mathbf{0} \\ \cdots & \cdots & \cdots & \cdots \\ \mathbf{0} & \mathbf{0} & \cdots & \mathbf{I}_s \\ -\mathbf{A}_{na} & -\mathbf{A}_{na-1} & \cdots & -\mathbf{A}_1 \end{pmatrix} \begin{pmatrix} \mathbf{V} \\ \mathbf{V}\Lambda_d \\ \cdots \\ \mathbf{V}\Lambda_d^{na-2} \\ \mathbf{V}\Lambda_d^{na-1} \end{pmatrix} = \begin{pmatrix} \mathbf{V} \\ \mathbf{V}\Lambda_d \\ \cdots \\ \mathbf{V}\Lambda_d^{na-2} \\ \mathbf{V}\Lambda_d^{na-1} \end{pmatrix} \Lambda_d , \tag{8.19}$$

where Λ_d is a diagonal matrix of the discrete-time eigenvalues, μ_i, and $\mathbf{V}$ is the matrix of mode shapes taken from the first s rows of the eigenvector matrix. The natural frequencies and damping are related to the discrete-time eigenvalues by the following equations [38]

$$\mu_i = \exp(\lambda_i T_s) \tag{8.20}$$

$$\lambda_i , \lambda_i^* = -\varsigma_i \omega_i \pm j\omega_{n\,i}\sqrt{1-\varsigma_i^2} \tag{8.21}$$

Desforges et al. [134] fitted the correlation functions of response measurements using an autoregressive (AR) model and developed a strategy for accounting for coloured input noise in a subsequent paper [135]. If the excitation signal is corrupted by white noise, the AR model can be estimated from correlation functions at lags other than zero, as the zeroth lag would be affected by the corrupting white noise. Similarly, a coloured excitation described by a moving average sequence containing a finite number of terms would have a correlation sequence corrupted at a finite number of lags and these could be avoided when estimating an AR model. The case where periodic excitations are present is also considered and in this case the AR model would identify poles at the frequencies of the periodic excitation. These spurious poles could be identified by the variability of the damping estimates or the phase of the correlation functions.

Correlation functions have also been used in the estimation of state-space models, which can be used to represent a vibrating structure. An early implementation involved applying the ERA algorithm to correlation functions [132] and further studies have pointed out that the ERA is a particular case of the subspace identification method [38, 129]. A state space model is represented by

$$\mathbf{x}[t+1] = \mathbf{A}\mathbf{x}[t] + \mathbf{w}[t] \tag{8.22}$$

$$\mathbf{y}[t] = \mathbf{C}\mathbf{x}[t] + \mathbf{v}[t]\,, \tag{8.23}$$

where $\mathbf{x}[t]$ is the *2n* dimension state vector (*n* the number of vibration modes), **A** is the state transition matrix, $\mathbf{w}[t]$ the contribution from unmeasured excitation and noise, **C** the output matrix relating the state vector to measured outputs, and $\mathbf{v}[t]$ is another disturbance term representing measurement noise and unmeasured excitations. The two disturbance terms are assumed to be zero-mean white noise sequences, but it has been shown that subspace modelling of systems with non-stationary white noise (i.e. having a time varying covariance matrix) inputs is possible [136].

The estimation of state-space models (see for example [20, 26, 38, 129, 133, 137-139]) involves constructing Toeplitz matrix (a matrix with constant negative-sloping diagonals) from the correlation functions of response measurements:

$$\mathbf{T}_{1|i} = \begin{pmatrix} \mathbf{R}_i & \mathbf{R}_{i-1} & \cdots & \mathbf{R}_1 \\ \mathbf{R}_{i+1} & \mathbf{R}_i & \cdots & \mathbf{R}_2 \\ \cdots & \cdots & \cdots & \cdots \\ \mathbf{R}_{2i-1} & \mathbf{R}_{2i-2} & \cdots & \mathbf{R}_i \end{pmatrix} = \begin{pmatrix} \mathbf{C} \\ \mathbf{CA} \\ \cdots \\ \mathbf{CA}^{i-1} \end{pmatrix} \left(\mathbf{A}^{i-1}\mathbf{G} \quad \cdots \quad \mathbf{AG} \quad \mathbf{G} \right) = \mathbf{O}_i \mathbf{\Gamma}_i \tag{8.24}$$

The second equality follows from the decomposition of the covariance matrix: $\mathbf{R}_i = \mathbf{CA}^{i-1}\mathbf{G}$; $\mathbf{G} = E\left[\, x[t+1] \;\; y^T[t] \,\right]$. $\mathbf{O}_i$ and $\mathbf{\Gamma}_i$ are the extended observability and reverse extended controllability matrices, respectively, and it can be shown that these can be obtained from the singular value decomposition of the covariance matrix [137]. $\mathbf{O}_i$ and $\mathbf{\Gamma}_i$ are subsequently used in a set of equations involving the unknown **A** and **C** matrices and modal parameters are then calculated by the eigenvalue decomposition of the state transition matrix

$$\mathbf{A} = \mathbf{\Psi}\mathbf{\Lambda}_d\mathbf{\Psi}^{-1}, \tag{8.25}$$

where $\mathbf{\Psi}$ is the eigenvector matrix and $\mathbf{\Lambda}_d$ a diagonal matrix of eigenvalues. Natural frequencies and damping are obtained from equations (8.20) and (8.21), and mode shapes are related to the eigenvectors by

$$\mathbf{V} = \mathbf{C}\mathbf{\Psi} \tag{8.26}$$

The size of the Toeplitz matrix in equation (8.24) is determined by *i*, however, its rank is 2*n*. The singular value decomposition of the Toeplitz matrix is calculated and a new truncated matrix (hence the name subspace methods) can be formed of dimension 2*n.* However, *n* is rarely known accurately so methods such as determining a significant drop in the singular values, statistical tests, or stabilisation diagrams are used to determine the correct size (rank) of the state transition matrix.

Weighting of the Toeplitz matrix leads to particular cases of subspace estimation algorithm; for example, canonical variate analysis (CVA), which may help identify poorly excited modes [20]. Balanced realisation (unweighted principal components (UPC)) involves no weighting.

A number of studies has used subspace estimation to identify modal parameters of real and simulated structures, for example, steel mast structures [137], and also bridges, cars and planes [20]. The quality of estimated modal parameters demonstrates the effectiveness of the algorithm in identifying lightly damped and in some cases closely spaced modes. The use of long data records allows averaging to be used when calculating correlation functions and this improves the s/n ratio. Stabilisation diagrams were found to be most useful for model order selection and selected models typically differed in order for each set of data used for a particular analysis.

Mevel et al [24] applied covariance driven subspace algorithms to vibration data from an aircraft during flight. Comparisons between I/O and response only algorithms suggested that if good quality excitation data is available, I/O modal parameter estimates were generally more accurate, particularly for short data records; however, if excitation data is of poor quality, response-only algorithms were more effective. Stabilisation diagrams were the main tool for model selection in this study. Another study of subspace identification of vibration data obtained from an airplane during flight was reported by Abdelghani et al [22]. Some difficulties were encountered when identifying very closely spaced modes and estimated damping for some modes was noted to be incorrect. In general, the results compared well with ground test results. The number of modes (approximately 27) modelled in this study was relatively large. The size of the model was therefore large and it was observed that modelling data from a large number of sensors did not have any advantage over a limited number of sensors (e.g. 4 – 6).

Basseville et al [26] investigated in-flight modal analysis of a helicopter and noted that periodic excitations due to main and tail rotors were modelled as poles by the subspace estimation algorithm. The vibration modes were distinguished from spurious modes due to rotating components by use of stabilisation diagrams and prior knowledge of the angular velocity of rotating components. In addition, modes modelling rotating components generally are found to have very low damping.

Another study investigating in-flight modal analysis of a helicopter was reported by Hermans et al [25]. Subspace estimation was used to estimate modal parameters from vibration measurements and results were shown to be sensitive to the sampling rate of the signals. Low frequency modes were poorly identified for data sampled at high frequencies. An additional consideration was the increased time taken to estimate correlation functions and the larger number of time lags (size of Toeplitz matrix in equation (8.24)) required to estimate subspace models from data sampled at high frequencies. Results demonstrated a significant amount of scatter in estimated damping values for all modes and the number of modes identified was sensitive to the sampling rate. Mode shapes did not correlate well with ground test results with MAC values below 50%. LSCE curve fitting of vibration response measurements yielded significantly better MAC values indicating the limitations of the subspace algorithms for this particular case.

The above discussion was limited to modal parameter estimation algorithms which utilised time-domain correlation functions as input data. Similar mathematical models that are identified from frequency domain data exist [33], and Shen et al [140] discussed the use of a polyreference frequency domain estimation algorithm for use with auto- and cross-spectra of response measurements. This technique is aimed at overcoming the well-known limitations of the peak-picking methods described above. Another frequency domain method is the PolyMAX technique [141], which identifies a frequency-domain model from auto- and cross-spectra. The latter algorithm is included in commercial software from LMS International, and application of the technique was reported in a number of studies [65].

The random decrement technique [30, 134, 142, 143] produces a signal, the random dec signature, which is similar to the free vibration response of a structure. The most basic form is calculated from the vibration responses due to a random excitation. For a given trigger condition, $Tx(t_i)$, records of length τ are ensemble-averaged. That is,

$$D_{XX}(\tau)=\frac{1}{M}\sum_{i=1}^{M}x(t_i+\tau)|\,Tx(t_i) \text{ and } D_{XY}(\tau)=\frac{1}{M}\sum_{i=1}^{M}y(t_i+\tau)|\,Tx(t_i) \tag{8.27}$$

are the auto and cross random dec signature, respectively, calculated from M averages.

The random dec signatures are proportional to the correlation functions of the responses under the assumptions of Gaussian zero-mean stationary excitation and a linear structure. Given these properties, all the modal parameter identification algorithms that can be applied to correlation functions can similarly be applied to random dec signatures or their Fourier transform. Rodrigues [142] pointed out that the random decrement technique is a more efficient computation than direct calculation of correlation functions, or under some circumstances, methods using auto- and cross-spectra. The use of FDD and stochastic subspace algorithms to estimate modal parameters from random dec signatures from ambient vibration tests of a bridge were reported by Rodrigues [142]. Both methods produce similar results and good quality mode shapes; however, comparisons with other techniques were not discussed.

Data driven state-space identification methods estimate a state-space model (equations (8.22) and (8.23)) directly from response data as opposed to the approach that utilises correlation functions, described above. Van Overschee and De Moor [42] outlined a method that applied QR decomposition to a matrix of response measurements. This technique was adapted by Peeters and De Roeck [137] to use a set of reference sensors, thereby reducing the dimension of matrices used in the estimation and improving computation time. Another benefit is that the reference sensors can be chosen to include the best response from all vibration modes, which may improve the quality of estimated modal parameters. Experimental studies that apply these techniques include testing a steel antenna mast [137], and wind turbine wing [130]. Data-driven subspace estimation results from the first study are in good agreement with the covariance-driven subspace algorithm, and in the second study results compare well with FDD and EFDD. It was pointed out that the reference-sensor based technique is faster in terms of computation time, though prediction errors were slightly higher at measurement points that were not used as reference sensors. Neither study compared the use of smaller numbers of response measurements in each measurement set with the use of reference sensors in a measurement set containing a larger number of response measurements. A version of the data-driven subspace identification is included in the ARTeMIS software from Structural Vibration Solutions. Different weighting methods can be applied in the subspace algorithms: unweighted principal components (UPC) (balanced realisation/no weighting), principal components (PC), or canonical variate analysis. Reference channels can also be selected.

As noted above, it can be shown that an ARMA model (equation (8.17)) can represent the dynamic behaviour of a mechanical system. He and De Roeck [144] and He and Fu [30] derived an ARMA model directly from the continuous-time transfer function and Peeters [38] reported that this result can be arrived at by establishing a relationship between an ARMA model and a state-space model. Estimation of an ARMA model directly from response measurements, as opposed to correlation functions, has been discussed by Desforges and Cooper [134]. They used a two-stage least squares method to first estimate a higher-order AR model and then solve for the coefficients of an

ARMA model with a least squares method. The required correlation functions between the measured response and unmeasured excitation were calculated by approximating the autocorrelation of the excitation as a scaled delta function (i.e. assuming the excitation is white noise) and using the AR coefficients obtained in the first stage. The authors noted that this method was very sensitive to model order. Prediction error methods can be used to estimate ARMA models [43], however, these solutions require non-linear optimisation and the application to structural dynamics problems have not been widely reported.

Papakos and Fassois [118] proposed another multistage algorithm to estimate ARMA models, which also started with estimation of a higher-order AR model. Their algorithm outperformed AR modelling of the response measurements, but they reported difficulties in estimating weak modes and anti-resonances. The algorithm included guaranteed stability of the estimated model.

Use of higher-order AR models in isolation has been reported in [47, 134, 144, 145]. It is well known that finite-order AR models cannot truly model the dynamics of a structure, however, high order AR models are able to produce very good approximations [43]. A subsequent difficulty is then distinguishing between vibration modes and spurious numerical modes. Cooper [47] and Hung & Ko [122] used a property of backwards AR models first reported by Kumaresan [120] to distinguish vibrational modes from numerical modes based on the position of AR model poles on the complex *z* plane. These studies modelled impulse response functions or correlation functions, which are approximately deterministic responses. Backwards ARX models were used in the I/O version of the ARMAX modal parameter estimation algorithm introduced in Chapter 5.

Gao & Randall [146, 147] discussed the estimation of FRFs from the cepstra of response measurements. The complex cepstrum is defined as the inverse Fourier transform applied to the logarithm of a complex spectrum [148], i.e.

$$C(\tau) = \Im^{-1}\{\log(X(f))\}. \tag{8.28}$$

An important characteristic of the cepstrum is that the convolution of time domain functions is represented as an addition in the cepstral domain [148].

Time domain convolution becomes a multiplication in the frequency domain:

$$b(t) = a(t) * h(t) \quad \Leftrightarrow \quad B(f) = A(f) \cdot H(f), \tag{8.29}$$

which becomes an addition after taking the logarithm:

$$\log B(f) = \log A(f) + \log H(f). \tag{8.30}$$

Equation (8.30) is transformed into the cepstral domain by inverse Fourier transform:

$$\Im^{-1}\{\log B(f)\} = \Im^{-1}\{\log A(f)\} + \Im^{-1}\{\log H(f)\}. \tag{8.31}$$

This allows excitation and transfer function properties to be separated as they are often in different parts (quefrency bands) of the cepstrum. Examples of the method were given by Gao & Randall [146, 147], demonstrating the use of two curve-fitting methods to extract transfer function data. It was also shown that the effects of double impact excitation can be removed. It should be noted that the technique assumes vibration response measurements are a result of a single dominant excitation source, however, techniques such as principal components analysis may be used to obtain appropriate responses [27]. Broad-band excitation (e.g. impulse excitation or random noise) is particularly effective for cepstral methods as it is represented only at very low quefrencies in the cepstrum and can be separated easily from transfer function components. An advantage of this technique is that it theoretically yields a correctly scaled FRF; hence, mode shapes will be correctly scaled. This contrasts with other response-only modal analysis methods, which produce relatively scaled mode shapes. Some solutions proposed to overcome this limitation include adding a known mass and scaling mode shapes using sensitivity relationships. This method requires the knowledge of the mass change and the resulting shift in natural frequencies [114]. Another technique was introduced by Bernal [115], which allowed more general modifications and eased computational requirements.

The response-only modal analysis methods discussed above make assumptions about the nature of the unmeasured excitation signal. The most common is that the excitation has a flat auto-spectrum. As discussed above, Cooper [135] investigated selectively choosing correlation function lags when modelling correlation functions. Mohanty and Rixen [110-113] adapted the eigensystem realisation algorithm (ERA), Ibrahim time domain method (ITD), single station time domain method (SSTD), and the least-squares complex exponential method, to account for periodic excitations with known frequencies. Other studies that have encountered significant periodic components superposed on broadband measurements [25, 26, 128] used damping and phase to identify spurious modes, or simply prior knowledge of the system under test.

In this section, well-known response-only modal analysis methods have been reviewed and aspects of their application, advantages, and limitations have been discussed.

8.3 Adaptation of ARMAX Estimation Algorithm for use with Response Measurements

The adaptation of the ARMAX estimation algorithm to estimate modal parameters from vibration response measurements is discussed in this section.

The ARMAX estimation algorithm has a number of desirable features including a special diagonal structure for the AR and MA matrices and also the estimation of backwards ARX models. The diagonal AR and MA matrices allow simple manipulation and stabilisation of the model elements and the use of backwards ARX models helps distinguish spurious numerical modes from vibration modes.

The ARMAX estimation algorithm could be modified to process response-only measurements simply by omitting the excitation data and replacing the estimation of backwards ARX models with the estimation of backwards AR models. The adapted estimation algorithm would therefore estimate an ARMA model subsequently used to calculate modal parameters. Initial numerical tests demonstrated that estimation of backwards AR models describing a system’s response due to a random excitation did not allow spurious numerical modes to be distinguished from vibration modes. It was also noted that the diagonal structure of the AR matrix did not include any information on system zeros, which are needed for the complete characterisation of a mechanical system, and an additional stage would be required to calculate zeros, for example using Shanks' method [121, 149]. In addition, it was found that the estimation of AR models was sensitive to the model order and high-dimension high-order models were often unstable. These points are discussed in more detail below.

8.3.1 Estimation of Backwards AR Models

Kumerasan [120] showed that sinusoids could be modelled as the zeros of a linear prediction filter and that a higher-order filter with coefficients chosen to have minimum Euclidean length would have extraneous zeros, i.e. those not corresponding to a sinusoid in the modelled signal, located inside the unit circle on the complex z-plane. This result was demonstrated for undamped, negatively, or positively damped sinusoids and therefore could be used as a method to distinguish between spurious numerical poles and poles corresponding to oscillating system components. An alternative proof for this result was given by Hollkamp & Batill [46] and was extended to apply to ARX models.

The use of backwards AR models (linear prediction filters) is limited to deterministic signals, e.g. sums of sinusoids, because the estimation of the AR model can be formulated as an over-determined set of linear equations with an infinite set of solutions. The proofs discussed by Hollkamp & Batill [46] and Kumerasan [120] showed that the minimum norm solution resulted in numerical poles (a subset of zeros of the AR matrix) being located inside the unit circle.

In the case of arbitrary non-deterministic excitation, the vibration response of a mechanical system will also be non-deterministic and the above result does not hold. More specifically, an AR model will converge to the true system as the data set and the AR model order approaches infinity [43] and therefore an over-determined AR model can never be estimated.

A number of approaches exist to obtain an approximately deterministic vibration response from a mechanical system in response-only modal analysis:

- Excitation of the structure using impulse or step loads allowing the free response to be modelled as a sum of decaying sinusoids. The magnitude of the applied load does not need to be measured but this technique still places significant constraints on the nature of testing.
- Application of the random decrement technique to long records of vibration response data obtained with random excitation.
- Auto- and cross-correlation functions of vibration response obtained with white noise excitation can be expressed as sums of decaying sinusoids as shown in section 8.2.

The use of the random dec signature or correlation functions requires long data records but has the advantage of significant rejection of uncorrelated noise through the averaging operations.

8.3.2 Limitations of the Diagonal AR Matrix Structure

The diagonal structure was adopted for the AR and consequently MA matrices in the ARMAX estimation algorithm to enable simple manipulation of these matrices, including stabilisation of the matrix polynomials, and the decomposition of MIMO ARX models into SIMO ARX models. Numerical testing comparing the performance of scalar AR and multi-dimensional AR models (the response-only analogue of ARX models) showed that the multi-dimensional models more accurately represented the simulated system. However, further tests using experimental data showed that high-order high-dimension AR models were often unstable. All models were estimated using least-squares estimation.

An additional limitation of adopting the diagonal AR structure is that no system zero information is included and therefore needs to be estimated in further stages. In contrast, the inverse of a MIMO AR model structure includes zero information.

8.4 Combined AR-ARMAX Estimation Algorithm

In response to the issues discussed above, two algorithms have been adapted from the I/O ARMAX algorithm to estimate modal parameters from vibration response measurements. The new algorithms are referred to as MISO AR-ARMAX and MIMO AR-ARMAX and the stages are summarised in the block diagram in figure 8.1.

The AR-ARMAX algorithms start by estimating a higher-order multidimensional AR model from the response measurements using a standard least-squares solution of an equivalent regression problem. The AR model innovations are then calculated and used as the 'excitation' in subsequent stages of the algorithm. A diagonal representation of the AR matrix estimated in stage 1 is also used in subsequent stages of the MISO AR-ARMAX algorithm. The MIMO AR-ARMAX algorithm estimates a fully parameterised MIMO ARMAX model from the AR model error and response measurements.

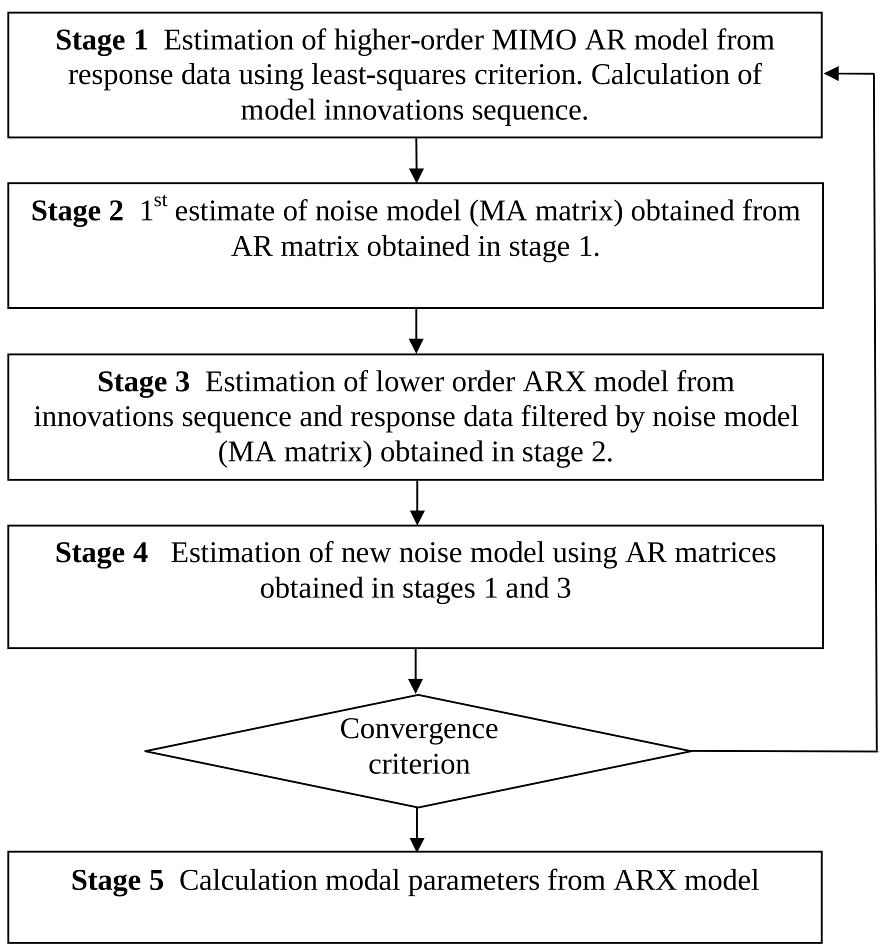

Figure 8.1 Block diagram of adapted estimation algorithm.

The reasoning behind these adaptations is that a linear system excited with white noise can be modelled using an AR model. Ljung [43] noted that an AR model of order p estimated using N data will converge to the true system as $N, p \rightarrow \infty, N > p$. In practice, p is restricted to a finite order, which is required to be large enough such that system dynamics and noise present in measurements are modelled adequately. It is assumed that if this condition is met then the AR model innovations will approximate white noise, which is then used as an excitation in the I/O ARMAX estimation algorithm. Initial numerical tests revealed that fitting lower-order backwards ARX models (as part of the I/O ARMAX algorithm) allowed poles due to vibration modes to be distinguished from numerical poles according to their position on the unit circle, as discussed above.

The estimation of a higher order AR model, model innovations, and diagonal AR matrix for use with the I/O ARMAX algorithm is outlined in the following section.

8.4.1 Stage 1: Estimation of Higher-Order AR Model

A discrete-time AR model of order p is defined as

$$\mathbf{H}_y(q) \cdot \mathbf{y}[t] = \mathbf{w}[t] \tag{8.32}$$

$\mathbf{y}[t]$ is the s dimensional response vector, $\mathbf{w}[t]$ is the innovations sequence, and $\mathbf{H}_y(q)$ is the fully parameterised $s \times s$ AR matrix; the elements are polynomials of order p, in terms of q, the backshift operator: $\mathbf{x}[t] \cdot q^j = \mathbf{x}[t\text{-}j]$.

The AR model can be rewritten as

$$\mathbf{y}[t] + \sum_{j=1}^{p} \mathbf{H}_y(j) \cdot \mathbf{y}[t-j] = \boldsymbol{\varepsilon}_1[t] \tag{8.33}$$

and then as a corresponding regression problem [118]:

$$\mathbf{y}[t] = \mathbf{\Phi}^T[t] \cdot \mathbf{h} + \boldsymbol{\varepsilon}_1[t] \tag{8.34}$$

where

$$\mathbf{\Phi}^T[t] = \mathbf{I}_s \otimes \mathbf{u}^T[t], \qquad [s \times p{\cdot}s^2] \tag{8.35}$$

$$\mathbf{u}[t] \equiv [\,-\mathbf{y}[t-1] \quad -\mathbf{y}[t-2] \quad \cdots \quad -\mathbf{y}[t-p]\,]^T, \qquad [p{\cdot}s \times 1] \tag{8.36}$$

$$\mathbf{h} \equiv col\big[H_y(1) \quad H_y(2) \quad \cdots \quad H_y(p)\big]^T. \qquad [p{\cdot}s^2 \times 1] \tag{8.37}$$

The regression problem in equation (8.34) is solved using a method discussed in section 5.3.1 and described in Ljung [43].

Once the AR matrix has been estimated the model innovations sequence can be calculated. The innovations and measured response are then used in subsequent stages of the estimation algorithm.

The AR matrix estimated in the first stage is also used in subsequent stages and is reformulated with a diagonal structure for the MISO AR-ARMAX algorithm. This is achieved by calculating the roots of the matrix polynomial, which are then expressed as a scalar AR polynomial. The new diagonal AR matrix has the scalar AR polynomial in its diagonal elements. The following stages of the MISO AR-ARMAX algorithm are taken directly from the ARMAX estimation algorithm, using $\boldsymbol{\varepsilon}_1[t]$ (equation (8.34)) as the excitation, $\mathbf{y}[t]$ as the response and the diagonal AR matrix described above in place of $\mathbf{H}_y(q)$, which is estimated in stage 1 of the I/O ARMAX estimation algorithm. Note that the algorithm name 'MISO AR-ARMAX' is used to emphasise that a diagonal structure is adopted for the AR matrices, and this allows decomposition of the model into a series of MISO models. In contrast, the MIMO AR-ARMAX algorithm estimates MIMO ARX models instead of MISO models, and therefore does not use the diagonal parameterisation of the AR and MA matrices in subsequent stages. The significance of the MIMO method is that it uses all response channels when estimating a model, i.e. a model is fitted to more data points. A disadvantage is that in the event an unstable model is estimated, it cannot be stabilised easily as is the case for the MISO algorithm. Details of the subsequent stages are discussed in sections 5.3.2 – 5.3.5.

In this section the adaptation of the I/O ARMAX algorithm to estimate modal parameters from vibration response measurements has been discussed. A number of issues prevent the algorithm from being directly applied to response measurements while maintaining the desirable properties of mode verification based on the sign of estimated damping, and simple stabilisation of unstable models. The proposed method overcomes these difficulties by using the innovations sequence from a high-order AR model as an excitation, which can be used with the response measurements in the I/O ARMAX algorithm.

8.5 Numerical Tests

This section discusses the testing of the AR-ARMAX modal parameter estimation algorithms using data simulating the response of a two degree-of-freedom system.

8.5.1 Two Degree-of-Freedom Damped Spring Mass System

Details of the simulated system are the same as those listed for System 1 introduced in Section 6.2. Table 8.1 lists the physical and modal parameters.

System	Physical Parameters	Mode	Frequency (Hertz)	Damping (%)	Magnitude (DOF 2)	Phase° (DOF 2)
1	$m_1 = 1$; $m_2 = 2$; $c_1=0.2$; $c_2= 0.4$; $c_3= 0$; $k_1=500$; $k_2= 300$; $k_3= 0$	1	1.485	0.4180	2.377	0.3211
		2	4.676	1.229	0.2104	179.0

Table 8.1 Physical and modal parameters for 2 DOF system used in numerical testing of adapted ARMAX algorithm.

The simulated response records were corrupted with random noise approximating the effects of measurement noise. The level of noise is specified as the ratio of RMS measurement noise to RMS system response expressed as a percentage.

8.5.2 AR-ARMAX Numerical Tests

Four tests were carried out to assess the performance of the MISO and MIMO versions of the AR-ARMAX algorithm. Each version of the algorithm was used to estimate modal parameters from time series data and also correlation functions calculated from the raw data. In addition, AR models were calculated from time-series data using least-squares estimation.

The correlation functions used for two of the tests were calculated using response spectra rather than from raw time-series data. The discrete Fourier transform (DFT) was applied to overlapping (66%) blocks of time series data, which were then zero-padded to twice the number of time-series samples. Auto- and cross-spectra were then calculated and averaged. Unbiased correlation functions were obtained by an inverse DFT of the averaged spectra and application of bow-tie compensation, which accounted for the zero padding of time-series data [128].

The details of each test are as follows:

Test 1

- MISO AR-ARMAX algorithm;
- 500 samples of time-series data, sampling frequency 50 Hz;
- 10% random measurement noise;
- Stage 1 AR model order = $2 \cdot na$; $na = 4, \ldots, 10$; $nb = na - 1$; $nc = na$;
- 8 iterations of stages 3 and 4;
- Model selection using NPDP.

Test 2

- MISO AR-ARMAX algorithm;
- Correlation function data; block size 1024 samples; sampling frequency 50 Hz; 190 averages (32768 samples of time-series data used);
- 10% random measurement noise added to time series data, i.e. before calculation of correlation functions;
- Stage 1 AR model order $p = 2 \cdot na$; $na = 4, \ldots, 10$; $nb = na - 1$; $nc = na$;
- 8 iterations of stages 3 and 4;
- Model selection using NPDP.

Test 3

- Multivariate AR model; least-squares estimation;
- 500 samples of time-series data, sampling frequency 50 Hz;
- 10% random measurement noise;
- AR model order; $p = 2, \ldots, 40;$
- Model selection using BIC.

Test 4

- MIMO AR-ARMAX algorithm;
- 500 samples of time-series data, sampling frequency 50 Hz;
- 10% random measurement noise;
- Stage 1 AR model order = $2 \cdot na$; $na = 4, \ldots, 10; nb = na - 1; nc = na$;
- 6 iterations of stages 3 and 4;
- Model selection using NPDP.

Test 5

- MIMO AR-ARMAX algorithm;
- Correlation function data; block size 1024 samples; sampling frequency 50 Hz; 190 averages (32768 samples of time-series data used);
- 100% random measurement noise added to time series data, i.e. before calculation of correlation functions;
- Stage 1 AR model order $p = 2 \cdot na$; $na = 4, \ldots, 8; nb = na - 1; nc = na$;
- 6 iterations of stages 3 and 4;
- Model selection using NPDP

Each test was repeated 50 times with independent realisations of response data and measurement noise. The mean and standard deviations of the estimated modal parameters are plotted in figures 8.2 and 8.3. The MISO AR-ARMAX algorithm produces s (i.e. the number of response measurements) estimates of modal parameters and these are marked DOF 1 and DOF 2 to indicate the measurement point. In contrast, only one set of modal parameters are estimated by the MIMO AR-ARMAX algorithm and the multivariate AR models, and these are denoted DOF 1.

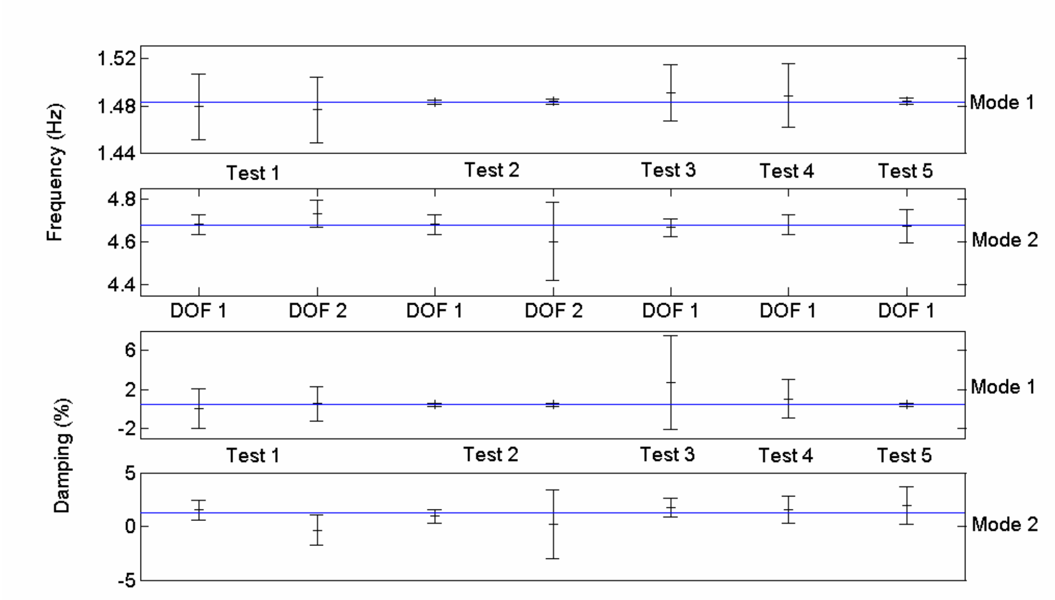

Figure 8.2 Mean and standard deviation of estimated modal frequencies and damping, tests 1 – 5. True parameter values are indicated by the horizontal line.

Modal frequencies are within 1.6% of true values for both modes in each test. It is worth noting that the estimates for mode 2, DOF 2 in tests 1 and 2 are relatively poor compared to other natural frequency estimates of these tests. This is due to the relatively low response of the second mode measured at DOF 2, as shown by figure 6.2 (a). Comparison of frequencies from Test 3 and Test 4 show only marginal improvement by the MIMO AR-ARMAX algorithm over the AR results, which demonstrates the effect of the extra stages (the first stage of the MIMO AR-ARMAX algorithm is estimation of a higher order AR model). Similarly, the most accurate results (obtained with DOF 1 as a reference) for each mode in Test 1 are only marginally better than the Test 3 results. Tests 2 and 5 clearly show that calculating correlation functions is beneficial if large amounts of data are available. Test 5 achieves significantly better results given that 100% random measurement noise was added to the response measurements. Recalling that 190 averages were used in the calculation of the correlation functions, the random noise would be attenuated by approximately 20dB, which equates to approximately 7% noise present in the correlation functions used for test 5, and less than 1% for test 2.

Similar comments apply to the modal damping estimates and it is interesting to note that the negative bias on results observed in tests described in Chapter 6 for the I/O ARMAX algorithm are not observed to the same degree for the response-only algorithms. The damping results also show the benefit of calculating correlation functions, but little improvement is gained by applying the ARMAX-based algorithms over the AR modelling apart from a marginal improvement in damping.

Mode shape results, shown in figure 8.3 are generally more accurate for the MIMO AR-ARMAX models and mode shape phase is relatively poorly estimated for the MISO AR-ARMAX algorithm.

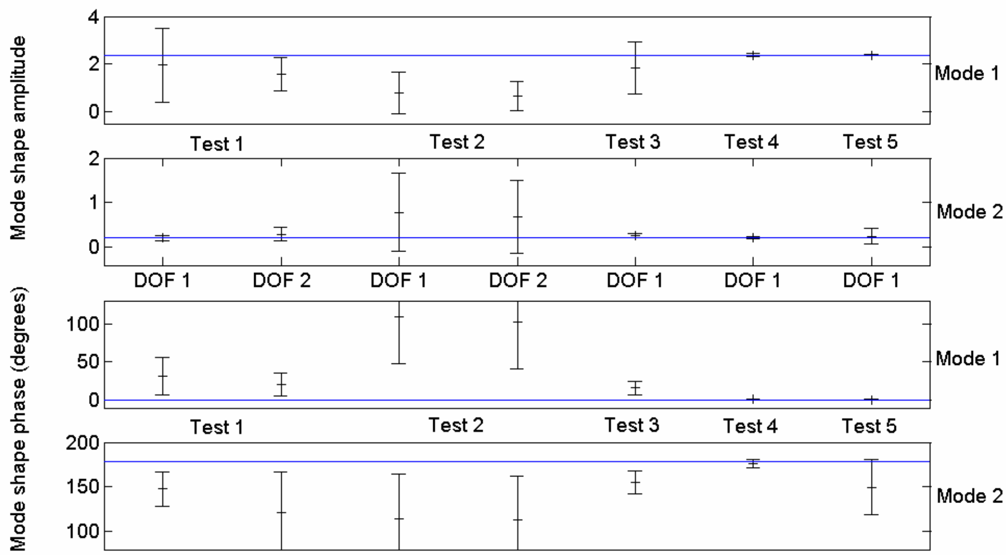

Figure 8.3 Mean and standard deviation of estimated mode shape magnitude and phase, tests 1 – 5. True parameter values are indicated by the horizontal line.

Mode shape results reveal significant errors associated with the MISO AR-ARMAX algorithm when estimating modal parameters from correlation functions. This is possibly due to leakage when calculating the correlation functions using the spectral method. Note that no window was applied to data in these tests, however, other numerical tests showed no improvement when a Hanning window was used. The MISO-ARMAX algorithm was found to estimate multiple poles around a resonant frequency, presumably due to leakage effects. This could potentially increase numerical sensitivity when transforming the discrete-time transfer function into pole-residue form and subsequently calculating modal parameters. This point needs to be further investigated for the response-only algorithm as well as the I/O algorithm because of the high order models that are estimated to account for the large frequency ranges commonly considered in structural dynamics analysis.

Comparing results from tests 1 and 4 shows that both the MISO and MIMO AR-ARMAX algorithms produce frequency and damping estimates of similar accuracy; that is, the best estimates from the MISO algorithm are similar to the results of the MIMO algorithm. Mode shape magnitudes and phase results are significantly better for the MIMO algorithm. This is due to the extra data points used in the estimation of the MIMO as opposed to the MISO model, which estimates a separate MISO model for each output. This reason, as well as the observations relating to the use of correlation functions discussed in the previous paragraph, are likely to have contributed to the poor mode shapes results estimated from correlation functions using the MISO AR-ARMAX algorithm.

The NPDP was found to be particularly sensitive to model order. In the most favourable cases, vibration-mode poles were found to be positively damped and all other poles (due to noise) were found to be negatively damped. This trend did not hold when the number of poles in the ARMAX model approached that of the stage 1 AR model. Therefore, distinguishing between vibration modes and numerical modes was not possible using the sign of the damping. Stabilisation diagrams assessing the stability of all modal parameters (i.e. frequency, damping and mode shape estimates) may be a more effective tool for model order selection and distinguishing between vibration modes and numerical modes.

The numerical testing of the AR-ARMAX algorithms has been described in this section. The MIMO AR-ARMAX algorithm produces the most accurate results from both time-series data and correlation functions. A benefit of using correlation functions is that averaging can be employed to attenuate random noise in the measurements.

8.6 Experimental Testing

Further testing of the AR-ARMAX estimation algorithm was carried out using vibration response data measured from a cantilever aluminium beam. In this section, the experimental apparatus, experiments to record time-series data and the processing of data using the AR-ARMAX estimation algorithm are described. For comparison purposes, the ARTeMIS commercial response-only modal analysis software, produced by Structural Vibration Solutions, was also used to estimate modal parameters.

8.6.1 Experimental Apparatus and Data Collection

Vibration response measurements were made on the cantilever aluminium beam used for experimental tests described in Chapter 6, and shown in figures 4.7 and 6.35. The beam was excited by independent random noise (band-limited to 0–1600Hz) applied to each of the four pairs of piezoceramic actuators. The actuators in each pair were driven in parallel with opposite polarity so that a distributed moment was applied to the beam.

Response measurements were made at 34 evenly-spaced locations along the beam using two B&K 4374 and two B&K 4393 accelerometers. As multiple sets of measurements were taken, a reference accelerometer was required to enable mode shape information from each set of measurements to be correctly scaled. The reference accelerometer is best placed at a location that experiences deflection for each mode of interest and therefore was placed at the free end of the beam for all experiments.

B&K 2635 charge amplifiers were used for accelerometer signal pre-conditioning, which included high and low-pass filtering with 2 Hz and 3 kHz (-10%) cut-off, respectively. A HP 3566A eight channel FFT analyser was used to record excitation and response time series data.

8.6.2 Experiment 1: Single-Input Multiple-Output

The first experiment used one pair of piezoceramic actuators to apply random excitation to the cantilever beam. Sixty seconds of excitation and response data were recorded with a sampling rate of 4096 Hz and modal parameters calculated from the excitation and response data were used to verify the results of the response-only algorithms. The HP 3566A FFT analyser calculated FRFs with the following characteristics:

- Frequency range: 0 – 1600 Hz;
- Resolution (line-spacing): 0.5 Hz;
- Hanning window;
- Up to 10 averages, 50% overlap.

Curve fitting of the FRFs was carried out with a rational fraction least squares (RFLS) algorithm, which is part of the Spectral Dynamics STAR Modal v5.23 software package. The second through to tenth transverse bending modes were successfully identified in the 0 – 1600 Hz frequency range. As expected, the first mode was not identified due to the poor excitation of this mode by one pair of piezoceramic actuators. The results are compared with results obtained from the FDD, EFDD, and SSI-UPC methods (discussed below) in Appendix D.

8.6.3 Experiment 2: Multiple-Excitation Response-Only Modal Analysis

The second experiment employed independent random excitation (band-limited to 0 – 1600Hz) applied by each of the four actuator pairs. Excitation and response data were measured in sixty second time records sampled at 4096 Hz. The response data from Experiment 2 were processed using the AR-ARMAX estimation algorithms, AR models and three algorithms available in the Structural Vibration Solutions ARTeMIS v 3.5 software.

8.6.4 FDD, EFDD and SSI-UPC Estimation

These methods were introduced in section 8.2 and the estimated modal parameters are compared in Appendix D. The FDD and EFDD methods require auto- and cross-spectra and these were calculated from the time records using blocks of data with 4096 samples and 66% overlap. The resulting spectra had a frequency range of 0 - 2048 Hz, 0.5 Hz frequency resolution.

The FDD is the quickest and simplest method and yields modal frequency and mode shape estimates. The accuracy of the modal frequency is dependent on the resolution of the auto- and cross spectra. FDD was the only method to identify all eleven transverse bending modes in the selected frequency range, even though the response of the first mode was relatively poor. The EFDD technique identified the second through to eleventh bending modes with a greater frequency resolution and also yielded modal damping estimates.

The SSI-UPC technique identified modes 3 - 11. The SSI-UPC method is a parametric method and identified a number of candidate models of differing order for each data set and a number of tools were available to help identify the model that best fitted the data [150]:

- Stabilisation diagrams based on the stability of frequencies, damping and mode shapes;
- Singular values (rank) of input-data matrix;
- Model stability;
- Stability of vibration modes and noise modes;
- Final prediction error criterion;
- Synthesised auto- and cross-spectra and correlation functions.

The combined use of the above tools for model selection produced the most accurate modal parameters as no single tool provided a robust criterion for model selection. A smaller frequency range would probably have aided the identification of the lower order modes as even very high order models failed to identify these modes. Note that different weighting matrices were used as part of the principal components (SSI-PC) and canonical variate analysis (SSI-CVA) SSI algorithms and similar results were obtained as for the SSI-UPC algorithm.

Results for the three ARTeMIS response-only algorithms are compared with the STAR results and plotted in Appendix D. Frequency and damping estimates obtained from EFDD (except for mode 1) are listed in table 8.2 and corresponding mode shapes are shown in Appendix D. Results from all tests show good agreement, except for the modes that were not identified as discussed above. It is worth noting that no difficulty was encountered identifying the eleventh bending mode even though the excitation was band-limited to 0 – 1600 Hz.

Mode	Frequency (Hz)	Damping (%)
1 (FDD)	6	-
2	36.69	0.85
3	105.49	0.28
4	208.02	0.28
5	346.54	0.26
6	515.89	0.62
7	728.34	0.35
8	977.93	0.33
9	1248.49	0.29
10	1578.69	0.32
11	1907.12	0.30

Table 8.2 Frequency and damping results from EFDD (except mode 1, which was estimated by the FDD method).

8.6.5 AR-ARMAX Results

Both the MISO and MIMO versions of the AR-ARMAX algorithm were used to estimate modal parameters from response measurements and correlation functions. In addition, AR models were also estimated from the response data and correlation functions. The correlation functions were calculated using the signal spectra as for numerical tests, outlined in section 8.5, with the exception that a Hanning window was applied to the blocks of response data before zero padding and transformation to spectral data. Application of the Hanning window produced smoother spectra and preliminary tests showed that estimated modal parameters were more accurate.

The details of each test are as follows:

MISO AR-ARMAX algorithm with time series data (MISO TS):

- 1024 samples of time-series data, sampling frequency 4096 Hz;
- Stage 1 AR model order = $2{\cdot}na$; $na = 20, \ldots , 26; nb = na; nc = na$;
- 8 iterations of stages 3 and 4;
- Model selection using NPDP.

MISO AR-ARMAX algorithm with correlation functions (MISO corr):

- Correlation function data; block size 1024 samples; sampling frequency 4096 Hz; 718 averages (245760 samples of time-series data used);
- Stage 1 AR model order = $2{\cdot}na$; $na = 20, \ldots , 26; nb = na; nc = na$;

- 8 iterations of stages 3 and 4;
- Model selection using NPDP.

MIMO AR-ARMAX algorithm with time series data (MIMO TS):

- 1024 samples of time-series data, sampling frequency 4096 Hz;
- Stage 1 AR model order = $2 \cdot na$; $na = 5, \ldots, 12; nb = na; nc = na$;
- 10 iterations of stages 3 and 4;
- Model selection using NPDP

MIMO AR-ARMAX algorithm (MIMO corr):

- Correlation function data; block size 1024 samples; sampling frequency 4096 Hz; 718 averages (245760 samples of time-series data used);
- Stage 1 AR model order = $2 \cdot na$; $na = 5, \ldots, 12; nb = na; nc = na$;
- 10 iterations of stages 3 and 4;
- Model selection using NPDP

Multivariate AR model with time series data (AR TS):

- 1024 samples of time-series data, sampling frequency 4096 Hz;
- Model order = *10 - 24* ;
- Model selection using BIC.

Multivariate AR model with time series data (AR corr):

- Correlation function data; block size 1024 samples; sampling frequency 4096 Hz; 718 averages (245760 samples of time-series data used);
- Model order = *10 - 24*;
- Model selection using BIC.

Results from the experimental tests reflect the observations in numerical test results, discussed in section 8.5.2. In particular, the MISO AR-ARMAX algorithm was found to yield good accuracy for frequency and damping results and the use of correlation functions improved the accuracy of estimates, and reduced the standard deviation of global parameter estimates. Mode shapes estimates were poor, though the results estimated from time series data were found to be slightly better than mode shapes estimated from correlation functions. The reasons discussed in section 8.5.2 regarding the sensitivity of the MISO AR-ARMAX algorithm to correlation functions also apply to these experimental results. The estimated modal parameters from the MISO AR-ARMAX algorithm are compared with results from EFDD in Appendix E.

Results obtained from the MIMO AR-ARMAX and AR algorithms are compared with EFDD results and plotted in figures 8.4 – 8.8. As with the SSI-UPC results, only modes 3 – 11 were identified by all tests. Frequency results are generally good, however, errors for mode 3 were greater than all other modes, suggesting that a smaller frequency range is appropriate for both MIMO AR-ARMAX and AR estimation. The limited ability of the piezoceramic actuators to excite low order modes is likely to have also contributed to these results.

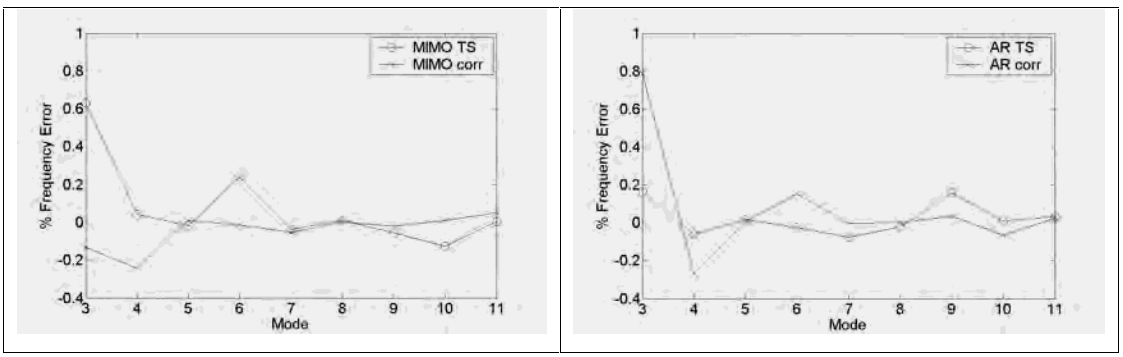

Figure 8.4 Frequency error estimated from MIMO AR-ARMAX and AR algorithms, compared with EFDD results.

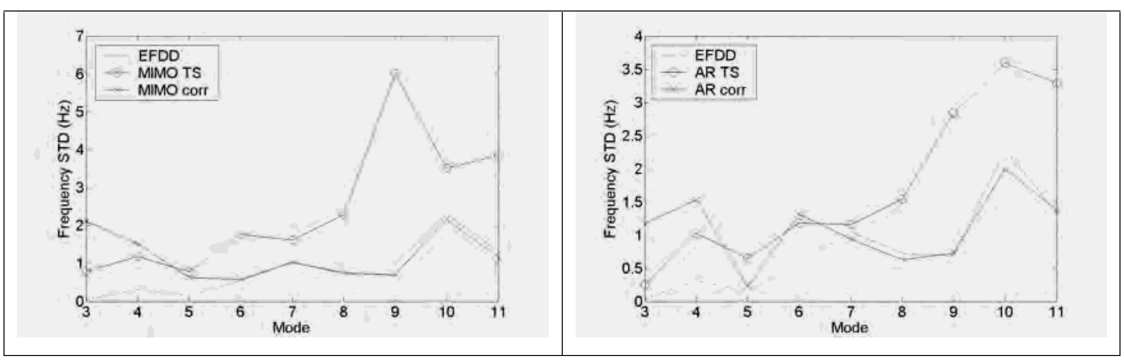

Figure 8.5 Frequency standard deviation estimated from MIMO AR-ARMAX and AR algorithms, compared with EFDD results.

Damping results for MIMO AR-ARMAX estimation are comparable to those obtained from EFDD results, accompanied by larger standard deviations. AR results estimated from time series data were found to have positive bias. Estimation of modal parameters from correlation functions improved the standard deviation of frequency and damping results with values approaching those obtained from EFDD results, which were estimated from the same amount of data as the correlation functions used for MIMO AR-ARMAX and AR estimation.

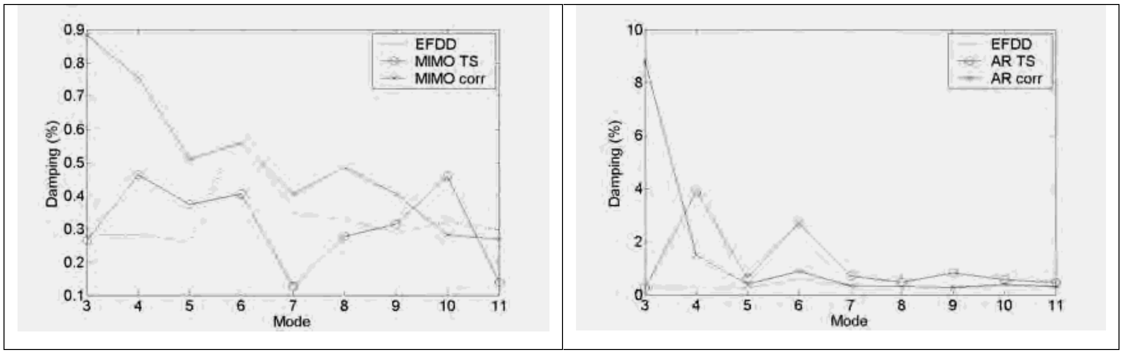

Figure 8.6 Modal damping estimated from MIMO AR-ARMAX and AR algorithms, compared with EFDD results.

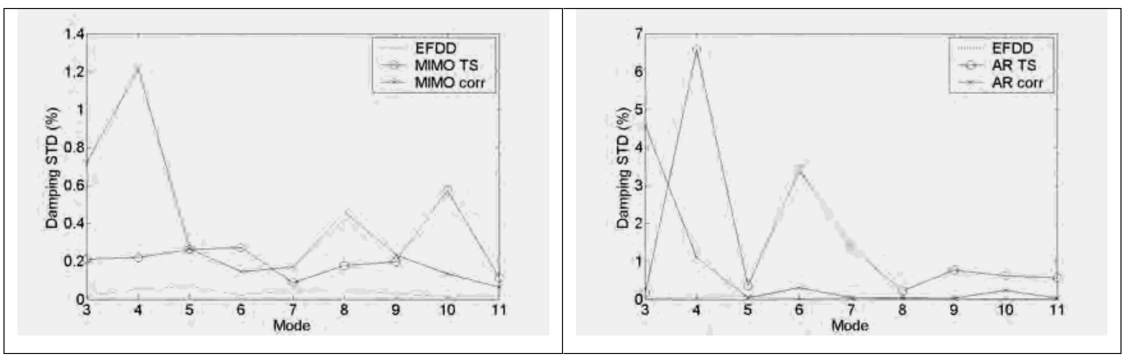

Figure 8.7 Modal damping standard deviation estimated from MIMO AR-ARMAX and AR algorithms, compared with EFDD results.

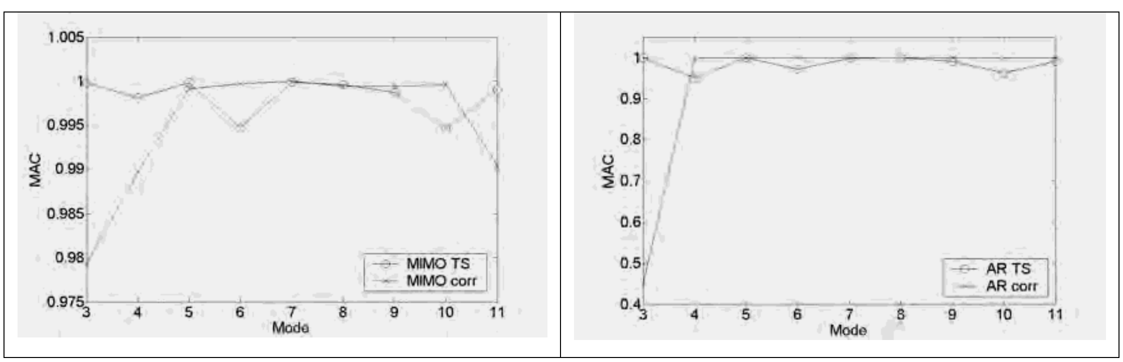

Figure 8.8 MAC values comparing mode shapes from MIMO AR-ARMAX and AR algorithms with results from EFDD.

The mode shapes estimated by the MIMO AR-ARMAX and AR algorithms were found to be in good agreement with EFDD results, except for mode 3 for the AR results estimated from correlation functions. This is due to a small number of poorly estimated measurement points, and potentially reflects the limitations of the BIC model selection criterion. It was found that the BIC consistently selected models of low order and in many cases model selection was limited to higher-order models. This generally lead to better results, however, numerical difficulties were sometimes encountered with high order AR models resulting in many spurious noise poles in the low and high frequency ranges. The numerical difficulties encountered with higher-order polynomial models suggests that a different model parameterisation or model structure (e.g. state-space representation) may be appropriate for high-order, large dimension problems, although the SSI-UPC algorithm also failed to properly model low order modes, as discussed above.

The results of the AR-ARMAX algorithm were observed to be sensitive to the model order of the stage 1 AR model and also the order of the ARX models estimated in the subsequent stages. In particular, the positively damped poles estimated in the ARX models did not always correspond to the vibration modes; hence the NPDP model selection criterion was ineffective. A disadvantage associated with the AR-ARMAX algorithm is that the orders of the stage 1 AR model (p) and the order of the AR (na) and MA (nc) matrices in the subsequent stages can be set independently, which leads to a large set of possible models. The range of models to be estimated in above tests was limited by setting p and nc as a function of na. It was found that if the order of the stage 1 AR model was set very high the quality of this model was typically poor as indicated by spurious poles in the high and low frequency ranges of the z-plane. In these cases iterations of stages 3 and 4 improved the results to a certain extent. When the order of the AR model was more appropriately set, further iterations had less of an effect, and as shown by the comparison of results in figures 8.4 – 8.8, little improvement over basic AR estimation is seen. A benefit of the MIMO AR-ARMAX algorithm over AR modelling is the elimination of positive bias on damping estimates when estimating results from time series data. In some cases, iterations of stages 3 and 4 lead to poorer estimates of some modes. This was often accompanied by positively-damped spurious poles being estimated, which also invalidated the NPDP model selection criterion. Therefore, model order specification and model selection remain a significant problem. A combination of model selection criteria, as used in the SSI-UPC algorithm, could potentially improve the quality of the estimated modal parameters.

An interesting result is that modes 3 – 11 were accurately estimated, which contrasts to the results obtained for the I/O ARMAX algorithm, presented in section 6.3.5. The low s/n at frequencies around poorly excited modes was suggested as a reason for the observed I/O ARMAX results. The response-only algorithms, on the other hand, assume independent sources of excitation and for these experiments four pairs of actuators were used to apply independent random excitation. Results in Chapter 4 showed that each actuator pair excited the low-order modes poorly and some actuators did not couple well to one or two higher modes. The estimation of fully parameterised ARMAX models in the MIMO AR-ARMAX and AR algorithms is likely to have contributed to the good results, as the model is estimated using all response data points. The adoption of the diagonal AR matrix in the I/O algorithm was partly based on the ease of stabilising and manipulating diagonal matrix polynomials and tests in Chapters 6 and 7 demonstrated that acceptable accuracy of modal parameters was achieved. These tests also showed that for data with moderate levels of noise, instability issues were rare due to the use of backwards ARX models and the fact that model selection could be carried out without having to recursively calculate the innovations sequence. An investigation into a MIMO ARMAX I/O algorithm is therefore suggested as future work.

In this section, the performance of a number of response-only modal parameter estimation methods has been assessed using vibration response data obtained from a cantilever aluminium beam. The non-parametric FDD and EFDD methods were found to be the simplest analysis tools and yielded good results, which correlated well with I/O modal testing results. The SSI-UPC, AR, and AR-ARMAX methods only identified modes 3 – 11 and each method yielded good accuracy for these modes.

8.7 Conclusions

This study has reviewed response-only modal analysis techniques and introduced a new method, the AR-ARMAX algorithm, which is adapted from an ARMAX I/O modal parameter estimation algorithm introduced in Chapter 5.

Numerical tests using data simulating the response of a two degree-of-freedom system demonstrated the MIMO AR-ARMAX algorithm could accurately estimate modal parameters from time series data and correlation functions with 10% and 100% added random measurement noise, respectively. The use of averaged correlation functions has the advantage of attenuating random noise present in the original time-series data; the attenuation is dependent on the number of averages used when calculating the correlation functions.

Experimental data obtained from a cantilever aluminium beam was used to assess the performance of the AR-ARMAX algorithm, as well as FDD, EFDD, SSI-UPC, and AR model estimation techniques. The FDD and EFDD non-parametric methods were found to be most effective; FDD was the only method to identify all modes but did not estimate modal damping. EFDD identified modes 2 – 11 and results correlated well with modal parameters obtained from I/O modal analysis. The parametric identification methods tested included SSI-UPC, AR modelling of time series and correlation functions, and the MISO and MIMO AR-ARMAX algorithm applied to time series data and correlation functions. Only modes 3 – 11 were identified by these methods and model order specification and model selection criteria were found to be critical to the accuracy of these methods. The NPDP model selection criterion was found to be sensitive to model order specification and was often ineffective due to positively-damped spurious numerical modes. Other model selection criteria, such as stabilisation diagrams based on stability of frequency, damping and mode shape results, could potentially improve the quality of estimated modal parameters. The numerical and experimental tests only investigated the effect of random measurement noise and suggested little benefit in using the more complex AR-ARMAX algorithm over basic AR modelling. Further tests using a more complex structure investigating the effect of localised excitation, non-white excitation and the presence of periodic components in the excitation would provide a better indication of the limitations of the methods. It is emphasised that this work is presented as a preliminary study into the adaptation of the I/O ARMAX algorithm presented in Chapter 5. Further insight has been gained into the operation of the algorithm with the recommendation to investigate the use of fully parameterised ARMAX models in the I/O ARMAX algorithm.

Chapter 9 Conclusions

9.1 Conclusions

The major focus of this thesis is the experimental determination of structural dynamic properties in cases where significant unmeasured excitation is present. This has been motivated by structural dynamics analysis of helicopters. In this application, modal analysis is a common method used for experimentally determining the structural dynamic behaviour and the reviewed literature suggested that boundary conditions of the helicopter under test significantly affect the results. Therefore, it is desirable to carry out testing while the helicopter is in flight. In Chapter 2, a literature review of existing modal analysis techniques revealed an extensive range of algorithms for classical input-output modal analysis under favourable noise conditions, assuming the measured excitation is the only source of excitation. More recently operational modal analysis or response-only modal analysis methods, reviewed in Chapter 8, have been developed, which only require vibration response measurements and assume the unmeasured excitation to be reasonably flat. The case where input-output modal analysis is carried out in the presence of unmeasured excitations has not been widely researched.

In Chapter 2 a preliminary study was carried out to assess the performance of an existing modal parameter estimation algorithm applied to representative structures with measured impulse excitation and unmeasured periodic and random excitation, which approximately corresponds to conditions present in a helicopter during flight. The first experimental case study involved a free-free aluminium beam, and piezoceramic plates were employed as an alternative means of applying multiple independent sources of structural excitation. The second experimental case study involved a steel helicopter-like structure, which exhibited a more complex dynamic behaviour. Synchronous averaging was employed to improve the signal-to-noise ratio of the measured excitation and response data and to attenuate unmeasured excitations. The results of these experimental case studies demonstrated that the existing RFLS modal parameter estimation algorithm was able to identify modal parameters in the presence of unmeasured excitation and synchronous averaging was effective in improving the accuracy of the results. A limitation of this approach was that the algorithm did not explicitly account for any noise in the data, which lead to practical problems of identifying vibration modes in poor quality FRFs and selecting appropriate frequency bands for curve fitting. A novel modal parameter estimation algorithm was therefore proposed in Chapter 5 to address these issues.

Advances in finite element modelling have produced powerful tools for the prediction of dynamic behaviour and the resulting structural loading. An initial step is model validation and updating using experimental data, which typically includes accurately determined modal parameters. Chapter 3 presented three case studies to demonstrate the performance and limitations of a sensitivity-based model updating strategy. The first case study showed that model updating significantly improved correlation between experimental and FEM results when experimental data was obtained under non-ideal conditions, for example when the structure exhibited non-linear behaviour. This case study also demonstrated the importance of having an initial FEM that adequately modelled the physical structure, in particular the joints and contacting surfaces. The remaining case studies reflected this in a situation where the initial FEM was very accurate, resulting in less scope for updating. The final case study demonstrated that apparently simple modifications can be difficult to model. In addition, an updated FEM yielded only very marginal improvements in terms of modal assurance criterion when predicting the effect of a significant modification, compared to a non-updated FEM. These results generally suggested that assessing the accuracy of experimental data at every measurement point is important to the outcome of FEM updating, and that the expected accuracy of experimental data should be used to better interpret the correlation of experimental and FEM results.

The use of piezoceramic actuators for structural vibration control has been widely reported and the aim is often to excite specific modes using a set of actuators, while minimising excitation of other modes. Experimental modal analysis typically requires excitation of a large number of modes and piezoelectric actuators have not been widely used in this application. The experimental case studies in Chapter 2 demonstrated that accurate modal parameters could be obtained using piezoceramic plates for structural excitation. An approximate analytical model of pairs of actuators bonded to a beam was reviewed in Chapter 4 to illustrate the characteristics of this type of actuation. The model showed that the effectiveness of a pair of actuators in exciting a particular vibration mode is related to the derivative of the mode shape at the edges of the actuator pairs; i.e. the slope of the mode shape at the edges of the actuator pairs. Modes with little change in slope over the actuator contact area were poorly excited. This has implications for exciting low order transverse modes of an aluminium beam and explains the results obtained in Chapter 2. Another issue considered was the extraction of mode shape information from estimated transfer functions when using piezoceramic actuators for structural excitation. Transfer functions cannot be measured at a point (e.g. point mobility) as for modal analysis with a point force, but it was shown that unscaled mode shapes can be obtained from transfer function residues, which verified observations made in the experimental case studies discussed in Chapter 2.

A novel algorithm to estimate modal parameters was presented in Chapter 5. The algorithm is based on the estimation of a discrete-time ARMAX model, which explicitly models unmeasured excitations and measurement noise. The algorithm included least-squares estimation of backwards ARX models, which allowed vibration modes and spurious numerical modes to be distinguished. It was also suggested that the number of positively damped poles (NPDP) estimated by a model could be used as a method to select the best model from a set of models of different order. The backwards ARX model resulted in the MA matrix of the ARMAX model being stable, which reduced the need for further operations to stabilise the MA matrix. A diagonal structure was used for the AR matrix and consequently for the MA matrix. This was adopted to limit the size of matrices used during least-squares estimation, with the benefit of simple stabilisation of unstable models. The diagonal structure also allowed simple manipulation of the model.

Extensive testing of the ARMAX estimation algorithm was described in Chapter 6. Simulated data from three two degree-of-freedom systems was used to test the ARMAX algorithm under different noise conditions: 10% random noise added to response measurements; and combinations of 100% periodic and 20% random unmeasured excitations with 10% random measurement noise. The results showed that the ARMAX algorithm and the NPDP model selection criterion performed reasonably well even in the presence of significant unmeasured excitations. It was also shown that results were poor when referenced to DOFs with relatively low response. Experimental testing carried out on a cantilever beam excited with pairs of piezoceramic actuators reflected the observations of the numerical tests. Unmeasured random excitation was found to affect the accuracy of the results to a greater extent than similar levels of unmeasured periodic excitation due to the differences in the way the ARMAX algorithm accounts for each type of unmeasured excitation. The unmeasured periodic excitation was often modelled as mode, however, the estimated damping was typically estimated as negative, as a consequence of the backwards ARX models, and this allowed these spurious modes to be distinguished from vibration modes. The ARMAX algorithm was found to be sensitive to poorly excited modes, which were due to the characteristics of the piezoceramic actuators, as discussed in Chapter 4. An additional observation was that wide frequency ranges resulted in low-order modes being estimated poorly.

Chapter 7 revisited the helicopter-like structure as a representative case for testing of the ARMAX estimation algorithm. A range of experiments incorporating unmeasured periodic and random excitation were carried out and the use of periodic measured excitation allowed synchronous averaging of the measured data. The ARMAX algorithm successfully identified modal parameters for cases where 200% unmeasured periodic excitations were present, which included components within 2 Hz of vibration modes. In addition, the algorithm was found to perform well when close to 90% unmeasured random excitation was present, as well as in a case with both unmeasured periodic and random excitation. Closely spaced modes were identified by the ARMAX algorithm although results reinforced the observation that modes with low response at particular measurement points were poorly identified. The sign of damping was again shown to be useful in distinguishing between spurious modes and vibration modes. The ARMAX algorithm was found to perform well when compared to a frequency domain RFLS algorithm, in particular using significantly less data. Mode identification was also found to be easier due to smoother synthesised FRFs produced as part of the ARMAX estimation procedure.

The experimental case studies presented in Chapters 6 and 7 suggested that while the ARMAX algorithm performed well for cases with moderate levels of unmeasured excitation, increasing the level of unmeasured excitation lead to a decrease in the quality of modal parameter estimates. A natural extension of this is when the unmeasured excitations are dominant and this corresponds to the case of operational or response-only modal analysis. Chapter 8 presented a review of existing response-only modal analysis methods and it was noted that most were adapted from input-output estimation algorithms. A preliminary study investigating the adaptation of the ARMAX estimation algorithm was undertaken. A number of factors limiting the direct application of the ARMAX algorithm to response measurements were identified, namely, the lack of zero information in a scalar AR model and the inability of backwards AR models to distinguish between vibration and spurious modes for non-deterministic vibration responses. Two algorithms were proposed to overcome these limitations while still maintaining the features to enable model selection and distinguish between spurious and vibration modes. Numerical tests demonstrated that the MIMO version of the algorithm performed reasonably well, and correlation functions calculated from response measurements were of benefit as averaging of correlation functions attenuated random noise present in the response measurements. Experimental tests verified the numerical test results; however, a number of observations were made that limited the practical implementation of the adapted algorithm in its current form. Results were found to be sensitive to model order specification, which was a potentially difficult task because the orders of three separate model components could be specified separately. The algorithm's sensitivity to model order had implications for the NPDP model selection criterion, which was found to be ineffective as spurious modes could be estimated with positive damping. This also prevented spurious modes being distinguished from vibration modes. Experimental results for the MIMO AR-ARMAX algorithm were found to compare well with results from an enhanced frequency domain decomposition method, and used considerably less data. However, AR modelling of the experimental data also yielded very good results, suggesting that the extra stages involved in the AR-ARMAX algorithm were of limited benefit. An exception to this was that damping estimates from AR modelling showed positive bias. The preliminary study presented in Chapter 8 nevertheless provided considerable insight into the development of a general algorithm for estimating modal parameters under all possible excitation conditions: measured excitation; measured excitation with unmeasured components; and ambient or fully unmeasured excitation.

9.2 Recommendations for Further Work

The ARMAX estimation algorithm incorporated a diagonal model structure, which allowed MIMO measurements to be decomposed into a series of MISO estimation problems. The work in Chapter 8 showed that MIMO AR(MAX) models had some benefits in terms of improved accuracy of modal parameters. Therefore, a study into

MIMO estimation of ARMAX models using a diagonal structure for the AR matrix (as opposed to separation into a series of MISO models) as well as estimation of a fully parameterised ARMAX model could potentially yield improvements in the accuracy of the ARMAX algorithm. This could also address the problems encountered with measurement points having low level responses for some modes.

Piezoceramic actuators have many advantages over other types of excitation used in modal analysis, particularly for permanent applications. Chapter 4 and experimental results in Chapter 6 demonstrated limitations of piezoceramic actuators when applied to beams. Studies of different actuator configurations applied to more complex structures in modal analysis are needed to better demonstrate their advantages and limitations. The consideration of piezoceramic actuators for experimental modal analysis of plates and cylinders would be a natural extension to the study on beams presented in Chapter 4. A general goal is the development of piezoceramic actuator configurations that could be applied to an arbitrary structure for effective excitation of a large number of vibration modes.

The literature reviews presented in Chapters 2 and 8 noted that many operational modal analysis algorithms had been adapted from input-output algorithms, although studies into their applications considered either measured excitation and response or response-only situations separately. Of interest is the adaptation of algorithms for dealing with any level of measured excitation in the presence of unmeasured excitation. In this thesis one such algorithm has been considered and similar studies could be applied to other algorithms. For example, state-space based modal parameter estimation may have more desirable numerical properties when considering models of high order and large dimension.

References

1. Johnson, W., *Helicopter Theory*. Princeton University Press, New Jersey, 1980.

2. Bielawa, R.L., *Rotary Wing Structural Dynamics and Aeroelasticity*. AIAA, Washington, DC, 1992.

3. Morairty, B.J., P.E. Keary, *The Analytical Substantiation of the SH-2G(E) Helicopter*, in *Proc. of the American Helicopter Society 53rd Annual Forum*. Virginia Beach, Virginia, 1997.

4. Uhl, T., W. Bochniak, W. Lisowski, H. Van der Auweraer, L. Hermans, *Finite Element Model Updating Procedure and it's Application for Helicopter Tail Boom*, in *Proc. of ISMA 23*, 1998.

5. Uhl, T., W. Bockniak, W. Lisowski, L. Hermans, H. Van der Auweraer, J. Malecki, *FE-Model Correlation of a Helicopter Using Ground Test Results*, in *Proc. of the International Modal Analysis Conference* **-** *IMAC*, 1999.

6. Yeo, H., I. Chopra, *Coupled Rotor/Fuselage Vibration Analysis Using Detailed 3-D Airframe Models*, Mathematical and Computer Modelling, **33**(10-11): pp. 1035-1054, 2001.

7. Durno, J.A., G.R. Howland, W.J. Twomey, *Comparison of Black Hawk Shake Test Results with Nastran Finite Element Analysis*, in *Proc. 43rd Annual Forum of the American Helicopter Society*. St. Louis, Missouri, 1987.

8. D'Ambrogio, W., A. Fregolent, *Results Obtained by Minimising Natural Frequency and Anti-Resonanace Errors of A Beam Model*, Mechanical Systems and Signal Processing, **17**(1): pp. 29-37, 2003.

9. Deraemaeker, A., P. Ladeveze, S. Le Loch, *Results Obtained by the CRE Updating Method Using a Plate Model*, Mechanical Systems and Signal Processing, **17**(1): pp. 47-54, 2003.

10. Dunn, S.A., *Optimised Structural Dynamic Aircraft Finite Element Models Involving Mass, Stiffness, and Damping Elements*, in *Proc. International Forum on Aeroelasticity and Structural Dynamics*. Madrid, Spain, 2001.

11. Goge, D., *Automatic Updating of Large Aircraft Models Using Experimental Data from Ground Vibration Testing*, Aerospace Science and Technology, **7**(1): pp. 33-45, 2003.

12. Goge, D., M. Link, *Results Obtained by Minimising Natural Frequency and Mode Shape Errors of a Beam Model*, Mechanical Systems and Signal Processing, **17**(1): pp. 21-27, 2003.

13. Imregun, M., W.J. Visser, D.J. Ewins, *Finite Element Model Updating Using Frequency Response Function Data–I. Theory and Initial Investigation*, Mechanical Systems and Signal Processing, **9**(2): pp. 187-202, 1995.

14. Thonon, C., J.-C. Golinval, *Results Obtained by Minimising Natural Frequency and MAC-Value Errors of A Beam Model*, Mechanical Systems and Signal Processing, **17**(1): pp. 65-72, 2003.

15. Foss, G., T. Rosenberger, *The CH-47D "CHINOOK" Helicopter Shake Test*, in *Proc. International Modal Analysis Conference - IMAC*. Orlando, Florida, 1997.

16. Lisowski, W., T. Uhl, A. Wasilak, *Modal Analysis of Helicopters - The Experimental Conditions*, in *Proc. of ISMA 23*, 1998.

17. Uhl, T., W. Lisowski, J. Malecki, *Strain Modal Testing of a Helicopter Tail Boom*, in *Proc. International Modal Analysis Conference - IMAC*. Santa Barbara, California, 1998.

18. Giansante, N., N. Calapodas, *Modal Analysis Using Helicopter Dynamic Test Data*, in *Proc. American Society of Mechanical Engineers Design Engineering Technical Conference*, 1981.

19. Farrar, C.R., G.H. James III, *System Identification from Ambient Vibration Measurements on a Bridge*, Journal of Sound and Vibration, **205**(1): pp. 1-18, 1997.

20. Hermans, L., H. Van der Auweraer, *Modal Testing and Analysis of Structures Under Operational Conditions: Industrial Applications*, Mechanical Systems and Signal Processing, **13**(2): pp. 193-216, 1999.

21. Abdelghani, M., M. Goursat, T. Biolchini, *On-Line Modal Monitoring of Aircraft Structures Under Unknown Excitation*, Mechanical Systems and Signal Processing, **13**(6): pp. 839-853, 1999.

22. Abdelghani, M., M. Goursat, T. Biolchini, L. Hermans, H. Van der Auweraer, *Performance of Output-Only Identification Algorithms for Modal Analysis of Aircraft Structures*, in *Proceedings of the International Modal Analysis Conference - IMAC*, 1999.

23. Hermans, L., H. Van der Auweraer, M. Abdelghani, P. Guillaume, *Evaluation of Subspace Identification Techniques for the Analysis of Flight Test Data*, in *Proceedings of the International Modal Analysis Conference - IMAC*, 1998.

24. Mevel, L., A. Benveniste, M. Basseville, M. Goursat, B. Peeters, H. Van der Auweraer, A. Vecchio, *In-Flight Structural Identification: Input/Output Versus Output-Only Data Processing*, Report 5108, INRIA (Institut National De Recherche en Informatique et en Automatique), 2004.

25. Hermans, L., H. Van der Auweraer, A. Hatami, J.E. Cooper, T. Uhl, W. Lisowski, A. Wasilak, *In-Flight Modal Testing and Analysis of a Helicopter*, in *Proc. International Modal Analysis Conference - IMAC*, 1999.

26. Basseville, M., A. Benveniste, M. Goursat, L. Hermans, H. Van der Auweraer, *Output-Only Subspace-Based Structural Identification: From Theory to Industrial Testing Practice*, Journal of Dynamic Systems, Measurement, and Control, **123**: pp. 668-676, 2001.

27. Randall, R.B., Y. Gao, J. Swevers, *Updating Modal Models from Response Measurements*, in *Proc. ISMA23*. Leuven, Belgium, 1998.

28. Ford, R., R.B. Randall, T. Wardrop, *Updating Modal Properties From Response-Only Measurements on a Rail Vehicle*, Report The University of New South Wales, School of Mechanical and Manufacturing Engineering, 2002.

29. Harris, C.M., *Shock & Vibration Handbook.* Third ed.,1988.

30. He, J., Z.-F. Fu, *Modal Analysis*. Butterworth-Heineman, Oxford, 2001.

31. Ewins, D.J., *Modal Testing: Theory and Practice*. Research Studies Press, 1991.

32. Shih, C.Y., Y.G. Tsuei, R.J. Allemang, D.L. Brown, *Complex Mode Indication Function and its Applications to Spatial Domain Parameter Estimation*, Mechanical Systems and Signal Processing, **2**(4): pp. 367-377, 1988.

33. Allemang, R.J., D.L. Brown, *A Unified Matrix Polynomial Approach to Modal Identification*, Journal of Sound and Vibration, **211**(3): pp. 301-322, 1998.

34. Yang, Q.J., P.Q. Zhang, C.Q. Li, X.P. Wu, *A System Theory Approach to Multi-Input Multi-Output Modal Parameters Identification Methods*, Mechanical Systems and Signal Processing, **8**(2): pp. 159-174, 1994.

35. Richardson, M.H., D.L. Formenti, *Global Curve Fitting of Frequency Response Functions Using the Rational Fraction Polynomial*, in *Proceedings of the 3rd International Modal Analysis Conference* - *IMAC*, 1985.

36. Van der Auweraer, H., J. Leuridan, *Multiple Input Orthogonal Polynomial Parameter Estimation*, in *Proceedings of the International Modal Analysis Conference* - *IMAC*, 1987.

37. Van der Auweraer, H., J. Leuridan, *Multiple Input Orthogonal Polynomial Parameter Estimation*, Mechanical Systems and Signal Processing, **1**(3): pp. 259-272, 1987.

38. Peeters, B., G. De Roeck, *Stochastic System Identification for Operational Modal Analysis: A Review*, Journal of Dynamic Systems, Measurement, and Control, **123**: pp. 659-667, 2001.

39. Petsounis, K.A., S.D. Fassois, *Parametric Time-Domain Methods for the Identification of Vibrating Structures—A Critical Comparison and Assessment*, Mechanical Systems and Signal Processing, **15**(6): pp. 1031-1060, 2001.

40. Lew, J.-S., J.-N. Juang, R.W. Longman, *Comparison of Several System Identification Methods for Flexible Structures*, Journal of Sound and Vibration, **167**(3): pp. 461-480, 1993.

41. Abdelghani, M., M. Verhaegen, P. Van Overschee, B. De Moor, *Comparison Study of Subspace Identification Methods Applied to Flexible Structures*, Mechanical Systems and Signal Processing, **12**(5): pp. 679-692, 1998.

42. Van Overschee, P., B. De Moor, *Subspace Identification for Linear Systems: Theory—Implementation—Applications*. Kluwer Academic Publishers, Dordrecht, The Netherlands, 1996.

43. Ljung, L., *System Identification Theory for the User*. 1st ed., Prentice-Hall, Englewood Cliffs, 1987.

44. Söderström, T., P. Stoica, *System Identification*. Prentice Hall International, UK, 1989.

45. Batill, S.M., J.J. Hollkamp, *Parameter Identification of Discrete-Time Series Models for Structural Response Prediction*, AIAA Journal, **27**(11): pp. 1636-1643, 1989.

46. Hollkamp, J.J., S.M. Batill, *Automated Parameter Identification and Order Reduction for Discrete Time Series Models*, AIAA Journal, **29**(1): pp. 96-103, 1991.

47. Cooper, J.E., *The Use of Backwards Models for Structural Parameter Identification*, Mechanical Systems and Signal Processing, **6**(3): pp. 217-228, 1992.

48. Yun, C.-B., H.-J. Lee, C.-G. Lee, *Sequential Prediction-Error Method for Structural Identification*, Journal of Engineering Mechanics, **123**(2): pp. 115-122, 1997.

49. Hu, S., Y.B. Chen, S.M. Wu, *Multi-Output Modal Parameter Identification by Vector Time Series Modeling*, in *Machinery Dynamics Applications and*

Vibration Control Problems: 12th Biennial Conference on Mechanical Vibration and Noise. Montreal, Quebec, Canada, 1989.

50. Golub, G.H., C.F. Van Loan, *Matrix Computations*. Johns Hopkins University Press, Baltimore, Maryland, 1983.

51. Park, B.-H., K.-J. Kim, *Vector ARMAX Modeling Approach in Multi-Input Modal Analysis*, Mechanical Systems and Signal Processing, **3**(4): pp. 373-387, 1989.

52. Fassois, S.D., J.E. Lee, *Suboptimum Maximum Likelihood Identification of ARMAX Processes*, Journal of Dynamic Systems, Measurement, and Control, **112**(4): pp. 586-595, 1990.

53. Fassois, S.D., J.E. Lee, *A Linear Multi-Stage Method for Multivariate ARMAX Process Identification, Part I: The Basic Forms of the Estimator*, in *Paper 10-WA/DSC-11, Proc. 1990 ASME Winter Annual Meeting*, 1990.

54. Fassois, S.D., J.E. Lee, *A Linear Multi-Stage Method for Multivariate ARMAX Process Identification, Part II: Effective Structure/Parameter Estimation and Performance Evaluation*, in *Paper 90-WA/DSC-12, Proc. 1990 ASME Winter Annual Meeting*, 1990.

55. Fassois, S.D., *MIMO LMS-ARMAX Identification of Vibrating Structures—Part I: The Method*, Mechanical Systems and Signal Processing, **15**(4): pp. 723-735, 2001.

56. Florakis, A., S.D. Fassois, F.M. Hemez, *MIMO LMS-ARMAX Identification of Vibrating Structures—Part II: A Critical Assessment*, Mechanical Systems and Signal Processing, **15**(4): pp. 737-758, 2001.

57. Lee, J.E., S.D. Fassois, *On The Problem of Stochastic Experimental Modal Analysis Based on Multiple-Excitation Multiple-Response Data, Part 1: Dispersion Analysis of Continuous-Time Structural Systems*, Journal of Sound and Vibration, **161**(1): pp. 33-56, 1993.

58. Fassois, S.D., K.F. Eman, S.M. Wu, *A Linear Time-Domain Method for Structural Dynamics Identification*, Journal of Vibration and Acoustics, **112**(1): pp. 98-106, 1990.

59. Fassois, S.D., *A Fast Rational Model Approach to Parametric Spectral Estimation--Part II: Properties and Performance Evaluation*, Journal of Vibration and Acoustics, **112**: pp. 328-336, 1990.

60. Fassois, S.D., *A Fast Rational Model Approach to Parametric Spectral Estimation—Part I: The Algorithm*, Journal of Vibration and Acoustics, **112**: pp. 321-327, 1990.

61. Mrad, R.B., S.D. Fassois, *Recursive Identification of Vibrating Structures from Noise-Corrupted Observations, Part 1: Identification Approaches*, ASME Journal of Vibration and Acoustics, **113**(3): pp. 354-361, 1991.

62. Mrad, R.B., S.D. Fassois, *Recursive Identification of Vibrating Structures from Noise-Corrupted Observations, Part 2: Performance Evaluation via Numerical and Laboratory Experiments*, ASME Journal of Vibration and Acoustics, **113**(3): pp. 362-368, 1991.

63. Verboven, P., P. Guillaume, B. Cauberghe, S. Vanlanduit, E. Parloo, *Modal Parameter Estimation from Input-Output Fourier Data Using Frequency-Domain Maximum Likelihood Identification*, Journal of Sound and Vibration, **276**(3-5): pp. 957-979, 2004.

64. Guillaume, P., R. Pintelon, J. Schoukens, *Description of a Parametric Maximum Likelihood Estimator in the Frequency Domain for Multi-Input, Multi-Output Systems and its Application to Flight Flutter Analysis*, Mechanical Systems and Signal Processing, **4**(5): pp. 405-416, 1990.

65. Brincker, R., N. Møller, eds., *Proc. 1st International Operational Modal Analysis Conference, Copenhagen, Denmark*, 2005.

66. Cauberghe, B., P. Guillaume, P. Verboven, E. Parloo, *Identification of Modal Parameters Including Unmeasured Forces and Transient Effects*, Journal of Sound and Vibration, **265**(3): pp. 609-625, 2003.

67. Vanlanduit, S., P. Guillaume, B. Cauberghe, E. Parloo, G. De Sitter, P. Verboven, *On-Line Identification of Operational Loads Using Exogenous Inputs*, Journal of Sound and Vibration, **285**(1-2): pp. 267-279, 2005.

68. Ernst, R.R., *Sensitivity Enhancement in Magnetic Resonance. I. Analysis of the Method of Time Averaging*, The Review of Scientific Instruments, **36**(12): pp. 1689-1695, 1965.

69. Braun, S., *The Extraction of Periodic Waveforms by Time Domain Averaging*, Acustica, **32**(2): pp. 69-77, 1975.

70. Braun, S., *Averaging*, in *Encyclopedia of Vibration*, S. Braun, D. Ewins, and S.S. Rao, Editors, Academic Press, 2002.

71. Liu, H., H. Zuo, C. Jiang, L. Qu, *An Improved Algorithm for Direct Time-Domain Averaging*, Mechanical Systems and Signal Processing, **14**(2): pp. 279-285, 2000.

72. McFadden, P.D., *A Revised Model for the Extraction of Periodic Waveforms by Time Domain Averaging*, Mechanical Systems and Signal Processing, **1**: pp. 83-95, 1987.

73. Gade, S., H. Herlufsen, *Windows to FFT Analysis (Part 1)*. B&K Technical Review No. 3, 1987.

74. Allemang, R.J., D.L. Brown, *A Correlation Coefficient for Modal Vector Analysis*, in *Proceedings of the 1st International Modal Analysis Conference - IMAC*, 1982.

75. Mottershead, J.E., M.I. Friswell, *Model Updating in Structural Dynamics: A Survey*, Journal of Sound and Vibration, **167**(2): pp. 347 - 375, 1993.

76. Link, M., M. Friswell, *Working Group 1: Generation of Validated Structural Dynamic Models—Results of a Benchmark Study Utilising the Garteur SM-AG19 Test-Bed*, Mechanical Systems and Signal Processing, **17**(1): pp. 9-20, 2003.

77. Mares, C., J.E. Mottershead, M.I. Friswell, *Results Obtained by Minimising Natural Frequency Errors and Using Physical Reasoning*, Mechanical Systems and Signal Processing, **17**(1): pp. 39-46, 2003.

78. Bohle, K., C.-P. Fritzen, *Results Obtained by Minimising Natural Frequency and MAC-Value Errors of a Plate Model*, Mechanical Systems and Signal Processing, **17**(1): pp. 55-64, 2003.

79. Levin, R.I., N.A.J. Lieven, *Dynamic Finite Element Model Updating Using Simulated Annealing and Genetic Algorithms*, Mechanical Systems and Signal Processing, **12**: pp. 91 -120, 1998.

80. Lu, Y., Z. Tu, *A Two-Level Neural Network Approach for Dynamic FE Model Updating Including Damping*, Journal of Sound and Vibration, **275**(3-5): pp. 931-952, 2004.

81. Dossing, O., *Structural Testing Part 1: Mechanical Mobility Measurements*. Bruel&Kjaer, 1988.

82. Endo, H., R. Randall, *Model Updating of Helicopter-Like Structure*, Report CEVA - 2002 - PR01, Defence Science and Technology Organisation Aeronautical and Maritime Research Laboratory, Australia, 2002.

83. *FEMtools Theoretical Manual v2.0*. Dynamic Design Solutions.

84. Mukherjee, A., S. Joshi, *Piezoelectric Sensor and Actuator Spatial Design for Shape Control of Piezolaminated Plates*, AIAA, **40**(6): pp. 1204-1210, 2002.

85. Moheimani, S.O.R., D. Halim, A.J. Fleming, *Spatial Control of Vibration: Theory and Experiments*. World Scientific, Singapore, 2003.

86. Moheimani, S.O.R., A.J. Fleming, *Piezoelectric Transducers for Vibration Control and Damping*. Springer-Verlag, London, 2006.

87. Fuller, C.R., S.J. Elliot, P.A. Nelson, *Active Control of Vibration*. Academic Press, London, 1996.

88. Barboni, R., A. Mannini, E. Fantini, P. Gaudenzi, *Optimal Placement of PZT Actuators for the Control of Beam Dynamics*, Smart Materials and Structures, **9**: pp. 110-120, 2000.

89. Crawley, E.F., J. de Luis, *Use of Piezoelectric Actuators as Elements of Intelligent Structures*, AIAA, **25**(10): pp. 1373-1385, 1987.

90. Dimitriadis, E.K., C.R. Fuller, C.A. Rogers, *Piezoelectric Actuators for Distributed Vibration Excitation of Thin Plates*, Journal of Vibration and Acoustics, **113**(1): pp. 100-107, 1991.

91. Gao, F., Y. Shen, L. Li, *The Optimal Design of Piezoelectric Actuators for Plate Vibroacoustic Control Using Genetic Algorithms with Immune Diversity*, Smart Materials and Structures, **9**: pp. 485-491, 2000.

92. Kapania, R.K., L. Sheng, *Toward More Effective Genetic Algorithms for the Optimization of Piezoelectric Actuator Locations*, AIAA, **40**(6): pp. 1246-1250, 2002.

93. Padula, S.L., R.K. Kincaid, *Optimisation Strategies for Sensor and Actuator Placement*, Report NASA/TM-1999-209126, NASA Langley Research Centre, 1999.

94. Park, C., C. Walz, I. Chopra, *Bending and Torsion Models of Beams with Induced-Strain Actuators*, Smart Materials and Structures, **5**: pp. 98-113, 1996.

95. Pota, H.R., S.O.R. Moheimani, M. Smith, *Resonant Controllers for Smart Structures*, Smart Materials and Structures, **11**: pp. 1-8, 2002.

96. Sadri, A.M., J.R. Wright, R.J. Wynne, *Modelling and Optimal Placement of Piezoelectric Actuators in Isotropic Plates Using Genetic Algorithms*, Smart Materials and Structures, **8**: pp. 490-498, 1999.

97. Yang, S., B. Ngoi, *Shape Control of Beams by Piezoelectric Actuators*, AIAA, **38**(12): pp. 2292-2298, 2000.

98. Bhalla, S., C.K. Soh, *Structural Health Monitoring by Piezo-Impedance Transducers. I: Modeling*, Journal of Aerospace Engineering, **17**(4): pp. 154-165, 2004.

99. Bhalla, S., C.K. Soh, *Structural Health Monitoring by Piezo-Impedance Transducers. II: Applications*, Journal of Aerospace Engineering, **17**(4): pp. 166-175, 2004.

100. Ong, C.W., Y. Lu, Y. Yang, *The Influence of Adhesive Bond on the Electro-Mechanical Admittance Response of a PZT Patch Coupled Smart Structure*, in *Proc. Second International Conference on Structural Stability and Dynamics*. Singapore, 2002.

101. Brennan, M.C., A.-M. Rivas McGowan, *Piezoelectric Power Requirements for Active Vibration Control*, in *SPIE's 4th Annual Symposium on Smart Structures and Materials*. San Diego, California, 1997.

102. Srinivasan, A.V., D.M. McFarland, *Smart Structures Analysis and Design*. Cambridge University Press, Cambridge, 2001.

103. Inman, D.J., *Engineering Vibration*. Prentice Hall, New Jersey, 1996.

104. Weisstein, E.W. *"Heaviside Step Function."* Mathworld -- A Wolfram Web Resource, http://mathworld.wolfram.com/HeavisideStepFunction.html 1999 [cited July 2006].

105. Weisstein, E.W. *"Delta Function."* Mathworld -- A Wolfram Web Resource, http://mathworld.wolfram.com/DeltaFunction.html 1999 [cited July 2006].

106. *Piezoelectric Ceramics Data Book for Designers*. Morgan Matroc Limited.

107. Bottega, W.J., *Engineering Vibrations*. CRC Press, Boca Raton, 2006.

108. Gawronksi, W.K., *Advanced Structural Dynamics and Active Control of Structures*. Springer-Verlag, 2004.

109. Friswell, M.I., *On The Design of Modal Actuators and Sensors*, Journal of Sound and Vibration, **241**(3): pp. 361 - 372, 2001.

110. Mohanty, P., D.J. Rixen, *Modified ERA Method for Operational Modal Analysis in the Presence of Harmonic Excitations*, Mechanical Systems and Signal Processing, **20**(1): pp. 114-130, 2006.

111. Mohanty, P., D.J. Rixen, *Operational Modal Analysis in the Presence of Harmonic Excitation*, Journal of Sound and Vibration, **270**(1-2): pp. 93-109, 2004.

112. Mohanty, P., D.J. Rixen, *A Modified Ibrahim Time Domain Algorithm for Operational Modal Analysis Including Harmonic Excitation*, Journal of Sound and Vibration, **275**(1-2): pp. 375-390, 2004.

113. Mohanty, P., D.J. Rixen, *Modified SSTD Method to Account for Harmonic Excitations During Operational Modal Analysis*, Mechanism and Machine Theory, **39**(12): pp. 1247-1255, 2004.

114. Parloo, E., P. Verboven, P. Guillaume, M. Van Overmeire, *Sensitivity-Based Operational Mode Shape Normalisation*, Mechanical Systems and Signal Processing, **16**(5): pp. 757-767, 2002.

115. Bernal, D., *Modal Scaling from Known Mass Perturbations*, Journal of Engineering Mechanics, **130**(9): pp. 1083-1088, 2004.

116. Ljung, L., *System Identification Theory for the User*. 2nd ed., Prentice-Hall, Englewood Cliffs, 1999.

117. Fassois, S.D., J.E. Lee, *On the Problem of Stochastic Experimental Modal Analysis Based on Multiple-Excitation Multiple-Response Data, Part II: The Modal Analysis Approach*, Journal of Sound and Vibration, **161**(1): pp. 57-87, 1993.

118. Papakos, V., S.D. Fassois, *Multichannel Identification of Aircraft Skeleton Structures Under Unobservable Excitation: A Vector AR/ARMA Framework*, Mechanical Systems and Signal Processing, **17**(6): pp. 1271-1290, 2003.

119. Weisstein, E.W., *et al. "Orthogonal Transformation."* Mathworld -- A Wolfram Web Resource, http://mathworld.wolfram.com/OrthogonalTransformation.html 1999 [cited September 2005].

120. Kumaresan, R., *On the Zeros of the Linear Prediction-Error Filter for Deterministic Signals*, IEEE Transactions on Acoustics, Speech, and Signal Processing, **31**(1): pp. 217-220, 1983.

121. Kumaresan, R., D.W. Tufts, *Estimating the Parameters of Exponentially Damped Sinusoids and Pole-Zero Modeling in Noise*, IEEE Transactions on Acoustics, Speech, and Signal Processing, **30**(6): pp. 833-840, 1982.

122. Hung, C.F., W.J. Ko, *Identification of Modal Parameters from Measured Output Data Using Vector Backward Autoregressive Model*, Journal of Sound and Vibration, **256**(2): pp. 249-270, 2002.

123. Oppenheim, A.V., R.W. Schafer, *Discrete-Time Signal Processing*. Prentice-Hall, Englewood Cliffs, 1989.

124. *Matlab v6.5 Function Reference*. The Mathworks, Natick, MA.

125. Kailath, T., *Linear Systems*. Prentice-Hall, Englewood Cliffs, 1980.

126. Fassois, S.D., K.F. Eman, S.M. Wu, *Sensitivity Analysis of the Discrete-to-Continuous Dynamic System Transformation*, ASME Journal of Dynamic Systems, Measurement and Control, **112**(1): pp. 1-9, 1990.

127. Fernandes, J.M., G.C. Goodwin, C.E. Desouza, *Estimation of Models for Systems Having Deterministic and Random Disturbances*, in *Proc. IFAC 10th Triennial World Congress on Automatic Control*, 1988.

128. Bendat, J.S., A.G. Piersol, *Engineering Applications of Correlation and Spectral Analysis*. John Wiley & Sons, 1980.

129. Peeters, B., C.E. Ventura, *Comparative Study of Modal Analysis Techniques for Bridge Dynamic Characteristics*, Mechanical Systems and Signal Processing, **17**(5): pp. 965-988, 2003.

130. Herlufsen, H., P. Andersen, S. Gade, N. Møller, *Identification Techniques for Operational Modal Analysis - An Overview and Practical Experiences*, in *Proc. 1st International Operational Modal Analysis Conference*. Copenhagen, Denmark, 2005.

131. Gade, S., N. Møller, H. Herlufsen, H. Konstantin-Hansen, *Frequency Domain Techniques for Operational Modal Analysis*, in *Proc. 1st International Operational Modal Analysis Conference*. Copenhagen, Denmark, 2005.

132. James III, G.H., T.G. Carne, J.P. Lauffer, *The Natural Excitation Technique (NExT) for Modal Parameter Extraction from Operating Wind Turbines*, Report SAND92 - 1666 UC-261, Sandia National Laboratories, 1993.

133. Pridham, B.A., J.C. Wilson, *A Study of Damping Errors in Correlation-Driven Stochastic Realizations Using Short Data Sets*, Probabilistic Engineering Mechanics, **18**(1): pp. 61-77, 2003.

134. Desforges, M.J., J.E. Cooper, J.R. Wright, *Spectral and Modal Parameter Estimation from Output-Only Measurements*, Mechanical Systems and Signal Processing, **9**(2): pp. 169-186, 1995.

135. Cooper, J.E., M.J. Desforges, J.R. Wright, *Modal Parameter Identification Using an Unknown Coloured Random Input*, Mechanical Systems and Signal Processing, **9**(6): pp. 685-695, 1995.

136. Benveniste, A., J.-J. Fuchs, *Single Sample Modal Identification of a Nonstationary Stochastic Process*, IEEE Transactions on Automatic Control, **AC-30**(1): pp. 66-74, 1985.

137. Peeters, B., G. De Roeck, *Reference-Based Stochastic Subspace Identification for Output-Only Modal Analysis*, Mechanical Systems and Signal Processing, **13**(6): pp. 855-878, 1999.

138. Lardies, J., *Modal Parameter Estimation and Model Order Selection of a Randomly Vibrating System*, Mechanical Systems and Signal Processing, **12**(6): pp. 825-838, 1998.

139. Lardies, J., *State-Space Identification of Vibrating Systems from Multi-Output Measurements*, Mechanical Systems and Signal Processing, **12**(4): pp. 543-558, 1998.

140. Shen, F., M. Zheng, D. Feng Shi, F. Xu, *Using The Cross-Correlation Technique to Extract Modal Parameters on Response-Only Data,* Journal of Sound and Vibration, **259**(5): pp. 1163-1179, 2003.

141. Peeters, B., H. Van der Auweraer, *PolyMAX: A Revolution in Operational Modal Analysis,* in *Proc. 1st International Operational Modal Analysis Conference.* Copenhagen, Denmark, 2005.

142. Rodrigues, J., R. Brincker, *Application of the Random Decrement Technique in Operational Modal Analysis,* in *Proc. 1st International Operational Modal Analysis Conference.* Copenhagen, Denmark, 2005.

143. Asmussen, J.C., R. Brincker, S.R. Ibrahim, *Statistical Theory of the Vector Random Decrement Technique*, Journal of Sound and Vibration, **226**(2): pp. 329-344, 1999.

144. He, X., G. De Roeck, *System Identification of Mechanical Structures by a High-Order Multivariate Autoregressive Model*, Computers & Structures, **64**(1-4): pp. 341-351, 1997.

145. Huang, C.S., *Structural Identification from Ambient Vibration Measurement Using The Multivariate AR Model*, Journal of Sound and Vibration, **241**(3): pp. 337-359, 2001.

146. Gao, Y., R.B. Randall, *Determination of Frequency Response Functions from Response Measurements–I. Extraction of Poles and Zeros from Response Cepstra*, Mechanical Systems and Signal Processing, **10**(3): pp. 293-317, 1996.

147. Gao, Y., R.B. Randall, *Determination of Frequency Response Functions from Response Measurements–II. Regeneration of Frequency Response from Poles and Zeros*, Mechanical Systems and Signal Processing, **10**(3): pp. 319-340, 1996.

148. Randall, R.B., *Frequency Analysis*. 3rd ed., Bruel & Kjaer, 1987.

149. Kopec, G.E., A.V. Oppenheim, J.M. Tribolet, *Speech Analysis by Homomorphic Prediction*, IEEE Transactions on Acoustics, Speech, and Signal Processing, **25**(1): pp. 40-49, 1977.

150. *ARTeMIS Extractor Pro, Release 3.5 Reference Manual*. Structural Vibration Solutions A/S.

Publications Arising from this Thesis Work

Journal Papers

1. Moore, S.M., Lai, J.C.S., Shankar, K., *ARMAX Modal Parameter Identification in the Presence of Unmeasured Excitation --I: Theoretical Background.* Mechanical Systems and Signal Processing, 2006. – *accepted for publication.*

2. Moore, S.M., Lai, J.C.S., Shankar, K., *ARMAX Modal Parameter Identification in the Presence of Unmeasured Excitation --II: Numerical and Experimental Verification.* Mechanical Systems and Signal Processing, 2006. – *accepted for publication.*

Conference Papers

1. Moore, S.M., Zhang, B., Lai, J., Shankar, K., *Model Updating and Determination of Structural Dynamic Properties in the Presence of a Second Source of Excitation.* in *3rd International Conference on Health and Usage Monitoring-Hums 2003*. 2003. Melbourne: Defence Science and Technology Organisation (DSTO) Australia.

2. Moore, S., Lai, J., and Shankar, K., *ARMAX Modal Parameter Estimation Using Random and Periodic Excitation.* in *Proc. 1st International Operational Modal Analysis Conference*. 2005. Copenhagen, Denmark.

3. Moore, S., Lai, J., and Shankar, K., *ARMAX Modal Parameter Identification for Structures Excited with Piezoceramic Actuators.* in *Proc. International Modal Analysis Conference (IMAC) XXIV*. 2006. St. Louis, U.S.A.

Reports

1. Moore, S., Lai, J., and Shankar, K., *Modal Analysis of a Simple Structure Using Periodic Impulsive Excitation and Synchronous Averaging*, Report AVU 0203, School of Aerospace and Mechanical Engineering, UNSW@ADFA, 2002.

2. Moore, S., Zhang, B., Lai, J., Shankar, K., *Finite Element Model Updating of a Helicopter-Like Structure*, Report AVU 0303, School of Aerospace and Mechanical Engineering, UNSW@ADFA, 2003.

3. Zhang, B., Moore, S., Lai, J., *Modal Analysis of a Helicopter-like Structure Using Periodic Impulsive Excitation and Synchronous Averaging*, Report AVU 0302, School of Aerospace and Mechanical Engineering, UNSW@ADFA, 2003.

4. Moore, S., Lai, J., and Shankar, K., *ARMAX Modal Parameter Identification for Structures Excited with Random and Periodic Signals*, Report AVU 0401, School of Aerospace, Civil, and Mechanical Engineering, UNSW@ADFA, 2004.

5. Moore, S., Lai, J., and Shankar, K., *ARMAX Modal Parameter Identification in the Presence of Unmeasured Periodic Excitation*, Report AVU 0501, School of Aerospace, Civil, and Mechanical Engineering, UNSW@ADFA, 2005.

6. Moore, S., Lai, J., and Shankar, K., *ARMAX Modal Parameter Identification in the Presence of Unmeasured Excitation*, Report AVU 0504, School of Aerospace, Civil, and Mechanical Engineering, UNSW@ADFA, 2005.

7. Moore, S., Lai, J., and Shankar, K., *Modal Parameter Identification from Vibration Response Measurements*, Report AVU 0601, School of Aerospace, Civil, and Mechanical Engineering, UNSW@ADFA, 2006.

Appendix A

A.1 Statistical Testing of Innovations Sequence

Section 5.3.3 discussed some statistical methods that can be used to test the assumptions made about the nature of innovations sequence and the correlation between the innovations sequence and the measured excitations. The BIC uses the covariance matrix of the innovations sequence to detect correlation between elements and also asses the magnitude of the innovations sequence. The auto- and cross-correlation functions can be used to extend this concept for different time lags, which potentially increases sensitivity to periodic components in the innovations sequence. The correlation functions were calculated for all combinations of innovations elements and two approaches to map the matrix of correlation functions to a scalar value were tested. The first approach calculated the sum of mean-square values for each correlation sequence and the second approach calculated the determinant of a matrix containing the mean-square of each correlation sequence. Figure A.1 shows values calculated using the first approach plotted for each iteration and model estimated from the same realisation of data as the BIC plots above. Figure A.2 shows values calculated by the second approach.

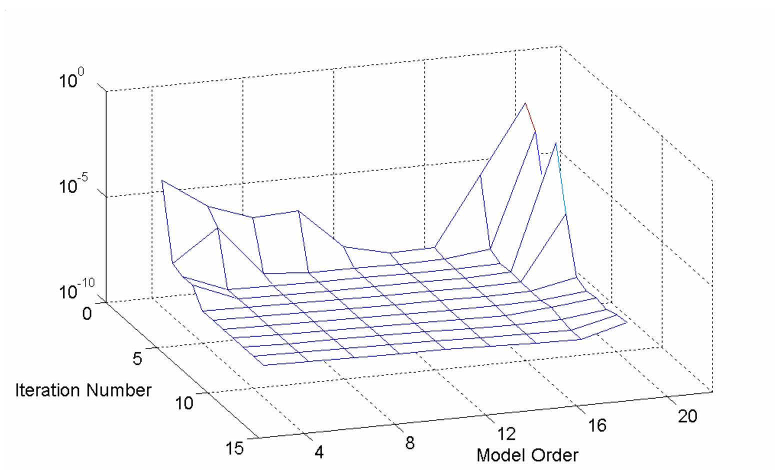

Figure A.1 Summed mean-square values of innovations correlation sequences for each model order and iteration estimated from a typical realisation of test 1 data.

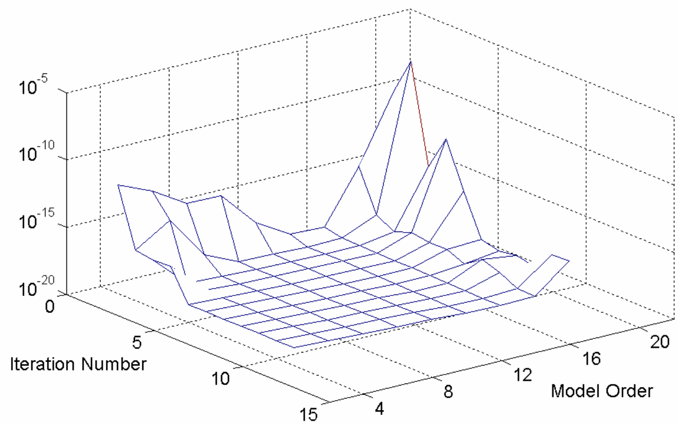

Figure A.2 Determinant of matrix of mean-square values calculated from each innovations correlation sequence for each model order and iteration estimated from a typical realisation of test 1 data.

Figures A.1 and A.2 both show similar topography to the modified BIC plot in figure 6.9 and similar conclusions apply.

The correlation between the innovations sequence and the measured input was tested using the two approaches discussed above. Figure A.3 shows the sum of mean square-values of the correlation sequence and figure A.4 shows the determinant of the matrix containing mean-square values of the correlation sequences.

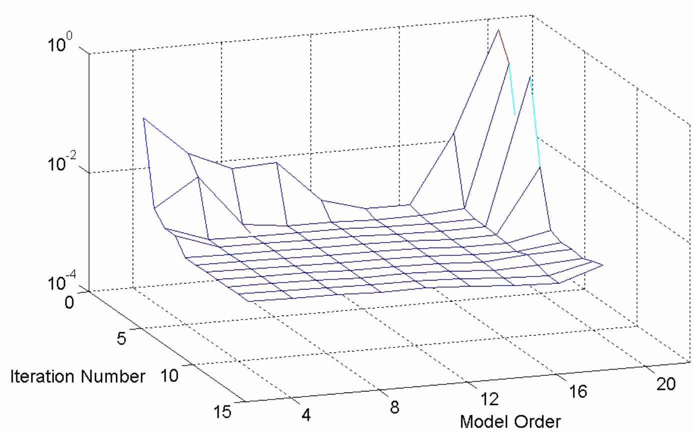

Figure A.3 Summed mean-square values of innovations-excitation correlation sequences for each model order and iteration estimated from a typical realisation of test 1 data.

The results in figure A.3 are similar to the innovations correlation tests shown in figures A.1 and A.2, however, the results for the determinant of the mean-square correlation sequence matrix shown in figure A.4 show an improved sensitivity to and a marginal improvement in the sensitivity to the iterations of stages 3 and 4.

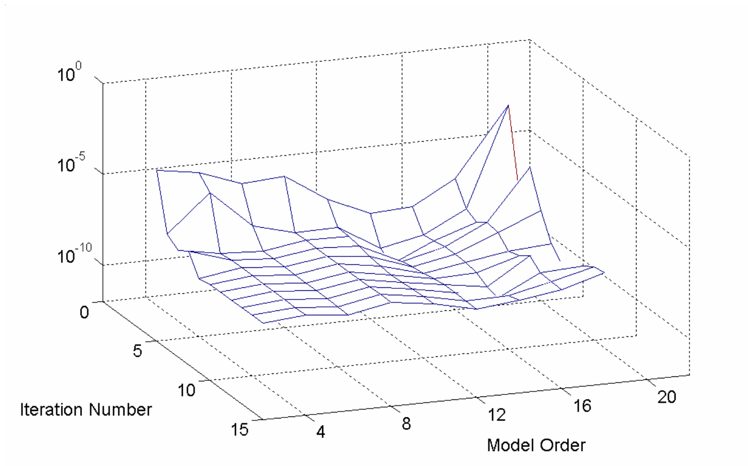

Figure A.4 Determinant of matrix of mean-square values calculated from innovations-excitation correlation sequences for each model order and iteration estimated from a typical realisation of test 1 data.

A.2 Condition Number of Regression Matrix

The conditioning of the regression matrix formed when solving the LS problems in stage 1 (see for example equation (5.20)) and stage 3 can give indications of the accuracy of the LS solution. Very high order models can lead to poor conditioning of the regression matrix and large numbers of iterations of stages 3 and 4 for large order models can also result in poor conditioning of the regression matrices due to filtering of the excitation and response sequences with an excessively high-order MA matrix. The use of the conditioning of the regression to indicate the best model order was investigated as this information could be easily calculated as part of the estimation procedure.

The condition number of the regression matrices used in each LS estimate in stage 1 and the iterations of stages 3 and 4 is shown in figure A.5 and A.6. Recall that the ARMAX estimation algorithm separates the MIMO model into *s* MISO models and solves each using the LS criterion.

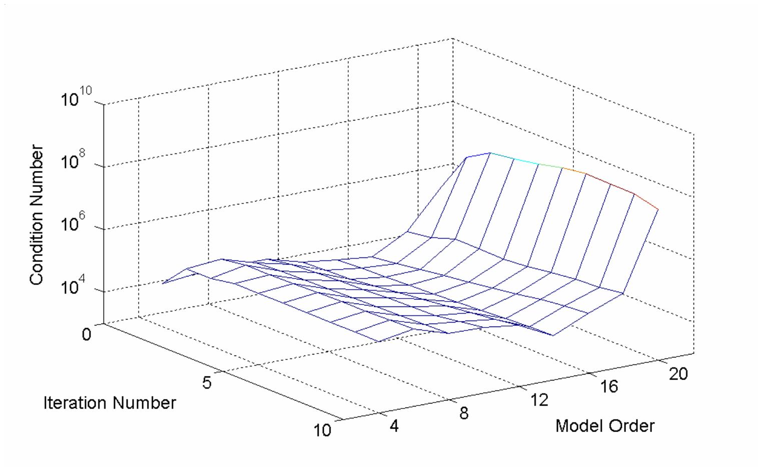

Figure A.5 Condition number of regression matrix for each model order and iteration used in LS estimate of ARX model, DOF 1 reference point.

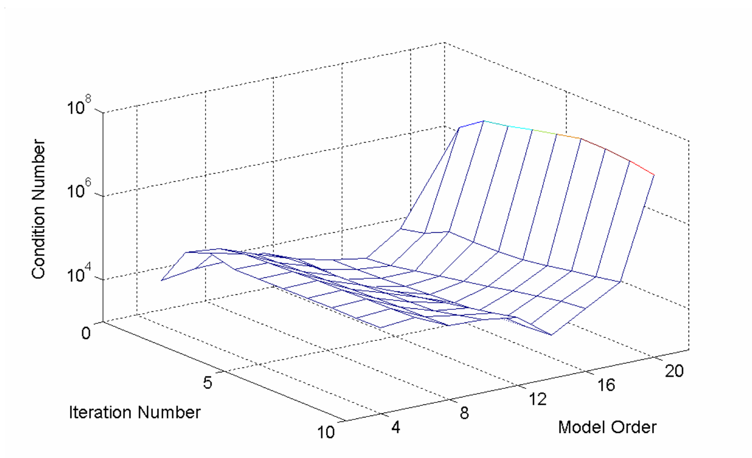

Figure A.6 Condition number of regression matrix for each model order and iteration used in LS estimate of ARX model, DOF 2 reference point.

The plots in figures A.5 and A.6 clearly show the poor conditioning of the regression matrix for higher order models. The condition number also increases relatively slowly for increasing numbers of iterations and this did not reflect the improvement in accuracy of the modal parameters after a number of iterations of stages 3 and 4.

Appendix B

This section shows FRFs synthesised from ARMAX models estimated in presence of unmeasured excitations, as discussed in section 7.4. The MIMO E2 results are used as a basis for comparing the ARMAX results obtained for different types of unmeasured excitations, and also for the analyses that included synchronous averaging of data records. FRFs are synthesised for four response measurement points (14, 18, 20, 29) well-separated on the structure (see figure 7.2 and table 7.1), including a point-inertance measurement (measurement point 29).

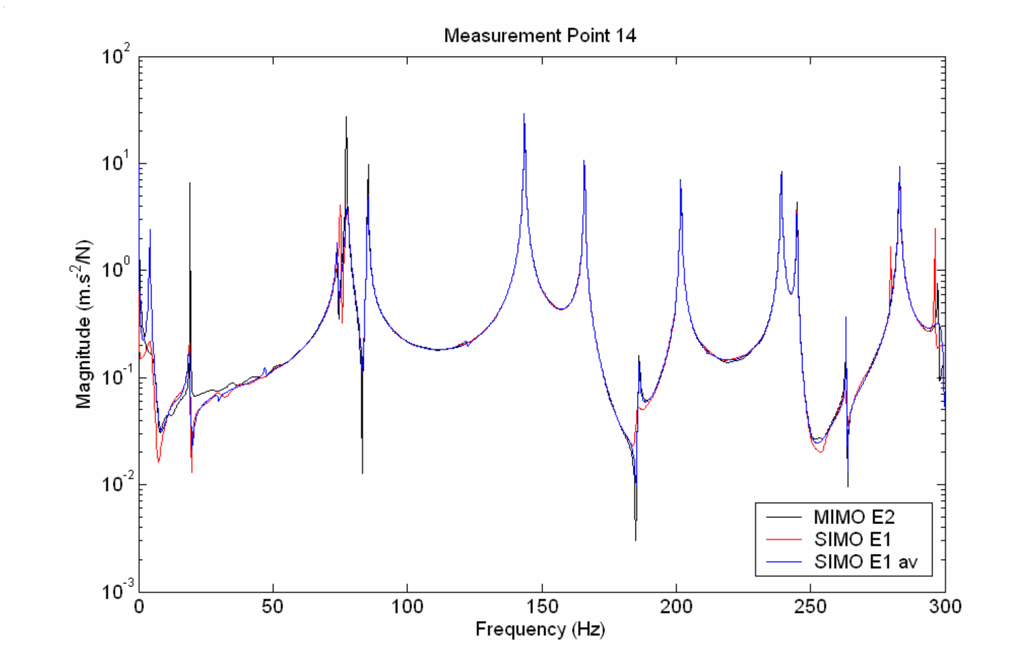

Figure B.1 Comparison of synthesised FRFs for measurement point 14 obtained from MIMO E2 (noise free), SIMO E1, and SIMO E1 av analyses.

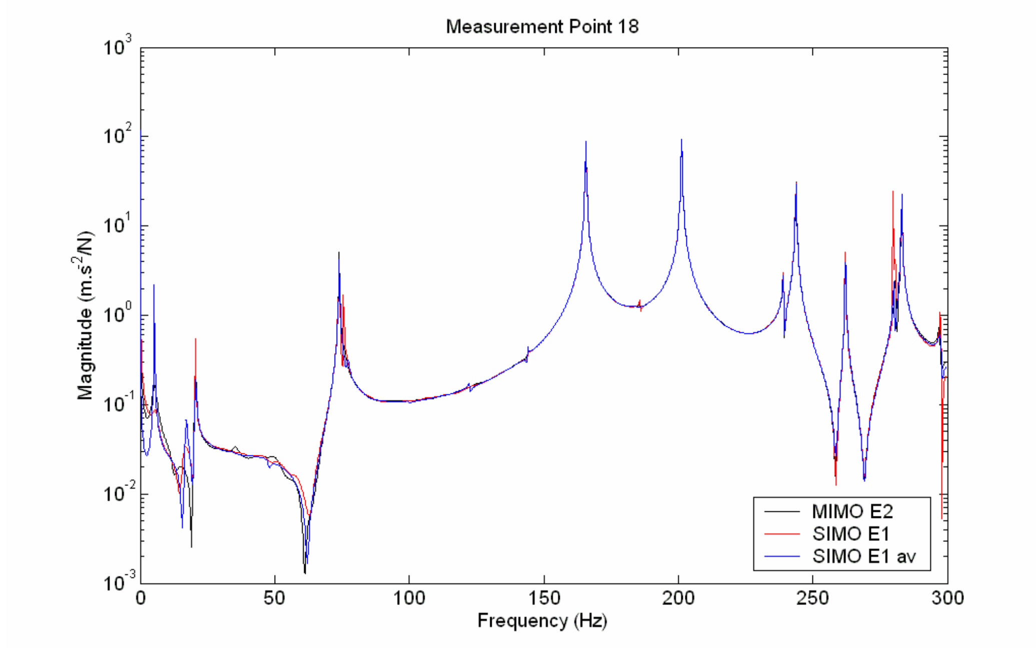

Figure B.2 Comparison of synthesised FRFs for measurement point 18 obtained from MIMO E2 (noise free), SIMO E1, and SIMO E1 av analyses.

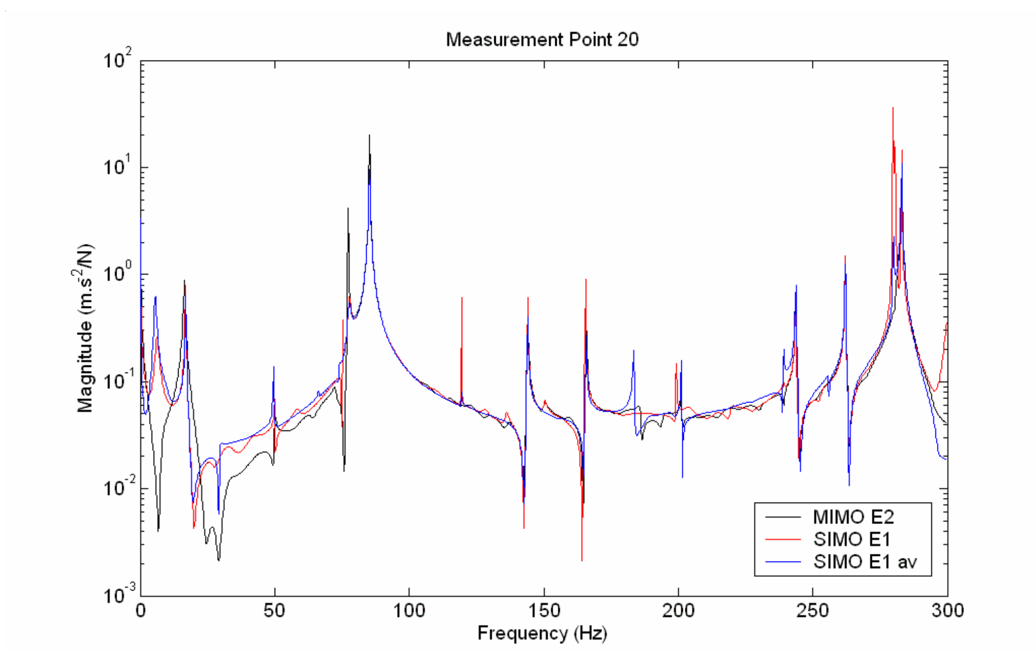

Figure B.3 Comparison of synthesised FRFs for measurement point 20 obtained from MIMO E2 (noise free), SIMO E2, and SIMO E2 av analyses.

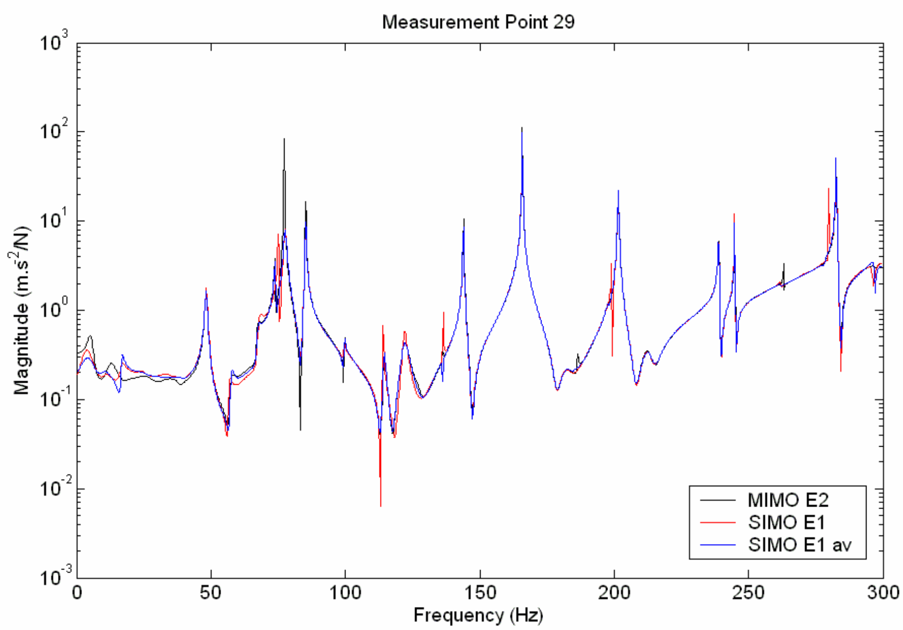

Figure B.4 Comparison of synthesised FRFs for measurement point 29 obtained from MIMO E2 (noise free), SIMO E1, and SIMO E1 av analyses.

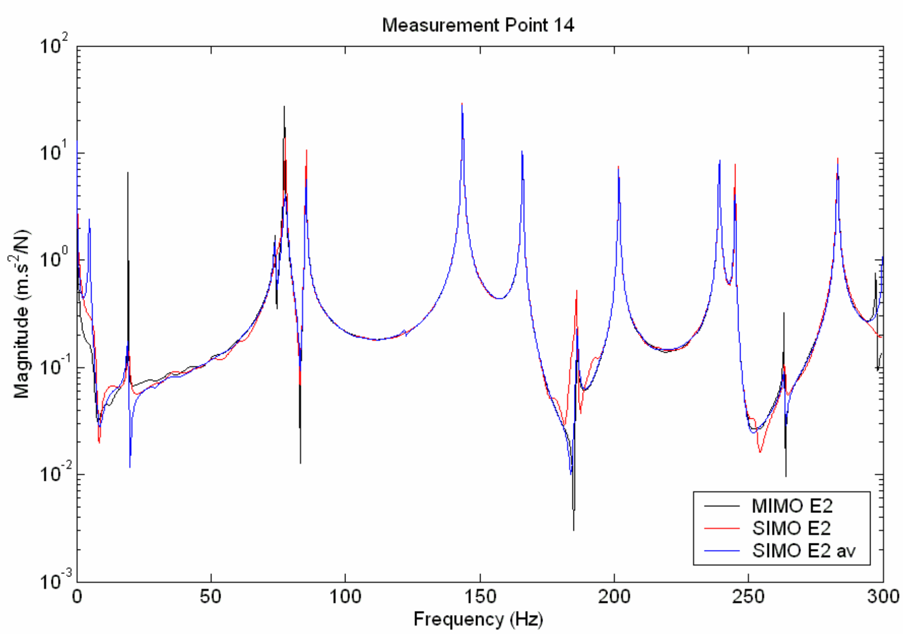

Figure B.5 Comparison of synthesised FRFs for measurement point 14 obtained from MIMO E2 (noise free), SIMO E2, and SIMO E2 av analyses.

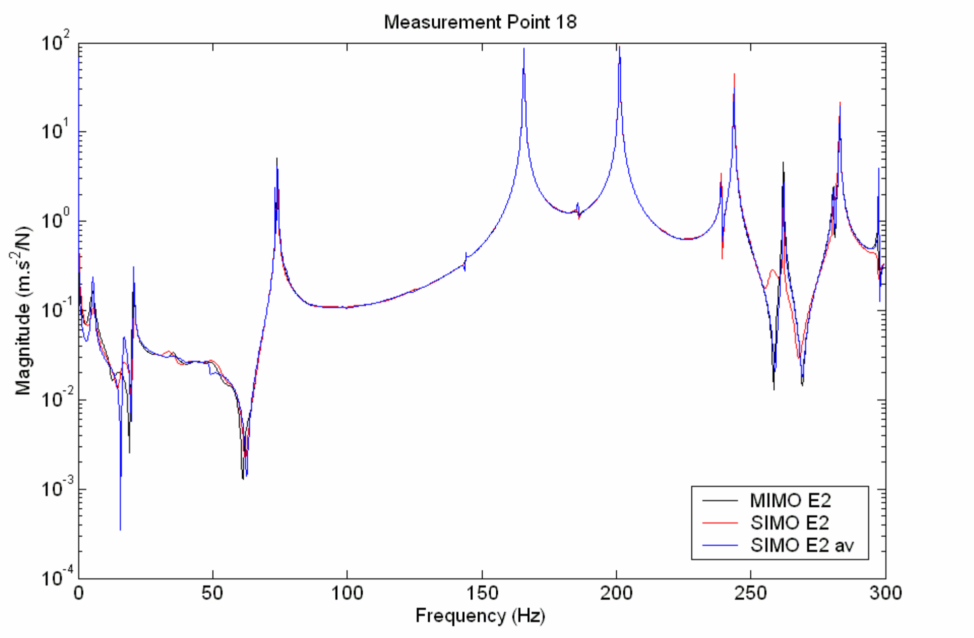

Figure B.6 Comparison of synthesised FRFs for measurement point 18 obtained from MIMO E2 (noise free), SIMO E2, and SIMO E2 av analyses.

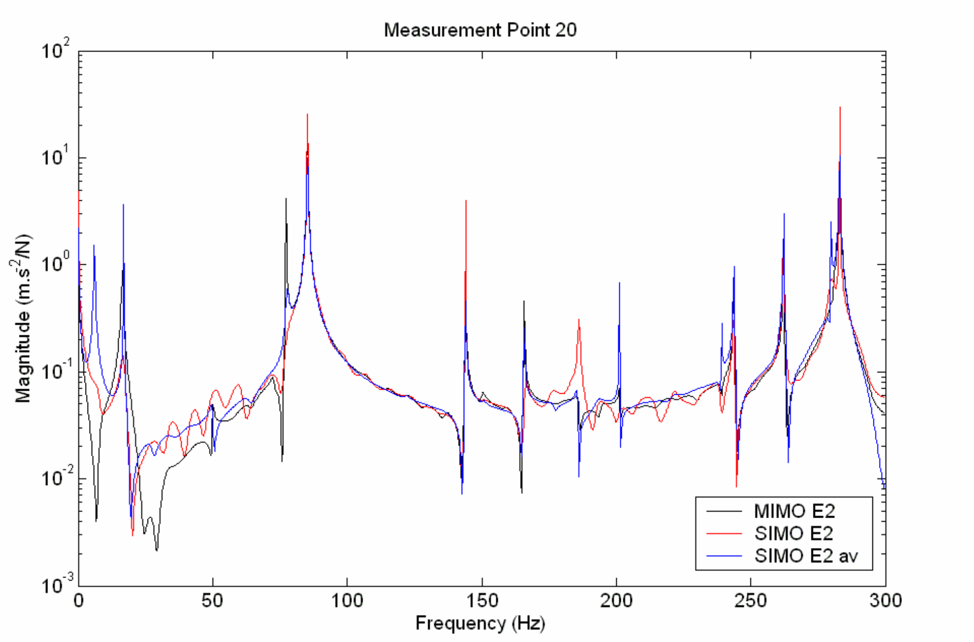

Figure B.7 Comparison of synthesised FRFs for measurement point 20 obtained from MIMO E2 (noise free), SIMO E2, and SIMO E2 av analyses.

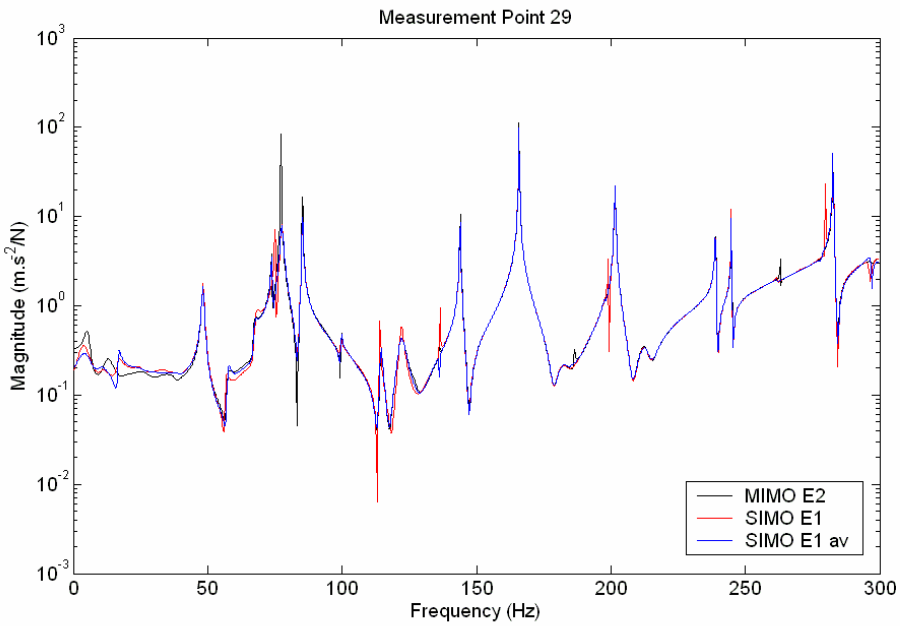

Figure B.8 Comparison of synthesised FRFs for measurement point 29 obtained from MIMO E2 (noise free), SIMO E2, and SIMO E2 av analyses.

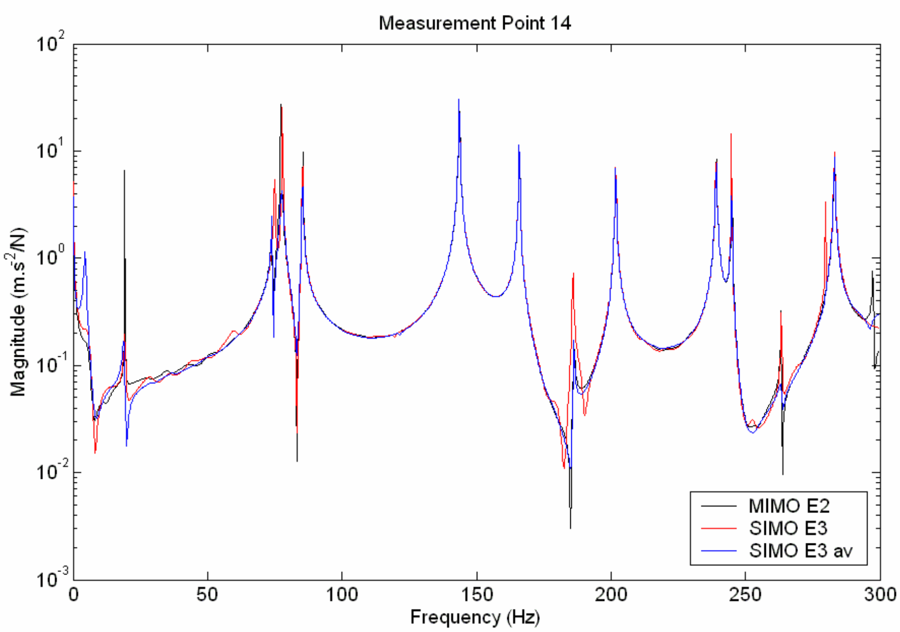

Figure B.9 Comparison of synthesised FRFs for measurement point 14 obtained from MIMO E2 (noise free), SIMO E3, and SIMO E3 av analyses.

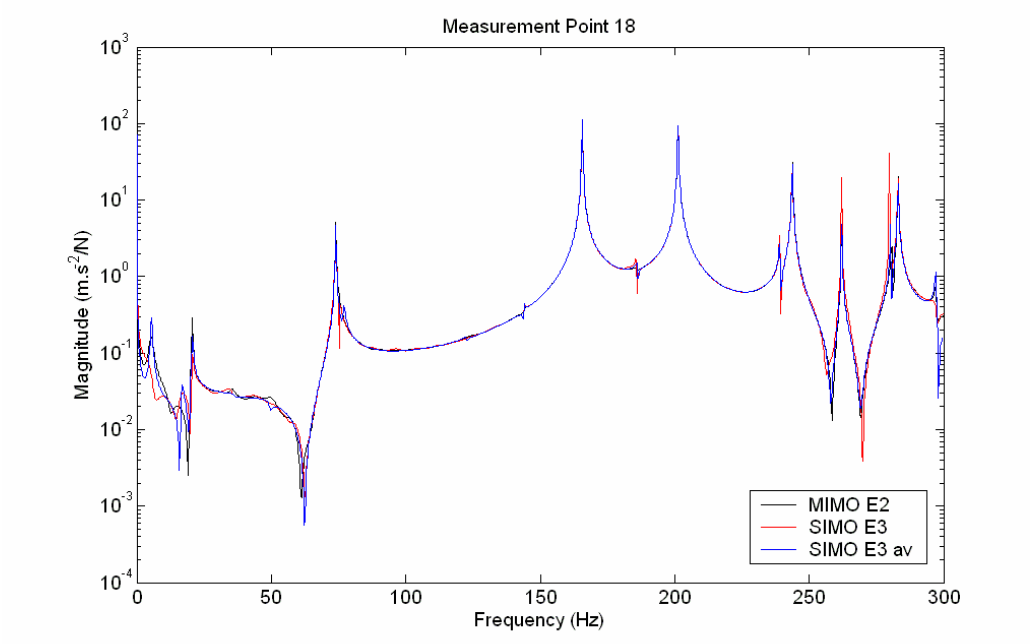

Figure B.10 Comparison of synthesised FRFs for measurement point 18 obtained from MIMO E2 (noise free), SIMO E3, and SIMO E3 av analyses.

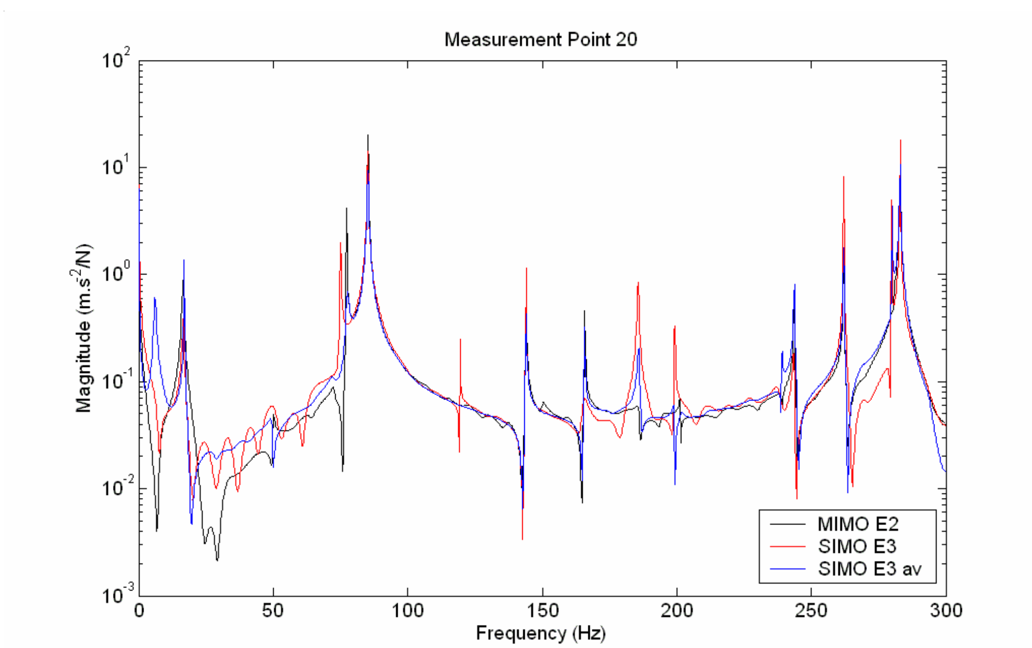

Figure B.11 Comparison of synthesised FRFs for measurement point 20 obtained from MIMO E2 (noise free), SIMO E3, and SIMO E3 av analyses.

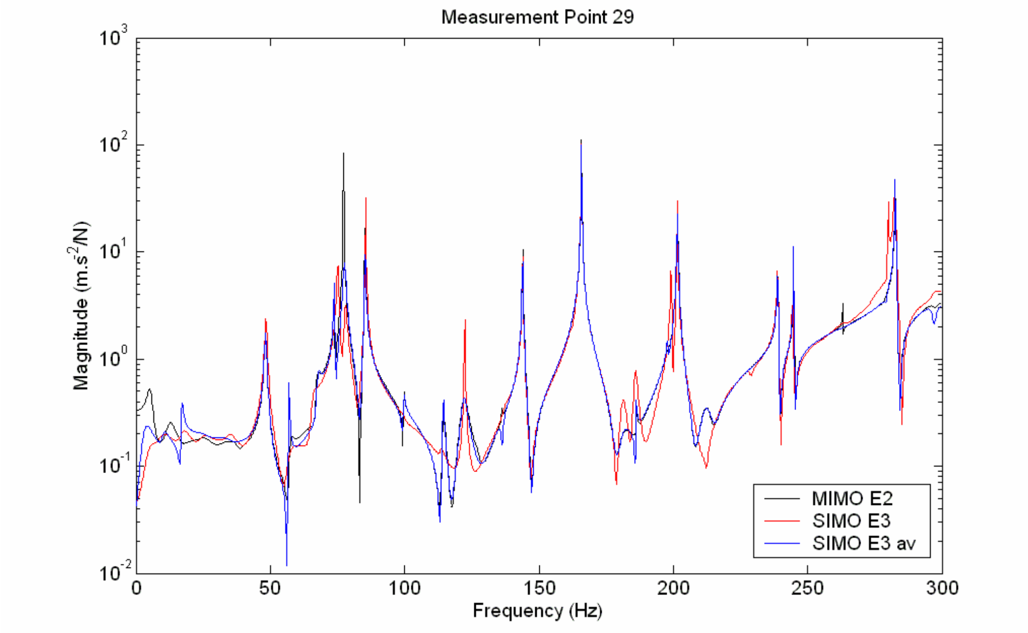

Figure B.12 Comparison of synthesised FRFs for measurement point 29 obtained from MIMO E2 (noise free), SIMO E3, and SIMO E3 av analyses.

Appendix C

The figures in this section illustrate the effect of synchronous averaging of excitation and response data before estimating modal parameters using a RFLS algorithm, as described in section 7.5. The modal parameters were estimated from excitation and response data corrupted by unmeasured excitations and are compared with results obtained under noise-free conditions using the ARMAX algorithm (ARMAX MIMO E2).

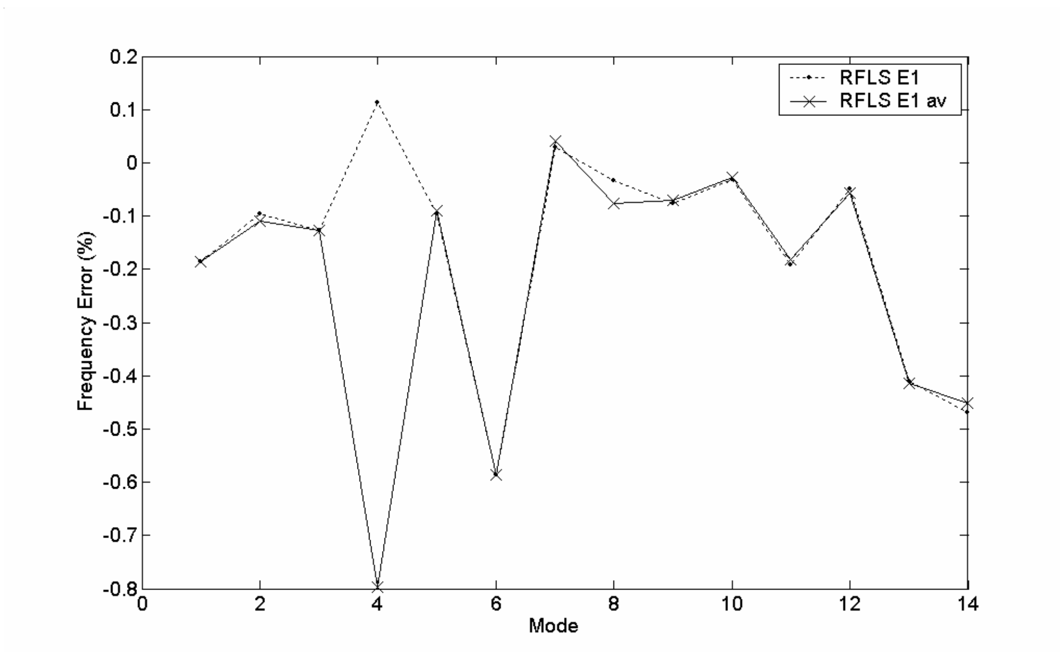

Figure C.1 Comparison of modal frequencies from RFLS FRF curve fitting of experiment 1 data with modal frequencies from ARMAX MIMO E2 analysis. RFLS E1 20 averages; RFLS E1 av 89 averages.

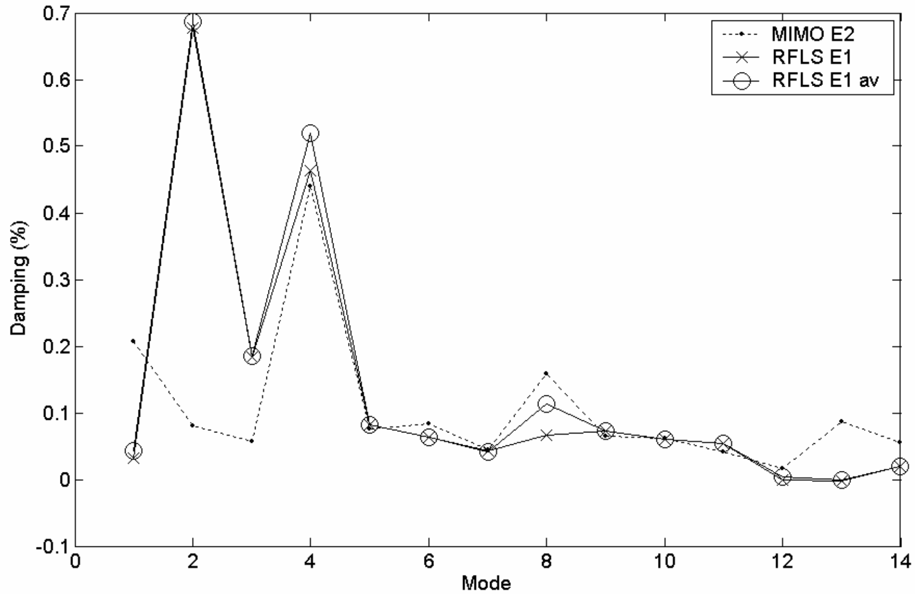

Figure C.2 Comparison of modal damping from RFLS FRF curve fitting of experiment 1 data with modal damping from ARMAX MIMO E2 analysis. RFLS E1 20 averages; RFLS E1 av 89 averages.

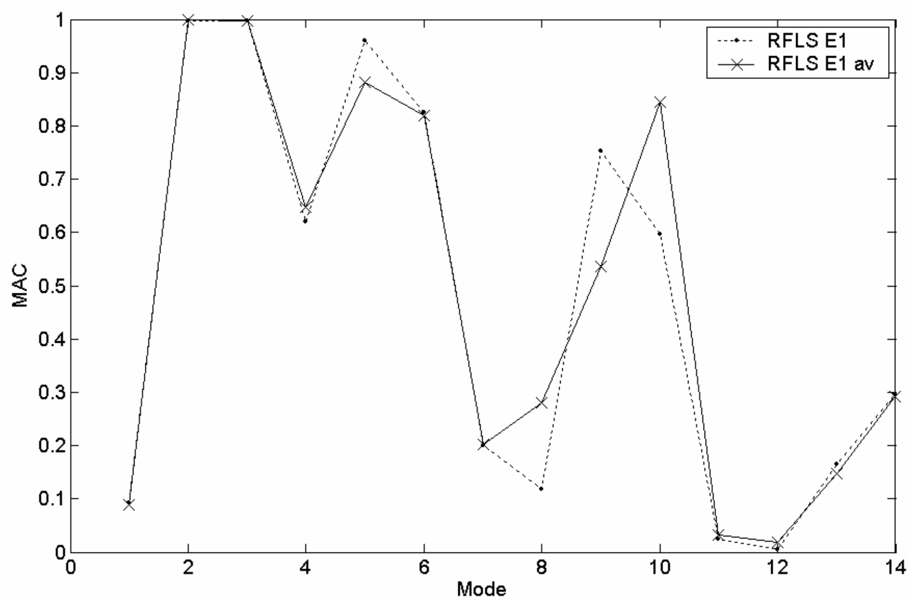

Figure C.3 MAC values comparing mode shapes from RFLS FRF curve fitting of experiment 1 data with mode shapes from ARMAX MIMO E2 analysis. RFLS E1 20 averages; RFLS E1 av 89 averages.

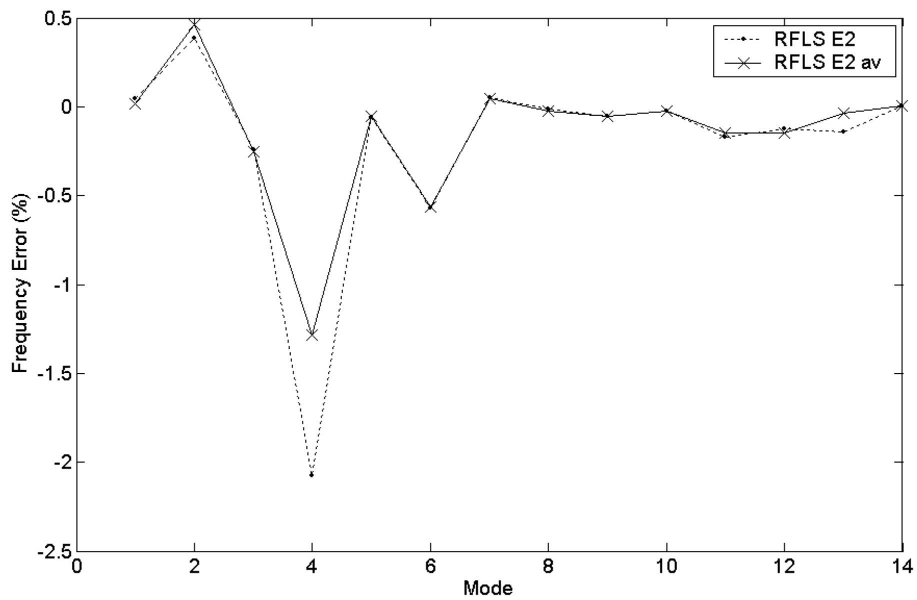

Figure C.4 Comparison of estimated modal frequencies from RFLS FRF curve fitting of experiment 2 data with modal frequencies from ARMAX MIMO E2 analysis. RFLS E2 20 averages; RFLS E2 av 89 averages.

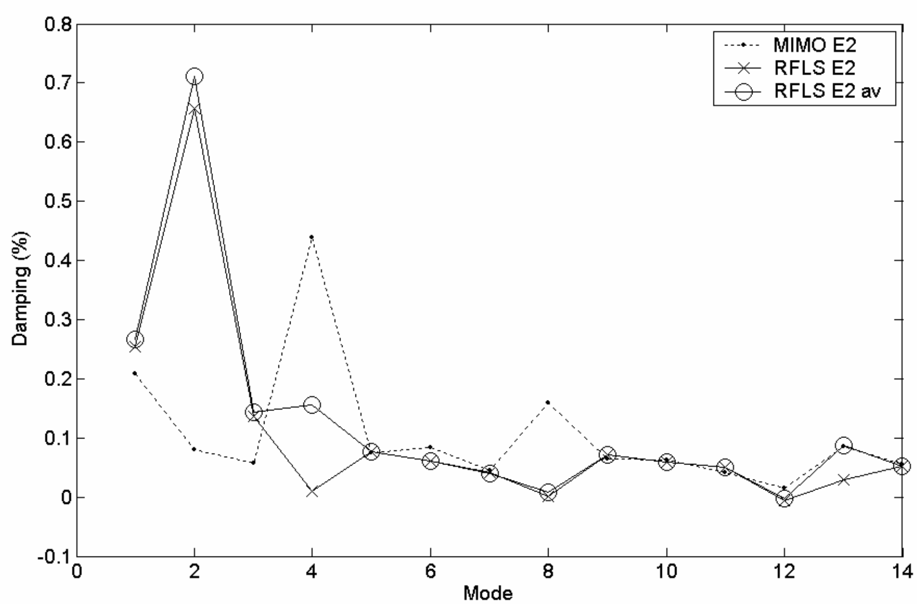

Figure C.5 Comparison of modal damping from RFLS FRF curve fitting of experiment 2 data with modal damping from ARMAX MIMO E2 analysis. RFLS E2 20 averages; RFLS E2 av 89 averages.

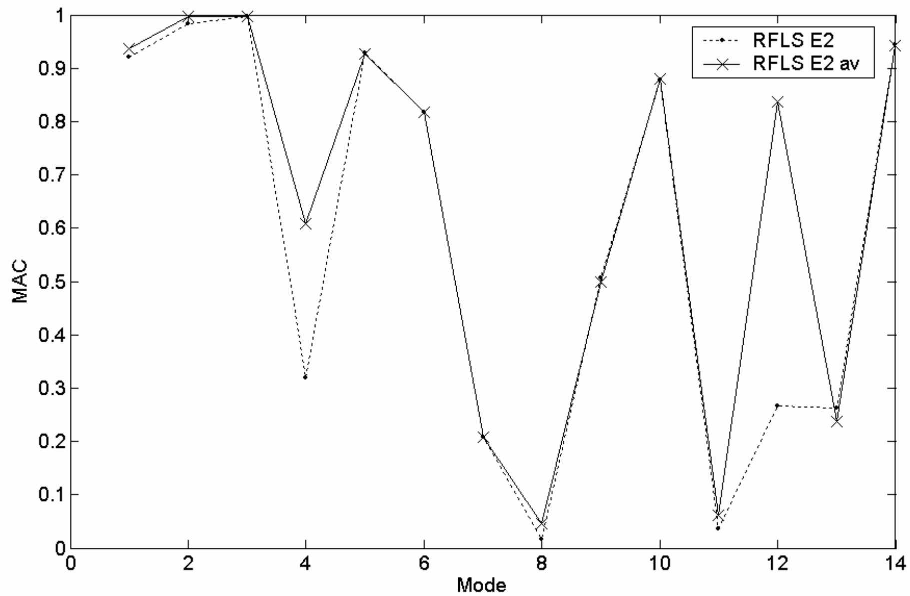

Figure C.6 MAC values comparing mode shapes from RFLS FRF curve fitting of experiment 2 data with mode shapes from ARMAX MIMO E2 analysis. RFLS E2 20 averages; RFLS E2 av 89 averages.

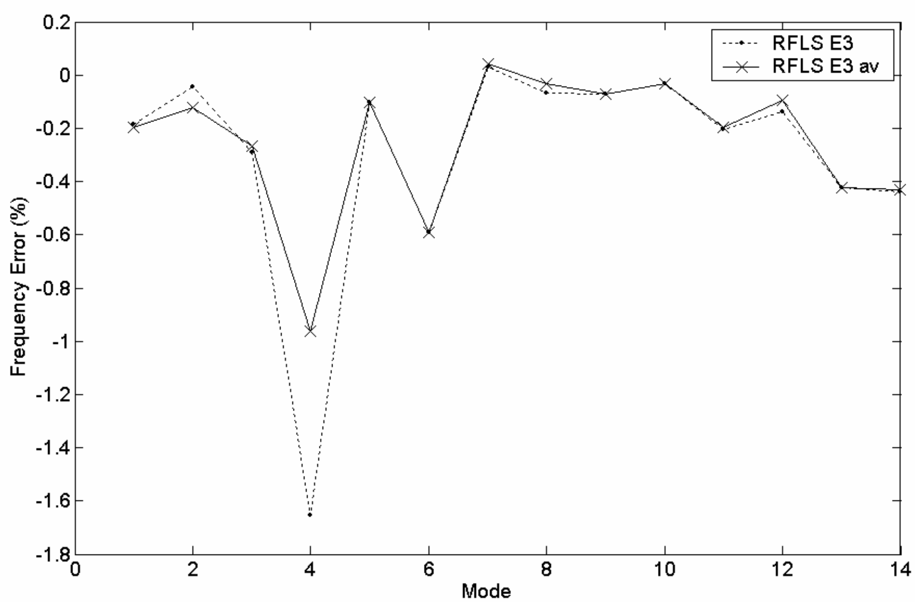

Figure C.7 Comparison of estimated modal frequencies from RFLS FRF curve fitting of experiment 3 data with modal frequencies from ARMAX MIMO E3 analysis. RFLS E3 20 averages; RFLS E2 av 89 averages.

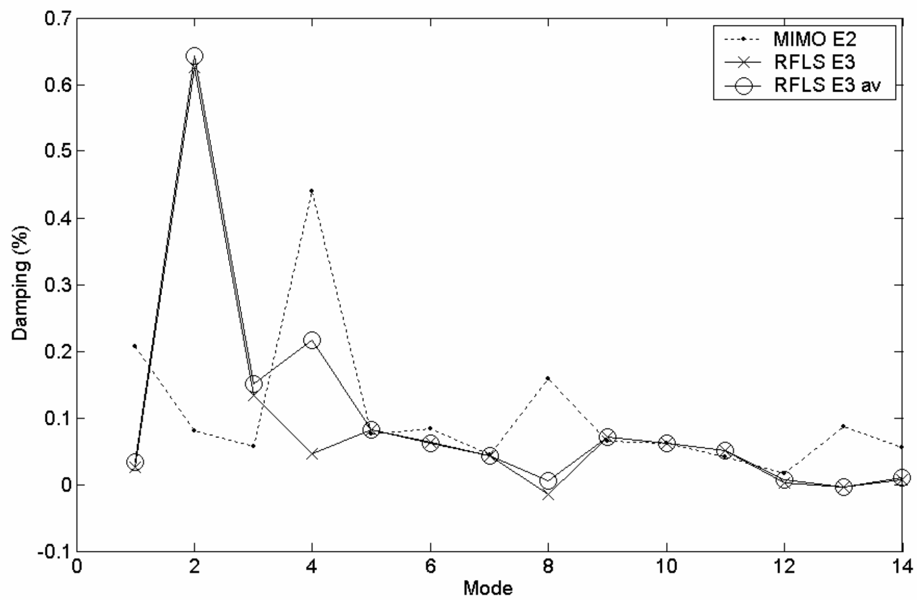

Figure C.8 Comparison of modal damping from RFLS FRF curve fitting of experiment 3 data with modal damping from ARMAX MIMO E2 analysis. RFLS E3 20 averages; RFLS E3 av 89 averages.

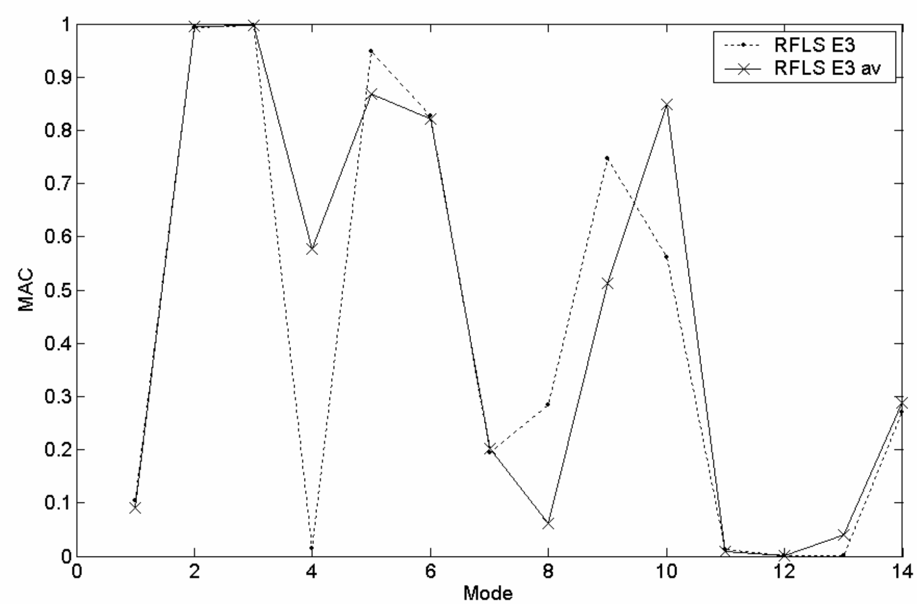

Figure C.9 MAC values comparing mode shapes from RFLS FRF curve fitting of experiment 3 data with mode shapes from ARMAX MIMO E2 analysis. RFLS E3 20 averages; RFLS E3 av 89 averages.

Appendix D

Modal parameters estimated using the FDD, EFDD, and SSI-UPC response-only modal analysis algorithms (included in the Structural Vibration Solutions ARTeMIS software), as discussed in section 8.6.4, are shown in this Appendix. Also shown are I/O modal analysis results obtained from a RFLS algorithm (implemented in the commercial STAR Modal software), discussed in section 8.6.2.

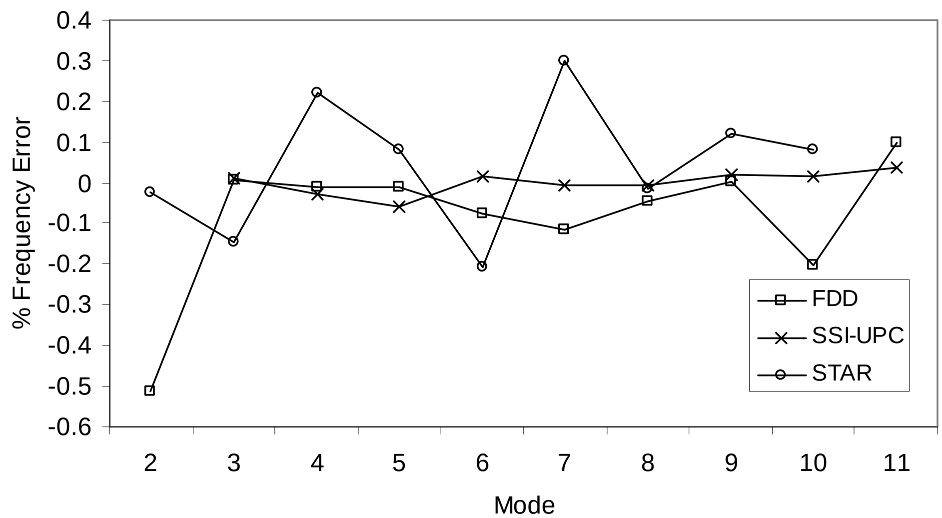

Figure D.1 Frequency Error for FDD, SSI-UPC & STAR results compared with EFDD results.

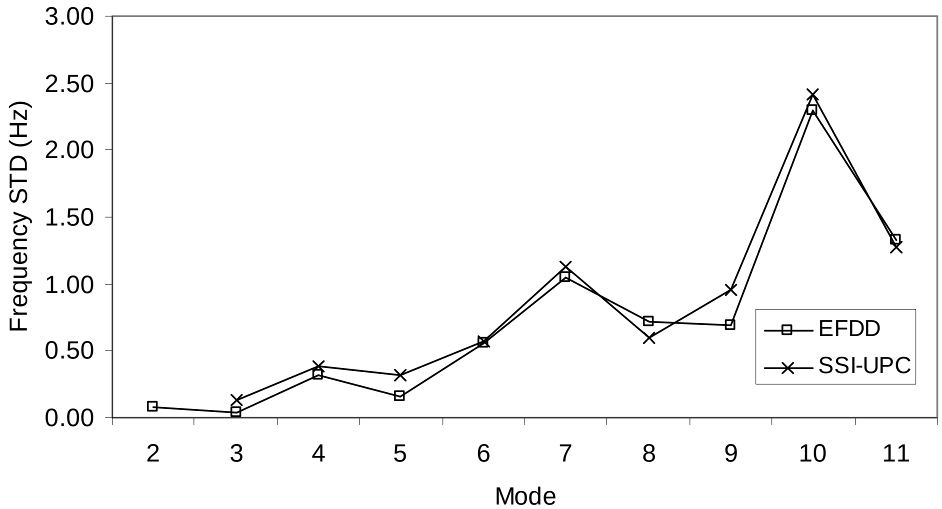

Figure D.2 Frequency standard deviation for EFDD & SSI-UPC results.

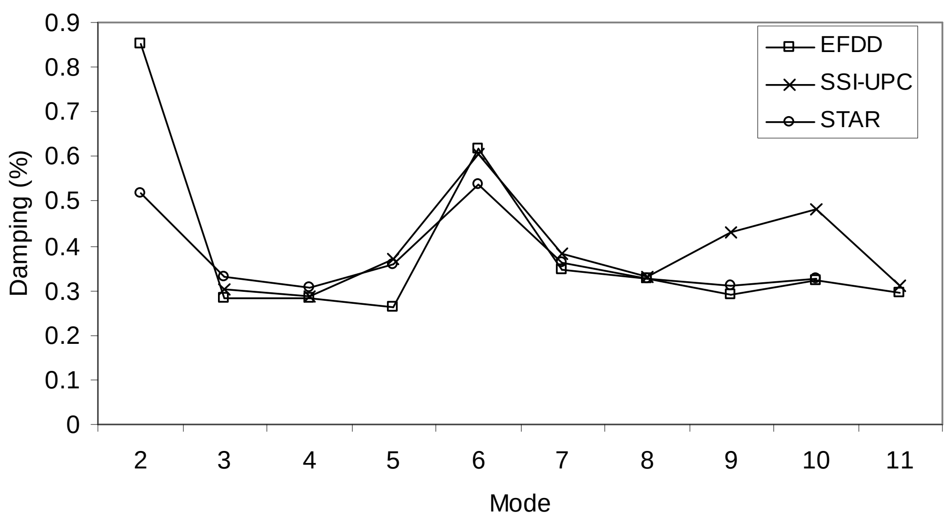

Figure D.3 Damping estimated from EFDD,SSI-UPC, & STAR algorithms.

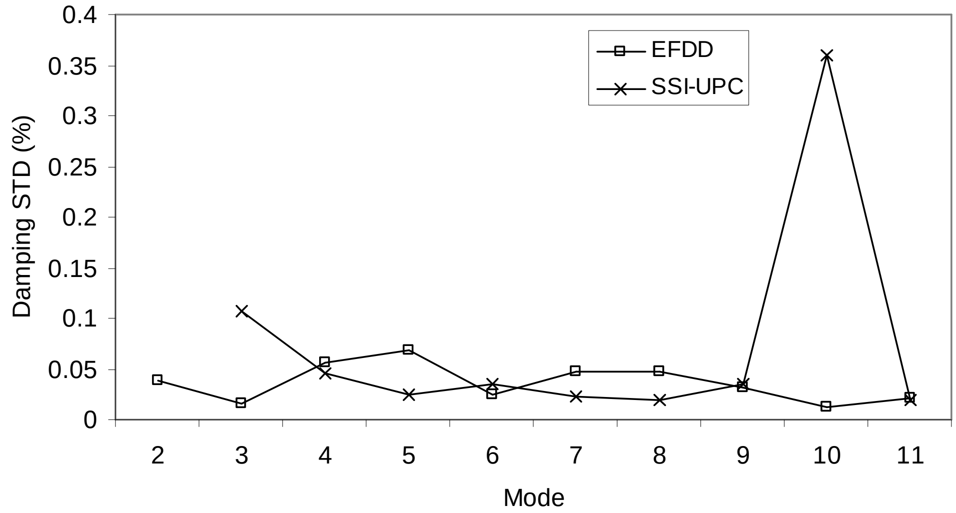

Figure D.4 Damping standard deviation for EFDD & SSI-UPC results.

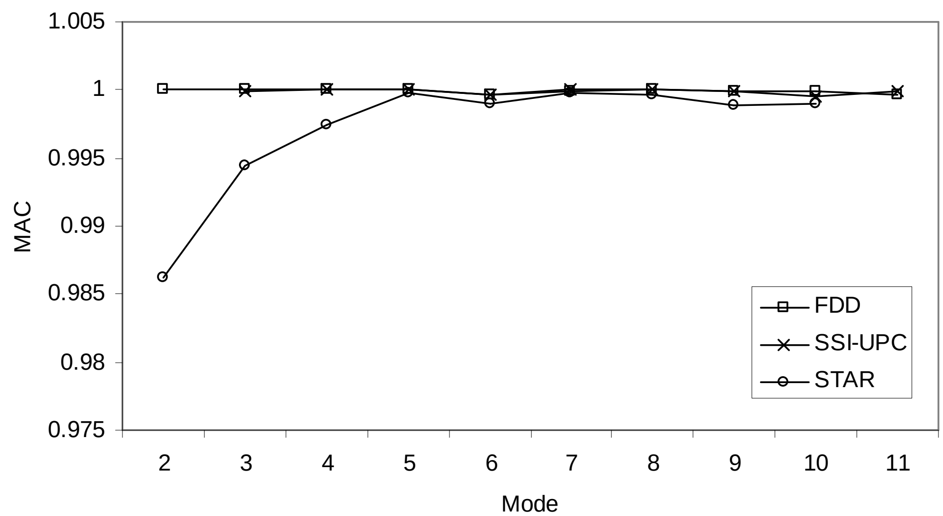

Figure D.5 MAC comparing mode shapes estimated from FDD,SSI-UPC, & STAR algorithms with mode shapes estimated from EFDD algorithm.

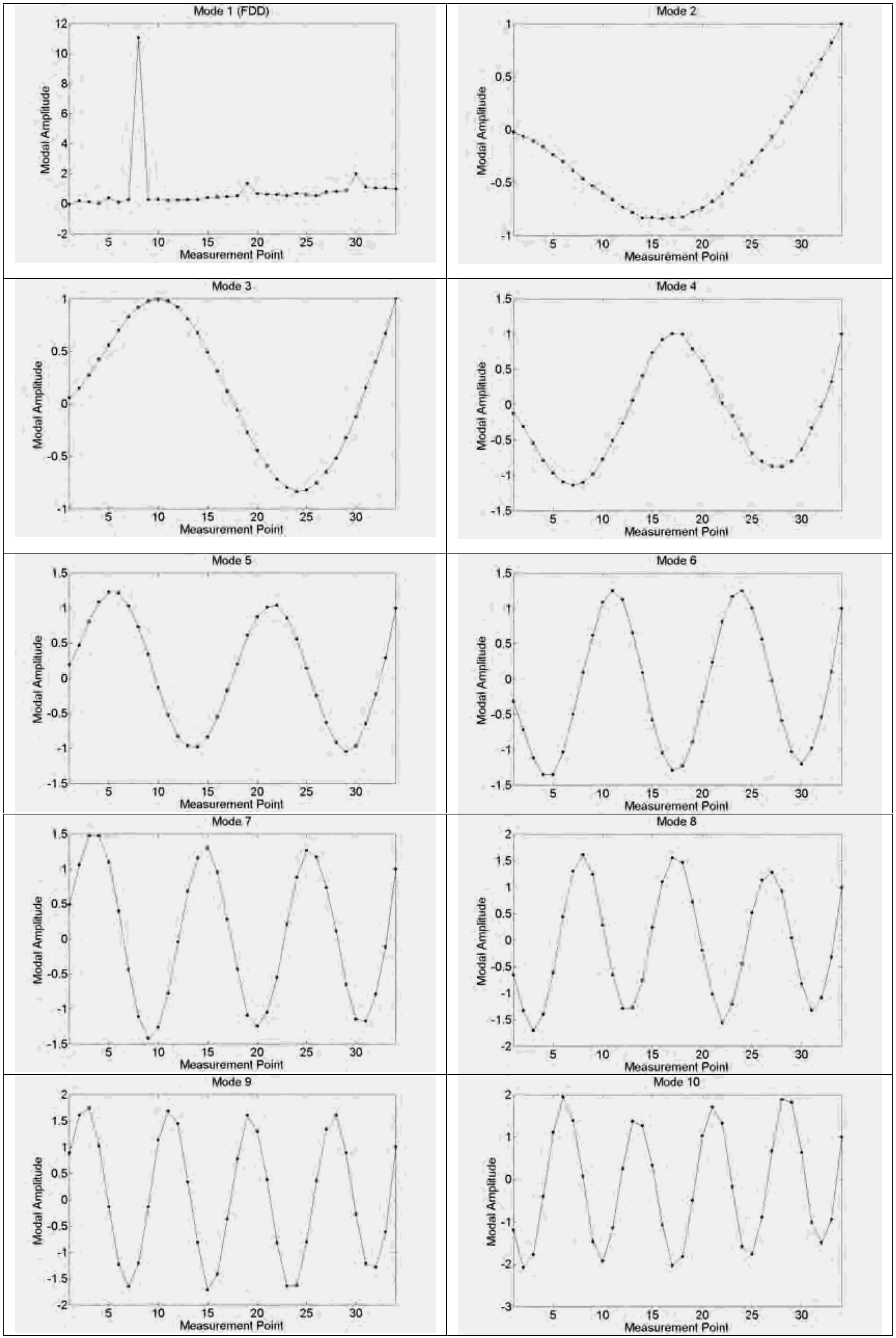

Figure D.6 (Continued over the page) Mode shapes estimated by EFDD (except mode 1, which was estimated by FDD).

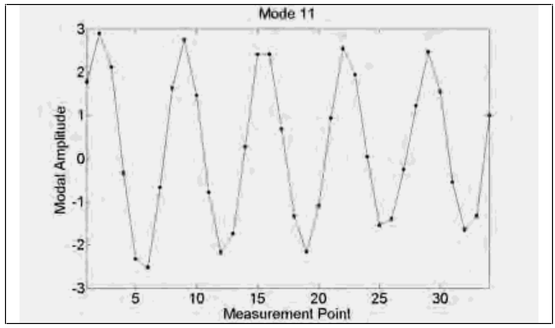

Figure D.6 (cont.) Mode shapes estimated by EFDD (except mode 1, which was estimated by FDD).

Appendix E

Modal parameters estimated by the MISO AR-ARMAX response-only modal analysis algorithm are shown in this section. Modal parameters were estimated from response measurements obtained from a cantilever aluminium beam excited with piezoceramic actuators, as discussed in section 8.6.5.

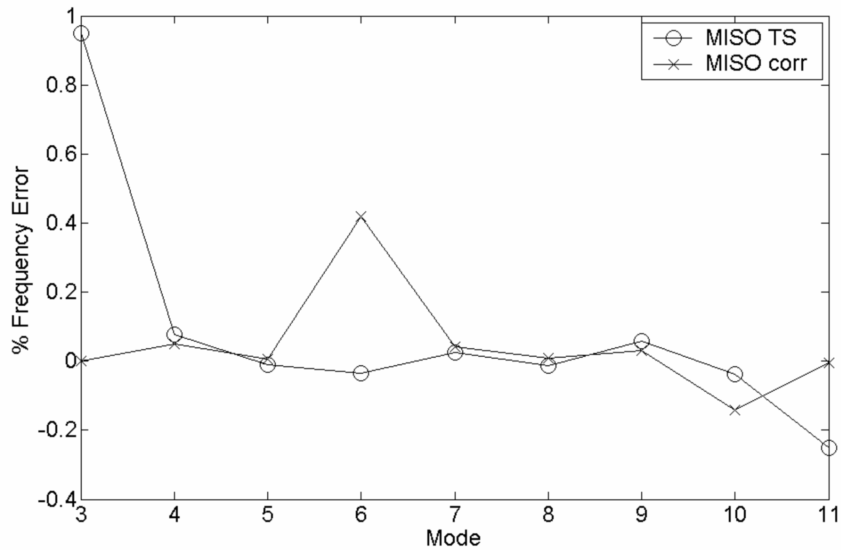

Figure E.1 Frequency Error for MISO AR-ARMAX results compared with EFDD results.

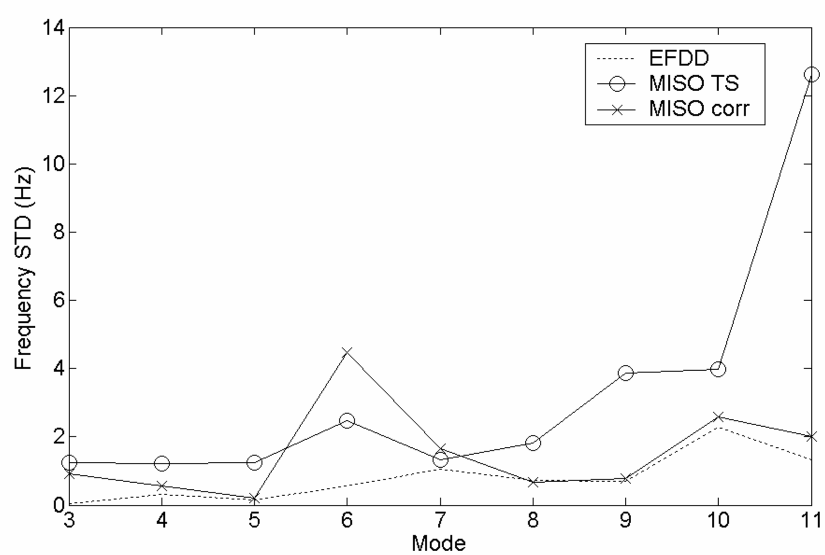

Figure E.2 Frequency standard deviation for MISO AR-ARMAX and EFDD results.

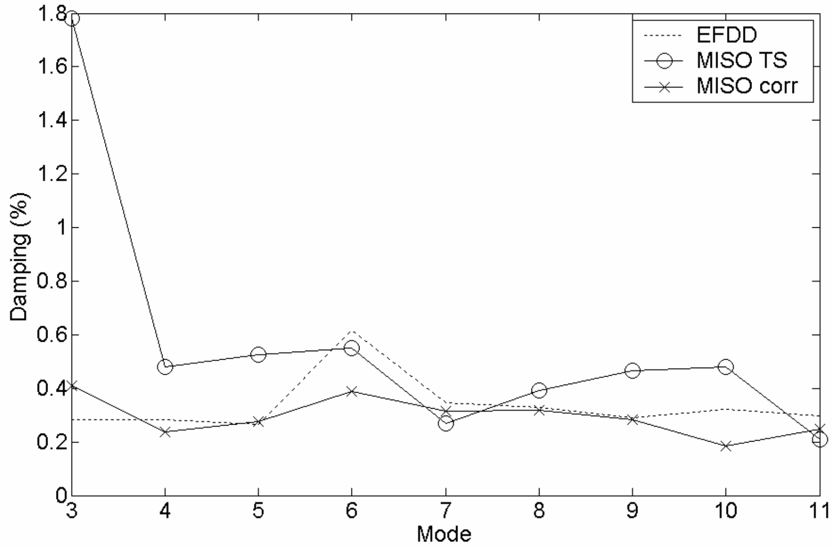

Figure E.3 Damping estimated from MISO AR-ARMAX and EFDD.

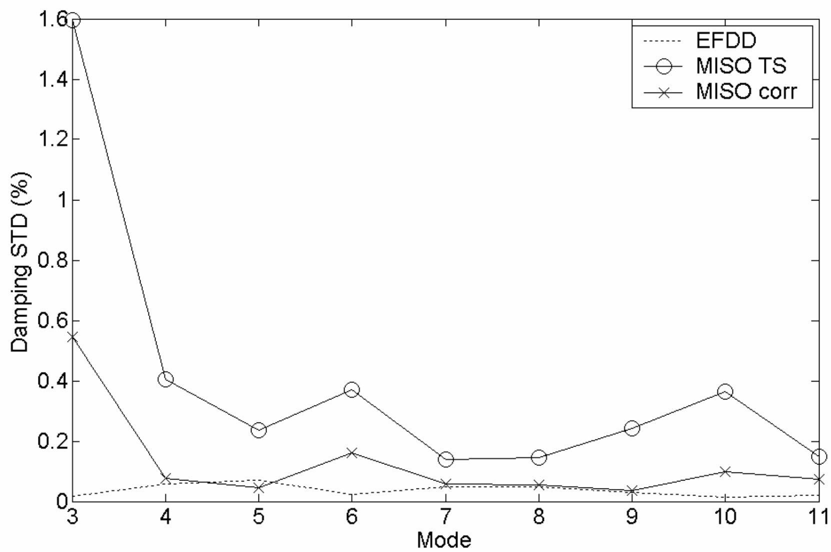

Figure E.4 Damping standard deviation for MISO AR-ARMAX and EFDD results.

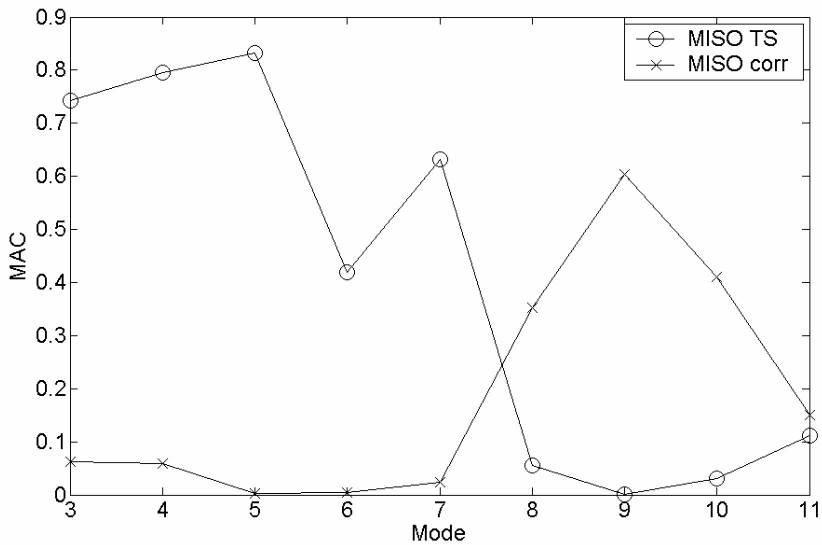

Figure E.5 MAC values comparing mode shapes from MISO AR-ARMAX results and EFDD results.

Appendix F

Matlab code for MIMO E2 analysis, described in section 7.4.1. The following code loads and resamples data, before calling functions that implement the stages of the ARMAX estimation algorithm (see Chapter 5). A function to calculate the innovations sequence for an estimated ARMAX model is included, and the final section of code details the calculation of modal parameters from the estimated ARMAX model.

```
%ARMAX model estimation for MIMO E2 analysis

for ii = 1:14
    %Load data
    load(['HT212_m' int2str(ii)])
    eval(['dat_temp = HT212_m' int2str(ii) ';'])

    %resample
    dat_temp = resample(dat_temp,300,512);

    %form excitation and response data vectors
    fn = [dat_temp(1025:3072,1) dat_temp(1025:3072,2)]';
    yn = [dat_temp(1025:3072,3) dat_temp(1025:3072,4)]';

    %sampling rate and record length (seconds)
    Ts = (512/300)*1/1024;
    Tt = Ts*2048;

    %set order and iterations
    min_ord = 80;
    max_ord = 90;
    arm34_iters = 8;

    %file name
    data_name = ['MISO_ARMAX_HT212_1_v1_m' int2str(ii)];

    %ARMAX estimation control
    RC_arm_ctrl(Tt,Ts,fn,yn,min_ord,max_ord,arm34_iters,data_name)
    clear
end

for ii = 15:15
    %Load data
    load(['HT212_m' int2str(ii)])
    eval(['dat_temp = HT212_m' int2str(ii) ';'])

    %resample
    dat_temp = resample(dat_temp,300,512);

    %form excitation and response data vectors
    fn = [dat_temp(1025:3072,1) dat_temp(1025:3072,2)]';
    yn = [dat_temp(1025:3072,3) dat_temp(1025:3072,4)
dat_temp(1025:3072,5)]';

    %sampling rate and record length (seconds)
    Ts = (512/300)*1/1024;
    Tt = Ts*2048;
```

```
    %set order and iterations
    min_ord = 80;
    max_ord = 90;
    arm34_iters = 8;

    %file name
    data_name = ['MISO_ARMAX_HT212_1_v1_m' int2str(ii)];

    %ARMAX estimation control
    RC_arm_ctrl(Tt,Ts,fn,yn,min_ord,max_ord,arm34_iters,data_name)
    clear
end

%_______________________________________________________________

%Notes: Data files 1 - 14: 2 input, 2 output; data file 15: 2 input, 3
output.
```

```
function RC_arm_ctrl(Tt,Ts,fn,yn,min_ord,max_ord,arm34_iters,data_name)
tic

%Define cell structures to store parameters and results
ord_numbers = 1  + (max_ord - min_ord)/2;

ls_stat1_cell = cell(ord_numbers,1);
ls_stat2_cell = cell(ord_numbers,arm34_iters);

BICrevmat = zeros(ord_numbers,arm34_iters + 1);
incovmsmat = zeros(ord_numbers,arm34_iters + 1);
incovmsdet = zeros(ord_numbers,arm34_iters + 1);
wtrevcell = cell(ord_numbers,arm34_iters + 1);
BICrev2mat = zeros(ord_numbers,arm34_iters + 1);
parmatcell = cell(ord_numbers,arm34_iters + 1,3);
stArootsmat = zeros(ord_numbers,arm34_iters);
freqdampmodemat2_cell = cell(ord_numbers,1);

save wt_data wtrevcell
clear wtrevcell

ind1  = 1;
prog_ind = 1;
for jj = min_ord:2:max_ord
    prog_ind
    %Model order
    itind = jj;

    %set nc
    nc = 2*round(0.25*itind);

    stage_ = 'arm1234'
    %Stages 1,2, and first iteration of stage 3
    [Amat, Bmat, Cmat, Hyestvec, ls_stat1] = RC_arm1234(yn,fn,itind,nc);
    ls_stat1_cell{ind1,1} = [ls_stat1{:}];
    %save system matrices estimated from first iteration of stage 3
    parmatcell{ind1,1,1} = Amat;
    parmatcell{ind1,1,2} = Bmat;
    parmatcell{ind1,1,3} = Cmat;

    %Calculate innovations sequence (for testing purposes, calculation of
    %BIC etc.
    stage_ = 'innov4 1'
     [wtbac,inncovrev,BICrev,BICrev2,inn_cov_ms_av_b,inn_cov_ms_det_b]  =
RC_innov4(Amat,Bmat,Cmat,yn,fn,Ts,Tt);
    BICrevmat(ind1,1) = BICrev;
    incovmsmat(ind1,1) = inn_cov_ms_av_b;
    incovmsdetmat(ind1,1) = inn_cov_ms_det_b;
    BICrev2mat(ind1,1) = BICrev2;

    load wt_data
    wtrevcell{ind1,1} = wtbac;

    save wt_data wtrevcell
    clear wtrevcell

    %Stage 3,4
    for ii = 1:arm34_iters
        stage_ = 'arm34'
        %iterations of stages 3 and 4
```

```
         [Amat, Bmat, Cmat, no_st_roots, ls_stat2] =
RC_arm34(Cmat,Hyestvec,yn,fn,itind);
        ls_stat2_cell{ind1,ii} = [ls_stat2{:}];
        stage_ = 'innov4 2'
        %Calculate innovations sequence (for testing purposes, calculation
of
        %BIC etc.
        [wtbac,inncovrev,BICrev,BICrev2,inn_cov_ms_av_b,inn_cov_ms_det_b]
= RC_innov4(Amat,Bmat,Cmat,yn,fn,Ts,Tt);

        %store and save system matrices and other data
        BICrevmat(ind1,ii + 1) = BICrev;
        incovmsmat(ind1,ii + 1) = inn_cov_ms_av_b;
        incovmsdetmat(ind1,ii + 1) = inn_cov_ms_det_b;
        BICrev2mat(ind1,ii + 1) = BICrev2;
        parmatcell{ind1,ii + 1,1} = Amat;
        parmatcell{ind1,ii + 1,2} = Bmat;
        parmatcell{ind1,ii + 1,3} = Cmat;
        stArootsmat(ind1,ii) = no_st_roots;

        load wt_data
        wtrevcell{ind1,ii + 1} = wtbac;
        save wt_data wtrevcell
        clear wt_data wtrevcell
    end

    load wt_data
    save(data_name,'wtrevcell');
    clear wtrevcell

    ind1 = ind1 + 1;
    prog_ind = prog_ind + 1;
end

altime = toc

f_name = strcat(data_name,'_full')

load wt_data
save(f_name)
```

```
function [Amat, Bmat, Cmat, Hyestvec, ls_stat] =
RC_arm1234(yn,fn,itind,nc)
%Function to estimate the system matrices of an ARMAX dynamic model
%
% Amat: [s x s x na] AR matrix polynomial of order na
% Bmat: [s x m x nb] X matrix polynomial of order nb
% Cmat: [s x s x nc] MA matrix polynomial of order nc
% s: number of response channels
% m: number of excitatoin channels
% yn: response data series [s x N], including additive noise and the
% effects of unmeasureed excitations
% fn: excitation data series [m x N], including any excitation measurement
% noise
% itind: order of model ie itind = f(na,nb,nc)
%
%
fid =1;
%Define N,s,m
N = size(yn,2);
s = size(yn,1);
m = size(fn,1);


%-----------------------------------------------------------------------
-

%Stage 1 of ARMA(X) model representation: Initial estimation of truncated
%AR(X) model

%set order p of ARX model:
p1 = 4*itind;
% p1: order of AR matrix polynomial in the stage 1 ARX model
% p2: order of X matrix polynomial in the stage 1 ARX model
p2=p1;
p = max(p1,p2);

%Check to see if there is sufficient data points for estimation of
%model of size itind
if N-(p + 1) < p + p*m + m
    error('Insufficient data points in excitation and response vectors.
Use smaller model order or longer input data series.')
end


%Form regression vector from excitation and response signals
fnvec = reshape(fn(:,1:N),m*N,1);

%Define matrix to store regression matrix statistics (size,condition,
%rank) for each iteration of stages 1, 3.
ls_stat = cell(2,s);


%LS estimation of ARX model using QR factorisation (see Ljung, 1999)
%This estimates s different MISO problems to avoid ill conditionin of
%the regression matrices. Results are stored in the Hyfest cell array.
Hyfest = cell(1,s);
for ii = 1:s
    PHIblok_k = cell(N-(p+1),1);
        for jj = 0:N-(p+2)
        ut_k = [-yn(ii,jj+2:jj+1+p1), fnvec(m*jj+1:m*(p2+jj+1),1)'];
        PHIblok_k{jj+1,1} = ut_k;
```

```
    end

    PHIblok_k = cell2mat(PHIblok_k);

%   ls_stat{1,ii} =  [size(PHIblok_k,2);
%                     rank(PHIblok_k);
%                     cond(PHIblok_k)];

    Ykvec = yn(ii,1:N-(p+1))';

    R0k = triu(qr([PHIblok_k Ykvec]));

    R1k = R0k(1:p1 + p2*m +m,1:p1 + p2*m +m);

    R2k = R0k(1:p1 + p2*m +m,p1 + p2*m +m +1);

    hest_k = R1k\R2k;

    Hyfest{1,ii} = hest_k;
end

%Extract AR and X matrix polynomials
Hyfest = cell2mat(Hyfest);

%Hy matrix append identity matrix for Hy(0)
Hyestrev = Hyfest(1:p1,:);
Hyestrev = [ones(s,1) Hyestrev'];

%Hf matrix
Hfestrev = Hyfest(p1+1:p1+p2*m +m,:);
Hfestrev = reshape(Hfestrev',s,m,p2+1);

%Similarly, reverse order of Hyest
Hyest(:,1:p1+1) = Hyestrev(:,p1+1:-1:1);


%Calculate roots of Hy matrix. Note that the iterative estimation scheme
%assumes that the Hy matrix polynomial has diagonal matrix
%coefficients.

Hyroots = cell(s,1);
for ii = 1:s
    Hyroots{ii,1} = roots(Hyest(ii,:));
end
Hyroots = cell2mat(Hyroots');

%Form Hy matrix to be used in subsequent stages. The iterative estimation
%method assumes a diagaonal structure for each coefficient matrix in the
Hy
%matrix polynomial.

Hyestmatrev = cell(1,p1+1);
Hyestmatrev(1:p1+1) = {zeros(s,s)};
for ii = 1:p1+1
    for jj = 1:s
        Hyestmatrev{1,ii}(jj,jj) = Hyestrev(jj,ii);
    end
end
Hyestmatrev = cell2mat(Hyestmatrev);
```

```
%-----------------------------------------------------------------------
-

%Stage 2 of ARMA(X) model representation: Initial estimation of MA
%matrices.

%Define matrix polynomial orders
na = itind;
nb = itind;

%Limits for creating matrices
r = max(na,nc) + nc;

ist2 = r-nc+1;

%form Hy matrix (toeplitz matrix) using Hyest matrices
Hyestvec = reshape(Hyestmatrev,s,s,p1+1);

blokH = cell(nc+1,nc+1);
for i4 = 1:nc+1
    for i3 = 1:nc+1
       if i4 - i3 <= p1 + 1 - ist2
          blokH{i4,i3} = Hyestvec(:,:,ist2+i4-i3)';
       else
          blokH{i4,i3} = zeros(s,s);
       end
    end
end

blokHyest = cell2mat(blokH);

clear blokH

%form matrix and vector and construct system of equations to solve for C
%matrix

Hymat = blokHyest(:,s+1:s*(nc+1));
Hyvec = -blokHyest(:,1:s);

clear blokHyest

Cest = Hymat\Hyvec;

clear Hymat
clear Hyvec

Cest3D = reshape(Cest',s,s,[]);


%-----------------------------------------------------------------------
%Stage 2s: Stabilise first estimate for MA matrix

%This procedure takes advantage of the diagonal structure of the
%Cmat matrix polynomial coefficients
tempC = cell(1,s);
Cest3D = cat(3,eye(s,s),Cest3D);
staCmat = zeros(size(Cest3D));
for ii = 1:s
    tempC{1,ii} = reshape(Cest3D(ii,ii,1:nc+1),1,nc + 1);
    tempC{1,ii} = polystab(tempC{1,ii});
    staCmat(ii,ii,1:nc+1) = reshape(tempC{1,ii},1,1,nc+1);
```

```
end

Cmat = staCmat;

Cest3D = Cmat(:,:,2:nc + 1);

%create cell array from Cest3D poly coefficients
Cestcell = cell(1,nc+1);
for i2s = 1:nc + 1
    Cestcell{1,i2s} = Cmat(:,:,i2s);
end


%set C matrix to Is: used for testing and dealing with unstable high
%order systems
%Cest3D = zeros(size(Cest3D));

%-------------------------------------------------------------------------
-
%Stage 3: Estimation of AR and X polynomial matrices

%Construct Yfk matrices
Yf = zeros(s,s^2,N);
for i5 = 1:N
    Yft3D = zeros(s,s,s);
    for i6 = 1:s
        i7=1;
        YiCestsum = zeros(s,s);
        while (i5-i7>0)&(i7<=nc)
             YiCest = Yf(:,(i6-1)*s+1:i6*s,i5-i7)*Cest3D(:,:,i7)’;
             YiCestsum = YiCestsum + YiCest;
             i7=i7+1;
        end
        Yft3D(:,:,i6) = yn(i6,i5)*eye(s) - YiCestsum;
    end
    Yft = reshape(Yft3D,s,s^2);
    Yf(:,:,i5) = Yft;
 end

%Construct Ff matrix
Ff = zeros(s,s*m,N);
for i5 = 1:N
    Fft3D = zeros(s,s,m);
    for i6 = 1:m
        i7 = 1;
        FiCestsum = zeros(s,s);
        while (i5-i7>0)&(i7<=nc)
            FiCest = Ff(:,(i6-1)*s+1:i6*s,i5-i7)*Cest3D(:,:,i7)’;
            FiCestsum = FiCestsum + FiCest;
            i7=i7+1;
        end
        Fft3D(:,:,i6) = fn(i6,i5)*eye(s) - FiCestsum;
    end
    Fft = reshape(Fft3D,s,s*m);
    Ff(:,:,i5) = Fft;
end

%Construct Uf
n1 = max(na,nb);

hest2mat = cell(1,s);
```

```
for ii = 1:s
    PHI2kblok = cell(N-n1,1);

    yf2kvec = cell(N-n1,1);

    for j1 = 1:N-n1
        Yfkvec = -reshape(Yf(:,(ii-1)*s+1:ii*s,j1+1:j1+na),s,na*s);

        Ffkvec = reshape(Ff(:,:,j1:j1+nb),s,[]);

        Ufk = [Yfkvec Ffkvec];

        PHI2kblok{j1,1} = Ufk;

        yftkvec = Yf(:,(ii-1)*s+ii,j1);

        yf2kvec{j1,1} = yftkvec;

    end

    PHI2kblok = cell2mat(PHI2kblok);

    %Information on the regression matrix
%   ls_stat{2,ii} = [size(PHI2kblok,2);
%                    rank(PHI2kblok);
%                    cond(PHI2kblok)];

    yf2kvec = cell2mat(yf2kvec);

    %QR factorisation
    R02k = triu(qr([PHI2kblok yf2kvec]));

    R12k = R02k(1:na*s + nb*m*s + m*s,1:na*s + nb*m*s + m*s);

    R22k = R02k(1:na*s + nb*m*s + m*s,na*s + nb*m*s + m*s + 1);

    hest2_k = R12k\R22k;

    hest2mat{1,ii} = hest2_k;
end

hest2mat  = cell2mat(hest2mat);

%Separate estimates into AR and X matrices
Aest3D = reshape(hest2mat(1:na*s,1:s)',s,s,na);

%Append identity matrix to AR matrix; ie A(0) = I
Aest3D = cat(3,eye(s,s),Aest3D);

Amat = Aest3D;

%Extract X matrix polynomial coefficients
Bestvec = nonzeros(hest2mat(na*s+1:na*s + nb*m*s + m*s,:)');

if size(Bestvec,1)*size(Bestvec,2) ~= s*m*(nb+1)
    error('Incorrect structure estimated for X matrix')
end

Best3D = reshape(Bestvec,s,m,nb+1);
```

```
%set very small elements to zero as these will contribute to very large
%roots, hence algorithmic instabilities ...
if length(find(abs(Best3D) < 1e-10)) > 0
%   Best3D(find(abs(Best3D) < 1e-10)) = 0;
    sprintf('X matrix coefficients < 1e-10 set to zero in arm1234')
end

Bmat = Best3D;

%--------------------------------------------------------------------------
-
%Stage 4: Estimation of the MA polynomial matrix and innovations

Hsize = size(Hyestvec,3);

%form matrix of V coefficients
blokAmat = cell(Hsize,nc+1);
blokAmat(:) = {zeros(s,s)};

for ii = 1:Hsize
    %define limits of convolution
    aa = max(1,ii + 1 - (na+1));
    bb = min(ii,nc+1);
    jj = aa;
    while (jj <= ii)&&(jj <= bb)
        blokAmat{ii,jj} = Aest3D(:,:,ii + 1 - jj);
        jj = jj+1;
    end
end

blokAmat = cell2mat(blokAmat);

Hyestvec_2 = reshape(Hyestvec,s,Hsize*s)';

Cmat = blokAmat\reshape(Hyestvec,s,Hsize*s)';

Cmat = reshape(Cmat',s,s,nc+1);

%Stabilise Cmat
%This procedure takes advantage of the diagonal structure of the
%Cmat matrix polynomial coefficients
tempC = cell(1,s);
staCmat = zeros(size(Cmat));
for ii = 1:s
    tempC{1,ii} = reshape(Cmat(ii,ii,1:nc+1),1,nc + 1);
    tempC{1,ii} = polystab(tempC{1,ii});
    staCmat(ii,ii,1:nc+1) = reshape(tempC{1,ii},1,1,nc+1);
end

Cmat = staCmat;
```

```
function [Amat, Bmat, Cmat, no_st_roots, ls_stat] =
RC_arm34(Cmat,Hyestvec,yn,fn,itind)
%This function carries out stages 3 and 4 of the ARMAX parameter
estimation
%algorithm.

%Function to estimate the system matrices of an ARMAX dynamic model
%
% Amat: [s x s x na] AR matrix polynomial of order na
% Bmat: [s x m x nb] X matrix polynomial of order nb
% Cmat: [s x s x nc] MA matrix polynomial of order nc
% s: number of response channels
% m: number of excitatoin channels
% yn: response data series [s x N], including additive noise and the
% effects of unmeasureed excitations
% fn: excitation data series [m x N], including any excitation measurement
% noise
% itind: order of model ie itind = f(na,nb,nc)
%
%
%Define N,s,m
N = size(yn,2);
s = size(yn,1);
m = size(fn,1);

%Define Cest23D
Cest23D = Cmat;

%Define matrix polynomial orders
na = itind;
nb = itind;
nc = size(Cest23D,3) - 1;

%Define matrix to store regression matrix statistics (size,condition,
%rank) for each iteration of stages 1.

ls_stat = cell(1,s);

%Check to see if there is sufficient data points for estimation of
%model of size itind
if N-2 < itind*(6 + 3*m) + m
    error('Insufficient data points in excitation and response vectors')
end

%---------------------------------------------------------------------
%Stage 3 estimate A and B matrices

%Stabilise Cest23D
tempC = cell(1,s);
staCest23D = zeros(size(Cest23D));
for ii = 1:s
    tempC{1,ii} = reshape(Cest23D(ii,ii,1:nc+1),1,nc + 1);
    tempC{1,ii} = polystab(tempC{1,ii});
    staCest23D(ii,ii,1:nc+1) = reshape(tempC{1,ii},1,1,nc+1);
end

%Filtering stage
c0_inv = inv(staCest23D(:,:,1));
for ii = 1:nc + 1
    staCest23D(:,:,ii) = c0_inv*staCest23D(:,:,ii);
end
```

```
Cest3D = staCest23D;

%Construct Yf matrix
Yf = cell(1,s);
for kk = 1:s
    Yfi = zeros(s,s,N);
    for ii = 1:N
        jj = 1;
        while (jj <= nc+1)&&(jj <=ii)
            Yfi(:,:,ii) = Yfi(:,:,ii) + yn(kk,ii - jj + 1)*Cest3D(:,:,jj);
            jj = jj + 1;
        end
    end
    Yf{1,kk} = Yfi;
end
Yf = cell2mat(Yf);

%Construct Ff matrix
Ff = cell(1,m);
for kk = 1:m
    Ffi = zeros(s,s,N);
    for ii = 1:N
        jj = 1;
        while (jj <= nc+1)&&(jj <=ii)
            Ffi(:,:,ii) = Ffi(:,:,ii) + fn(kk,ii - jj + 1)*Cest3D(:,:,jj);
            jj = jj + 1;
        end
    end
    Ff{1,kk} = Ffi;
end
Ff = cell2mat(Ff);


%Construct Uf
n1 = max(na,nb);

hest2mat = cell(1,s);

for ii = 1:s
    PHI2kblok = cell(N-n1,1);

    yf2kvec = cell(N-n1,1);

    for j1 = 1:N-n1
        Yfkvec = -reshape(Yf(:,(ii-1)*s+1:ii*s,j1+1:j1+na),s,na*s);

        Ffkvec = reshape(Ff(:,:,j1:j1+nb),s,[]);

        Ufk = [Yfkvec Ffkvec];

        PHI2kblok{j1,1} = Ufk;

        yftkvec = Yf(:,(ii-1)*s+ii,j1);

        yf2kvec{j1,1} = yftkvec;

    end

    PHI2kblok = cell2mat(PHI2kblok);
```

```
    %Information on the regression matrix
%    ls_stat{1,ii} = [size(PHI2kblok,2);
%                      rank(PHI2kblok);
%                      cond(PHI2kblok)];

    yf2kvec = cell2mat(yf2kvec);

    %QR factorisation
    R02k = triu(qr([PHI2kblok yf2kvec]));

    R12k = R02k(1:na*s + nb*m*s + m*s,1:na*s + nb*m*s + m*s);

    R22k = R02k(1:na*s + nb*m*s + m*s,na*s + nb*m*s + m*s + 1);

    hest2_k = R12k\R22k;

    hest2mat{1,ii} = hest2_k;
end

hest2mat  = cell2mat(hest2mat);

%Separate estimates into AR and X matrices
Aest3D = reshape(hest2mat(1:na*s,1:s)',s,s,na);

%Append identity matrix to AR matrix; ie A(0) = I
Aest3D = cat(3,eye(s,s),Aest3D);

Amat = Aest3D;

Aestcell = cell(1,na+1);
for ii = 1:na+1
    Aestcell{1,ii} = Aest3D(:,:,ii);
end

%Calculate roots of the AR matrix polynomial. Note that the polyeig
%function will calculate roots with the correct damping sign when the
%order of coefficient of the function argument not changed
Aestroots = polyeig(Aestcell{:});

%Calculate the number of roots with positive damping (ie, that appear
%within the unit circle)

no_st_roots = length(find(abs(Aestroots) < 1));

Aestroots = reshape(Aestroots,na,s);

%Extract X matrix polynomial coefficients
Bestvec = nonzeros(hest2mat(na*s+1:na*s + nb*m*s + m*s,:)');

if size(Bestvec,1)*size(Bestvec,2) ~= s*m*(nb+1)
    error('Incorrect structure estimated for X matrix')
end

Best3D = reshape(Bestvec,s,m,nb+1);

Bmat = Best3D;

%----------------------------------------------------------------------
%Stage 4 extract updated C matrix

Hsize = size(Hyestvec,3);
```

```
%form matrix of V coefficients
blokAmat = cell(Hsize,nc+1);
blokAmat(:) = {zeros(s,s)};

for ii = 1:Hsize
    %define limits of convolution
    aa = max(1,ii + 1 - (na+1));
    bb = min(ii,nc+1);
    jj = aa;
    while (jj <= ii)&&(jj <= bb)
        blokAmat{ii,jj} = Aest3D(:,:,ii + 1 - jj);
        jj = jj+1;
    end
end

blokAmat = cell2mat(blokAmat);

Hyestvec_2 = reshape(Hyestvec,s,Hsize*s)’;

Cmat = blokAmat\reshape(Hyestvec,s,Hsize*s)’;

Cmat = reshape(Cmat’,s,s,nc+1);


%Stabilise Cmat
tempC = cell(1,s);
staCmat = zeros(size(Cmat));
for ii = 1:s
    tempC{1,ii} = reshape(Cmat(ii,ii,1:nc+1),1,nc + 1);
    tempC{1,ii} = polystab(tempC{1,ii});
    staCmat(ii,ii,1:nc+1) = reshape(tempC{1,ii},1,1,nc+1);
end

Cmat = staCmat;
```

```
function [wtbac,inncovrev,BICrev,BICrev2,inn_cov_ms_av_b,inn_cov_ms_det_b]
= RC_innov4(Amat,Bmat,Cmat,yn,fn,Ts,Tt)

%Function to calculate the innovations covariance, BIC, modified BIC and
%covariance functions of innovations sequence

%Define system matrices
Aest3D = Amat;
Best3D = Bmat;
Cest23D = Cmat;

%Define N,s,m
N = size(yn,2);
s = size(yn,1);
m = size(fn,1);

%Define order of system matrices
na = size(Aest3D,3) - 1;
nb = size(Best3D,3) - 1;
nc = size(Cest23D,3) - 1;

Ccell_tempbac = cell(nc+1,1);
for ii = 1:nc+1
    Ccell_tempbac{ii,1} = Cest23D(:,:,ii);
end

%Construct Yf matrix
Yf = cell(1,s);
for kk = 1:s
    Yfi = zeros(s,s,N);
    for ii = 1:N
        jj = 1;
        while (jj <= nc+1)&&(jj <=ii)
            Yfi(:,:,ii) = Yfi(:,:,ii) + yn(kk,ii - jj +
1)*Cest23D(:,:,jj);
            jj = jj + 1;
        end
    end
    Yf{1,kk} = Yfi;
end
Yf = cell2mat(Yf);


%Construct Ff matrix
Ff = cell(1,m);
for kk = 1:m
    Ffi = zeros(s,s,N);
    for ii = 1:N
        jj = 1;
        while (jj <= nc+1)&&(jj <=ii)
            Ffi(:,:,ii) = Ffi(:,:,ii) + fn(kk,ii - jj +
1)*Cest23D(:,:,jj);
            jj = jj + 1;
        end
    end
    Ff{1,kk} = Ffi;
end
Ff = cell2mat(Ff);

%-----------------------------------------------------------------------
%Recursive estimation of ARMAX prediction errors for BACKWARDS ARMAX model
```

```
%i.e using the original estimated parameter matrices and REVERSED time
%series. Note that the estimated system modes will be unstable and may
lead
%to numerical instability

%Construct Pt
n1 = max(na,nb);

Avec = reshape(Amat,na*s^2+s^2,1);
Bvec=  reshape(Bmat,nb*m*s + m*s,1);

wtbac = zeros(s,N-n1);
AYfbac = zeros(s,N-n1);
BFfbac = zeros(s,N-n1);

%Calculate innovations sequence
for tt = 1:N-n1
    Yfvec = reshape(Yf(:,:,tt:tt+na),s,na*s^2 + s^2);

    Ffvec = reshape(Ff(:,:,tt:tt+nb),s,nb*m*s + m*s);

    AYfbac(:,tt) = Yfvec*Avec;

    BFfbac(:,tt) = Ffvec*Bvec;

    wtbac(:,tt) = BFfbac(:,tt) - AYfbac(:,tt);
end

%----------------------------------------------------------------------

%innovations covariance for reverse innovations covariance

inncovsumrev = zeros(s,s);
for tt = 1:N-max([na,nb,nc])
    inncovsumrev = inncovsumrev + wtbac(:,tt)*wtbac(:,tt)’;
end

inncovrev = inncovsumrev/(N-(max([na,nb,nc])+1));


%Calculation of BIC for reverse innovations covariance

dbicrev = na*s^2 + nb*s*m + nc*s^2;
BICrev = log(det(abs(inncovrev))) + dbicrev*(log(N)/N);
BICrev2 = log(det(abs(inncovrev)));

%----------------------------------------------------------------------

%Calculate sum of mean-square covariance sequence and determinant of
%mean-square covariance sequence matrix

%wtbac:
inn_cov_b = xcorr(wtbac’);
inn_cov_ms_b = mean(inn_cov_b.^2);
inn_cov_ms_av_b = sum(inn_cov_ms_b’) - trace(reshape(inn_cov_ms_b,s,s));
inn_cov_ms_det_b = det(reshape(inn_cov_ms_b,s,s)’);
```

```
%Synthesise FRFs and calculate modal parameters from estimated ARMAX
models

%set the number of measurement files
n_fils = 15;

%set file name for loading ARMAX model data and for saving FRF and mode
%shape data
dat_file_name = ['MISO_ARMAX_HT212_1_v1_m'];
FRF_file_name = [dat_file_name '_FRFs'];
Mod_file_name = [dat_file_name '_modes'];
load([dat_file_name '1_full'])

%arrange columns of mod_par_cell into order of measurement points
pos_vec = 1:31;

%set driving pt vector, which should be a 1xm vector with elements
%corresponding to the excitation points
drv_pt = [29 9];

%variables to store FRF magnitude and phase data
magcell = cell(1,n_fils);
phacell = cell(1,n_fils);

s = size(Amat,1);
m = size(Bmat,2);

%initialise cell array to store modal parameters
n_meas = 31;
pol_res_cell = cell(1,n_meas,m);

%model selection for each results file
res_cell_ind = 0;
for kk = 1:n_fils
    %load file
    file_name = [dat_file_name num2str(kk) '_full']
    load(file_name)

    [n_mods, n_iters, d_v] = size(parmatcell);

    %NPDP
    [ia,ib] = max(stArootsmat(:,:)');
    [ic,id] = max(ia);

    [id,ib(id)]

    Amat = parmatcell{id,ib(id) + 1,1};
    Bmat = parmatcell{id,ib(id) + 1,2};
    Cmat = parmatcell{id,ib(id) + 1,3};

    na = size(Amat,3) - 1;
    nb = size(Bmat,3) - 1;
    s = size(Amat,1);
    m = size(Bmat,2);

    %reverse AR matrix
    Ana_inv = inv(Amat(:,:,na + 1));
    Amat_rev = zeros(size(Amat));
    for jj = 1:na + 1
        Amat_rev(:,:,jj) = Ana_inv*Amat(:,:,na + 2 - jj);
    end
```

```
    %set the reverse A(0) to Is
    Amat_rev(:,:,1) = eye(s,s);

    %reverse X matrix
    Bmat_rev = zeros(size(Bmat));
    for jj = 1:nb + 1
        Bmat_rev(:,:,jj) = Ana_inv*Bmat(:,:,nb + 2 - jj);
    end

    %Calculate natural frequencies, damping, and mode shapes for each SISO
    %system
    freqdamprescell = cell(1,s,m);
    for mm = 1:s
        Apoly = reshape(Amat_rev(mm,mm,:),1,na + 1);
        for nn = 1:m
            Bpoly = reshape(Bmat_rev(mm,nn,:),1,nb + 1);
            [ttr,ttp,ttk] = residuez(Bpoly,Apoly);
            nroots = size(ttr,1);
            wr = zeros(nroots,1);
            damp = zeros(nroots,1);
            for i2 = 1:nroots
               wr(i2,1) =
(1/Ts)*sqrt(log(ttp(i2,1))*log(conj(ttp(i2,1))));
                damp(i2,1) = -
100*log(ttp(i2,1)*conj(ttp(i2,1)))/(2*wr(i2,1)*Ts);
            end
            freqdamprescell{1,mm,nn} = [wr/(2*pi),damp,ttr];
        end

        for nn = 1:m
           freqdamprescell{1,mm,nn} =
sortrows(freqdamprescell{1,mm,nn},1);
        end
    end

    pol_res_cell(1,res_cell_ind + 1:res_cell_ind + s,:) = freqdamprescell;
    res_cell_ind = res_cell_ind + s;

    %Create Matlab sysID ARX model
    Piezo_1_arx = idarx(Amat_rev,Bmat_rev,Ts);

    %Calculate FRF for specified frequency scale
    wscale = [0:0.25:0.5/Ts - 0.25];
    [mag,phase] = ffplot(Piezo_1_arx,wscale);
    mag_cell{kk,1} = mag;
    pha_cell{kk,1} = phase;
    %dimensions of arguments are as follows (number of outputs)x(number of
inputs)x(length of w)
end

%save FRF data
save(FRF_file_name,'wscale','mag_cell','pha_cell')

%form matrices for FRF magnitude data (this only uses data for the first
%measured excitation

mag_temp = [];
for kk = 1:n_fils
    n_outputs = size(mag_cell{kk,1},1);
    for mm = 1:n_outputs
```

```
        mag_temp = [mag_temp reshape(mag_cell{kk,1}(mm,1,:),1200,1)];
    end
end

n_resps = size(mag_temp,2);

%form matrices for FRF phase data
pha_temp = [];
for kk = 1:n_fils
    n_outputs = size(mag_cell{kk,1},1);
    for mm = 1:n_outputs
        pha_temp = [pha_temp reshape(pha_cell{kk,1}(mm,1,:),1200,1)];
    end
end

%plot FRF data
figure
semilogy(wscale,mag_temp)
xlabel('Frequency (Hz)')
ylabel('Magnitude ms^{-2}/N')
title('Estimated FRF magnitudes')

% figure
% semilogy(wscale,sum(abs(mag_temp'.*sin(pha_temp')))/n_resps)
% xlabel('Frequency (Hz)')
% ylabel('Magnitude m.s^{-2}/N')
% title('Averaged FRF Imaginary Part')
%
% figure
% semilogy(wscale,sum(abs(mag_temp'.*cos(pha_temp')))/(n_resps))
% xlabel('Frequency (Hz)')
% ylabel('Magnitude m.s^{-2}/N')
% title('Averaged FRF Real Part')

figure
semilogy(wscale,sum((mag_temp'))/(n_resps))
xlabel('Frequency (Hz)')
ylabel('Magnitude m.s^{-2}/N')
title('Averaged FRF Magnitudes')


% %select frequency ranges for modes
% display(['Select modal peaks, press enter when finished'])
% [c_freq,amp] = ginput

%Results estimated for MIMO E2 data (used for testing purposes, i.e. to
%ensure repeatability of results)
c_freq = [73.89; 77.3; 85.38; 113.62; 143.6; 164.2; 165.85; 186.05;
201.63; 239.03; 244.78; 263.05; 281.06; 282.9];

n_bands = size(c_freq,1);
%use selected frequency ranges to collect modal data
mod_par_cell = cell(n_bands,n_resps,m);
for mm = 1:m
    for nn = 1:n_resps
        freq_temp = pol_res_cell{1,nn,mm}(:,1);
        for kk = 1:n_bands
            [inda,indb] = min(abs(freq_temp - c_freq(kk,1)));
            %if there is no pole within 2% then set damping and residues
            %to zero
            if abs(inda/c_freq(kk,1)) < 0.02
```

```
                mod_par_cell{kk,nn,mm} = pol_res_cell{1,nn,mm}(indb,:);
            else
                mod_par_cell{kk,nn,mm} = [NaN NaN NaN];
            end
        end
    end
end

mod_par_mat = cell2mat(mod_par_cell);

%sort data according to measurement position
pos_vec2 = pos_vec;
[pos_vec2,ind_s] = sort(pos_vec2);

mod_par_cell_temp = mod_par_cell;

for mm = 1:m
    for kk = 1:size(pos_vec2,2)
        mod_par_cell(:,kk,mm) = mod_par_cell_temp(:,ind_s(kk),mm);
    end
end

drv_pt_ind = zeros(1,m);
for mm =1:m
    drv_temp = find(pos_vec2 == drv_pt(1,mm));
    drv_pt_ind(1,mm) = drv_temp(1);
end

mod_par_mat = cell2mat(mod_par_cell);

%calculate average modal parameters and variance
av_freq = zeros(n_bands,1);
std_freq = zeros(n_bands,1);

av_damp = zeros(n_bands,1);
std_damp = zeros(n_bands,1);

av_damp2 = zeros(n_bands,1);
std_damp2 = zeros(n_bands,1);

for kk = 1:1
    for mm = 1:n_bands
       %modal frequency
       av_freq(mm,kk) = nanmean(mod_par_mat(mm,[1:3:3*n_resps],kk));
       std_freq(mm,1) = nanstd(mod_par_mat(mm,[1:3:3*n_resps],kk));
       temp_damp_vec = mod_par_mat(mm,[2:3:3*n_resps],kk);
       %only positive damped modes
       av_damp(mm,kk) = nanmean(temp_damp_vec(find(temp_damp_vec > 0)));
       std_damp(mm,1) = nanstd(temp_damp_vec(find(temp_damp_vec > 0)));
       %all identified modes
       av_damp2(mm,kk) = nanmean(temp_damp_vec);
       std_damp2(mm,1) = nanstd(temp_damp_vec);
   end
end

[av_freq av_damp av_damp2]

%scaled mode shapes. If no point-mobility residue is calculated for a
%particular mode then the mode is left unscaled.
unsc_mod_cell = cell(n_bands,m);
sc_mod_cell2 = cell(n_bands,m);
```

```
figure
for kk = 1:m
    for mm = 1:n_bands
        if mod_par_mat(mm,drv_pt_ind(kk)*3,kk) == 0;
            mod_scale = 1;
            d2c_scale = 1;
        else
            mod_scale = (mod_par_mat(mm,drv_pt_ind(kk)*3,kk));
        end
        %scaled shapes
        mod_temp3 = mod_par_mat(mm,[3:3:3*n_resps],kk)/mod_scale;
        mod_temp3 = abs(mod_temp3).*cos(angle(mod_temp3));
        %unscaled shapes
        mod_temp1 = mod_par_mat(mm,[3:3:3*n_resps],kk);
        mod_temp1 = abs(mod_temp1).*cos(angle(mod_temp1));
        unsc_mod_cell{mm,kk} = mod_temp1;
        sc_mod_cell2{mm,kk} = mod_temp3;
        plot(reshape(mod_temp3',n_meas,1))
        title(['Mode ' int2str(mm) ': ' num2str(av_freq(mm,1)) ' Hz'])
        pause
    end
end

% plot estimated frequency values for each mode and model

% figure
% for kk = 1:m
%     for mm = 1:n_bands
%         plot(pos_vec2,mod_par_mat(mm,[1:3:3*n_resps],kk))
%         xlabel('Measurement Point')
%         ylabel('Modal Frequency (Hz)')
%         title(['Mode ' int2str(mm) ': ' num2str(av_freq(mm,1)) ' Hz'])
%         pause
%     end
% end
%
%
% %plot estimated damping values for each mode and each model
% figure
% for kk = 1:m
%     for mm = 1:n_bands
%         plot(pos_vec2,mod_par_mat(mm,[2:3:3*n_resps],kk))
%         xlabel('Measurement Point')
%         ylabel('Modal Damping (%)')
%         title(['Mode ' int2str(mm) ': ' num2str(av_freq(mm,1)) ' Hz'])
%         pause
%     end
% end

save(Mod_file_name,'n_bands','pos_vec2','mod_par_mat','av_freq','av_damp',
'av_damp2','std_freq','std_damp','std_damp2','unsc_mod_cell','sc_mod_cell2
')
```